NANYANG
TECHNOLOGICAL
UNIVERSITY

NODAL-BASED DISCONTINUOUS
DEFORMATION ANALYSIS

BAO HUIRONG

2010

NODAL-BASED DISCONTINUOUS DEFORMATION ANALYSIS

BAO HUIRONG

SCHOOL OF CIVIL AND ENVIRONMENTAL ENGINEERING

2010

NODAL-BASED DISCONTINUOUS DEFORMATION ANALYSIS

BAO HUIRONG

School of Civil and Environmental Engineering

A thesis submitted to the Nanyang Technological University
in fulfillment of the requirement for the degree of
Doctor of Philosophy

2010

ACKNOWLEDGEMENTS

The work presented in this thesis would not been possible without the help and support of many people.

First of all, I would give my deep appreciation to my supervisor, Prof. Zhao Zhiye, for his supervision and encouragement during my research work. It has been a great privilege and honor to work with him.

I would also like to express my appreciation to Dr. Shi Genhua for his supply of the original DDA source code and valuable encouragement and suggestion.

I am grateful to Prof. Ma Guowei for providing valuable information and support during my research.

The financial support for my graduate study from Nanyang Technological University is appreciated.

I would also like to thank my friends, He Lei, Huang Xin, Ning Youjun and An Xinmei, et al. for their accompanying and valuable advices.

Finally, I would give my special thanks to my parents and my wife for their support and love, without which there will never be this thesis. I would like to say that they deserve my entire honor in my life for what they have done for me.

TABLE OF CONTENTS

ABSTRACT

This thesis presents an enhanced nodal-based discontinuous deformation analysis (NDDA) based on the coupling of the discontinuous deformation analysis (DDA) and the finite element method (FEM), for modeling blocky systems, especially for simulating crack propagation in rock mass. The NDDA can provide a more accurate stress and strain distribution in each block and has a higher computational efficiency than the standard DDA in dealing with continuum materials. Furthermore, the enhanced NDDA allows for tensile and shear fracturing happening inside an intact block, which provides a way for material transforming from continuum into discontinuum. A computer program named 2D-NDDA was developed to handle the combination of continuous and discontinuous in large displacement problems, as well as large deformation and failure analysis, under external loads and boundary conditions.

After a brief introduction of the concept of the standard DDA, detailed reviews of the validation and enhancement of the DDA in the past decades are given in the thesis. The formulae of NDDA, including the analytical solutions for the inertia matrix and contact matrices which control the stability of the open-close iterations of block kinematics, are provided and discussed. In the strict sense of the word, the NDDA is not a simple couple of the FEM and the DDA but a unifying of them. It can work at three states: pure FEM, pure DDA and mixed. The NDDA works in an FEM mode when the system is continuous, in a DDA mode if the system is totally discontinuous, or in a mixed mode for mixed state.

There is no difficult to carry out the idea of NDDA since the FEM and the DDA are both derived from the minimization of the total potential energy of the system. More conveniently, any FEM code can be easily transformed into a DDA code when the kinematics part is considered. To transform an FEM algorithm into a DDA

algorithm, two steps are necessary: (1) scheme for the fracture of the continuous material; (2) introducing of the inertia and kinematics matrices.

Finally, applications of the newly enhanced NDDA are shown by several numerical examples with comparison to the analytical or experimental results. The simulation results show that the NDDA can model wave propagating inside continuous and elastic media and the brittle fracture of rock as well. Indeed, the NDDA can be applied to more engineering problems other than the above applications if more mature FEM algorithms are applied into it.

Like any other numerical methods in their early developing stage, the NDDA still has a lot of shortcomings. The fracture scheme including crack criterion and node splitting algorithm in the NDDA program is still in the developing and testing stage. The quality of the mesh and the shape of element have an important effect on the simulation results of the NDDA as well as that from the FEM. However, all these limitations can be solved in the future work and cannot prevent the NDDA from being a powerful numerical tool.

LIST OF FIGURES

LIST OF TABLES

CHAPTER 1 INTRODUCTION

1.1 Background

Numerical simulation has increasingly become a very important approach for solving complex practical problems in engineering and science. The finite element method (FEM) is perhaps the most widely applied numerical method. A basic concept of the FEM is discretization, i.e., a continuum system is subdivided into a finite number of well-defined elements. Each element is defined by certain nodes, and nodal displacements are selected as the unknowns of the governing equation. For each element, a polynomial is often used to describe the displacement field of that element so that the displacement field can be interpolated by the nodal displacements. To obtain a complete solution, the conditions of compatibility and equilibrium must be fulfilled. Since the nodes of elements sharing common node numbers will have identical displacements, the first condition is automatically satisfied on nodes. The second condition is achieved by minimizing the total potential energy equation of the system.

Representation of rock fractures by the FEM has been motivated by rock mechanics since the late 1960s, with the wide application of the ‘Goodman joint element’ (Goodman, Taylor et al. 1968) in the FEM codes. However, these models are also formulated based on the continuum assumption which does not permit large-scale opening, sliding, and complete detachment of elements. The treatment of fractures and fracture propagation remains as one of the most important limiting factors in the application of the FEM for rock mechanics problems. The FEM suffers from the fact that the global stiffness matrix tends to be ill-conditioned when many fracture elements are incorporated. Block rotations, complete detachment and large-scale fracture opening cannot be treated because the general continuum assumption in the FEM formulations requires that fracture elements cannot be torn apart. When simulating the process of fracture propagation, the FEM is handicapped by the contact problem and heavy computational burden caused by continuous re-meshing with fracture growth. This overall shortcoming makes the FEM less efficient in dealing with fracture problems than the discontinuum-based methods.

The distinct element method (DEM) (Cundall 1971) is one of the discontinuum-based methods and has been broadly used for the numerical computations of jointed or blocky rock engineering problems. The key concept of the DEM is to treat the domain of interest as an assemblage of rigid or deformable blocks. The contacts between blocks need to be identified and continuously updated during the entire deformation/motion process, and be represented by appropriate constitutive models. The theoretical foundation of the method is the formulation and solution of equations of motion of blocks using explicit formulations. Nevertheless, it is a force method which incorporates fictitious forces to satisfy the contact conditions and obtain the equilibrium state of the whole system.

The discontinuous deformation analysis (DDA) (Shi 1988) is the other member of the discontinuum-based methods. Different from the DEM, the DDA is an implicit method like the FEM. It chooses the displacements and strains as variables and solves the equilibrium equations in the same way as the FEM does. Moreover, the DDA has two advantages over the DEM: (1) less restrictions on the time step interval, i.e., relatively larger time steps are allowed; and (2) closed-form integrations for the stiffness matrices of blocks are performed. Another attractive advantage of the DDA is that an existing FEM code can be readily transformed into a DDA code while retaining all the advantageous features of the FEM.

The DDA has emerged as an attractive model for geomechanical problems because its advantages cannot be replaced by the continuum-based methods or the explicit discrete element methods. Different from the FEM whose mesh is arbitrarily created by the analyzer, the DDA deals with a mesh that is real rock joints. The DDA does not imply continuity at block boundaries, i.e., they can be totally discontinuous. In fact, the blocks are independent and they only have connections while contacting each other. These connections are performed by adding contact springs to the contact positions. To find the correct contact pairs optimally, the DDA requires the development of a complete block kinematic theory which can obtain large displacement and deformation solutions for blocky systems under general loading and boundary conditions.

The DDA chooses the complete first order polynomial as the displacement function for a two-dimensional block, which restricts the block to constant stresses and limits the deformation abilities of the block. If a more complicated stress field and more deformable block boundary are desired, enhancements to the original DDA method are necessary. During the past decades, three kinds of enhancement had been developed. By incorporating higher order displacement functions or two-dimensional Fourier series (Koo, Chern et al. 1995; Hsiung 2001), the DDA obtained an improved stress distribution inside blocks and a better description of the block deformation. This enhancement is easy to be applied but when the block shape is very odd, the stress and strain distribution still cannot satisfy the requirement. And the high order displacement functions will lead the boundary of blocks to deform into curve lines, which makes the contact detection much more complex, if the deformed boundary is considered. The other enhancement was fulfilled by introducing artificial joints into real blocks (Ke 1993; Lin 1995). This method cuts a real block into a number of sub-blocks, and sub-blocks are connected together at contacts by unbreakable springs which are held fixed to assure continuity across any artificial joint up to a certain limit. However, the remarkable increase of contact number between blocks causes a heavy computation burden. The last but most promising enhancement is coupling the finite element mesh into a block (Shyu 1993; Chang 1994). This enhancement largely increased the deformation ability of blocks and refined the stress distribution inside blocks. Moreover, it avoided the ambiguity of curved contact encountered by the higher order method, and avoided introducing unnecessary and artificial contacts which characterized the sub-block method. Furthermore, the coupling method provided a bridge between the FEM and the DDA. The nodal-based DDA (NDDA) presented in this thesis is based on this idea but with an extension of the fracture ability in intact blocks.

1.2 Objectives

The main goal of this thesis is to develop a two-dimensional nodal displacements based discontinuous deformation analysis method to simulate crack initiation and propagation in rock materials. The objectives of this study are outlined as follows:

(1) Develop an improved discontinuous deformation analysis method (NDDA) based on the original DDA but with nodal displacements as unknowns. The newly developed NDDA method should be able to solve continuous problems as well as discontinuous problems.

(2) Develop an auto mesh generator to generate finite element mesh inside DDA blocks as a preprocessor for the NDDA.

(3) Develop a scheme to provide block fracture capability with proper fracture criterion in the NDDA.

(4) Improve the precision of vertex-vertex contact treating for both the original DDA and the newly developed NDDA.

(5) Use the newly developed NDDA method to analyze crack propagation problems, and comparing numerically obtained results to existing experiments to verify its validation for real problems.

(6) To develop a suitable computer program (2D-NDDA), which can achieve the above purpose and easy to use.

1.3 Organization of the Thesis

The Thesis consists of eight chapters. Chapter 1 gives an introduction to the research work and provides the general objectives of the study as well as the outline of the thesis.

Chapter 2 provides a literature review of the numerical methods mostly used in rock mechanics. Furthermore, a review of the DDA theory and related validation and application works done in the past decades are presented. A detailed review of the enhancements to the DDA is presented.

Chapter 3 derives the formulations employed in the proposed NDDA. The formulations are confined to traditional triangular finite element mesh.

Chapter 4 discusses the automatic triangular mesh generation algorithm which is employed in preprocess of newly developed NDDA code. A high efficiency Delaunay triangulation refinement algorithm is proposed and implemented.

Chapter 5 provides a scheme for fragmentizing an intact block into smaller blocks using the Mohr-Coulomb failure criterion. A mesh boundary update algorithm is provided.

Chapter 6 discusses the indeterminacy of the vertex-vertex contact in the DDA and provides alternative methods based on the motion of vertexes to handle the indeterminacies.

Chapter 7 presents numerical examples that serve as an illustration of the potential usage of the developed NDDA method for the analysis of rock fracture problems.

Chapter 8 summarizes the major conclusions drawn from the study and presents possible further research.

CHAPTER 2 LITERATURE REVIEW

2.1 Introduction

In section 2.2, a review of numerical methods applied in rock engineering is presented. In section 2.3, theory of the standard DDA is presented. In section 2.4, the standard DDA program flowcharts are proposed. In section 2.5, the validation and enhancement of the DDA carried out by other researchers are introduced.

2.2 Numerical Methods in Rock Mechanics

With the increasing needs to design and evaluate practical rock engineering structures, numerical simulation for rock mechanics has been developed for decades with widely different purposes, and a wide spectrum of numerical approaches have been developed to assist various numerical investigations. The purpose of numerical modelling in rock mechanics is not only to provide specific values of stresses and displacements at specific points but also to enhance our understanding of the processes involved, particularly the changes that result from the perturbations introduced by engineering activities.

The development of numerical models and computer hardware now provide essential support for the rock mechanics analyses and understanding. Moreover, such developments and progress in computer methods for rock engineering will continue because they are mainly stimulated by the prospect that they will provide the information that cannot be obtained by experiments, because conducting large-scale in situ experiments is most often not possible.

The fractured rock mass comprising the Earth's upper crust is a discrete system. Closed-form solutions do not exist for such geometries and numerical methods must be used for solving practical problems. Due to the differences in the underlying material assumptions, different numerical methods have been developed for continuous and discrete systems. The most commonly applied numerical methods for rock mechanics problems are sorted into three categories according to Jing (2003) with a minor revision:

(1) Continuum methods ---- Finite Difference Method (FDM), Finite Element Method (FEM), Boundary Element Method (BEM);

(2) Discontinuum methods ---- Distinct Element Method (DEM), Discrete Fracture Network (DFN) methods, Discontinuous Deformation Analysis (DDA);

(3) Hybrid continuum/discontinuum methods ---- hybrid FEM/BEM, hybrid DEM/BEM, hybrid FEM/DEM.

The choice of continuum or discontinuum methods depends on many problem-specific factors, but mainly on the problem scale and fracture system geometry. Figure 2.1 illustrates the discretization concepts of the FDM/FEM, BEM, and DEM/DDA for fractured rocks. The continuum approach can be used if only a few fractures are present and no fracture opening and no complete block detachment is possible. The discontinuum approach is more suitable for moderately fractured rock masses where the number of fractures is too large for the continuum approach, or where large-scale displacements of individual blocks are possible.

Modelling fractured rocks demands high performance numerical methods and computer codes, especially regarding the discontinuities representation, material heterogeneity and non-linearity, coupling with fluid flow and heat transfer and scale effects. There are no absolute advantages of one method over the other and it is unnecessary to restrict the application to only one method. Some of the disadvantages inherent in one method can be overcome by hybrid models.

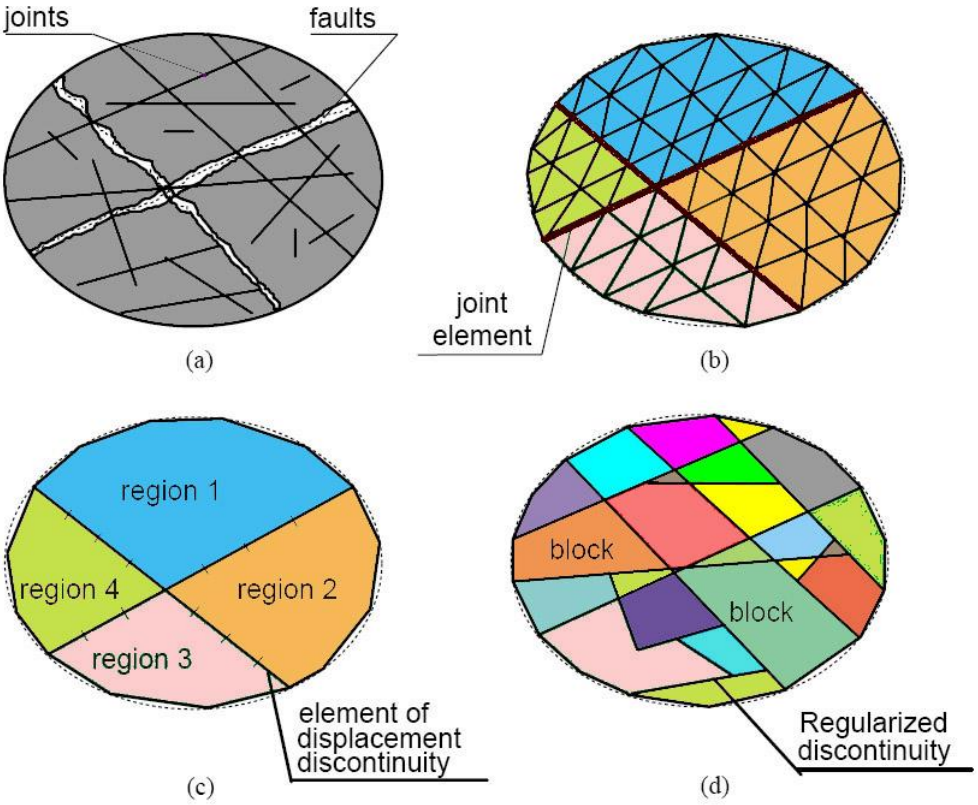

Figure 2.1 schematization of a fractured rock mass: (a) real model; (b) by FDM or FEM; (c) by BEM; (d) by DEM or DDA (Jing 2003)

2.2.1 Finite Difference Method

The FDM is a classical numerical method developed by mathematicians for obtaining the approximate solutions to partial differential equations (PDEs) in engineering problems. The basic concept of FDM is to replace the partial derivatives of the objective function by differences defined over certain spatial intervals in the coordinate directions on the domain of definition and transforming the differential problem into an algebraic linear system of equations for the values of objective functions at all grid (mesh) nodes over the domain of interest (Greenspan 1965; Richtmyer and Morton 1967). Solution of the simultaneous equations, incorporating boundary conditions defined at boundary nodes, gives an approximate numerical solution of the given problem.

The conventional FDM utilizes a regular grid of nodes to generate objective function values at sampling points with small enough intervals between them, so that errors thus introduced are small enough to be acceptable. It has some shortcomings when dealing with problems involving fractures, complex boundary conditions or material inhomogeneity. This makes the standard FDM generally unsuitable for modelling practical rock mechanics problems. Although irregular meshes had been introduced into FDM by Perrone and Kao (1975) which can enhance the applicability of the FDM for rock mechanics problems, the most significant improvement comes from the so-called Finite Volume Method (FVM).

As a branch of the FDM, the FVM can overcome the inflexibility of the grid generation and boundary conditions in the traditional FDM with unstructured grids of arbitrary shape. It has similarities with the FEM and is also regarded as a bridge between FDM and FEM, as pointed out in Selim (1993) and Fallah et al. (2000). A FVM model can be readily constructed using a standard FEM mesh, as shown in Bailey and Cross (1995). Similar examples of FVM for non-linear stress analysis with elasto-plastic and visco-plastic material models were given in Fryer et al. (1991).

2.2.2 Finite Element Method

Clough (1960) appeared to be the first to use the term ‘finite element’ for plane stress problems (Zienkiewicz and Taylor 2000). Since the early 1960s much progress has been made, and the method was rapidly adopted and promoted in many scientific and engineering fields, as illustrated by the books of Zienkiewicz (1977) and Bathe (1982).

Generally, an FEM analysis includes three steps: (1) domain discretization; (2)

local approximation; (3) assemblage and solution of the global matrix equation. Firstly, the domain discretization involves dividing a domain into a finite number of sub-domains (elements) of smaller size and standard shape (triangle, quadrilateral, tetrahedral, etc.) with fixed number of nodes at the vertices and/or on the sides. Secondly, the trial functions, usually polynomial, are used to approximate the behavior of PDEs at the element level and generate the local algebraic equations representing the behavior of the elements. Finally, the local elemental equations are assembled, according to the topologic relations between the nodes and elements, into a global system of algebraic equations whose solution then produces the required information in the solution domain, after imposing the properly defined initial and boundary conditions.

The FEM is perhaps the most widely applied numerical method in engineering today because of its flexibility in handling material heterogeneity, non-linearity and boundary conditions, with many well developed and verified commercial codes with large capacities in terms of computing power, material complexity and user friendliness. But the application of FEM to rock mechanics was very limited in its early stage because of the widely spread of discontinuities inside the rock mass. A great improvement was only obtained after the introduction of interface models (Goodman, Taylor et al. 1968; Zienkiewicz, Best et al. 1970; Ghaboussi, Wilson et al. 1973; Michael 1983; Desai, Zaman et al. 1984) in the FEM. However, even with this improvement, the FEM was still limited to the small displacement assumptions.

The application of FEM to simulate the process of fracture propagation is not efficient because of the heavy computation burden caused by continuous re-meshing with fracture growth. In the past decades, a special class of FEM, often called ‘enriched FEM’, has been developed especially for fracture analysis with minimal or no re-meshing (Babuska and Osborn 1983; Belytschko and Black 1999; Nicolas, John et al. 1999; Christophe, Nicolas et al. 2000; Duarte, Babuska et al. 2000; Strouboulis, Babuska et al. 2000; Sukumar, Moes et al. 2000; Duarte, Hamzeh et al. 2001; Strouboulis, Copps et al. 2001; Sukumar and Prevost 2003; Combescure, Gravouil et al. 2008; Guidault, Allix et al. 2008; Tabarraei and Sukumar 2008). The ‘enriched FEM’ with jump functions and crack tip functions has improved the FEM’s capacity in fracture analysis. But, it is still limited to few cracks. Another FEM model for the analysis of fracture problem without re-meshing is the cohesive zone type interface model (Needleman 1987; Needleman 1990; Xu and Needleman 1994; Camacho and Ortiz 1996; Xu and Needleman 1996). In this model, the finite element discretization is based on linear displacement triangular elements. Each node at an intersection is connected by cohesive surfaces, belongs to different element and has different node number although their coordinates are identical. The continuum is characterized by two constitutive relations: a volumetric constitutive law that relates stress and strain; and a cohesive surface constitutive relation between the tractions and displacement jumps across a specified set of cohesive surfaces that are interspersed throughout the continuum.

Another limitation of the FEM is that it cannot simulate infinitely large domains (as sometimes presented in rock engineering problems, such as half-plane or half-space problems) and the efficiency of the FEM will decrease significantly when the degrees of freedom is too large, which is in general proportional to the number of nodes.

2.2.3 Boundary Element Method

The developments and applications of BEM in the field of rock mechanics can be found in many BEM works (Brady and Bray 1978; Hoek and Brown 1981; Crouch and Starfield 1983; Pande, Beer et al. 1990). The BEM requires discretization at the boundary of the problem domains only, thus reducing the problem dimensions by one and greatly simplifying the input requirements. The information required in the solution domain is separately calculated from the information on the boundary, which is obtained by solution of a boundary integral equation, instead of direct solution of the PDEs, as in the FDM and FEM. The BEM is often more accurate than the FDM and FEM at the same level of discretization and is also the most efficient technique for fracture propagation analysis and simulating infinitely large domains.

However, in general, the BEM is not as efficient as the FEM in dealing with material heterogeneity, because it cannot have as many sub-domains as elements in the FEM. The BEM is also not as efficient as the FEM in simulating non-linear material behaviour, such as plasticity and damage evolution processes, because domain integrals are often presented in these problems.

The BEM is more suitable for solving problems of fracturing in homogeneous and linearly elastic bodies. But, it is difficult to analyze fracturing processes for rock mechanics problems. On the one hand, what happens exactly at the fracture tips in rocks still needs to be further understood, with the additional complexities caused by the microscopic heterogeneity and non-linearity at the fracture tip scale, especially regarding the fracture growth rate. On the other hand, complex numerical manipulations are still needed for re-meshing following the fracture growth process so that the tip elements are added to where new fracture tips are predicted, and updating of system equations following the re-meshing, although the task is much less cumbersome than that required for domain discretization methods such as standard FEM.

2.2.4 Distinct Element Method

The distinct element method (DEM) is a member of the discrete element family with explicit form. Since Cundall (1971) first introduced the DEM to simulate progressive movements in blocky rock systems, the DEM has been well developed over the past decades and has become the most widely used discontinuum method in rock mechanics. The first version of DEM only handled a system of discrete rigid blocks. Cundall et al. (1978) then extended it for deformable blocks. The DEM has been widely applied to different engineering problems as shown in many works (Fairhurst and Pei 1990; Kusano, Aoyagi et al. 1992; Chuhan, Pekau et al. 1997; Kim, Kim et al. 1997; Esaki, Jiang et al. 1998; Su and Stephansson 1999; Moon, Nakagawa et al. 2007; Jiang, Li et al. 2009).

In the DEM, a rock mass is represented as an assembly of discrete blocks. Joints are viewed as interfaces between distinct bodies i.e. the discontinuity is treated as a boundary condition rather than a special element in the model. At the start of every step, contacts are detected based on the current penetrations between blocks. Given the elastic contact stiffness, the amount of penetration at each contact determines the contact forces between blocks, which are regarded as additional external forces of the system at the current step. Then, unbalanced forces drive the solution process, and a mathematical damping is used to dissipate the extra kinetic energy. Because of its incomplete block kinematics and mathematical damping, the explicit scheme used in the DEM cannot guarantee the dynamic equilibrium state of a system at any time. Moreover, because the DEM employs a central difference procedure which requires that the time step size is small enough to assure stability. This requirement is one of the main disadvantages of this method.

2.2.5 Discontinuous Deformation Analysis

The DDA is another member of the discrete element family and is used for analyzing force-displacement interactions of block systems. This method is an implicit method which uses the displacements and strains as unknowns and solves the equilibrium equations in the same manner as the matrix analysis of structures in the FEM. Although it is intended primarily for discontinuous block systems, the

DDA is based on strict adherence to the rules of classical mechanics. Displacements and deformations are permitted for each block, and sliding, opening and closing of block interfaces are permitted for the entire block system.

Since the DDA was first introduced by Shi (1988), it obtained great development and application in various engineering problems as shown in many DDA works (Yeung 1991; Chen 1993; Ke 1993; Shyu 1993; Yeung 1993; Chang 1994; Ke 1995; Koo, Chern et al. 1995; Lin 1995; Ohnishi, Chen et al. 1995; Amadei, Lin et al. 1996; Ke 1996; MacLaughlin and Sitar 1996; Huang 1997; Ke 1997; Koo and Chern 1997; Lin and Chen 1997; MacLaughlin 1997; Ma 1999; Mortazavi 1999; Jing, Ma et al. 2001; MacLaughlin, Sitar et al. 2001; Hatzor, Talesnick et al. 2002; Hatzor, Arzi et al. 2004; Sasaki, Hagiwara et al. 2005; MacLaughlin and Doolin 2006; Ohnishi and Nishiyama 2007; Shi 2007; Zhao, Gu et al. 2007) over the past decades. Detailed reviews will be given in section 2.5.

The DDA has many common features with the FEM: displacements as unknowns, implicit scheme, and the way of building the governing equations. However, an important difference between the FEM and the DDA is the treatment of displacement compatibility conditions. In the FEM, the displacement compatibility must be enforced between internal elements and it is satisfied automatically by the displacement functions, while in the DDA, displacement compatibility is obtained by the contact conditions between blocks.

2.2.6 Numerical Manifold Method

The numerical manifold method (NMM) is developed as a general method for numerical analysis of the material response to external and internal changes in loads (Shi 1991; Shi 1992). The NMM uses different displacement functions in different material domains which overlapped each other to cover the whole material space to form a finite cover system. Based on the finite covers, the NMM combines the FEM and the DDA in a unified form. Both the FEM and DDA can be viewed as special cases of the NMM. The large displacements of jointed or blocky materials of complex shape and moving boundaries can be computed in a mathematically consistent manner.

The NMM has two independent meshes: mathematical mesh and physical mesh. The mathematical mesh defines the displacement functions while the physical mesh limits the integration zones. The mathematical mesh, which can be chosen artificially, consists of finite overlapping individual domains which cover the whole material space. Regular grids, finite element meshes or randomly distributed convergency regions of series can be combined to form overlapping domains of the mathematical mesh. The physical mesh, which cannot be chosen artificially, represents material conditions include boundaries of the rock masses, joints, cracks and free water surfaces, etc.

The NMM has its own advantages over the other numerical methods. Comparing with continuum-based methods, the NMM can handle discontinuities more easily. Comparing with discontinuum-based methods, the NMM can provide a more accuracy displacement and deformation analysis in the block itself. The most attractive feature of the NMM is that it can generate mesh inside the analysis area in a very fast and convenient way, which is the main advantage of the NMM over the FEM when handling continuous media. Hence, the NMM received various developments and applications in the past two decades (Li, Wang et al. 1995; Salami and Banks 1996; Ohnishi 1997; Amadei 1999; Bicanic 2001; Hatzor 2002; Lu 2003; MacLaughlin and Sitar 2005; Ju, Fang et al. 2008; Ma and Zhou 2009). However, the mesh generation procedure also makes the NMM more easily suffer from the ‘tiny elements’ which will have a negative effect on the stability of the governing equations and should be avoided. Although the NMM can analyze block systems with pre-existing discontinuities as well as the DDA, it cannot handle the fracture propagation inside the block.

2.3 Theory of the Discontinuous Deformation Analysis

For a better understanding of the NDDA, it is necessary to briefly provide the theory of the standard DDA here. The DDA is a discrete element method originated from backward analysis to find a best fit solution to the deformed configuration of a blocky system from measured displacements and deformations (Shi and Goodman 1985). The DDA is intended primarily for discontinuous block systems but it has many common properties with the FEM: choosing displacements as variables; minimizing the total potential energy to establish the equilibrium equations; adding stiffness, mass and loading submatrices to the coefficient matrix of the simultaneous equations. Although the DDA and the DEM both deal with block systems and belong to the discrete element family, their difference from one another is significant: the DDA is a displacement-based implicit method while the DEM is a force-based explicit method.

From a theoretical point of view, the DDA is a generalization of the FEM and the DEM. Furthermore, the DDA has its own features. In the DDA, mesh is the description of joints between blocks in a blocky system. A problem is solved in which all of the elements are physically isolated blocks bounded by pre-existing discontinuities. The block is the basic analysis object and can be convex or non-convex of any shape. Large displacements and deformations are the accumulation of small displacements and deformations of each time step. It can consider both static and dynamic problems by setting the velocities of blocks at the beginning of each time step. A complete kinematic theory is employed in the DDA and Coulomb’s frictions law controls the contact modes between blocks. The continually updated positions and shapes of blocks introduce new contacts and interactive forces. Within each time step, normal and shear springs, which represent contacts between blocks, are repeatedly added or removed until the position remains constant with no tension and no penetration between blocks. Three types of contact states are defined: open, closed, and sliding. It has perfect first order displacement approximation, strict postulate of equilibrium, correct energy consumption and high computing efficiency. The analysis is very close to the mathematical description of real mechanical phenomena associated with block movements.

2.3.1 Block Deformations and Displacements

Within each time step, the displacements of all points are small and can be reasonably represented by the first order approximation. By adopting such approximation, the DDA method assumes that each block has constant stress and strain distribution throughout. The complete first order approximation of block displacements has the following general forms (Shi 1988):

$$\begin{aligned} u &= a_1 + a_2 x + a_3 y \\ v &= b_1 + b_2 x + b_3 y \end{aligned} \tag{2.1}$$

where (u, v) are the displacements at point (x, y) in a Cartesian reference frame. $a_i, b_i \ (i = 1, 2, 3)$ are six constant coefficients which can be evaluated easily by solving the geometrical equations.

At a point (x_0, y_0) inside the block, denote the displacements as (u_0, v_0), from Eq.(2.1) we have:

$$\begin{aligned} u_0 &= a_1 + a_2 x_0 + a_3 y_0 \\ v_0 &= b_1 + b_2 x_0 + b_3 y_0 \end{aligned} \tag{2.2}$$

Subtracting Eq.(2.2) from Eq.(2.1), then:

$$\begin{aligned} u &= a_2 (x - x_0) + a_3 (y - y_0) + u_0 \\ v &= b_2 (x - x_0) + b_3 (y - y_0) + v_0 \end{aligned} \tag{2.3}$$

In Eq.(2.3), the parameters, a_2, a_3, b_2, b_3, can be obtained from the following geometrical equation and rotation relationship:

$$\begin{aligned}
&\varepsilon_x = \frac{\partial u}{\partial x} = a_2 \quad \Rightarrow \quad a_2 = \varepsilon_x \\
&\varepsilon_y = \frac{\partial v}{\partial y} = b_3 \quad \Rightarrow \quad b_3 = \varepsilon_y \\
&\left.\begin{aligned}
\frac{1}{2}\gamma_{xy} &= \frac{1}{2}\left(\frac{\partial v}{\partial x} + \frac{\partial u}{\partial y}\right) = \frac{1}{2}(b_2 + a_3) \\
r_0 &= \frac{1}{2}\left(\frac{\partial v}{\partial x} - \frac{\partial u}{\partial y}\right) = \frac{1}{2}(b_2 - a_3)
\end{aligned}\right\} \Rightarrow \left\{\begin{aligned}
a_3 &= \frac{1}{2}\gamma_{xy} - r_0 \\
b_2 &= \frac{1}{2}\gamma_{xy} + r_0
\end{aligned}\right.
\end{aligned} \tag{2.4}$$

Substituting these four parameters obtained from Eq.(2.4) into Eq. (2.3):

$$\begin{aligned}
u &= \varepsilon_x(x - x_0) + \left(\frac{1}{2}\gamma_{xy} - r_0\right)(y - y_0) + u_0 \\
v &= \left(\frac{1}{2}\gamma_{xy} + r_0\right)(x - x_0) + \varepsilon_y(y - y_0) + v_0
\end{aligned} \tag{2.5}$$

Written in a matrix form, the complete first order approximation of displacements of any point within the block is given as:

$$\begin{Bmatrix} u \\ v \end{Bmatrix} = \begin{bmatrix} 1 & 0 & -(y - y_0) & (x - x_0) & 0 & (y - y_0)/2 \\ 0 & 1 & (x - x_0) & 0 & (y - y_0) & (x - x_0)/2 \end{bmatrix} \begin{Bmatrix} u_0 \\ v_0 \\ r_0 \\ \varepsilon_x \\ \varepsilon_y \\ \gamma_{xy} \end{Bmatrix} \tag{2.6}$$

where (x, y) are the coordinates of any point within the block; (x_0, y_0) are the coordinates of a point within the block (for convenience, this point is usually taken at the centroid of the block). In the DDA, each block has six degrees of freedom, among which three components are rigid body motion terms and the other three are constant strain terms.

The unknowns for block *i* usually denoted in vector form by

$$\mathbf{d}_i = \{u_0, v_0, r_0, \varepsilon_x, \varepsilon_y, \gamma_{xy}\}^{\mathrm{T}} \tag{2.7}$$

where u_0, v_0 are the rigid body translations at the point (x_0, y_0) along the x and y directions, respectively; r_0 is the rigid rotation angle in radian around the point (x_0, y_0); $\varepsilon_x, \varepsilon_y, \gamma_{xy}$ are normal and shear strains of the block. The six unknowns are corresponding to the general block deformation and movement as shown in Figure 2.2.

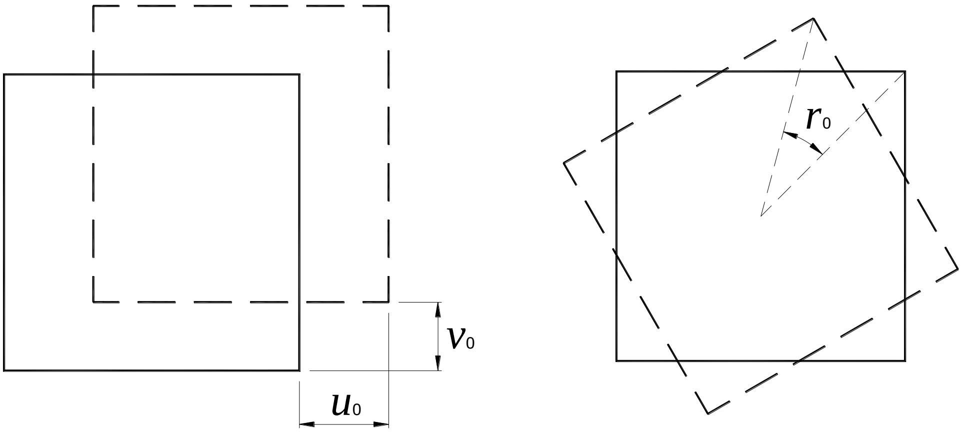

(a) rigid body translation (b) rigid body rotation

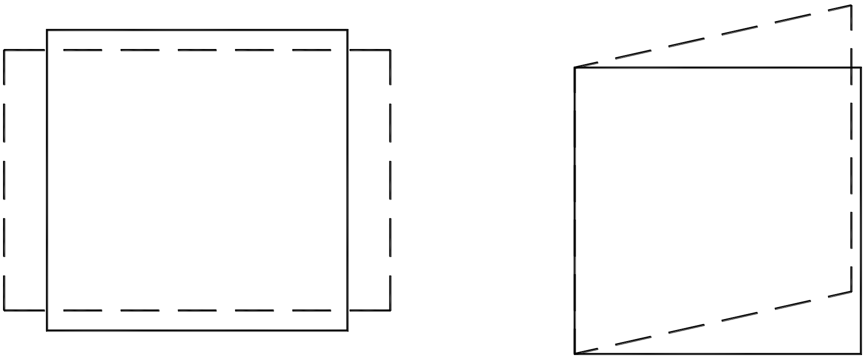

(c) normal deformation (d) shear deformation

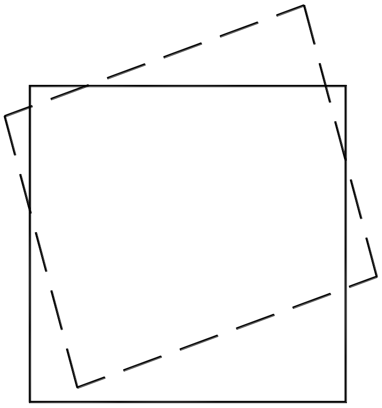

(e) combination of basic deformation and movement

Figure 2.2 schematization of block deformation and movement in the DDA

Eq. (2.6) can be written in a more generalized form:

$$\begin{Bmatrix} u \\ v \end{Bmatrix} = \begin{bmatrix} t_{11} & t_{12} & t_{13} & t_{14} & t_{15} & t_{16} \\ t_{21} & t_{22} & t_{23} & t_{24} & t_{25} & t_{26} \end{bmatrix} \begin{Bmatrix} d_{1i} \\ d_{2i} \\ d_{3i} \\ d_{4i} \\ d_{5i} \\ d_{6i} \end{Bmatrix} \tag{2.8}$$

$$\mathbf{u} = \mathbf{T}_i \mathbf{d}_i \tag{2.9}$$

Eq.(2.9) enables the calculation of the displacements at any point (x, y) within the block *i* (in particular, at the corners), when the displacements are given at the center of rotation and when the strains (constant within the block) are known.

2.3.2 Simultaneous Equilibrium Equations

The process of yielding the global equations is similar to the FEM. First, all the potential energies of elastic strains, initial stresses, point loading, line loading, volume loading, viscosity and inertia force are computed. Second, the derivatives of individual potential energy with respect to deformation variables are computed and the corresponding sub-matrices are formed separately. Finally, the global equations are established by adding the sub-matrices to the matrices of the global equation at the corresponding position.

In general, the potential energy of a block i can be expressed as

$$\Pi_i = \mathbf{f}^T \mathbf{d}_{\mathrm{B}} + \frac{1}{2}\int \boldsymbol{\varepsilon}^T \boldsymbol{\sigma} dA \tag{2.10}$$

where $\mathbf{f}$ is the force vector (including the contact forces), $\mathbf{d}_{\mathrm{B}}$ is the boundary displacement vector, $\boldsymbol{\varepsilon}$ is the strain vector, and $\boldsymbol{\sigma}$ is the stress vector. Minimization of the potential energy for block i with respect to the displacement variables in that block leads to six equations

$$\frac{\partial \Pi_i}{\partial d_{ri}} = 0, \text{ r=1, 2, …, 6} \tag{2.11}$$

where d_{ri} are the displacement variables of block i defined in Eq.(2.7). $\frac{\partial \Pi}{\partial u_0} = 0, \frac{\partial \Pi}{\partial v_0} = 0$ represent the equilibrium of all the loads and contact forces acting on block i along the X and Y axes respectively; $\frac{\partial \Pi}{\partial r_0} = 0$ represents the moment equilibrium of all the loads and contact forces acting on block i; $\frac{\partial \Pi}{\partial \varepsilon_x} = 0, \frac{\partial \Pi}{\partial \varepsilon_y} = 0$, $\frac{\partial \Pi}{\partial \gamma_{xy}} = 0$ represent the equilibrium of all the external forces and stresses of block i. Carrying out the differentiation, rearranging and extracting the displacements d_{ri} gives the system

$$\mathbf{K}_{ii} \mathbf{d}_i = \mathbf{f}_i \tag{2.12}$$

where $\mathbf{f}_i$ is the force matrix, $\mathbf{K}_{ii}$ is the local stiffness matrix and $\mathbf{d}_i$ is the displacement matrix of block *i*. Since each block *i* has six degrees of freedom defined by the components of matrix $\mathbf{d}_i$ as shown in Eq.(2.7), each $\mathbf{K}_{ii}$ is itself a 6×6 submatrix. Also, each $\mathbf{f}_i$ is a 6×1 submatrix that represents the loading on block *i*. Further details of this procedure can be found in Shi (1988).

Another potential energy expression Π_k, which is related to the displacement constraints between blocks can be derived. It can be shown that minimization of this potential energy is equivalent to imposing certain constraints on corresponding block. The minimization again leads to another 6×6 system of equations

$$\mathbf{K}_j\mathbf{d}_j = \mathbf{f}_j, \quad j = 1, 2, \ldots, m \tag{2.13}$$

for each pair of blocks in contact. Here, *m* is the total number of contacts, $\mathbf{f}_j$ is the contact force vector of contact *j* and $\mathbf{K}_j$ is the spring stiffness matrix of contact *j*. The contact equations are equivalent to applying hard springs to lock the relative movements of two blocks according to the contact status between them.

In the DDA method, individual blocks form a system of blocks through contacts among blocks and displacement constraints on single blocks. Assuming that *n* blocks are defined in a block system, Shi (1988) showed that the simultaneous equilibrium equations can be written in matrix form as follows

$$\begin{bmatrix} \mathbf{K}_{11} & \mathbf{K}_{12} & \mathbf{K}_{13} & \cdots & \mathbf{K}_{1n} \\ \mathbf{K}_{21} & \mathbf{K}_{22} & \mathbf{K}_{23} & \cdots & \mathbf{K}_{2n} \\ \mathbf{K}_{31} & \mathbf{K}_{32} & \mathbf{K}_{33} & \cdots & \mathbf{K}_{3n} \\ \vdots & \vdots & \vdots & \ddots & \vdots \\ \mathbf{K}_{n1} & \mathbf{K}_{n2} & \mathbf{K}_{n3} & \cdots & \mathbf{K}_{nn} \end{bmatrix} \begin{Bmatrix} \mathbf{d}_1 \\ \mathbf{d}_2 \\ \mathbf{d}_3 \\ \vdots \\ \mathbf{d}_n \end{Bmatrix} = \begin{Bmatrix} \mathbf{F}_1 \\ \mathbf{F}_2 \\ \mathbf{F}_3 \\ \vdots \\ \mathbf{F}_n \end{Bmatrix} \tag{2.14}$$

where $\mathbf{d}_i$, $\mathbf{F}_i$ are 6×1 sub-matrices, and $\mathbf{d}_i$ represents the deformation variables: $(u_0, v_0, r_0, \varepsilon_x, \varepsilon_y, \gamma_{xy})$ of block *i*, while $\mathbf{F}_i$ is the loading distributed to the six deformation variables; each (6×6) sub-matrix $\mathbf{K}_{ij}$ ($i\neq j$) is of the form given in Eq. (2.13) and each (6×6) sub-matrix $\mathbf{K}_{ii}$ is of the form given in Eq.(2.12). Eq.(2.14) can also be expressed in a more compact form as $\mathbf{Kd} = \mathbf{F}$ where $\mathbf{K}$ is a $6n\times6n$ stiffness matrix and **d** and **F** are $6n \times 1$ displacement and force vectors, respectively. In total, the number of displacement unknowns is the sum of the degrees of freedom of all the blocks. It is noteworthy that the system of Eq.(2.14) is similar in form to that in the FEM. Figure 2.4 provides an illustration of the structure of the global stiffness matrix of a three-block system as shown in Figure 2.3.

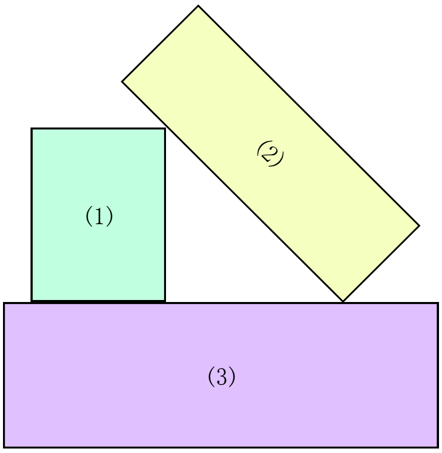

Figure 2.3 a three-block DDA model

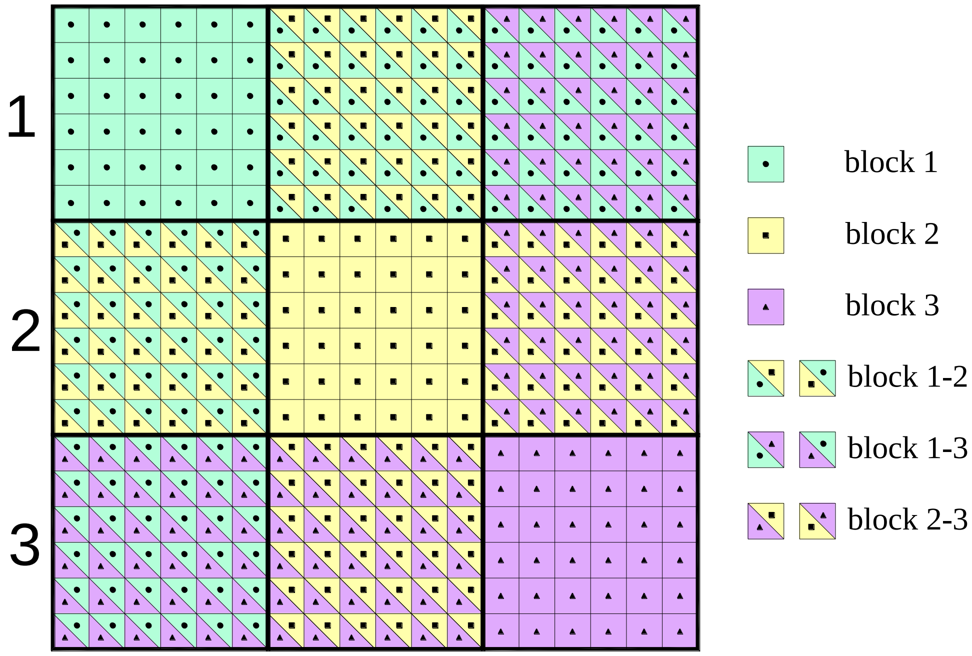

Figure 2.4 schematic illustration of the global stiffness matrix for a three-block DDA model

In Eq. (2.14), $\mathbf{K}_{ij}$ comes from the differentiations:

$$\frac{\partial^2 \Pi}{\partial \mathbf{d}_i \partial \mathbf{d}_j} \tag{2.15}$$

$\mathbf{F}_i$ comes from the differentiations:

$$-\frac{\partial \Pi(0)}{\partial \mathbf{d}_i} \tag{2.16}$$

The system of Eq. (2.14) is solved for the displacement variables again and again in a time step when implementing open-close iteration. The solution is constrained by a system of inequalities associated with block kinematics (e.g. no penetration and no tension between blocks) and Coulomb friction for sliding along block interfaces. A typical open-close iteration is fulfilled as follows. The solution obtained from previous iteration is checked to see how well the constraints are satisfied. If tension or penetration is found at any contact, the constraints are adjusted by selecting new locks and constraining positions and a modified version of **K** and **F** are formed from which a new solution is obtained. This process is repeated until no tension and no penetration are found among all of the block contacts. Hence, the final displacement variables for a given time step are actually obtained by a trial iterative process.

2.3.3Submatrices of Elastic Strains

The condition of every block can be plane stress or plane strain. For each displacement step, assuming the material behaviors of the blocks are linearly elastic, the relationship of stress and strain can be expressed as:

$$\boldsymbol{\sigma}_i = \mathbf{E}_i \boldsymbol{\varepsilon}_i \tag{2.17}$$

For plane stress problem:

$$\begin{Bmatrix} \sigma_x \\ \sigma_y \\ \tau_{xy} \end{Bmatrix} = \frac{E}{1-\upsilon^2} \begin{bmatrix} 1 & \upsilon & 0 \\ \upsilon & 1 & 0 \\ 0 & 0 & \frac{1-\upsilon}{2} \end{bmatrix} \begin{Bmatrix} \varepsilon_x \\ \varepsilon_y \\ \gamma_{xy} \end{Bmatrix} \tag{2.18}$$

For plane strain problem:

$$\begin{Bmatrix} \sigma_x \\ \sigma_y \\ \tau_{xy} \end{Bmatrix} = \frac{E}{(1+\upsilon)(1-2\upsilon)} \begin{bmatrix} 1-\upsilon & \upsilon & 0 \\ \upsilon & 1-\upsilon & 0 \\ 0 & 0 & \frac{1-2\upsilon}{2} \end{bmatrix} \begin{Bmatrix} \varepsilon_x \\ \varepsilon_y \\ \gamma_{xy} \end{Bmatrix} \tag{2.19}$$

For the *i*-th block, the rigid body motion terms do not induce strain, so $\boldsymbol{\varepsilon}_i$ can be replaced by $\mathbf{d}_i$, and the matrix $\mathbf{E}_i$ can be extended to a 6 × 6 matrices.

The strain energy Π_e produced by the elastic stress of the *i*-th block is:

$$\Pi_e = \iint \frac{1}{2} (\varepsilon_x \quad \varepsilon_y \quad \gamma_{xy}) \begin{Bmatrix} \sigma_x \\ \sigma_y \\ \tau_{xy} \end{Bmatrix} dxdy \tag{2.20}$$

Substituting Eq.(2.17) into Eq.(2.20), the strain energy can be represented in terms of the block deformation parameters:

$$\begin{aligned} \Pi_e &= \iint \frac{1}{2} (\varepsilon_x \quad \varepsilon_y \quad \gamma_{xy}) \mathbf{E} \begin{Bmatrix} \varepsilon_x \\ \varepsilon_y \\ \gamma_{xy} \end{Bmatrix} dxdy \\ &= \frac{1}{2} \iint \mathbf{d}_i^T \mathbf{E}_i \mathbf{d}_i dxdy \\ &= \frac{S}{2} \mathbf{d}_i^T \mathbf{E}_i \mathbf{d}_i \end{aligned} \tag{2.21}$$

where *S* is the area of the *i*-th block.

The derivatives are computed to minimize the strain energy Π_e:

$$\mathbf{k}_{ii} = \frac{\partial^2 \Pi_e}{\partial \mathbf{d}_i \partial \mathbf{d}_i} = S\mathbf{E}_i \rightarrow \mathbf{K}_{ii} \tag{2.22}$$

$\mathbf{k}_{ii}$ forms a 6 × 6 submatrix which is added to $\mathbf{K}_{ii}$ in the global Eq.(2.14).

2.3.4 *Submatrices of initial stress*

In the DDA program, the *i*-th block can have initial constant stresses $(\sigma_x^0\ \sigma_y^0\ \tau_{xy}^0)^T$ as the load conditions from the measured record. Its potential energy can be represented as:

$$\begin{aligned} \Pi_\sigma &= -\iint (\varepsilon_x \sigma_x^0 + \varepsilon_y \sigma_y^0 + \gamma_{xy} \tau_{xy}^0) dxdy \\ &= -S(\varepsilon_x \sigma_x^0 + \varepsilon_y \sigma_y^0 + \gamma_{xy} \tau_{xy}^0) \\ &= -S\mathbf{d}_i^T \begin{Bmatrix} 0 \\ 0 \\ 0 \\ \sigma_x^0 \\ \sigma_y^0 \\ \tau_{xy}^0 \end{Bmatrix} \\ &= -S\mathbf{d}_i^T \boldsymbol{\sigma}_0 \end{aligned} \tag{2.23}$$

By taking the derivatives we minimize Π_σ:

$$\mathbf{f}_i = -\frac{\partial \Pi_\sigma}{\partial \mathbf{d}_i} = S\boldsymbol{\sigma}_0 \rightarrow \mathbf{F}_i \tag{2.24}$$

$\mathbf{f}_i$ forms a 6×1 submatrix which is added to $\mathbf{F}_i$ in the global Eq.(2.14).

2.3.5 *Submatrices of point loading*

Assuming the point loading force acting on point (x, y) of *i*-th block is (F_x, F_y), the potential energy of the point loading is simply expressed as:

$$\begin{aligned}\Pi_p &= -(F_x u + F_y v) \\ &= -\{u \quad v\}\begin{Bmatrix} F_x \\ F_y \end{Bmatrix} \\ &= -\mathbf{d}_i^T \mathbf{T}_i^T(x,y)\begin{Bmatrix} F_x \\ F_y \end{Bmatrix}\end{aligned} \tag{2.25}$$

The derivatives can be computed by minimizing Π_p:

$$\mathbf{f}_i = -\frac{\partial \Pi_p(0)}{\partial \mathbf{d}_i} = \begin{bmatrix} t_{11} & t_{21} \\ t_{12} & t_{22} \\ t_{13} & t_{23} \\ t_{14} & t_{24} \\ t_{15} & t_{25} \\ t_{16} & t_{26} \end{bmatrix}\begin{Bmatrix} F_x \\ F_y \end{Bmatrix} \to \mathbf{F}_i \tag{2.26}$$

$\mathbf{f}_i$ forms a 6×1 submatrix which is added to $\mathbf{F}_i$ in the global Eq.(2.14).

2.3.6 Submatrices of line load

Assume the loading is distributed on a straight line from point (x_1, y_1) to point (x_2, y_2) (see Figure 2.5). The equation of the loading line is

$$\begin{aligned} x &= (x_2 - x_1)t + x_1 \\ y &= (y_2 - y_1)t + y_1 \end{aligned} \qquad (0 \le t \le 1 \tag{2.27}$$

The length of this line segment is

$$l = \sqrt{(x_2 - x_1)^2 + (y_2 - y_1)^2}$$

The loading is

$$\begin{aligned} F_x &= F_x(t) \\ F_y &= F_y(t) \end{aligned} \qquad (0 \le t \le 1 \tag{2.28}$$

which is a variant along the loading line. The potential energy of the line loading $(F_x(t), F_y(t))$ is

$$\Pi_l = -\int_0^1 \{u \quad v\} \begin{Bmatrix} F_x(t) \\ F_y(t) \end{Bmatrix} l dt \tag{2.29}$$

$$\Pi_l = -\mathbf{d}_i^T \int_0^1 \mathbf{T}_i^T \begin{Bmatrix} F_x(t) \\ F_y(t) \end{Bmatrix} l dt \tag{2.30}$$

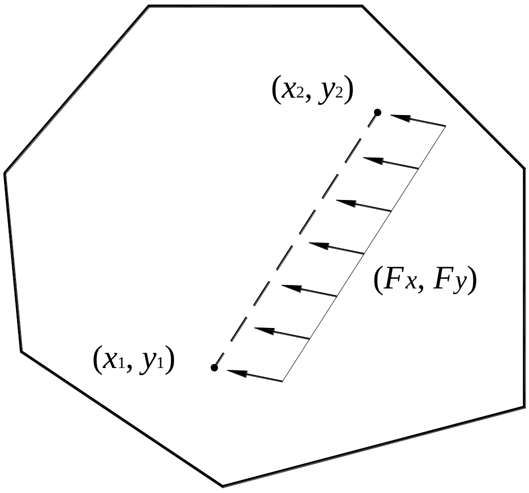

Figure 2.5 line load on a block

The derivatives of Π_l are computed to minimize the potential energy Π_l :

$$\mathbf{f}_i = -\frac{\partial \Pi_l}{\partial \mathbf{d}_i} = \int_0^1 \mathbf{T}_i^T \begin{Bmatrix} F_x(t) \\ F_y(t) \end{Bmatrix} l dt \to \mathbf{F}_i \tag{2.31}$$

$\mathbf{f}_i$ forms a 6×1 submatrix which is added to $\mathbf{F}_i$ in the global equation.

When the line loading ($F_x(t)$, $F_y(t)$)=(F_x, F_y) is constant, the matrix integration of Eq.(2.31) has the analytical formula, which is derived in the following:

$$\int_0^1 \mathbf{T}_i^T \begin{Bmatrix} F_x \\ F_y \end{Bmatrix} l dt = \left(\int_0^1 \mathbf{T}_i^T l dt\right) \begin{Bmatrix} F_x \\ F_y \end{Bmatrix} \tag{2.32}$$

The integrations of the elements have to be computed in order to compute integration of matrix $\mathbf{T}_i$:

$$\begin{aligned}\int_0^1 (x-x_0)ldt &= \int_0^1 ((x_2-x_1)t+(x_1-x_0))ldt \\ &= \frac{l}{2}(x_2+x_1-2x_0) \\ \int_0^1 (y-y_0)ldt &= \int_0^1 ((y_2-y_1)t+(y_1-y_0))ldt \\ &= \frac{l}{2}(y_2+y_1-2y_0)\end{aligned} \tag{2.33}$$

Therefore,

$$(\int_0^1 \mathbf{T}_i^T ldt)\begin{Bmatrix} F_x \\ F_y \end{Bmatrix} = l\begin{Bmatrix} F_x \\ F_y \\ -\frac{1}{2}(y_2+y_1-2y_0)F_x+\frac{1}{2}(x_2+x_1-2x_0)F_y \\ \frac{1}{2}(x_2+x_1-2x_0)F_x \\ \frac{1}{2}(y_2+y_1-2y_0)F_y \\ \frac{1}{4}(y_2+y_1-2y_0)F_x+\frac{1}{4}(x_2+x_1-2x_0)F_y \end{Bmatrix} \rightarrow \mathbf{F}_i \tag{2.34}$$

This 6 × 1 submatrix is added to the submatrix $\mathbf{F}_i$ in the global equation.

When the line loading $(F_x(t), F_y(t)) = (F_x, F_y)$ is changed linearly at different points along the straight line, we set $F_x(t) = F_{1x}$ and $F_y(t) = F_{1y}$ when t=0; $F_x(t) = F_{2x}$ and $F_y(t) = F_{2y}$ when t=1, then the matrix integration Eq.(2.31) has the analytical formula, which is derived in the following:

$$\begin{aligned}&\int_0^1 (x-x_0)\left(F_{1x}+(F_{2x}-F_{1x})t\right)ldt \\ &= \int_0^1 ((x_2-x_1)t+(x_1-x_0))\left(F_{1x}+(F_{2x}-F_{1x})t\right)ldt \\ &= \frac{1}{6}(2x_1+x_2-3x_0)F_{1x}+\frac{1}{6}(x_1+2x_2-3x_0)F_{2x}\end{aligned} \tag{2.35}$$

$$\begin{aligned}&\int_0^1 (y-y_0)\left(F_{1y}+(F_{2y}-F_{1y})t\right)ldt \\ &= \int_0^1 ((y_2-y_1)t+(y_1-y_0))\left(F_{1y}+(F_{2y}-F_{1y})t\right)ldt \\ &= \frac{1}{6}(2y_1+y_2-3y_0)F_{1y}+\frac{1}{6}(y_1+2y_2-3y_0)F_{2y}\end{aligned} \tag{2.36}$$

Therefore,

$$(\int_0^1 \mathbf{T}_i^T l dt)\begin{Bmatrix} F_x \\ F_y \end{Bmatrix} =$$

$$l\left\{\begin{matrix} F_x \\ F_y \\ \begin{pmatrix} -\frac{1}{6}(2y_1+y_2-3y_0)F_{1y}-\frac{1}{6}(y_1+2y_2-3y_0)F_{2y} \\ +\frac{1}{6}(2x_1+x_2-3x_0)F_{1x}+\frac{1}{6}(x_1+2x_2-3x_0)F_{2x} \end{pmatrix} \\ \frac{1}{6}(2x_1+x_2-3x_0)F_{1x}+\frac{1}{6}(x_1+2x_2-3x_0)F_{2x} \\ \frac{1}{6}(2y_1+y_2-3y_0)F_{1y}+\frac{1}{6}(y_1+2y_2-3y_0)F_{2y} \\ \begin{pmatrix} \frac{1}{12}(2y_1+y_2-3y_0)F_{1y}+\frac{1}{12}(y_1+2y_2-3y_0)F_{2y} \\ +\frac{1}{12}(2x_1+x_2-3x_0)F_{1x}+\frac{1}{12}(x_1+2x_2-3x_0)F_{2x} \end{pmatrix} \end{matrix}\right\} \to \mathbf{F}_i \qquad (2.37)$$

This 6 × 1 submatrix is added to the submatrix $\mathbf{F}_i$ in the global equation.

2.3.7 Submatrices of volume force

If the body force loading (f_x, f_y) is constant, the potential energy is:

$$\begin{aligned} \Pi_V &= -\iint (f_x u + f_y v)dxdy \\ &= -\mathbf{d}_i^T \iint \mathbf{T}_i^T dxdy \begin{Bmatrix} f_x \\ f_y \end{Bmatrix} \end{aligned} \qquad (2.38)$$

Where:

$$\iint \mathbf{T}_i^T dxdy = \begin{bmatrix} S & 0 \\ 0 & S \\ -S_y + y_0 S & S_x - x_0 S \\ S_x - x_0 S & 0 \\ 0 & S_y - y_0 S \\ (S_y - y_0 S)/2 & (S_x - x_0 S)/2 \end{bmatrix} = \begin{bmatrix} S & 0 \\ 0 & S \\ 0 & 0 \\ 0 & 0 \\ 0 & 0 \\ 0 & 0 \end{bmatrix} \qquad (2.39)$$

The derivatives can be computed by minimizing Π_V:

$$\mathbf{f}_i = -\frac{\partial \Pi_V(0)}{\partial \mathbf{d}_i} = \begin{Bmatrix} f_x S \\ f_y S \\ 0 \\ 0 \\ 0 \\ 0 \end{Bmatrix} \rightarrow \mathbf{F}_i \tag{2.40}$$

$\mathbf{f}_i$ forms a 6×1 submatrix which is added to $\mathbf{F}_i$ in the global equation.

2.3.8 Submatrices of the bolt connection

Consider a bolt or a bar connecting point (x_1, y_1) of block i and point (x_2, y_2) of block j which are not necessarily the vertices of the blocks. The length of the bar is

$$l = \sqrt{(x_1 - x_2)^2 + (y_1 - y_2)^2} \tag{2.41}$$

$$dl = (\mathbf{d}_i^T \mathbf{T}_i^T \begin{Bmatrix} l_x \\ l_y \end{Bmatrix} - \mathbf{d}_j^T \mathbf{T}_j^T \begin{Bmatrix} l_x \\ l_y \end{Bmatrix}) \tag{2.42}$$

Where l_x and l_y are the direction cosines of the bar.

Assuming the stiffness of the bar is s, the bar force is

$$f = -s \frac{dl}{l}$$

The strain energy of the bar is

$$\begin{aligned} \Pi_b &= -\frac{1}{2} f dl \\ &= \frac{s}{2l} dl^2 \\ &= \frac{s}{2l} \mathbf{d}_i^T \mathbf{E}_i \mathbf{E}_i^T \mathbf{d}_i - \frac{s}{l} \mathbf{d}_i^T \mathbf{E}_i \mathbf{G}_j^T \mathbf{d}_j + \frac{s}{2l} \mathbf{d}_j^T \mathbf{G}_j \mathbf{G}_j^T \mathbf{d}_j \end{aligned} \tag{2.43}$$

where

$$\mathbf{E}_i = \mathbf{T}_i^T \begin{Bmatrix} l_x \\ l_y \end{Bmatrix}$$

$$\mathbf{G}_j = \mathbf{T}_j^T \begin{Bmatrix} l_x \\ l_y \end{Bmatrix}$$

The derivatives of Π_b

$$\mathbf{k}_{ii} = \frac{\partial^2 \Pi_b}{\partial \mathbf{d}_i \partial \mathbf{d}_i} = \frac{s}{l} \mathbf{E}_i \mathbf{E}_i^T \to \mathbf{K}_{ii} \tag{2.44}$$

which is added to the submatrix $\mathbf{K}_{ii}$ in the global equation.

$$\mathbf{k}_{ij} = \frac{\partial^2 \Pi_b}{\partial \mathbf{d}_i \partial \mathbf{d}_j} = -\frac{s}{l} \mathbf{E}_i \mathbf{G}_j^T \to \mathbf{K}_{ij} \tag{2.45}$$

which is added to the submatrix $\mathbf{K}_{ij}$ in global equation.

$$\mathbf{k}_{ji} = \frac{\partial^2 \Pi_b}{\partial \mathbf{d}_j \partial \mathbf{d}_i} = -\frac{s}{l} \mathbf{G}_j \mathbf{E}_i^T \to \mathbf{K}_{ji} \tag{2.46}$$

which is added to the submatrix $\mathbf{K}_{ji}$ in global equation.

$$\mathbf{k}_{jj} = \frac{\partial^2 \Pi_b}{\partial \mathbf{d}_j \partial \mathbf{d}_j} = \frac{s}{l} \mathbf{G}_j \mathbf{G}_j^T \to \mathbf{K}_{jj} \tag{2.47}$$

which is added to the submatrix $\mathbf{K}_{jj}$ in global equation.

2.3.9 Submatrices of inertia force

The force of inertia per unit area of the block is the products of its time dependent acceleration and mass. Using the $(u(t), v(t))$ as the time dependent displacement of any point (x, y) of the i-th block and m as the mass per unit area, it can be represented as:

$$\begin{Bmatrix} f_x \\ f_y \end{Bmatrix} = -m \begin{Bmatrix} \dfrac{\partial^2 u(t)}{\partial t^2} \\ \dfrac{\partial^2 v(t)}{\partial t^2} \end{Bmatrix} \tag{2.48}$$

The potential energy of the inertia force of the *i*th block is:

$$\begin{aligned} \Pi_i &= -\iint \{u \quad v\} \begin{Bmatrix} f_x \\ f_y \end{Bmatrix} dxdy \\ &= m \iint \mathbf{d}_i^T \mathbf{T}_i^T \mathbf{T}_i \frac{\partial^2 \mathbf{d}(t)}{\partial t^2} dxdy \\ &= \frac{m}{\Delta^2} \mathbf{d}_i^T \iint \mathbf{T}_i^T \mathbf{T}_i dxdy (\mathbf{d}_i - \mathbf{d}_0) \end{aligned} \tag{2.49}$$

$$\mathbf{k}_{ii} = \frac{\partial^2 \Pi_i}{\partial \mathbf{d}_i \partial \mathbf{d}_i} = \frac{2m}{\Delta^2} \iint \mathbf{T}_i^T \mathbf{T}_i dxdy \to \mathbf{K}_{ii} \tag{2.50}$$

which is added to the submatrix $\mathbf{K}_{ii}$ in the global equation.

$$\mathbf{f}_i = -\frac{\partial \Pi_i}{\partial \mathbf{d}_i} = \frac{m}{\Delta^2} \left(\iint \mathbf{T}_i^T \mathbf{T}_i dxdy\right) \mathbf{d}_0 \to \mathbf{F}_i \tag{2.51}$$

$\mathbf{f}_i$ forms a 6×1 submatrix which is added to $\mathbf{F}_i$ in the global equation.

2.3.10 Submatrices of viscosity

The DDA method could be applied to problems involving a viscous stratum in shear, as encountered in plate tectonics, or in regard to floating ice blocks.

The resistance force from viscosity is proportional to the velocity as well as the block area. When the displacement increment is given per unit time, the force is:

$$\begin{Bmatrix} f_x \\ f_y \end{Bmatrix} = \frac{\mu}{\Delta} \begin{Bmatrix} u \\ v \end{Bmatrix} \tag{2.52}$$

where Δ: is the time step; u and v are the displacement increment per unit time. The potential energy of the force of viscosity of block *i* is

$$\begin{aligned}\Pi_v &= \iint \begin{pmatrix} u & v \end{pmatrix} \begin{pmatrix} f_x \\ f_y \end{pmatrix} dxdy \\ &= \mathbf{d}_i^T \iint \mathbf{T}_i^T \begin{pmatrix} f_x \\ f_y \end{pmatrix} dxdy\end{aligned} \tag{2.53}$$

The force of viscosity can be considered as body loading. In order to reach equilibrium, Π_v is minimized with respect to block displacement variables. We have

$$\mathbf{k}_{ii} = \frac{\partial \Pi_v}{\partial \mathbf{d}_i \partial \mathbf{d}_i} = \frac{2\mu}{\Delta} \iint \mathbf{T}_i^T \mathbf{T}_i dxdy \to \mathbf{K}_{ii} \tag{2.54}$$

which is added to the submatrix $\mathbf{K}_{ii}$ in the global equation.

2.3.11 Submatrices of displacement constraints at a point

When some of the blocks are fixed at specific points, their constraints can be applied to the block system by using two very stiff springs in x and y directions. Assume the fixed point is (x, y) of i-th block, with the displacements $(u(x, y), v(x, y)) = (0, 0)$.

There are two springs which are along the x and y directions respectively. The stiffness of the springs is the same as p, and the spring forces are:

$$\begin{Bmatrix} f_x \\ f_y \end{Bmatrix} = \begin{Bmatrix} -pu \\ -pv \end{Bmatrix} \tag{2.55}$$

The strain energy of this spring is:

$$\begin{aligned}\Pi_m &= \frac{p}{2} \begin{pmatrix} u & v \end{pmatrix} \begin{pmatrix} u \\ v \end{pmatrix} \\ &= \frac{p}{2} \mathbf{d}_i^T \mathbf{T}_i^T \mathbf{T}_i \mathbf{d}_i\end{aligned} \tag{2.56}$$

The derivatives are computed to minimize the spring strain energy Π_m:

$$\mathbf{k}_{ii} = \frac{\partial^2 \Pi_m}{\partial \mathbf{d}_i \partial \mathbf{d}_i} = p\mathbf{T}_i^T \mathbf{T}_i \rightarrow \mathbf{K}_{ii} \tag{2.57}$$

which is added to the submatrix $\mathbf{K}_{ii}$ in the global equation.

2.3.12 Submatrices of displacement constraints in a direction

As a boundary condition, some of the blocks are fixed at specific points in specified directions. More generally, the existing displacement δ along a direction at a point can be an input. The measured displacements can be applied to the block system by using a very stiff spring which has the measured displacement as pre-tension distance. Denote

$$(l_x, l_y) \qquad l_x^2 + l_y^2 = 1$$

as the direction along which the displacement δ exists. The spring displacement is

$$d = (\delta - (l_x u + l_y v)).$$

The spring force is

$$f = -pd = -p(\delta - (l_x u + l_y v)),$$

where p denotes the stiffness of the spring. Here p is a very large positive number, normally from $10E$ to $1000E$, to guarantee the displacement of the spring is 10^{-3} to 10^{-4} times the total displacement. If p is large enough, the computation result will be independent of the choices of p.

The strain energy of this spring is

$$\begin{aligned} \Pi_c &= \frac{p}{2} d^2 \\ &= \frac{p}{2} \{u \quad v\} \begin{Bmatrix} l_x \\ l_y \end{Bmatrix} \{l_x \quad l_y\} \begin{Bmatrix} u \\ v \end{Bmatrix} - p\delta \{u \quad v\} \begin{Bmatrix} l_x \\ l_y \end{Bmatrix} + \frac{p}{2}\delta^2 \end{aligned} \tag{2.58}$$

Let

$$\mathbf{L} = \begin{Bmatrix} l_x \\ l_y \end{Bmatrix}$$

$$\mathbf{c} = \mathbf{T}^T \mathbf{L}$$

then

$$\{u \quad v\} \begin{Bmatrix} l_x \\ l_y \end{Bmatrix} = \mathbf{d}_i^T \mathbf{T}_i^T \mathbf{L} = \mathbf{d}_i^T \mathbf{c}_i$$

$$\{l_x \quad l_y\} \begin{Bmatrix} u \\ v \end{Bmatrix} = \mathbf{L}_i^T \mathbf{T}_i \mathbf{d}_i = \mathbf{c}_i^T \mathbf{d}_i$$

Therefore, we have

$$\Pi_c = \frac{p}{2} \mathbf{d}_i^T \mathbf{c}_i \mathbf{c}_i^T \mathbf{d}_i - p\delta \mathbf{d}_i^T \mathbf{c}_i + \frac{p}{2} \delta^2 \tag{2.59}$$

A 6×6 matrix is obtained by taking the derivatives of the strain energy of the stiff spring

$$\mathbf{k}_{ii} = \frac{\partial^2 \Pi_c}{\partial \mathbf{d}_i \partial \mathbf{d}_i} = p \mathbf{c}_i \mathbf{c}_i^T \rightarrow \mathbf{K}_{ii} \tag{2.60}$$

which is added to the submatrix $\mathbf{K}_{ii}$ in the global equation.

We minimize the spring strain energy Π_c by taking the derivatives of Π_c at $\mathbf{d} = \mathbf{0}$:

$$\mathbf{f}_i = -\frac{\partial \Pi_c(0)}{\partial \mathbf{d}_i} = p\delta \mathbf{c}_i \tag{2.61}$$

$\mathbf{f}_i$ forms a 6×1 submatrix which is added to $\mathbf{F}_i$ in the global equation.

2.3.13 Submatrices of contact

Two vertices, (x_1, y_1) and (x_2, y_2), come from block *i* and *j* separately. The distances between them, along *x* and *y* direction, are

$$(d_x, d_y) = (x_1 + u_1 - x_2 - u_2, y_1 + v_1 - y_2 - v_2).$$

The contact spring forces are

$$(F_x, F_y) = -p(x_1 + u_1 - x_2 - u_2, y_1 + v_1 - y_2 - v_2).$$

here p is the stiffness of the contact spring. And the strain energy of the spring forces is

$$\Pi_f = -\frac{1}{2}(F_x d_x + F_y d_y)$$

$$\begin{aligned}\Pi_f = \frac{p}{2}(&\mathbf{d}_i^T \mathbf{T}_i^T \mathbf{T}_i \mathbf{d}_i - \mathbf{d}_i^T \mathbf{T}_i^T \mathbf{T}_j \mathbf{d}_j - \mathbf{d}_j^T \mathbf{T}_j^T \mathbf{T}_i \mathbf{d}_i + \mathbf{d}_j^T \mathbf{T}_j^T \mathbf{T}_j \mathbf{d}_j \\ &+ 2\mathbf{d}_i \mathbf{T}_i \begin{Bmatrix} x_1 - x_2 \\ y_1 - y_2 \end{Bmatrix} - 2\mathbf{d}_j \mathbf{T}_j \begin{Bmatrix} x_1 - x_2 \\ y_1 - y_2 \end{Bmatrix} + \begin{Bmatrix} x_1 - x_2 & y_1 - y_2 \end{Bmatrix} \begin{Bmatrix} x_1 - x_2 \\ y_1 - y_2 \end{Bmatrix})\end{aligned} \tag{2.62}$$

To minimize the strain energy Π_f the derivatives are computed.

$$\mathbf{k}_{ii} = \frac{\partial^2 \Pi_f}{\partial \mathbf{d}_i \partial \mathbf{d}_i} = p\mathbf{T}_i^T \mathbf{T}_i \rightarrow \mathbf{K}_{ii} \tag{2.63}$$

form a 6×6 submatrix which is then added to the submatrix $\mathbf{K}_{ii}$ in the global equation.

The derivatives of Π_f

$$\mathbf{k}_{ij} = \frac{\partial^2 \Pi_f}{\partial \mathbf{d}_i \partial \mathbf{d}_j} = p\mathbf{T}_i^T \mathbf{T}_j \rightarrow \mathbf{K}_{ij} \tag{2.64}$$

form a 6×6 submatrix which is then added to the submatrix $\mathbf{K}_{ij}$ in the global equation.

The derivatives of Π_f

$$\mathbf{k}_{ji} = \frac{\partial^2 \Pi_f}{\partial \mathbf{d}_j \partial \mathbf{d}_i} = p\mathbf{T}_j^T \mathbf{T}_i \rightarrow \mathbf{K}_{ji} \tag{2.65}$$

form a 6×6 submatrix which is added to the submatrix $\mathbf{K}_{ji}$ in the global equation.

The derivatives of Π_f

$$\mathbf{k}_{jj} = \frac{\partial^2 \Pi_f}{\partial \mathbf{d}_j \partial \mathbf{d}_j} = p\mathbf{T}_j^T \mathbf{T}_j \rightarrow \mathbf{K}_{jj} \tag{2.66}$$

form a 6×6 submatrix which is added to the submatrix $\mathbf{K}_{jj}$ in the global equation.

The derivatives of Π_f at 0

$$\mathbf{f}_i = -\frac{\partial \Pi_f(0)}{\partial \mathbf{d}_i} = p\mathbf{T}_i^T \begin{Bmatrix} x_1 - x_2 \\ y_1 - y_2 \end{Bmatrix} \rightarrow \mathbf{F}_i \tag{2.67}$$

form a 6×1 submatrix which is added to the submatrix $\mathbf{F}_i$ in the global equation.

The derivatives of Π_f at 0

$$\mathbf{f}_j = -\frac{\partial \Pi_f(0)}{\partial \mathbf{d}_j} = p\mathbf{T}_j^T \begin{Bmatrix} x_1 - x_2 \\ y_1 - y_2 \end{Bmatrix} \rightarrow \mathbf{F}_j \tag{2.68}$$

finally form a 6×1 submatrix which is added to the submatrix $\mathbf{F}_j$ in the global equation.

2.4 DDA Program Framework

The main program consists of DC, DF and DG. Program DC is a preprocessor which generates the block mesh from individual lines. Program DF performs the forward analysis of a block system. Program DG is a graphic post-processor which displays graphic on the screen and produces postscript files. The flowcharts of programs DC and DF are shown in Figure 2.6 and Figure 2.7.

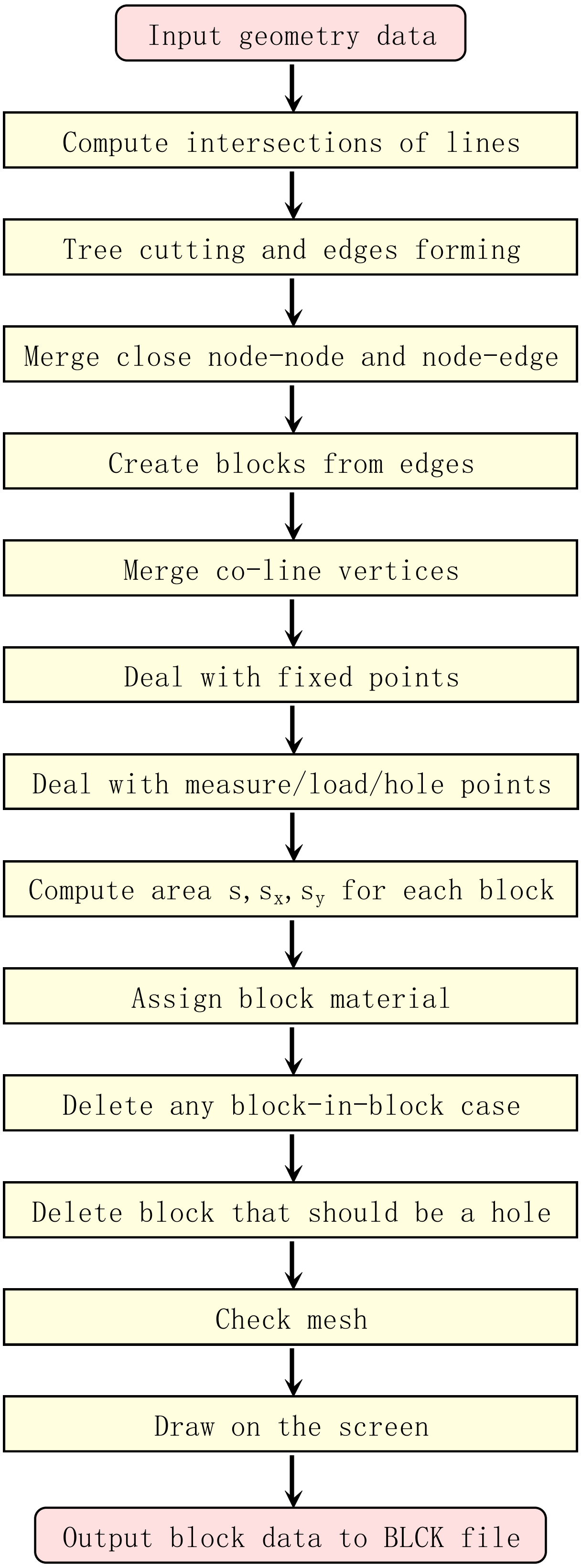

Figure 2.6 flowchart of program DC

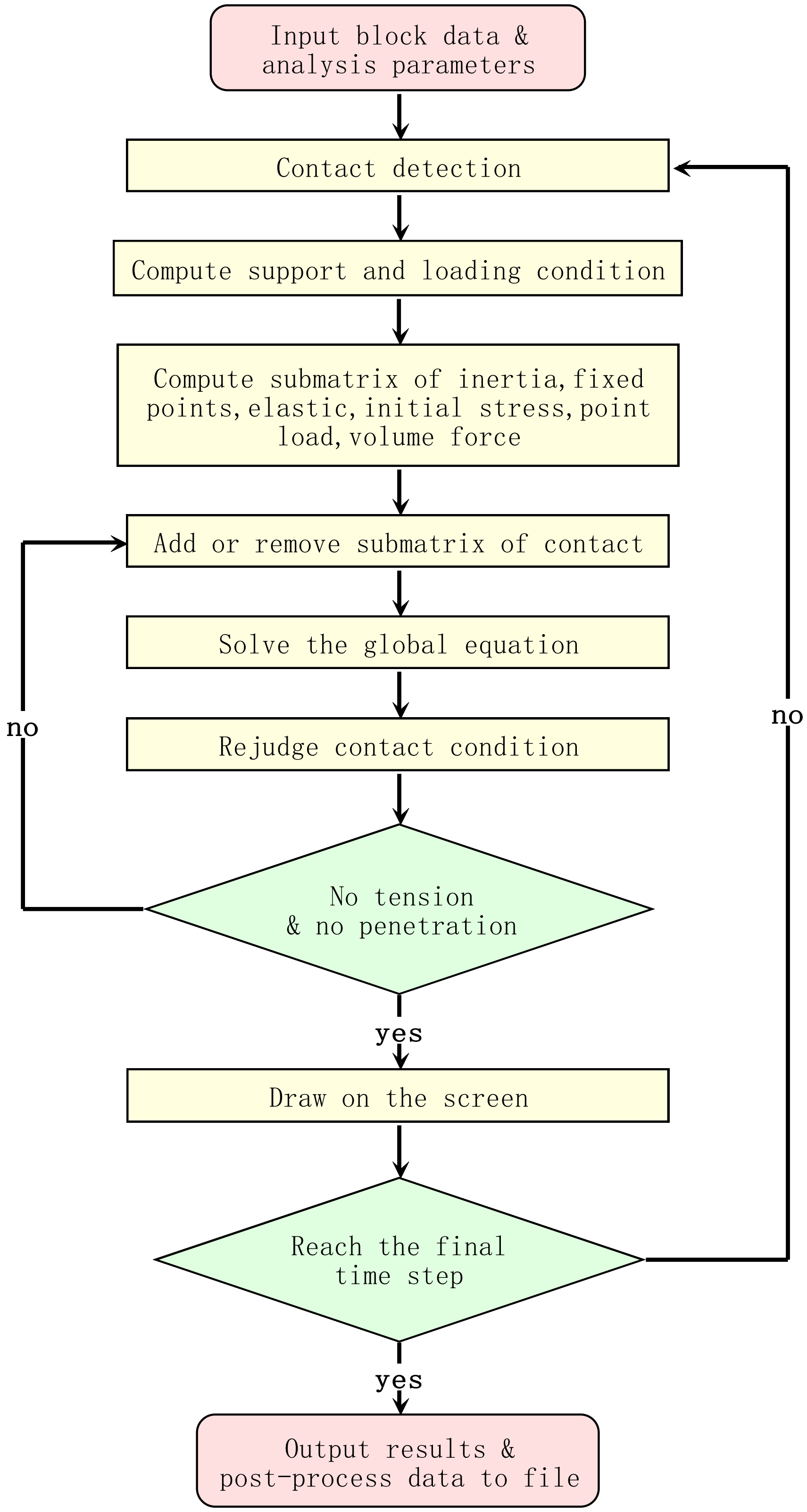

Figure 2.7 flowchart of program DF

2.5 Validation and Enhancements of the DDA

Over the last decades, researchers have done a great deal of work to validate and enhance the standard DDA. Since the main work of this thesis is on a two-dimensional forward DDA enhancement, the review of the backward DDA is excluded here. And since the 3D DDA is still under developing before a perfect 3D contact algorithm could be carried out, the review of the development of the 3D DDA is also excluded to keep the content compact and focus.

2.5.1 Validation and Application

In a recent review (MacLaughlin and Doolin 2006), a summary of more than one hundred published and unpublished validation studies was presented, and a conclusion was given that the DDA simulations can provide an acceptable accuracy for many engineering purposes. In particular, the DDA is good at dealing with frictional sliding problems, block kinematics problems, and quasi-static problems.

MacLaughlin and Hayes (2005) tested the DDA block motions on a slope and corresponding failure modes (sliding or toppling) by using laboratory models. Two types of models were constructed: 1) sets of three blocks on a single incline, and 2) multiple vertical blocks on a double incline. In the single-incline experiments, the displacements of the real blocks were typically greater than those of the DDA blocks. The explanations from the paper are that “the actual friction angle on the blocks was lower than measured in the tilt tests (and consequently used in the DDA models), or that the real blocks displayed a reduction in friction coefficient from static to dynamic once movement initiated.” The double-incline experiment was designed to demonstrate that the same geometric configuration can display either sliding or toppling failure mode depending on the friction angles of the different surfaces. The results from the DDA simulation are extremely sensitive to the friction angles of the contacting surfaces. The initial results of several of the DDA models did not match the observed behavior of the physical models, but only very small changes in friction angles were required in order to produce the same failure mode. Although this validation study did provide some useful results, there was quite a bit of uncertainty associated with it.

Wright et al. (2005) did a series of test to validate the capability of DDA to model the deformability of blocks that are not rectangular. Results from the DDA were compared with an analytical solution and it was found that the results were insensitive to variations in load, material properties, and size of block, but sensitive to changes in block shape. The percentage error can vary between 0% and 40%. These results quantified and put in question the DDA's ability to correctly model the deformation of non-equidimensional blocks due to the stresses and strains within any given block in the analysis being constant across the whole region of the block regardless of shape and size.

DDA has been successfully applied to a wide variety of engineering problems. Chen (1993) and Mclaughlin (1997) employed the DDA as a tool for engineering analysis in slope stability, to predict the initiation and mode failure, and to study the subsequent kinematics of the failed mass. Ke (1993) presented the DDA for simulated testing of two dimensional heterogeneous and discontinuous rock masses. Lin and Chen (1997) had used the DDA to determine the safety factors of soil slopes and to investigate the post-failure configuration. In addition, the DDA had been used to study the effects of loading, joint friction angles, and rock bolting on the stability of a cross-jointed mine roof model (Yeung 1993). The DDA results confirmed existing rock bolting concepts and validated the assumptions made in the reinforced rock arch method. Kim (1998; 1999) extended the application of the DDA for the hydro-mechanical coupling between rock blocks and water flow in fractures, sequential loading and unloading, and forms of rock-blocks reinforcement such as rock bolts and concrete lining.

In general, the DDA had been adopted extensively in rock engineering in which different applications have been successfully simulated and investigated (Ohnishi 1995, 2006; Ma 1999). The DDA had been employed in the studying of rock behavior (Chang, Monteiro et al. 1996), underground excavation (Yeung 1991; Kim, Amadei et al. 1999), tunneling (Yeung and Leong 1997), slope stability (Yeung 1991; Sitar and MacLaughlin 1997; MacLaughlin, Sitar et al. 2001; Doolin and Sitar 2002; Hatzor, Arzi et al. 2004; Sitar, MacLaughlin et al. 2005), rock fall (Sasaki, Hagiwara et al. 2005), stability of rock cavern (Hatzor, Talesnick et al. 2002), and rock blast (Mortazavi 1999; Zhao, Gu et al. 2007). Pearce et al. (2000) applied the DDA to model concrete fracture. Simulating the behavior of granular media (Ke and Bray 1995; Thomas 1997; Thomas and Bray 1999; O'Sullivan and Bray 2003) is another important applied area of the DDA. Jing (2001) presented a numerical model for coupled hydro-mechanical processes in fractured hard rock using the DDA method. Tsesarsky et al. (2002) and Ishikawa et al. (2002) applied the DDA to simulate the shaking table test. Jiao (2007) applied the DDA to model crack propagation in rock material based on the idea of virtual joint.

2.5.2 Rigid Body Rotation Enhancement

In the original DDA formulation, a linear displacement function term is used. In the formulation, angular rotation will induce strain term which may be very significant if the angular rotation within a time-step is “large”. However, rigid body rotation should not induce strain or distortion of block, and this phenomenon is particularly important if the time-step is relatively large. Another error is the rotation of the local reference frame and hence distortion of the stress and strain within a block. It may however be difficult to determine beforehand the amount of angular rotation within a time-step for a general problem unless a trial-and-error process is performed. If a small time step interval is used to control the amount of rotation, it will be very time consuming to perform the DDA analysis which is a computationally demanding process.

Ke (1995; 1996) studied the free expansion problem, and proposed an ‘exact post-adjustment’ to ensure correct rotations. The post-adjustment consists of using the non-rotational parts of the solution vector as usual, but using sine and cosine to compute the exact rotation corresponding to the angle of the solution vector. Ke also examined rotationally induced stress and velocity distortions, and proposed a simple change of basis procedure for correction. Numerical investigation of both proposed corrections showed that the results were numerically exact.

MacLaughlin and Sitar (1996) and MacLaughlin (1997) proposed a second order formulation derived by truncating Taylor series for sine and cosine at the quadratic terms. The resulting expression was used to derive modified potential energy terms, including terms for inertia, point loads, volume loads, etc., many of which were identical to the original terms proposed by Shi. Implementing the modification was straightforward. The authors found that for rotations of 0.2 radians or less, the error was negligible, for approximately 1% increase in computation time.

Cheng and Zhang (2000) proposed two modifications to the DDA to account for blocks undergoing large rotation and for blocks too large for the constant strain assumption. The proposed rotation correction modifies the displacement function to solve for $\sin r_0$ instead of r_0. New energy terms and the corresponding mass matrix are derived. The rotation value is arrived at by iteration, which may be performed during the existing open-close iteration. If the rotation is rigid, or if there is no angular acceleration, the iteration converges to the exact value. Based on a validation example, the rotations were found considerably more accurate (relative error less than 0.0005%) than the usual linear scheme, or the second order scheme proposed by MacLaughlin and Sitar (1996), with a negligible performance penalty.

2.5.3 Refinement of Stress Distribution inside Block

In the standard DDA formulation, the stress and strain obtained within any block are constant everywhere. These constant values are basically the average values of the actual stress and strain within a block. If the size of a block is small, this approach may be acceptable. But for a large block where the variation of stress and strain within the block may be significant, this approach is obviously unacceptable.

2.5.3.1 Couple with Finite Element Mesh

Shyu (1993) presented a numerical model that can add a finite element mesh into each block of the DDA to enhance DDA block's deformation ability, and to refine its stress distribution field. The conventional triangular element and four-node isoparametric element are used in the formulations. The displacement function for the triangular element is exactly defined and the integrations of the matrices are analytically accurate. However, the displacement function of the first order is too simple and the computation will be time-consuming if good approximation is required. The four-node element uses a higher order displacement function, but the polynomial is not exactly defined. The integrations of the elastic and initial stress matrix must be made numerically through the natural coordinates. Nevertheless, the integration of the inertia matrix can be exactly calculated. Validation examples show that the idea works well.

Chang (1994) used the case of a cantilever beam as an example of enhanced deformability facilitated by the incorporation of finite element meshes within the DDA blocks, but the results presented were qualitative. Clatworthy and Scheele (1999) proposed a sub-meshing-scheme to enhance block deformability. They validated the approach with comparisons to the FEM solutions for the deflection of the Cook cantilever beam and stress distribution within a specimen under uniaxial compression, and reported that the results were identical ‘within the range of rounding errors’. Grayeli and Mortazavi (2006) derived a second-order displacement functions based on six-node triangular mesh inside each block. Validation examples showed close agreement with the theoretical solutions.

2.5.3.2 Introduce Artificial Joints and Sub-blocks

Ke (1993) enhanced the capability of the DDA by using “artificial joints” without sacrificing the beauty and simplicity of the original DDA. As artificial joints are added within a block, the continuous domain of the block is divided into many sub-blocks and such features as holes, interior blocks and cracks can also be modeled. If the artificial joints are assumed to be infinitely strong, a refined stress distribution within the block can be acquired. The formulation is implemented by extending the original Mohr–Coulomb contact law (friction, cohesion) to allow a tensile force to exist at the boundary of each sub-block. The adequacy of refining a block by three regular types of artificial joints was examined through three examples, including a tip-loaded cantilever beam, a top-loaded square block, and a uniaxially compressed square block. The performance of each type of artificial joints depends upon the block geometry and loading patterns.

Lin (1995; 1996) presented a sub-block system, whereby blocks are discretized into sub-blocks, for analysis of jointed rock mass and other blocky system. A better resolution of stress and strain within each block can then be obtained. In the stability analysis of masonry structures, the enhanced DDA method can handle in a more straightforward manner than using the FEM. And in rock-fall analysis, the enhanced DDA method is capable of capturing quite well block trajectories with free falling, rolling, sliding, bouncing and even the impact with rock barriers, which could not be simulated by the FEM.

Cheng and Zhang (2000) applied constant strain triangular sub-blocks within a block, with nodal connectivity enforced by springs similar to the scheme proposed by Lin. The sub-blocking was tested using a hexagonal block with 0.5m sides subdivided into 24 constant strain triangular sub-blocks and dropped 1m. They found that a zone of tensile stress develops on the upper and outer parts of the hexagon, which would be expected from a real solid, but provide no quantitative analysis.

The "continuous" body generated by sub-block system has some limitations. Since the contact is done by penalty method, the contact springs experience a small amount of normal and shear deformations even if high contact stiffness is used. As a result, continuous strain is not definable along the sub-block joints although force equilibrium is continuous because internal forces between sub-blocks are equilibrated, transferred by contact normal and shear springs with tiny deformations. And a block refined by more sub-blocks is "softer" in a certain direction or in a certain zone, depending on the special distribution of these inter sub-block joints. If a real block is homogeneous and isotropic, the same block refined by sub-blocks may become slightly inhomogeneous or anisotropic.

2.5.3.3 Employ Higher Order Displacement Functions

Incorporation of a higher order displacement function for the DDA is another way to provide more accurate distribution of stress and strain in a block. The original first-order formulation of DDA assumed that the displacement function is linear and the stress and strain are constant within any given block. Lin and Lee (1996) had pointed out that the basic variables of formulations are not independent, and presented an alternative framework formulation. This approach has been adopted in many of the high order formulations that followed. Studies involving a high order DDA have shown its advantages as well as great deal of additional computational effort. To develop a high order DDA, the number of parameters for each block has to be increased from the original 6 degrees of freedom to 12 or 20 for second and third order, respectively.

It has been extensively validated for various beam bending conditions. Using the infinitesimal strain measures, Koo et al. (1995) and Koo and Chern (1996) had also developed the second and third order displacement functions, respectively. Each term of the stiffness matrices and force vectors was explicitly derived according to the basic functions used, and then coded into a program. Koo et al. (1995) also presented a plot showing very good agreement between their second order DDA and the Kirsch solution with respect to radial, tangential, and shear stress concentration factors around a circular opening in an elastic plate. Hsiung (2001) also included an example involving buckling of a beam. Higher order DDA is suitable for many problems but may still be inadequate when the size of the block is very large or odd or when stress and strain vary rapidly.

2.5.4 Fracture Propagation Simulation and Enhancement

Many geotechnical engineering problems and other scientific problems are characterized by a transformation from a continuum to a discontinuum state. For example, material separation and progressive failure phenomena can be found in applications such as concrete structural failure, rock blasting operations and fracture of ceramic or other quasi-brittle materials under high velocity impact. The problems are initially represented by a small number of discrete regions prior to the deformation process. During the loading phase, the bodies are progressively damaged. A few of works were dedicated to the application of DDA to handle this kind of problems.

Ke (1993; 1997) noted that a physically plausible fracture simulation must incorporate: the initiation of fracture, the stress and strain distribution as fracturing proceeds, the fracture path, energy losses resulting from fracture, and, importantly, the behavior of the solid in the presence of the evolving discontinuity. Accordingly, Ke proposed a DDA code extended to incorporate ‘artificial’ joints for numerically simulating fracture propagation. Validation examples using the artificial joint implementation were found physically plausible.

Lin (1995) had extended the DDA to allow shear or tensile stress to induce fractures in intact blocks without a predetermined direction of fracture by introducing two block fracturing algorithms: one for intact blocks and the other for sub-blocks. As a result of fracturing, the intact blocks can be broken into smaller blocks. Based on a three parameter Mohr-Coulomb criterion, intact blocks can be broken into smaller blocks and sub-block fractures are allowed to propagate in a continuous manner across sub-block contacts.

Koo and Chern (1997) proposed an algorithm based on principal stresses for fracturing blocks, which allows for progressive fracturing of blocks as simulations proceed. At each time-step, the stress in each block is compared to the block’s material strength. When the strengths are exceeded, an appropriate direction for fracturing is computed, and the fracture plane is taken to propagate through the centroid of the block. Simple validation tests for uniaxial compression and uniaxial tension were performed. The algorithm appears reasonable for simple fracture behaviour involving convex, regularly shaped blocks. Fracture energy dissipation, a necessary component for physically viable simulation, is not discussed.

2.5.5 Other Enhancements

The penalty technique is used in the DDA to prevent interpenetration between blocks. The theoretical solution can be achieved if the penalty value increases to infinity. The augmented Lagrangian method is an alternative to the penalty method for the DDA model. Lin J. and Hynes (1998) applied the augmented Lagrangian formulation for earthquake engineering problems with limited success. Also, Lin (1995) and Amadie et al. (1996) showed that the augmented Lagrangian method can be successfully implemented within the DDA code with satisfactory results.

Koo and Chern (1998) improved the DDA program efficiency by replacing the original SOR by the preconditioned conjugate gradient (PCG) solver. The adoption of this efficient solver reduced the consumption of CPU time and reduced the iteration number. By adopting the rigid body formulation simultaneously, the amount of calculation may be significantly reduced, which makes it possible to analyze and solve actual engineering problems with super large number of blocks.

Zhao and Gu (2009) proposed a post-processing procedure for the determination of inter-block forces and nodal stresses when gluing DDA blocks together to simulate the behavior of continuous media. The method can provide a more accurate stress state at the node surrounded by irregular or coarse blocks than the average method. The advantage of this recovery method becomes not so evident in the case of regular block systems, but it still provides additional equilibrated inter-block forces and stress across the planes surrounding the measured points.

2.6 Summary

DDA is a powerful method for analyzing discontinuous material such as rock mass. It was widely used in the study of slope stability, underground excavation, rock fall, rock blast etc.

Comparing with the DEM, the DDA has four basic advantages (Jing 1998). First, the equilibrium condition is automatically satisfied for quasi-static problems without using excessive iteration cycles. Second, the length of the time step can be relatively larger without inducing numerical instability. Third, there is no contact overlap. Last and most attractive, it is easy to convert an existing FEM code into a DDA code and include many mature FEM techniques without inheriting the limitations of ordinary FEM.

The DDA still has many limitations like any other numerical method such as the FEM and the DEM in their early stage. A lot of extension work had been done in the past decades to enhance the original DDA as reviewed in the previous section. Among all of the enhancements of DDA, great effort was put on improving the deformation capability of blocks by using sub-mesh, include finite element mesh and sub-block, or higher order displacement function.

The introduction of a finite element mesh into the block is a significant development in the DDA. It not only overcomes the difficulties of using a simple constant strain concept to represent deformations of geometrically complex blocks, but also provides a platform for developing algorithms for material failure, stress wave propagation, fluid flow and thermal effects for the blocky system. It is possible to take advantages of the continuum mechanics principles used in the FEM and the discontinuum mechanics used by the DDA method.

To sum up, the DDA emerged as a very attractive model for geotechnical problems since its advantages can hardly be replaced by any other continuum methods or the discontinuum methods.

CHAPTER 3 FORMULAE OF THE NDDA

3.1 Introduction

As reviewed in the previous chapter, the chief disadvantage of the original DDA is the constant stress and strain distribution inside a big block. When block size is relatively small and the variation of size among blocks is tiny, this limitation is acceptable. However, many engineering problems cannot meet this pre-condition, which limits the application of the DDA or reduces the accuracy of the results.

In the past decades, many works (Ke 1993; Shyu 1993; Chang 1994; Koo, Chern et al. 1995; Lin 1995; Koo and Chern 1996; Lin and Lee 1996; Clatworthy and Scheele 1999; Cheng and Zhang 2000; Hsiung 2001; Grayeli and Mortazavi 2006) concentrated on improving this problem, which can be classified into three classes: 1) couple with finite element mesh; 2) employ sub-block system; 3) introduce higher order displacement functions. Among them, the coupling with finite element mesh is more attractive than the others since it is easy to apply many mature FEM techniques into the code without losing any advantages of the original DDA.

The name, Nodal-based DDA (NDDA), was first used by Shyu (1993). It provided the idea of introducing finite element mesh into the DDA block to enhance the deformation ability of blocks and to refine the stress distribution inside blocks. The conventional triangular and four-node isoparametric elements are used in Shyu’s work. In this chapter, the formulations of the NDDA are formulized according to the principle of minimization of the total potential energy to show its FEM origin. The original DDA block’s kinematics is fully adopted, which is an important feature to distinguish the NDDA from the FEM.

The method provided in this thesis is developed on the basis of Shyu's work (1993) with an enhancement. Indeed, the NDDA is far more than a simple coupling of the DDA with finite element mesh. When analyzing continuous media, the NDDA becomes the FEM. With the development of fracture mechanics, a lot of modified FEMs were introduced to handle the crack propagation problems. Although the DDA can deal well with pre-existing discontinuities, the propagation of a crack inside the block is not allowed. Hence, an important improvement to the original NDDA is to give the fracturing ability inside an intact block. Details about the fracture scheme will be introduced and discussed in chapter 5.

Since any polygon can be discretized by triangles, the block still can be any shape, convex or concave, like the standard DDA. In the NDDA, the triangular element is the basic analysis object and the nodal displacements are the unknowns of simultaneous equations. A group of triangular elements build up a block. The triangular grid lines can be referred to as virtual joints, which will fracture when certain failure criterion is triggered. The topology of the NDDA block system is illustrated by a two-block model as shown in Figure 3.1.

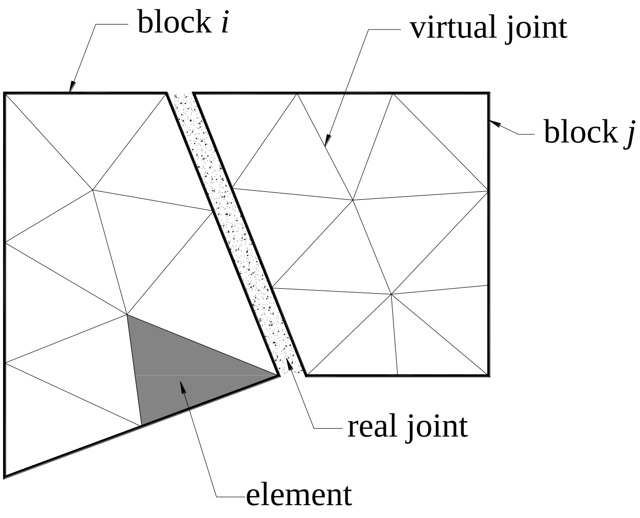

Figure 3.1 schematic illustration of an NDDA model

In the standard DDA, basic unknowns are six displacements of a block, $\{u_0, v_0, r_0, \varepsilon_x, \varepsilon_y, \gamma_{xy}\}$, which are independent of the block shape. It is not accurate to use six variables to describe the deformation of a big block under complex loading conditions. In the NDDA, the basic analysis object is the triangular element and the nodal displacements are the basic unknowns. Hence, the degrees of freedom of a block are now depending on the number of nodes it has. The more nodes a block has, the better deformation ability it will have.

For a triangular element, three nodes provide six unknown displacements, $\{u_i, v_i, u_j, v_j, u_m, v_m\}^{\mathrm{T}}$. In a special case where the block is triangular and include only one triangular element, the six unknowns of NDDA is equivalent to the unknowns of the standard DDA. The advantage of using $\{u_i, v_i, u_j, v_j, u_m, v_m\}^{\mathrm{T}}$ as element unknowns makes it possible to unify continuous and discontinuous region in analysis.

In the standard DDA, the block is undividable. When dealing with crack propagation, especially in the case that one big block split into several sub-blocks in a cracking zone, the DDA cannot handle. In the NDDA, a fracture mechanism is introduced to make it possible for the fracture to occur in an intact block. Crack will occur along the virtual joint when the failure criterion is satisfied. With the virtual joint concept, the NDDA possesses the ability of dealing with a mixed continuous/discontinuous problem with high accuracy and efficiency.

3.2 Displacement Functions

Contents in the section are similar with the classic FEM theory (Zienkiewicz and Taylor 2000) about triangular element. Figure 3.2 shows the typical triangular element considered, with nodes *i*, *j*, *m*, numbered in an anticlockwise order.

The displacements of *node i* have two components, written in vector as

$$\mathbf{d}_i = \begin{Bmatrix} u_i \\ v_i \end{Bmatrix} \tag{3.1}$$

And the six components of element displacements are listed as a vector

$$\mathbf{a} = \begin{Bmatrix} \mathbf{d}_i \\ \mathbf{d}_j \\ \mathbf{d}_m \end{Bmatrix} = \begin{Bmatrix} u_i \\ v_i \\ u_j \\ v_j \\ u_m \\ v_m \end{Bmatrix} \tag{3.2}$$

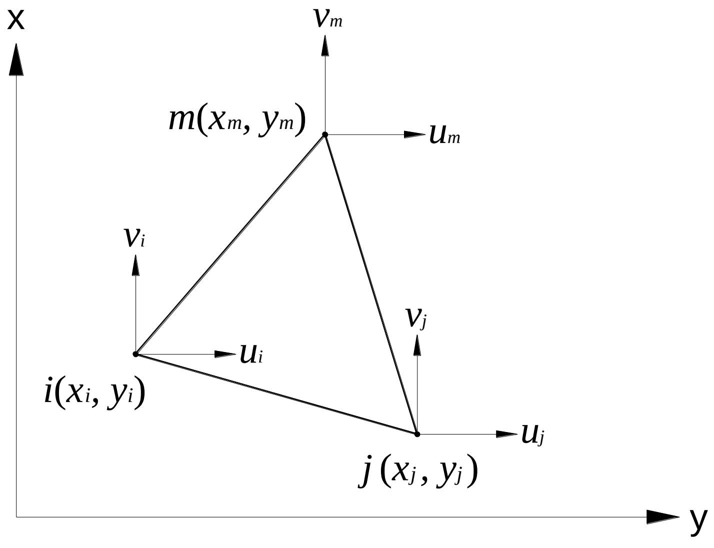

Figure 3.2 an triangular finite element, showing notation used

The displacements within an element have to be uniquely defined by these six values. The simplest representation is clearly given by two linear polynomials

$$\begin{cases} u = \alpha_1 + \alpha_2 x + \alpha_3 y \\ v = \alpha_4 + \alpha_5 x + \alpha_6 y \end{cases} \tag{3.3}$$

where (u, v) are the displacements at point (x, y) inside the element.

The six constants α_i can be evaluated easily by solving the two sets of three simultaneous equations which will arise if the nodal coordinates are inserted and the displacements equated to the appropriate nodal displacements. For example, we have the following relationships along the global *x*-axis direction:

$$\begin{aligned} u_i &= \alpha_1 + \alpha_2 x_i + \alpha_3 y_i \\ u_j &= \alpha_1 + \alpha_2 x_j + \alpha_3 y_j \\ u_m &= \alpha_1 + \alpha_2 x_m + \alpha_3 y_m \end{aligned} \tag{3.4}$$

We can easily solve for α_1, α_2 and α_3 in terms of the nodal displacements u_i, u_j, u_m, and finally obtain

$$u = \frac{1}{2\Delta}[(a_i + b_i x + c_i y)u_i + (a_j + b_j x + c_j y)u_j + (a_m + b_m x + c_m y)u_m] \tag{3.5}$$

in which

$$\begin{aligned} a_i &= x_j y_m - x_m y_j \\ b_i &= y_j - y_m \\ c_i &= x_m - x_j \end{aligned} \tag{3.6}$$

with the other coefficients obtained by a cyclic permutation of subscripts in the order *i, j, m*, and where Δ is the area of $\triangle ijm$ obtained by

$$\Delta = \frac{1}{2}\begin{vmatrix} 1 & x_i & y_i \\ 1 & x_j & y_j \\ 1 & x_m & y_m \end{vmatrix} \tag{3.7}$$

The vertical displacement *v* can be obtained similarly as

$$v = \frac{1}{2\Delta}[(a_i + b_i x + c_i y)v_i + (a_j + b_j x + c_j y)v_j + (a_m + b_m x + c_m y)v_m] \tag{3.8}$$

Though not strictly necessary at this stage, we can represent the above relations Eq. (3.5) and (3.8) in the standard form:

$$\mathbf{u} = \begin{Bmatrix} u \\ v \end{Bmatrix} = \mathbf{Na} = \begin{bmatrix} N_i & 0 & N_j & 0 & N_m & 0 \\ 0 & N_i & 0 & N_j & 0 & N_m \end{bmatrix} \begin{Bmatrix} u_i \\ v_i \\ u_j \\ v_j \\ u_m \\ v_m \end{Bmatrix} \tag{3.9}$$

where

$$\begin{aligned} N_i &= \frac{a_i + b_i x + c_i y}{2\Delta} \\ N_j &= \frac{a_j + b_j x + c_j y}{2\Delta} \\ N_m &= \frac{a_m + b_m x + c_m y}{2\Delta} \end{aligned} \tag{3.10}$$

The chosen displacement function automatically guarantees continuity of displacements with adjacent elements because the displacements vary linearly along any side of the triangle and, with identical displacement imposed at the nodes, the same displacement will clearly exist along an interface.

The total strain at any point within the element can be defined by its three components which contribute to internal work. Thus

$$\boldsymbol{\varepsilon} = \begin{Bmatrix} \varepsilon_x \\ \varepsilon_y \\ \gamma_{xy} \end{Bmatrix} = \begin{bmatrix} \frac{\partial}{\partial x} & 0 \\ 0 & \frac{\partial}{\partial y} \\ \frac{\partial}{\partial y} & \frac{\partial}{\partial x} \end{bmatrix} \begin{Bmatrix} u \\ v \end{Bmatrix} = \mathbf{Su} \tag{3.11}$$

where

$$\mathbf{S} = \begin{bmatrix} \frac{\partial}{\partial x} & 0 \\ 0 & \frac{\partial}{\partial y} \\ \frac{\partial}{\partial y} & \frac{\partial}{\partial x} \end{bmatrix}$$

Substituting Eq. (3.9) into Eq. (3.11), we have

$$\boldsymbol{\varepsilon} = \mathbf{SNa} = \mathbf{Ba} = [\mathbf{B}_i \quad \mathbf{B}_j \quad \mathbf{B}_m] \begin{Bmatrix} \mathbf{d}_i \\ \mathbf{d}_j \\ \mathbf{d}_m \end{Bmatrix} \tag{3.12}$$

where

$$\mathbf{B} = \mathbf{SN} = \begin{bmatrix} \dfrac{\partial N_i}{\partial x} & 0 & \dfrac{\partial N_j}{\partial x} & 0 & \dfrac{\partial N_m}{\partial x} & 0 \\ 0 & \dfrac{\partial N_i}{\partial y} & 0 & \dfrac{\partial N_j}{\partial y} & 0 & \dfrac{\partial N_m}{\partial y} \\ \dfrac{\partial N_i}{\partial y} & \dfrac{\partial N_i}{\partial x} & \dfrac{\partial N_j}{\partial x} & \dfrac{\partial N_j}{\partial y} & \dfrac{\partial N_m}{\partial x} & \dfrac{\partial N_m}{\partial y} \end{bmatrix}$$

$$= \frac{1}{2\Delta} \begin{bmatrix} b_i & 0 & b_j & 0 & b_m & 0 \\ 0 & c_i & 0 & c_j & 0 & c_m \\ c_i & b_i & c_j & b_j & c_m & b_m \end{bmatrix} \tag{3.13}$$

It will be noted that the matrix **B** is independent of the position within the element in this case, and hence the strains are constant throughout the element.

3.3 Simultaneous Equations

Since the NDDA uses an incremental solution procedure, the equations of motion are solved at every time step and the incremental change in energy components is determined at each time step as the system attempts to reach equilibrium.

For any virtual displacement, the sum of internal and external work for the whole system should be zero, which can be written as

$$\delta(U + W) = \delta(\Pi) = 0 \tag{3.14}$$

where U is the internal energy of the whole system, W is the work done by the external loads including the contact forces or any other forces interact between blocks, and Π is the total potential energy of the system.

Individual triangular elements are connected by nodes to form a block, and blocks are connected by joints and contact springs to build a system. Assuming there are n nodes in the system, the global equilibrium equations will have the following form:

$$\mathbf{KD}=\mathbf{F} \tag{3.15}$$

where **K** is the global stiffness matrix, a $2n\times 2n$ matrix. **D** is the unknown vector and **F** is the equivalent force vector. Write in submatrix form, we have:

$$\begin{bmatrix} \mathbf{k}_{11} & \mathbf{k}_{12} & \mathbf{k}_{13} & \cdots & \mathbf{k}_{1n} \\ \mathbf{k}_{21} & \mathbf{k}_{22} & \mathbf{k}_{23} & \cdots & \mathbf{k}_{2n} \\ \mathbf{k}_{31} & \mathbf{k}_{32} & \mathbf{k}_{33} & \cdots & \mathbf{k}_{3n} \\ \vdots & \vdots & \vdots & \ddots & \vdots \\ \mathbf{k}_{n1} & \mathbf{k}_{n2} & \mathbf{k}_{n3} & \cdots & \mathbf{k}_{nn} \end{bmatrix} \begin{Bmatrix} \mathbf{d}_1 \\ \mathbf{d}_2 \\ \mathbf{d}_3 \\ \vdots \\ \mathbf{d}_n \end{Bmatrix} = \begin{Bmatrix} \mathbf{f}_1 \\ \mathbf{f}_2 \\ \mathbf{f}_3 \\ \vdots \\ \mathbf{f}_n \end{Bmatrix} \tag{3.16}$$

in which, each element $\mathbf{k}_{ij}$ in the coefficient matrix is a 2×2 submatrix. $\mathbf{d}_i$ is a 2×1 submatrix and denotes the displacements unknowns $\{u_i, v_i\}^T$ of *node i*. $\mathbf{f}_i$ is a 2×1 submatrix and denotes the equivalent nodal forces $\{f_{ix}, f_{iy}\}^T$ applied on *node i*.

The above equilibrium equations are derived by minimizing the total potential energy Π. The *i-th* row of Eq. (3.16) consists of two linear equations

$$\begin{cases} \dfrac{\partial \Pi}{\partial u_i}=0 \\ \dfrac{\partial \Pi}{\partial v_i}=0 \end{cases} \tag{3.17}$$

3.4 Elastic Submatrices

The strain energy Π_e of an *element i* is defined as

$$\Pi_e^{\,i}=\frac{1}{2}\iint \boldsymbol{\varepsilon}_i^{\mathrm{T}}\boldsymbol{\sigma}_i dxdy+\iint \boldsymbol{\varepsilon}_i^{\mathrm{T}}\boldsymbol{\sigma}_i^0 dxdy \tag{3.18}$$

where $\boldsymbol{\sigma}_i^0$ is the initial stress of *element i*, and the integration is over the entire area of *element i*. For each time step, assuming the elements are generally linearly elastic, the relationship between stresses and strains will be linear and of the form

$$\boldsymbol{\sigma}=\mathbf{E}\boldsymbol{\varepsilon} \tag{3.19}$$

where **E** is an elasticity matrix containing the appropriate material properties.

For plane stress in an isotropic material, we obtain the matrix **E** as

$$\mathbf{E} = \frac{E}{1-\nu^2}\begin{bmatrix} 1 & \nu & 0 \\ \nu & 1 & 0 \\ 0 & 0 & (1-\nu)/2 \end{bmatrix} \tag{3.20}$$

and for plane strain, we obtain the matrix **E** as

$$\mathbf{E} = \frac{E}{(1+\nu)(1-2\nu)}\begin{bmatrix} 1-\nu & \nu & 0 \\ \nu & 1-\nu & 0 \\ 0 & 0 & (1-2\nu)/2 \end{bmatrix} \tag{3.21}$$

where E is Young's modulus and ν is Poisson's ratio.

If non-linear stress-strain relationships are considered, **E** will have the following general form:

$$\mathbf{E} = \begin{bmatrix} e_{11} & e_{12} & e_{13} \\ e_{21} & e_{22} & e_{23} \\ e_{31} & e_{32} & e_{33} \end{bmatrix} \tag{3.22}$$

By substituting Eq. (3.19), the Eq. (3.18) can be rewritten as

$$\Pi_e{}^i = \frac{1}{2}\iint \boldsymbol{\varepsilon}_i^{\mathrm{T}}\mathbf{E}_i\boldsymbol{\varepsilon}_i dxdy + \iint \boldsymbol{\varepsilon}_i^{\mathrm{T}}\boldsymbol{\sigma}_0 dxdy \tag{3.23}$$

Substituting Eq. (3.12), we have

$$\begin{aligned} \Pi_e{}^i &= \frac{1}{2}\iint \mathbf{a}_i^{\mathrm{T}}\mathbf{B}_i^{\mathrm{T}}\mathbf{E}_i\mathbf{B}_i\mathbf{a}_i dxdy + \iint \mathbf{a}_i^{\mathrm{T}}\mathbf{B}_i^{\mathrm{T}}\boldsymbol{\sigma}_i^0 dxdy \\ &= \frac{1}{2}\mathbf{a}_i^{\mathrm{T}}\mathbf{B}_i^{\mathrm{T}}\mathbf{E}_i\mathbf{B}_i\mathbf{a}_i \iint dxdy + \mathbf{a}_i^{\mathrm{T}}\mathbf{B}_i^{\mathrm{T}}\boldsymbol{\sigma}_i^0 \iint dxdy \\ &= \frac{A_0}{2}\mathbf{a}_i^{\mathrm{T}}\mathbf{B}_i^{\mathrm{T}}\mathbf{E}_i\mathbf{B}_i\mathbf{a}_i + A_0\mathbf{a}_i^{\mathrm{T}}\mathbf{B}_i^{\mathrm{T}}\boldsymbol{\sigma}_i^0 \end{aligned} \tag{3.24}$$

where A_0 is the initial area of *element i*.

Minimize the strain energy $\Pi_e{}^i$ and obtain the following 6×6 submatrix

$$\mathbf{k}_e{}^i = \frac{\partial^2 \Pi_e{}^i}{\partial \mathbf{a}_i \partial \mathbf{a}_i} = \frac{A_0}{2}\frac{\partial^2(\mathbf{a}_i^{\mathrm{T}}\mathbf{B}_i^{\mathrm{T}}\mathbf{E}_i\mathbf{B}_i\mathbf{a}_i)}{\partial \mathbf{a}_i \partial \mathbf{a}_i} = A_0\mathbf{B}_i^{\mathrm{T}}\mathbf{E}_i\mathbf{B}_i \tag{3.25}$$

and the equivalent nodal force vector

$$\mathbf{f}_e{}^i = -\left.\frac{\partial \Pi_e{}^i}{\partial \mathbf{a}_i}\right|_0 = -A_0 \left.\frac{\partial(\mathbf{a}_i^{\mathrm{T}}\mathbf{B}_i^{\mathrm{T}}\boldsymbol{\sigma}_i^0)}{\partial \mathbf{a}_i}\right|_0 = -A_0\mathbf{B}_i^{\mathrm{T}}\boldsymbol{\sigma}_i^0 \tag{3.26}$$

The matrix form is

$$\mathbf{k}_e{}^i = \begin{bmatrix} \mathbf{k}_{aa} & \mathbf{k}_{ab} & \mathbf{k}_{ac} \\ \mathbf{k}_{ba} & \mathbf{k}_{bb} & \mathbf{k}_{bc} \\ \mathbf{k}_{ca} & \mathbf{k}_{cb} & \mathbf{k}_{cc} \end{bmatrix}$$

$$\mathbf{f}_e{}^i = \begin{Bmatrix} \mathbf{f}_a \\ \mathbf{f}_b \\ \mathbf{f}_c \end{Bmatrix}$$

where a, b, and c denote the node indexes of *element i*. Each component $\mathbf{k}_{ij}$ (i, j=a, b, c) is a 2×2 submatrix which is added to the corresponding position in the global stiffness matrix **K**, such as $\mathbf{k}_{ab}$ is add to the intersection of *a-th* row and *b-th* column in the coefficient matrix in Eq. (3.16). Each component $\mathbf{f}_i$ (i=a, b, c) is a 2×1 submatrix which is added to the free term at the right hand side of Eq. (3.16) according to the node index, such as $\mathbf{f}_a$ is added to the *a-th* row of vector **f**.

3.5 Equivalent nodal forces

3.5.1 Point load

The point loading force $\mathbf{p} = \{p_x,\ p_y\}^{\mathrm{T}}$ acts on point (x, y) inside *element i*. The displacements at point (x, y) of *element i* (see Figure 3.3) are

$$\mathbf{u} = \mathbf{N}_i\mathbf{a}_i$$

The potential energy of the point loading **p** is

$$\Pi_p{}^i = -(p_x u + p_y v) = -\mathbf{u}^{\mathrm{T}}\mathbf{p} = -\mathbf{a}_i^{\mathrm{T}}\mathbf{N}_i^{\mathrm{T}}\mathbf{p} \tag{3.27}$$

To minimize $\Pi_p{}^i$, the derivatives are computed:

$$\mathbf{f}_i = \begin{Bmatrix} \mathbf{f}_a \\ \mathbf{f}_b \\ \mathbf{f}_c \end{Bmatrix} = -\left.\frac{\partial \Pi_p{}^{i}}{\partial \mathbf{a}_i}\right|_0 = \left.\frac{\partial(\mathbf{a}_i^{\mathrm{T}}\mathbf{N}_i^{\mathrm{T}}\mathbf{p})}{\partial \mathbf{a}_i}\right|_0 = \mathbf{N}_i^{\mathrm{T}}\mathbf{p} \tag{3.28}$$

where $\mathbf{f}_i$ forms a 6×1 submatrix which is added to the right side of global equations according to the indexes of element nodes.

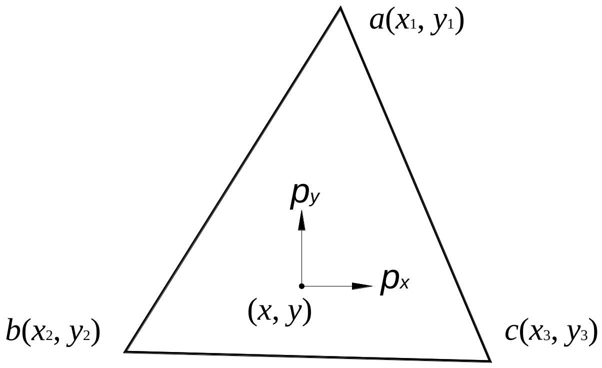

Figure 3.3 point load in an element

3.5.2Distributed linear load along element boundary

Assume the loading is distributed on the element boundary between *node i* and *node j* (see Figure 3.4). The coordinates for node i and node j are (x_i, y_i) and (x_j, y_j), separately. The equations for segment $\overline{ij}$ are

$$\begin{cases} x = (x_j - x_i)t + x_i \\ y = (y_j - y_i)t + y_i \end{cases} \quad (0\le t \le 1 \tag{3.29}$$

The length of line $\overline{ij}$ is

$$l = \sqrt{(x_j - x_i)^2 + (y_j - y_i)^2}$$

The load is

$$\mathbf{q}(t) = \begin{Bmatrix} q_x(t) \\ q_y(t) \end{Bmatrix} \quad (0\le t \le 1 \tag{3.30}$$

which vary along the boundary $\overline{ij}$.

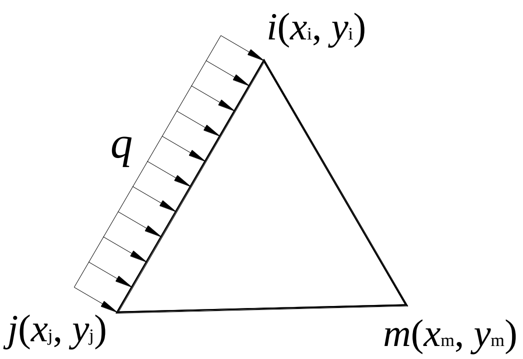

Figure 3.4 distributed load on the element boundary

The potential energy of the line load is

$$\Pi_l = -\int_0^1 \mathbf{u}_l^{\mathrm{T}}(t)\mathbf{q}(t)l\,dt \tag{3.31}$$

where $\mathbf{u}_l(t)$ denote the displacements along boundary $\overline{ij}$.

$$\mathbf{u}_l(t) = \mathbf{N}_l\mathbf{d} = \mathbf{N}_l\begin{Bmatrix}\mathbf{d}_i\\ \mathbf{d}_j\end{Bmatrix} = \begin{bmatrix}1-t & 0 & t & 0\\ 0 & 1-t & 0 & t\end{bmatrix}\begin{Bmatrix}u_i\\ v_i\\ u_j\\ v_j\end{Bmatrix} \tag{3.32}$$

where

$$\mathbf{N}_l = \begin{bmatrix}1-t & 0 & t & 0\\ 0 & 1-t & 0 & t\end{bmatrix}$$

$$\mathbf{d} = \begin{Bmatrix}\mathbf{d}_i\\ \mathbf{d}_j\end{Bmatrix} = \begin{Bmatrix}u_i\\ v_i\\ u_j\\ v_j\end{Bmatrix}$$

substituting Eq. (3.32) into Eq. (3.31), we have

$$\Pi_l = -\mathbf{d}^{\mathrm{T}}\int_0^1 \mathbf{N}_l^{\mathrm{T}}\mathbf{q}(t)l\,dt \tag{3.33}$$

The derivatives of Π_l are computed to minimize the potential energy:

$$\mathbf{f}_l = \begin{Bmatrix}\mathbf{f}_i\\ \mathbf{f}_j\end{Bmatrix} = -\left.\frac{\partial \Pi_l}{\partial \mathbf{d}}\right|_0 = \int_0^1 \mathbf{N}_l^{\mathrm{T}}\mathbf{q}(t)l\,dt \tag{3.34}$$

When the line load is uniformly distributed along the boundary $\overline{ij}$, the above equation can be written as

$$\mathbf{f}_l=\int_0^1\begin{bmatrix}1-t & 0\\ 0 & 1-t\\ t & 0\\ 0 & t\end{bmatrix}\begin{Bmatrix}q_x\\ q_y\end{Bmatrix}l dt=\begin{bmatrix}l/2 & 0\\ 0 & l/2\\ l/2 & 0\\ 0 & l/2\end{bmatrix}\begin{Bmatrix}q_x\\ q_y\end{Bmatrix}=\frac{l}{2}\begin{Bmatrix}q_x\\ q_y\\ q_x\\ q_y\end{Bmatrix} \tag{3.35}$$

3.5.3 Distributed body forces

Assuming that $\mathbf{b}=\{b_x,b_y\}^{\mathrm{T}}$ is the constant body force applied on the *element i*. The potential energy of the constant body force **b** is

$$\begin{aligned}\Pi_{bd}{}^i&=-\iint \mathbf{u}_i^{\mathrm{T}}\mathbf{b}dxdy\\ &=-\iint \mathbf{a}_i^{\mathrm{T}}\mathbf{N}_i^{\mathrm{T}}\mathbf{b}dxdy\\ &=-\mathbf{a}_i^{\mathrm{T}}\left(\iint \mathbf{N}_i^{\mathrm{T}}dxdy\right)\mathbf{b}\end{aligned} \tag{3.36}$$

Since

$$\iint \mathbf{N}_i^{\mathrm{T}}dxdy=\frac{A_0}{3}\begin{bmatrix}1 & 0\\ 0 & 1\\ 1 & 0\\ 0 & 1\\ 1 & 0\\ 0 & 1\end{bmatrix} \tag{3.37}$$

Substituting Eq. (3.37) into Eq. (3.36), we have

$$\Pi_{bd}{}^i=-\mathbf{a}_i^{\mathrm{T}}\frac{A_0}{3}\begin{bmatrix}1 & 0\\ 0 & 1\\ 1 & 0\\ 0 & 1\\ 1 & 0\\ 0 & 1\end{bmatrix}\begin{Bmatrix}b_x\\ b_y\end{Bmatrix}=-\frac{A_0}{3}\mathbf{a}_i^{\mathrm{T}}\begin{Bmatrix}b_x\\ b_y\\ b_x\\ b_y\\ b_x\\ b_y\end{Bmatrix} \tag{3.38}$$

The derivatives of $\Pi_{bd}{}^i$ are computed to minimize the potential energy:

$$\mathbf{f}_{bd}{}^{i} = \begin{Bmatrix} \mathbf{f}_a \\ \mathbf{f}_b \\ \mathbf{f}_c \end{Bmatrix} = -\left.\frac{\partial \Pi_b{}^{i}}{\partial \mathbf{a}_i}\right|_0 = \frac{A_0}{3} \begin{Bmatrix} b_x \\ b_y \\ b_x \\ b_y \\ b_x \\ b_y \end{Bmatrix} \tag{3.39}$$

where $\mathbf{f}_{bd}{}^{i}$ forms a 6×1 submatrix which is added to the free term at right side of global equations according to the nodes index *a*, *b* and *c*.

3.6 Bolting Connection Submatrices

Consider a bolt or a bar connecting *node i* and *node j* on two different blocks (see Figure 3.5). The displacements of the ends are $\{u_i, v_i\}^T$ and $\{u_j, v_j\}^T$, respectively. The length of the bolt is

$$l = \sqrt{(x_i - x_j)^2 + (y_i - y_j)^2} \tag{3.40}$$

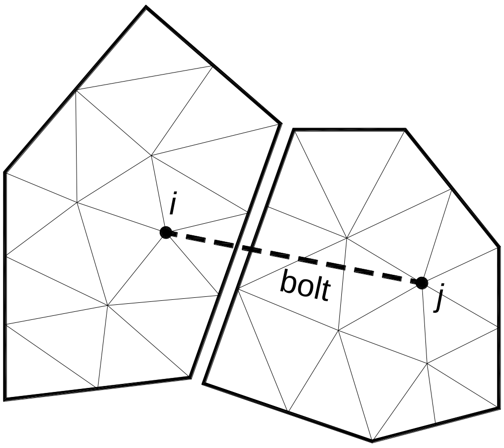

Figure 3.5 bolt connection between two blocks

The length variation of the bolt is

$$\Delta = \frac{1}{l}[(x_i - x_j)(u_i - u_j) + (y_i - y_j)(v_i - v_j)] \tag{3.41}$$

Denote the direction cosines of the bar by

$$l_x = \frac{x_i - x_j}{l}, \quad l_y = \frac{y_i - y_j}{l}$$

then we have

$$\begin{aligned} \Delta &= \begin{Bmatrix} u_i & v_i \end{Bmatrix} \begin{Bmatrix} l_x \\ l_y \end{Bmatrix} - \begin{Bmatrix} u_j & v_j \end{Bmatrix} \begin{Bmatrix} l_x \\ l_y \end{Bmatrix} \\ &= \begin{Bmatrix} u_i - u_j & v_i - v_j \end{Bmatrix} \begin{Bmatrix} l_x \\ l_y \end{Bmatrix} \end{aligned}$$

$$\Delta = (\mathbf{d}_i^{\mathrm{T}} - \mathbf{d}_j^{\mathrm{T}}) \begin{Bmatrix} l_x \\ l_y \end{Bmatrix} \tag{3.42}$$

Assuming the stiffness of the bar is k_b, the bar force is

$$f = k_b \Delta \tag{3.43}$$

The potential energy of the bar is

$$\Pi_{blt} = \frac{1}{2} f \Delta = \frac{1}{2} k_b \Delta^2 \tag{3.44}$$

$$\Pi_{blt} = \frac{k_b}{2} (\mathbf{d}_i^{\mathrm{T}} - \mathbf{d}_j^{\mathrm{T}}) \begin{Bmatrix} l_x \\ l_y \end{Bmatrix} \begin{Bmatrix} l_x & l_y \end{Bmatrix} (\mathbf{d}_i - \mathbf{d}_j)$$

Let

$$\mathbf{L} = \begin{Bmatrix} l_x \\ l_y \end{Bmatrix} \begin{Bmatrix} l_x & l_y \end{Bmatrix} = \begin{bmatrix} l_x^2 & l_x l_y \\ l_x l_y & l_y^2 \end{bmatrix} \tag{3.45}$$

then

$$\Pi_{blt} = \frac{k_b}{2} (\mathbf{d}_i^{\mathrm{T}} - \mathbf{d}_j^{\mathrm{T}}) \mathbf{L} (\mathbf{d}_i - \mathbf{d}_j) \tag{3.46}$$

The derivatives of Π_{blt}

$$\mathbf{k}_{ii} = \frac{\partial^2 \Pi_{blt}}{\partial \mathbf{d}_i \partial \mathbf{d}_i} = k_b \mathbf{L} \tag{3.47}$$

$$\mathbf{k}_{jj} = \frac{\partial^2 \Pi_{blt}}{\partial \mathbf{d}_j \partial \mathbf{d}_j} = k_b \mathbf{L} \tag{3.48}$$

$$\mathbf{k}_{ij} = \frac{\partial^2 \Pi_{blt}}{\partial \mathbf{d}_i \partial \mathbf{d}_j} = -k_b \mathbf{L} \tag{3.49}$$

$$\mathbf{k}_{ji} = \frac{\partial^2 \Pi_{blt}}{\partial \mathbf{d}_j \partial \mathbf{d}_i} = -k_b \mathbf{L} \tag{3.50}$$

forms four 2×2 submatrices which are added to the global stiffness matrix **K** according to the index i and j, for example, $\mathbf{k}_{ij}$ is added to the intersection of *i-th* row and *j-th* column.

3.7 Inertia Submatrices

The time steps are used by both statics and dynamics. The only difference is that the static computation assumes the velocity as zero at the beginning of each time step while the dynamics computation inherits the velocity from last time step.

Denote $\{u, v\}^T$ as the time dependent displacement at point (x, y) of *element i* and m as the mass per unit area. Then, the force of inertia per unit area is

$$\begin{Bmatrix} f_x \\ f_y \end{Bmatrix} = -m \begin{Bmatrix} \dfrac{d^2u}{dt^2} \\ \dfrac{d^2v}{dt^2} \end{Bmatrix} \tag{3.51}$$

The potential energy of the inertia force of *element i* is

$$\begin{aligned}\Pi_m{}^i &= -\iint \{u \quad v\} \begin{Bmatrix} f_x \\ f_y \end{Bmatrix} dxdy \\ &= m\iint \{u \quad v\} \begin{Bmatrix} \dfrac{d^2u}{\partial t^2} \\ \dfrac{d^2v}{\partial t^2} \end{Bmatrix} dxdy \end{aligned} \tag{3.52}$$

and

$$\begin{Bmatrix} \dfrac{d^2u}{dt^2} \\ \dfrac{d^2v}{dt^2} \end{Bmatrix} = \frac{d^2}{dt^2}\begin{Bmatrix} u \\ v \end{Bmatrix} = \frac{d^2(\mathbf{N}_i\mathbf{a}_i)}{dt^2} = \mathbf{N}_i \frac{d^2\mathbf{a}_i}{dt^2} \tag{3.53}$$

where $\mathbf{N}_i$ is independent of time t.

$$\Pi_m{}^i = m\iint \mathbf{a}_i^{\mathrm{T}}\mathbf{N}_i^{\mathrm{T}}\mathbf{N}_i \frac{d^2\mathbf{a}_i}{dt^2} dxdy \tag{3.54}$$

For the time dimension, we use the finite difference method:

$$\begin{aligned}\frac{d^2\mathbf{a}(t)}{dt^2} &= \frac{1}{\delta^2}(\mathbf{a}(t) - 2\mathbf{a}(t-\delta) + \mathbf{a}(t-2\delta)) \\ &= \frac{1}{\delta^2}\{[\mathbf{a}(t)-\mathbf{a}(t-\delta)] - [\mathbf{a}(t-\delta)-\mathbf{a}(t-2\delta)]\}\end{aligned} \tag{3.55}$$

$$\mathbf{a} = \mathbf{a}(t) - \mathbf{a}(t-\delta) \tag{3.56}$$

$$\mathbf{a}_0 = \mathbf{a}(t-\delta) - \mathbf{a}(t-2\delta) \tag{3.57}$$

$$\frac{d^2\mathbf{a}_i}{dt^2} = \frac{1}{\delta^2}(\mathbf{a}_i - \mathbf{a}_{i0}) \tag{3.58}$$

Here $\mathbf{a}_i$ is the displacements of *element i* in current time step, $\mathbf{a}_{i0}$ is the displacement of last time step, δ is the time interval.

Substitute Eq. (3.58) into Eq. (3.54), then

$$\Pi_m{}^i = \frac{m}{\delta^2}\iint \mathbf{a}_i^{\mathrm{T}}\mathbf{N}_i^{\mathrm{T}}\mathbf{N}_i(\mathbf{a}_i - \mathbf{a}_{i0}) dxdy \tag{3.59}$$

To reach equilibrium, $\Pi_m{}^i$ is minimized with respect to element displacement variables. Then

$$\mathbf{k}_m{}^i = \frac{\partial^2 \Pi_m{}^i}{\partial \mathbf{a}_i \partial \mathbf{a}_i} = \frac{2m}{\delta^2} \iint \mathbf{N}_i^{\mathrm{T}} \mathbf{N}_i \, dxdy \tag{3.60}$$

where $\mathbf{k}_m{}^i$ is a 6×6 submatrix with the same structure like elastic submatrix $\mathbf{k}_e{}^i$, similar operation is done when being added to the global stiffness matrix **K**.

$$\begin{aligned} \mathbf{f}_m{}^i &= -\left.\frac{\partial \Pi_m{}^i}{\partial \mathbf{a}_i}\right|_0 \\ &= -\frac{m}{\delta^2} \iint \mathbf{N}_i^{\mathrm{T}} \mathbf{N}_i (2\mathbf{a}_{i0} - \mathbf{a}_{i0}) dxdy \\ &= -\frac{m}{\delta^2} (\iint \mathbf{N}_i^{\mathrm{T}} \mathbf{N}_i dxdy) \mathbf{a}_{i0} \end{aligned} \tag{3.61}$$

forms a 6×1 vector, which is added to the free term of Eq. (3.16) according to the index of element nodes.

3.8 Viscosity Submatrices

The DDA method could be applied to problems involving a viscous stratum in shear, as encountered in plate tectonics, or in regard to floating ice blocks.

The resistance force from viscosity is proportional to the velocity as well as the block area. When the displacement increment is given per unit time, the force is:

$$\begin{Bmatrix} f_x \\ f_y \end{Bmatrix} = -\mu \begin{Bmatrix} \dfrac{u}{\delta} \\ \dfrac{v}{\delta} \end{Bmatrix} = -\frac{\mu}{\delta} \begin{Bmatrix} u \\ v \end{Bmatrix} \tag{3.62}$$

where δ is the time step; u and v are the displacement increment per unit time. The potential energy of the force of viscosity of *element i* is

$$\begin{aligned} \Pi_v{}^i &= -\{u \quad v\} \begin{Bmatrix} f_x \\ f_y \end{Bmatrix} dxdy \\ &= \frac{\mu}{\delta} \iint \{u \quad v\} \begin{Bmatrix} u \\ v \end{Bmatrix} dxdy \end{aligned} \tag{3.63}$$

$$\begin{aligned}\Pi_v{}^i &= \frac{\mu}{\delta}\iint \mathbf{a}_i^{\mathrm{T}}\mathbf{N}_i^{\mathrm{T}}\mathbf{N}_i\mathbf{a}_i dxdy \\ &= \mathbf{a}_i^{\mathrm{T}}(\frac{\mu}{\delta}\iint \mathbf{N}_i^{\mathrm{T}}\mathbf{N}_i dxdy)\mathbf{a}_i\end{aligned} \tag{3.64}$$

The force of viscosity can be considered as body loading. In order to reach equilibrium, $\Pi_v{}^i$ is minimized with respect to element displacement variables. We have

$$\mathbf{k}_v{}^i = \frac{\partial \Pi_v}{\partial \mathbf{a}_i \partial \mathbf{a}_i} = \frac{\mu}{\delta}\iint \mathbf{N}_i^{\mathrm{T}}\mathbf{N}_i dxdy \tag{3.65}$$

forms a 6×6 submatrix.

3.9 Displacement Constraints

There are three kinds of boundary conditions: free, fixed and rolling along a direction. The rolling boundary can be subdivided into rolling along *x* direction, rolling along *y* direction, and rolling along a specified angle. And the fixed bearing can be considered as compound effect of two rolling bearing: rolling along *x* direction and rolling along *y* direction. Therefore, we only need to deduce the submatrix of rolling along a specified angle. More generally, supports may have displacements at their constraint direction, which need to be considered in the constraint submatrix.

Assume the direction angle of the rolling slope is α, the direction angle of normal is α+90º (see Figure 3.6). The displacement of support along the normal direction of the rolling slope is δ. Denote the normal vector of the slope as

$$\mathbf{n} = \begin{Bmatrix} l_x \\ l_y \end{Bmatrix} \tag{3.66}$$

In the current case, we have

$$\begin{aligned} l_x &= \cos(\alpha + 90°) = -\sin\alpha \\ l_y &= \sin(\alpha + 90°) = \cos\alpha \end{aligned} \tag{3.67}$$

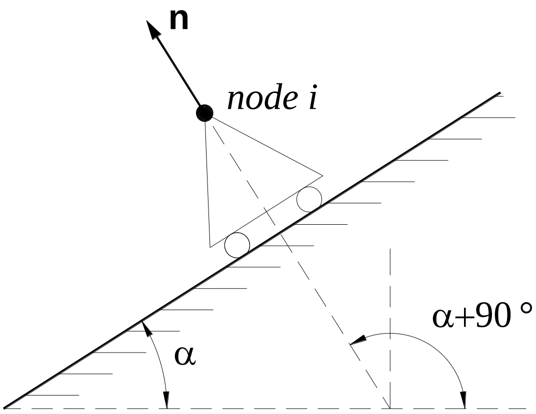

Figure 3.6 constraint along a specified direction

We use a very stiff spring in the constraint direction to achieve the equivalent constraint effect. Denote the stiffness of the constraint spring by k. It is a very large positive number, normally from 100E to 1000E (E is Young's Modulus of element), to guarantee the displacement of the restricted node is 10^{-4}~10^{-3} times of the total displacement. If k is large enough, the computation result will be independent of the choice of k.

Denote (u_i, v_i) as the displacement of the constraint point, then the deformation of constraint spring is

$$d = \delta - (l_x u_i + l_y v_i) = \delta - \mathbf{n}^{\mathrm{T}} \mathbf{d}_i$$

The constraint spring force is

$$f = -kd = -k(\delta - \mathbf{n}^{\mathrm{T}} \mathbf{d}_i)) \tag{3.68}$$

The potential energy of this spring is

$$\begin{aligned} \Pi_c &= \frac{k}{2} d^2 = \frac{k}{2} (\delta - \mathbf{n}^{\mathrm{T}} \mathbf{d}_i)^2 \\ &= \frac{k}{2} \mathbf{d}_i^{\mathrm{T}} \mathbf{n} \mathbf{n}^{\mathrm{T}} \mathbf{d}_i - k\delta \mathbf{n}^{\mathrm{T}} \mathbf{d}_i + \frac{k}{2} \delta^2 \end{aligned} \tag{3.69}$$

Taking the derivatives of the potential energy of the constraint spring, we have

$$\mathbf{k}_c = \frac{\partial^2 \Pi_c}{\partial \mathbf{d}_i \partial \mathbf{d}_i} = k \mathbf{n} \mathbf{n}^{\mathrm{T}} \tag{3.70}$$

where $\mathbf{k}_c$ is a 2×2 submatrix which is added to the intersection of *i-th* row and *i-th* column in global stiffness matrix.

By minimizing the potential energy Π_c and taking the derivatives at $\mathbf{d}_i = 0$, we have

$$\mathbf{f}_c = -\left.\frac{\partial \Pi_c}{\partial \mathbf{d}_i}\right|_0 = \delta k \mathbf{n} \tag{3.71}$$

which is a 2-dimensional vector which is added to the *i-th* row of **F** in Eq. (3.16).

For the case where there is no movement along the constraint direction **n**, $\delta = 0$ is set in Eq. (3.71) and only the submatrix of Eq. (3.70) needs to be computed and added to global stiffness matrix.

For rolling support at *x*-direction, we have α = 90°, and the normal vector now becomes

$$\mathbf{n} = \begin{Bmatrix} -1 \\ 0 \end{Bmatrix}$$

and the constraint stiffness matrix becomes

$$\mathbf{k}_c = \begin{bmatrix} 1 & 0 \\ 0 & 0 \end{bmatrix} \tag{3.72}$$

For rolling support at *y*-direction, we have α = 0°, and the normal vector now becomes

$$\mathbf{n} = \begin{Bmatrix} 0 \\ 1 \end{Bmatrix}$$

and the constraint stiffness matrix becomes

$$\mathbf{k}_c = \begin{bmatrix} 0 & 0 \\ 0 & 1 \end{bmatrix} \tag{3.73}$$

For a fixed point, which can be considered as superimposition of two rolling supports of both x-direction and y-direction, the constraint stiffness submatrix becomes

$$\mathbf{k}_c = \begin{bmatrix} 1 & 0 \\ 0 & 1 \end{bmatrix} \tag{3.74}$$

which is the superimposition of Eq.(3.72) and Eq.(3.73).

3.10 Contact Submatrices

In two dimensional problems, basic contact model is vertex to edge. The formulas for the vertex-edge contact model are derived in this section. In N-DDA, only boundary nodes will take part in the contact process, as shown in Figure 3.7.

The coordinates of *vertex* i are (x_i, y_i) and the coordinates of its target contact edge $\overline{jm}$ ends are (x_j, y_j) and (x_m, y_m), respectively. Two contact springs are added along normal and tangent directions of edge $\overline{jm}$ (see Figure 3.8).

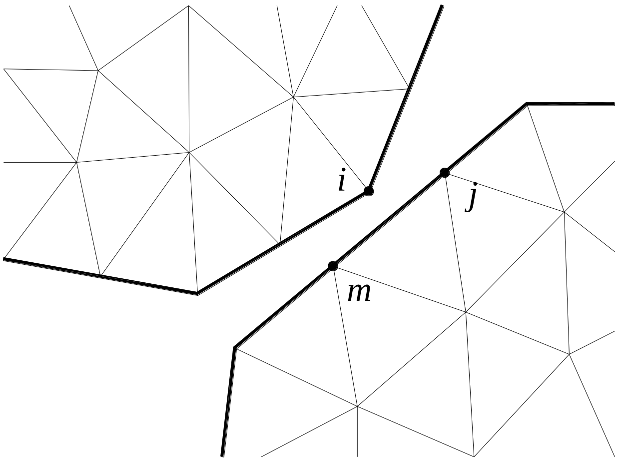

Figure 3.7 vertex-edge contact model

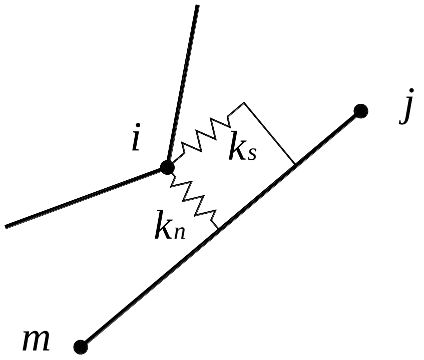

Figure 3.8 schematic illustration of normal and shear contact spring

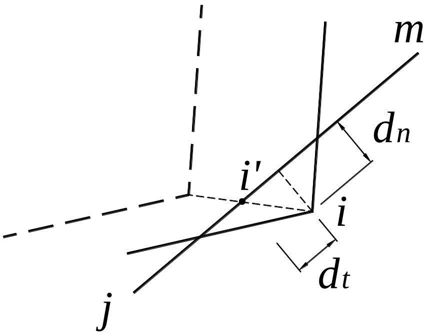

Figure 3.9 normal and shear contact displacements

The corresponding contact point of *node i* on edge $\overline{jm}$ is denoted by *i'*. (see Figure 3.9) The normal and shear displacements at contact point are denoted by d_n and d_t, respectively. The displacements of *node i, j, m* are

$$\begin{aligned} \mathbf{d}_i &= \{u_i \quad v_i\}^{\mathrm{T}} \\ \mathbf{d}_j &= \{u_j \quad v_j\}^{\mathrm{T}} \\ \mathbf{d}_m &= \{u_m \quad v_m\}^{\mathrm{T}} \end{aligned} \tag{3.75}$$

3.10.1 Normal contact spring submatrix

The normal spring displacement at the end of current time step is

$$d_n = \frac{\Delta}{l} = \frac{1}{l}\begin{vmatrix} 1 & x_i + u_i & y_i + v_i \\ 1 & x_j + u_j & y_j + v_j \\ 1 & x_m + u_m & y_m + v_m \end{vmatrix} \tag{3.76}$$

where Δ is the area of $\triangle ijm$ at the end of current time step and l is the length of edge $\overline{jm}$

$$\begin{aligned} l &= \sqrt{(x_j + u_j - x_m - u_m)^2 + (y_j + v_j - y_m - v_m)^2} \\ &\approx \sqrt{(x_j - x_m)^2 + (y_j - y_m)^2} \end{aligned} \tag{3.77}$$

$$\begin{aligned} \Delta &= \begin{vmatrix} 1 & x_i + u_i & y_i + v_i \\ 1 & x_j + u_j & y_j + v_j \\ 1 & x_m + u_m & y_m + v_m \end{vmatrix} \\ &= \begin{vmatrix} 1 & x_i & y_i \\ 1 & x_j & y_j \\ 1 & x_m & y_m \end{vmatrix} + \begin{vmatrix} 1 & u_i & y_i \\ 1 & u_j & y_j \\ 1 & u_m & y_m \end{vmatrix} + \begin{vmatrix} 1 & x_i & v_i \\ 1 & x_j & v_j \\ 1 & x_m & v_m \end{vmatrix} + \begin{vmatrix} 1 & u_i & v_i \\ 1 & u_j & v_j \\ 1 & u_m & v_m \end{vmatrix} \end{aligned} \tag{3.78}$$

The last term in the above equation is a second order infinitesimal which can be neglected. Denote A_0 as the area of $\triangle ijm$ at the beginning of current time step.

$$A_0 = \begin{vmatrix} 1 & x_i & y_i \\ 1 & x_j & y_j \\ 1 & x_m & y_m \end{vmatrix} \tag{3.79}$$

Then

$$\Delta \approx A_0 + \begin{vmatrix} 1 & u_i & y_i \\ 1 & u_j & y_j \\ 1 & u_m & y_m \end{vmatrix} + \begin{vmatrix} 1 & x_i & v_i \\ 1 & x_j & v_j \\ 1 & x_m & v_m \end{vmatrix} \tag{3.80}$$

$$\begin{aligned} \Delta \approx A_0 &+ u_i(y_j - y_m) + v_i(x_m - x_j) \\ &+ u_j(y_m - y_i) + v_j(x_i - x_m) \\ &+ u_m(y_i - y_j) + v_m(x_j - x_i) \end{aligned} \tag{3.81}$$

$$\begin{aligned}\Delta \approx A_0 &+ \left\{ y_j - y_m \quad x_m - x_j \right\} \begin{Bmatrix} u_i \\ v_i \end{Bmatrix} \\ &+ \left\{ y_m - y_i \quad x_i - x_m \right\} \begin{Bmatrix} u_j \\ v_j \end{Bmatrix} \\ &+ \left\{ y_i - y_j \quad x_j - x_i \right\} \begin{Bmatrix} u_m \\ v_m \end{Bmatrix}\end{aligned} \tag{3.82}$$

denote

$$\mathbf{n} = \begin{Bmatrix} \mathbf{n}_i \\ \mathbf{n}_j \\ \mathbf{n}_m \end{Bmatrix} = \begin{Bmatrix} y_j - y_m \\ x_m - x_j \\ y_m - y_i \\ x_i - x_m \\ y_i - y_j \\ x_j - x_i \end{Bmatrix} \tag{3.83}$$

$$\mathbf{d} = \begin{Bmatrix} \mathbf{d}_i \\ \mathbf{d}_j \\ \mathbf{d}_m \end{Bmatrix} = \begin{Bmatrix} u_i \\ v_i \\ u_j \\ v_j \\ u_m \\ v_m \end{Bmatrix} \tag{3.84}$$

then

$$\Delta \approx A_0 + \mathbf{n}^{\mathrm{T}}\mathbf{d} \tag{3.85}$$

$$d_n = \frac{\Delta}{l} \approx \frac{1}{l}\left(A_0 + \mathbf{n}^{\mathrm{T}}\mathbf{d}\right) \tag{3.86}$$

Denote the stiffness of the normal contact spring as k_n, then the potential energy of the contact spring is

$$\Pi_{kn} = \frac{k_n}{2} d_n^2 \tag{3.87}$$

substituting Eq. (3.86), we have

$$\begin{aligned}\Pi_{kn} &= \frac{k_n}{2l^2}\left(A_0+\mathbf{n}^{\mathrm{T}}\mathbf{d}\right)^2 \\ &= \frac{k_n}{2l^2}\left(\mathbf{d}^{\mathrm{T}}\mathbf{n}\mathbf{n}^{\mathrm{T}}\mathbf{d}+2A_0\mathbf{n}^{\mathrm{T}}\mathbf{d}+A_0^2\right)\end{aligned} \tag{3.88}$$

To minimize the strain energy Π_f the derivatives are computed. The derivatives of Π_f

$$\mathbf{k}_{kn} = \begin{bmatrix} \mathbf{k}_{ii} & \mathbf{k}_{ij} & \mathbf{k}_{im} \\ \mathbf{k}_{ji} & \mathbf{k}_{jj} & \mathbf{k}_{jm} \\ \mathbf{k}_{mi} & \mathbf{k}_{mj} & \mathbf{k}_{mm} \end{bmatrix} = \frac{\partial^2\Pi_{kn}}{\partial\mathbf{d}\partial\mathbf{d}} = \frac{k_n}{l^2}\mathbf{n}\mathbf{n}^{\mathrm{T}} \tag{3.89}$$

forms a 6×6 matrix, where each component is a 2×2 submatrix. The components are added to the global stiffness matrix according to the index of *node i*, *j* and *m*.

In order to compute the submatrices on the right side of global equations, we minimize Π_k by taking the derivatives at $\mathbf{d}=\mathbf{0}$.

$$\mathbf{f}_{kn} = \begin{Bmatrix} \mathbf{f}_i \\ \mathbf{f}_j \\ \mathbf{f}_m \end{Bmatrix} = -\frac{\partial\Pi_{kn}(0)}{\partial\mathbf{d}} = -\frac{k_n A_0}{l^2}\mathbf{n} \tag{3.90}$$

forms a 6×1 matrix and $\mathbf{f}_i$, $\mathbf{f}_j$, and $\mathbf{f}_m$ are 2×1 submatrix.

3.10.2 Shear contact spring submatrix

Assume the positive direction along edge $\overline{jm}$ is from *j* to *m*, i.e. the direction of $\overrightarrow{jm}$. The shear spring deformation, at the end of current time step, is

$$\begin{aligned} d_t &= \frac{\overrightarrow{i'i}\bullet\overrightarrow{jm}}{l} \\ &= \frac{1}{l}\left\{x_i+u_i-x_{i'}-u_{i'} \quad y_i+v_i-y_{i'}-v_{i'}\right\}\begin{Bmatrix} x_m+u_m-x_j-u_j \\ y_m+v_m-y_j-v_j \end{Bmatrix} \\ &= \frac{1}{l}\left\{x_i-x_{i'}+u_i-u_{i'} \quad y_i-y_{i'}+v_i-v_{i'}\right\}\begin{Bmatrix} x_m-x_j \\ y_m-y_j \end{Bmatrix}\end{aligned}$$

$$+\frac{1}{l}\{x_i - x_{i'} + u_i - u_{i'} \quad y_i - y_{i'} + v_i - v_{i'}\}\begin{Bmatrix} u_m - u_j \\ v_m - v_j \end{Bmatrix} \tag{3.91}$$

Assume time step is small enough that the displacements of *node* i, *j*, and *m* are tiny. Then

$$\{u_i - u_{i'} \quad v_i - v_{i'}\}\begin{Bmatrix} u_m - u_j \\ v_m - v_j \end{Bmatrix}$$

and

$$\{x_i - x_{i'} \quad y_i - y_{i'}\}\begin{Bmatrix} u_m - u_j \\ v_m - v_j \end{Bmatrix}$$

are infinitesimal and neglectable. Taking this into consideration, Eq. (3.91) can be rewritten as

$$d_t \approx \frac{1}{l}\{x_i - x_{i'} + u_i - u_{i'} \quad y_i - y_{i'} + v_i - v_{i'}\}\begin{Bmatrix} x_m - x_j \\ y_m - y_j \end{Bmatrix} \tag{3.92}$$

Denote

$$S_0 = \{x_i - x_{i'} \quad y_i - y_{i'}\}\begin{Bmatrix} x_m - x_j \\ y_m - y_j \end{Bmatrix}$$

and note that

$$x_{i'} = (1-t)x_j + tx_m$$

$$y_{i'} = (1-t)y_j + ty_m$$

$$u_{i'} = (1-t)u_j + tu_m$$

$$v_{i'} = (1-t)v_j + tv_m$$

where 0≤t≤1, and

$$t = \frac{\overrightarrow{ji'} \bullet \overrightarrow{jm}}{l^2} = \frac{1}{l^2}\{x_{i'} - x_j \quad y_{i'} - y_j\}\begin{Bmatrix} x_m - x_j \\ y_m - y_j \end{Bmatrix} \tag{3.93}$$

Hence

$$\begin{aligned} d_t &\approx \frac{S_0}{l} + \frac{1}{l}\begin{Bmatrix} x_m - x_j & y_m - y_j \end{Bmatrix}\begin{Bmatrix} u_i - u_{i'} \\ v_i - v_{i'} \end{Bmatrix} \\ &= \frac{S_0}{l} + \frac{1}{l}\begin{Bmatrix} x_m - x_j & y_m - y_j \end{Bmatrix}\left(\begin{Bmatrix} u_i \\ v_i \end{Bmatrix} - (1-t)\begin{Bmatrix} u_j \\ v_j \end{Bmatrix} - t\begin{Bmatrix} u_m \\ v_m \end{Bmatrix}\right) \end{aligned} \tag{3.94}$$

Denote

$$\mathbf{t} = \begin{Bmatrix} x_m - x_j \\ y_m - y_j \\ (t-1)(x_m - x_j) \\ (t-1)(y_m - y_j) \\ -t(x_m - x_j) \\ -t(y_m - y_j) \end{Bmatrix}$$

$$\mathbf{d}\begin{Bmatrix} \mathbf{d}_i \\ \mathbf{d}_j \\ \mathbf{d}_m \end{Bmatrix} = \begin{Bmatrix} u_i \\ v_i \\ u_j \\ v_j \\ u_m \\ v_m \end{Bmatrix}$$

And Eq. (3.94) can be rewrite in a more concise form as

$$d_t \approx \frac{1}{l}\left(S_0 + \mathbf{t}^{\mathrm{T}}\mathbf{d}\right) \tag{3.95}$$

The potential energy of shear contact spring is

$$\Pi_{kt} = \frac{k_t}{2} d_t^2 \tag{3.96}$$

Substituting Eq. (3.95),

$$\Pi_{kt} = \frac{k_t}{2l^2}\left(S_0 + \mathbf{t}^{\mathrm{T}}\mathbf{d}\right)^2 = \frac{k_t}{2}\left(\mathbf{d}^{\mathrm{T}}\mathbf{t}\mathbf{t}^{\mathrm{T}}\mathbf{d} + 2S_0\mathbf{t}^{\mathrm{T}}\mathbf{d} + S_0^2\right) \tag{3.97}$$

Derivatives of Π_{kt},

$$\mathbf{k}_{kt} = \begin{bmatrix} \mathbf{k}_{ii} & \mathbf{k}_{ij} & \mathbf{k}_{im} \\ \mathbf{k}_{ji} & \mathbf{k}_{jj} & \mathbf{k}_{jm} \\ \mathbf{k}_{mi} & \mathbf{k}_{mj} & \mathbf{k}_{mm} \end{bmatrix} = \frac{\partial^2 \Pi_{kt}}{\partial \mathbf{d} \partial \mathbf{d}} = \frac{k_t}{l^2}\mathbf{t}\mathbf{t}^{\mathrm{T}} \tag{3.98}$$

$$\mathbf{f}_{kt} = \begin{Bmatrix} \mathbf{f}_i \\ \mathbf{f}_j \\ \mathbf{f}_m \end{Bmatrix} = -\frac{\partial \Pi_{kt}(0)}{\partial \mathbf{d}} = -\frac{k_t S_0}{l^2}\mathbf{t} \tag{3.99}$$

forms a 6×6 matrix and a 6-dimensional vector, resemble normal contact spring submatrix which are added to the coefficient matrix and free term in Eq. (3.16), respectively, according to the node index i, j, and m.

3.10.3 Friction submatrix

When contacting surfaces moves relative to each other, the friction between the two surfaces convert kinetic energy into thermal energy, or heat. Hence, it is necessary to consider the energy consumed by friction when calculate the total potential energy of a discontinuous system with friction contact. Here, we will only investigate the dry friction or Coulomb friction between two solid bodies. According to the Coulomb/Amonton friction law, the friction force is proportional to the normal force and independent from the speed. This first order approximation is sufficient for many engineering applications. The important property of dry friction lies in the fact that in a first order approximation, it is dependent neither on contact area nor on roughness.

In the case of sliding, the shear contact spring disappears from the contact point and the sliding displacement along the contact edge $\overline{jm}$ is denoted by d_t (see Figure 3.8). Denote φ as the friction angle of the contact interface, then the coefficient of friction is $\tan\varphi$. If two contact interfaces have different friction angles, the smaller one will be chosen. According to Coulomb friction law, the kinetic friction at this contact point is

$$F = -k_n d_n \tan\varphi \tag{3.100}$$

and the work done by friction force is

$$\Pi_f = -Fd_t = k_n d_n d_t \tan\varphi \tag{3.101}$$

substituting Eq. (3.86)(3.94), we have

$$\begin{aligned}\Pi_f &= \frac{k_n}{l^2}\tan\varphi\left(A_0 + \mathbf{n}^{\mathrm{T}}\mathbf{d}\right)\left(S_0 + \mathbf{t}^{\mathrm{T}}\mathbf{d}\right)\\ &= \frac{k_n}{l^2}\tan\varphi\left(\mathbf{d}^{\mathrm{T}}\mathbf{t}\mathbf{n}^{\mathrm{T}}\mathbf{d} + A_0\mathbf{t}^{\mathrm{T}}\mathbf{d} + S_0\mathbf{n}^{\mathrm{T}}\mathbf{d} + A_0 S_0\right)\end{aligned} \tag{3.102}$$

Assuming constant friction angle during sliding, then derivatives of Π_f can be obtained by

$$\mathbf{k}_f = \begin{bmatrix}\mathbf{k}_{ii} & \mathbf{k}_{ij} & \mathbf{k}_{im}\\ \mathbf{k}_{ji} & \mathbf{k}_{jj} & \mathbf{k}_{jm}\\ \mathbf{k}_{mi} & \mathbf{k}_{mj} & \mathbf{k}_{mm}\end{bmatrix} = \frac{\partial^2\Pi_f}{\partial\mathbf{d}\partial\mathbf{d}} = \frac{k_n\tan\varphi}{l^2}\mathbf{t}\mathbf{n}^{\mathrm{T}} \tag{3.103}$$

$$\mathbf{f}_f = \begin{Bmatrix}\mathbf{f}_i\\ \mathbf{f}_j\\ \mathbf{f}_m\end{Bmatrix} = -\frac{\partial\Pi_f(0)}{\partial\mathbf{d}} = -\frac{k_n\tan\varphi}{l^2}\left(S_0\mathbf{n} + A_0\mathbf{t}\right) \tag{3.104}$$

forms a 6×6 matrix and a 6-dimensional vector, which are added to the coefficient matrix and free term in Eq. (3.16), respectively, according to the node index *i*, *j*, and *m*.

If a pair of contact face has two contact points rather than one, since the friction force is related to the normal contact force and the contact force now is only half of the case of one contact point, the value of friction force at each contact point is reduced by half and the total potential energy contributed by two contact points is still equal to the energy of one contact point. Therefore, the consideration of friction potential energy is based on the contact point.

3.11 Procedure Framework of the 2D-NDDA

The 2D-NDDA program includes two parts: MESH and ANALYSIS. The MESH code is the preprocessor which generates the block system and triangulates in each block. The ANALYSIS code performs the forward analysis. The flowcharts for the two codes are shown in Figure 3.10 and Figure 3.11, respectively.

The Delaunay triangulation and refinement algorithm employed in the MESH program are discussed in Chapter 4. The submatrices system of the ANALYSIS program is provided and discussed in the previous sections of this chapter. The crack initiation and propagation algorithm employed in the ANALYSIS program are discussed in the Chapter 5.

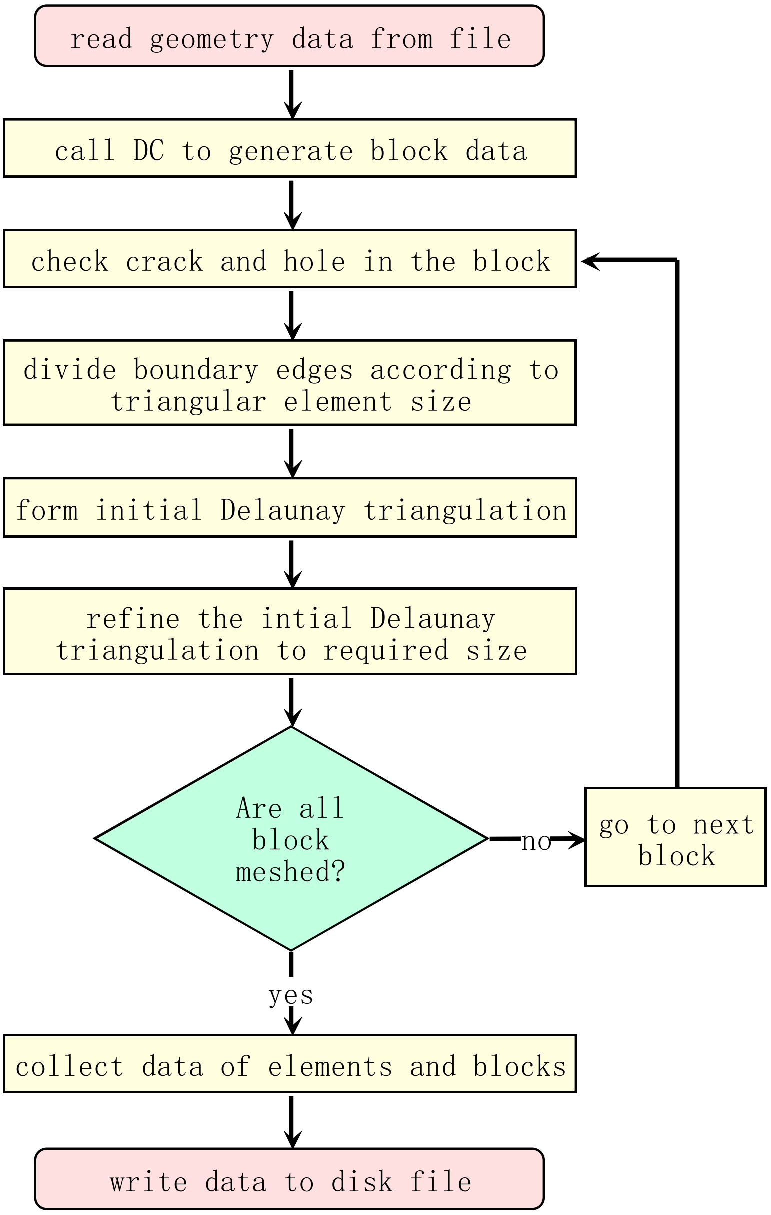

Figure 3.10 flowchart of MESH program for NDDA

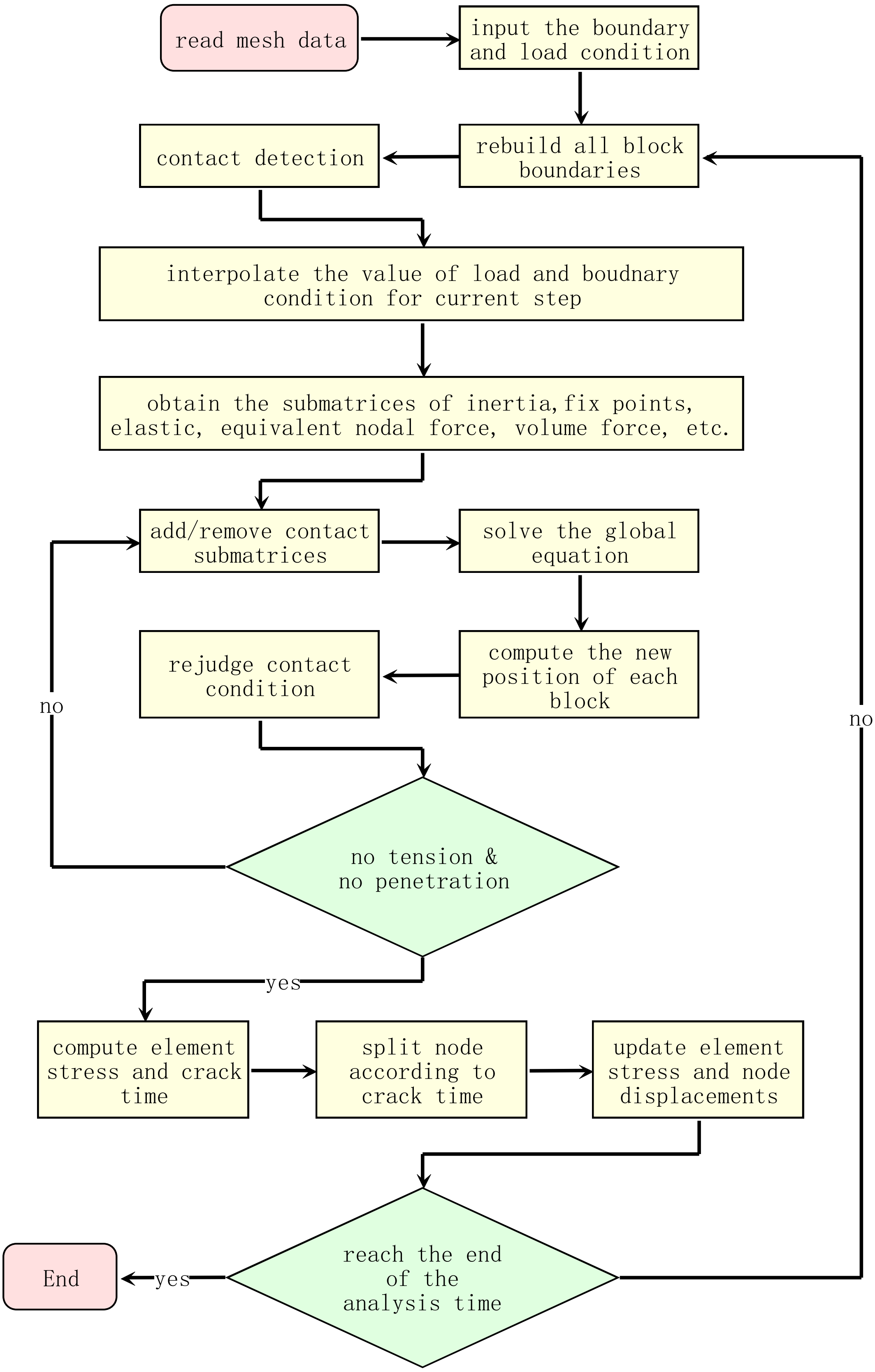

Figure 3.11 flowchart of ANALYSIS program for NDDA

3.12 Summary

This chapter derives the formulae for the NDDA from the standard DDA and the work done by other researchers in this field. Most of the formulae have corresponding part in the FEM, which makes the application of existing FEM algorithms into the NDDA much easier. The part of contact matrices is the most important part which distinguishes the NDDA from the FEM. All the formulae are implemented into the newly developed 2D-NDDA program with validation examples in the Chapter 7.

CHAPTER 4 TRIANGULATION IN THE BLOCK

4.1 Introduction

Consider the problem: how to divide a polygonal region (a block) in the plane into triangles in such a way that these triangles are as close as possible to equilateral triangles? The process of dividing a region into triangles is referred to as triangulation and the resulting set of triangles is called a triangular mesh for the region. Triangular elements are preferred here because they can be easily made to fit complex boundaries and crack propagating path. If the triangles are as close as possible to equilateral triangle, error bounds are best and good fracture path is provided.

In this chapter, a Delaunay refinement algorithm is presented based on the method introduced by Chew (1989). And it is employed in the NDDA program for triangulating planar regions. This algorithm comes with a guarantee: for a triangulation produced by the algorithm, all angles are between 30 °and 120 °and all edge lengths are between h and $2h$ where h is a parameter chosen by the user to control the grid density.

The guarantee associated with this algorithm is particularly important. With such a guarantee, the triangular mesh can provide a good and proper path for the crack propagation. In the NDDA, the original mesh grid is used for the crack propagating path, which needs this guarantee to provide a better result.

4.2 Background – Delaunay Triangulation

The guaranteed-quality triangulation technique is based on the properties of Delaunay triangulations. This section presents some of the properties of the Delaunay triangulations and explains a special type of Delaunay triangulation, called a constrained Delaunay triangulation (CDT), which has characteristics particularly useful for mesh generators.

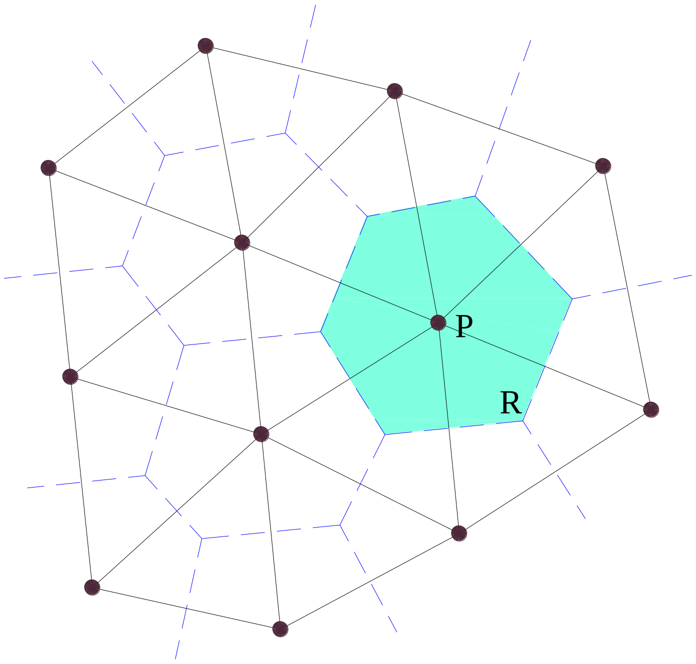

Figure 4.1 a Voronoi diagram and the corresponding Delaunay triangulation (the Voronoi diagram -- dashed lines; the Delaunay triangulation – solid lines)

The Delaunay triangulation of a set **S** of points in the plane is most easily introduced by reference to the Voronoi diagram of **S** (see Figure 4.1). The Voronoi diagram of **S** divides the plane into regions, one region for each point in **S**, such that for each region **R** and corresponding point **P**, every point within **R** is closer to **P** than to any other point of **S**. The boundaries of these regions form a planar graph. The Delaunay triangulation of **S** is the straight-line dual of the Voronoi diagram of **S**; that is, we connect a pair of points in **S** if they share a Voronoi boundary. The

Voronoi diagram and its dual, the Delaunay triangulation, have been found to be among the most useful data structures in computational geometry.

Each triangle of the Delaunay triangulation of **S** has the empty circle property: a circle circumscribed about a Delaunay triangle contains no points of **S** in its interior. Indeed, this property can be used as the definition of Delaunay triangulation.

Definition: Let **S** be a set of points in the plane. A triangulation **T** is a Delaunay triangulation of **S** if for each triangular face Δ of **T** there exists a circle **C** circumscribes Δ with no vertex of **S** is in the interior of **C**. (Chew 1989)

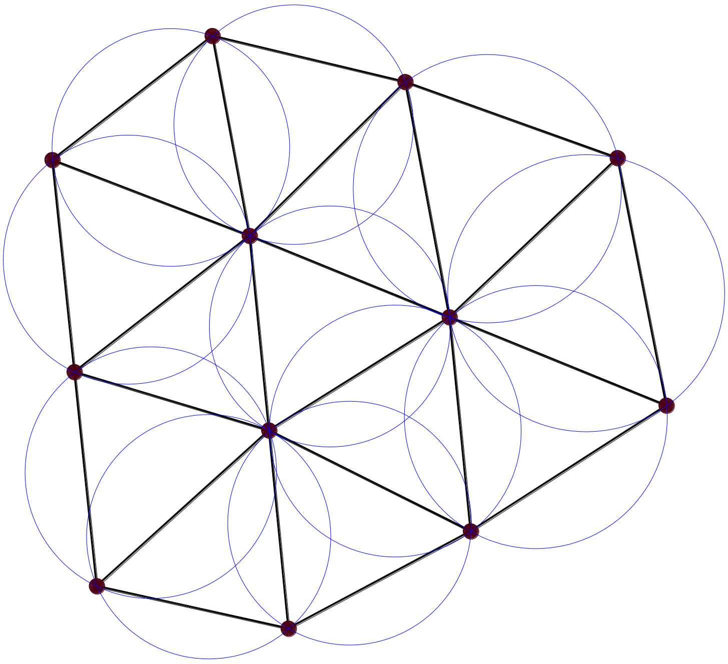

Figure 4.2 a Delaunay triangulation and the corresponding circumcircles

A circle circumscribed about a Delaunay triangle is called a Delaunay circle (see Figure 4.2). If **S** contains four points that are co-circular then the Delaunay triangulation is not necessarily unique. For the NDDA program, if there is not a unique Delaunay triangulation, any of them will do.

The Delaunay triangulation has some properties indicating that it might lead to good finite element meshes. In particular, the Delaunay triangulation maximizes the minimum angle for a set of points. In other words, among all triangulations of a given set of points, the Delaunay triangulation has the largest minimum angle (Edelsbrunner 1987).

Unfortunately, the Delaunay triangulation cannot fully meet the requirement of the NDDA. The problem is, sometimes, certain edges must be used as part of the final triangulation (e.g., those that describe the boundaries or, perhaps, those that describe a crack in the block to be analyzed). Such edges do not always correspond to legal Delaunay edges. Schroeder and Shephard (1988) discussed some of the difficulties of using a Delaunay triangulation to create a mesh for an object.

Many of these difficulties can be resolved by using a constrained Delaunay triangulation (CDT). Intuitively, a CDT is as close as possible to a Delaunay triangulation given that certain prespecified edges must be included in the triangulation (see Figure 4.3). The same term, Delaunay circle, is used for a circle circumscribed about either a standard Delaunay triangle or a CDT triangle. The CDT, also called a generalized Delaunay triangulation (Lee 1978; Lee and Lin 1986), was first introduced by Lee.

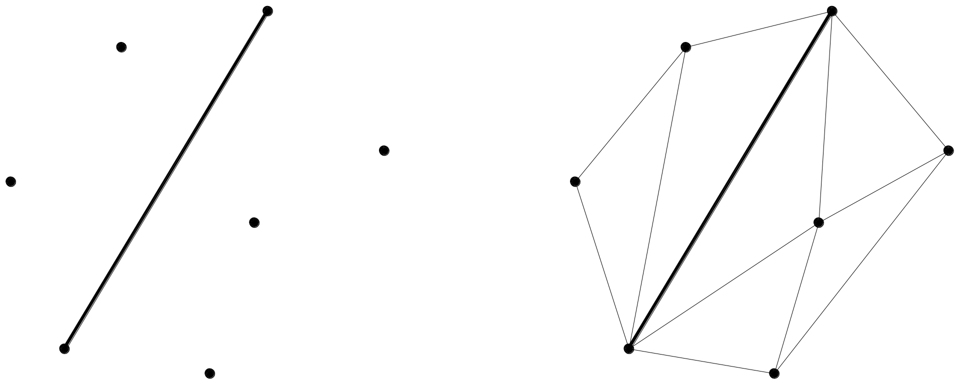

Figure 4.3 a graph G and the corresponding constrained Delaunay triangulation

4.3 Constrained Delaunay Algorithm

This section briefly introduces the constrained Delaunay triangulation algorithm provided by Lee and Lin (1986). For more details about this algorithm, please check the original work of Lee and Lin (1986). It is the foundation of the Delaunay refinement algorithm used in the NDDA mesh program.

Definition 1. For any planar straight-line graph (PSLG) *G*=(*V*, *E*), a triangulation T(*G*) of *G* is a PSLG *G'*=(*V*, *E'*), where $E' \subseteq E$, such that no edges can be added without intersecting an existing edge.

Definition 2. For any PSLG *G*=(*V*, *E*) the constrained Delaunay triangulation (CDT) of *G*, denoted by CDT(*G*) is a triangulation T(*G*)=(*V*, *E'*) in which the circumcircle of each face or triangle $\triangle v_i v_j v_k$, denoted by $\bigcirc(v_i, v_j, v_k)$ does not contain in its interior any other vertex which is visible from the vertices v_i, v_j, and v_k of the triangle. The edges of the set $E' - E$ are called Delaunay edges, and the edges of *E* are called sides. The vertices *u* and *v*, $u, v \in V$, are visible from each other if the line segment *u*, *v* does not intersect an edge of *E* at an interior point.

Note that for graphs $G = (V, \phi)$, the CDT(*G*) becomes the conventional Delaunay triangulation of a set *V* of points. The following lemma, which relates the numbers of triangles and edges to the number of vertices in *V*, can be established fairly easily. They are the basement of the constrained Delaunay algorithm. The proof of them can be found in Lee and Lin (1986).

Lemma 1. Given any PSLG *G=(V, E),* any triangulation T(G) has $2(|V|-1)-B$ triangles, and $3(|V|-1)-B$ edges, where *B* is the number of vertices that are on the convex hull of the set *V* of points and |*V*| denotes the cardinality of *V*.

Lemma 2. Let *abcd* be a convex quadrilateral such that vertex *c* is outside the circle $O(a,b,d)$. The minimum angle of the triangulation obtained by adding diagonal $\overline{b,d}$ is strictly larger than the minimum angle obtained by adding diagonal $\overline{a,c}$.

Lemma 3. The edges of a triangulation T(*G*) of a PSLG *G*=(*V*, *E*) are locally optimal if and only if each triangle of T(*G*) satisfies the circle property, i.e., circumcircle of any triangle Δabc of T(*G*) does not contain in its interior any vertex of *V* visible from all three vertices *a*, *b*, and *c*.

Lemma 4. For any PSLG *G*=(*V*, *E*), an edge $\overline{v,t}$ is a Delaunay edge in CDT(*G*) if and only if *v* and *t* are visible from each other and there exists a circle passing through *v* and *t* that does not contain any vertex visible from both *v* and *t*.

Given a problem of constructing the CDT of *G* of a given PSLG *G*=(*V*, *E*). An $O(|V|^2)$ algorithm for computing the CDT(*G*) of a given PSLG *G*=(*V*, *E*) is presented below. The main idea is to compute for each vertex $v \in V$, the Delaunay edges incident with it.

Now proceed to find for each vertex $v \in V$ the set S_v of vertices visible from *v*, i.e., $S_v = \{u \mid u \text{ is visible from } v\}$. The graph obtained by connecting *v* to all $u \in S_v$ for each $u \in V$ is called the visibility graph and it has been shown that the visibility graph can be computed in $O(|V|^2)$ time (Asano, Guibas et al. 1986). Once the visibility graph is obtained, those edges that are not Delaunay edges are eliminated based on the above lemma.

Note that the vertices in S_v for *v* are ordered by angles around *v* when they are computed. First, find $u \in S_v$ such that the edge $\overline{u,v}$ is the shortest. Since the circle ***K*** with $\overline{u,v}$ as the diameter is totally contained in the circle of radius

$d(u,v)$ and centered at *v*, no vertex in S_v is interior to ***K.*** (see Figure 4.4a). It follows from Lemma 1 that $\overline{u,v}$ must be a Delaunay edge. Then scan the vertices in S_v around vertex *v* in counterclockwise order starting with the vertex after *u*. Take three consecutive vertices *x, y, z* at a time, and these three vertices along with vertex *v* form a quadrilateral *vxyz*. At each step, the local optimization procedure is applied to the edge $\overline{v,y}$ of the quadrilateral, if $\overline{v,y} \notin E$. If $z \in O(v,x,y)$, the vertex *y* is deleted from S_v since edge is not a Delaunay edge (see Figure 4.4b). Once vertex *y* is deleted from S_v, backtrack to consider vertices *w*, *x* and *z*, since deletion of *y* may make edge $\overline{v,x}$ non-Delaunay.

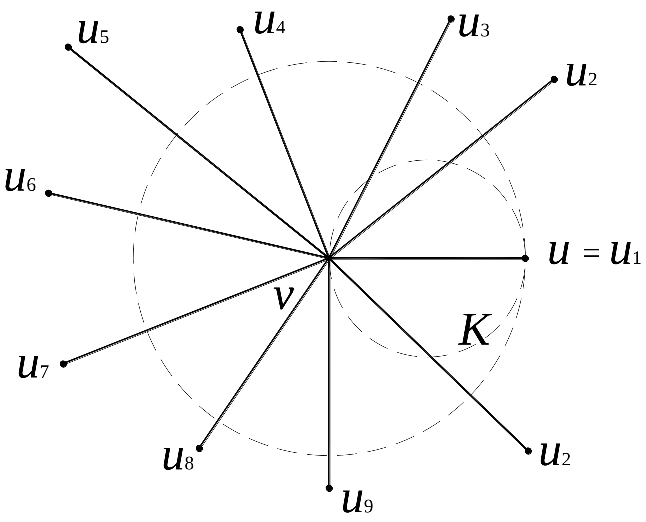

(a) select the shortest edge as the start edge

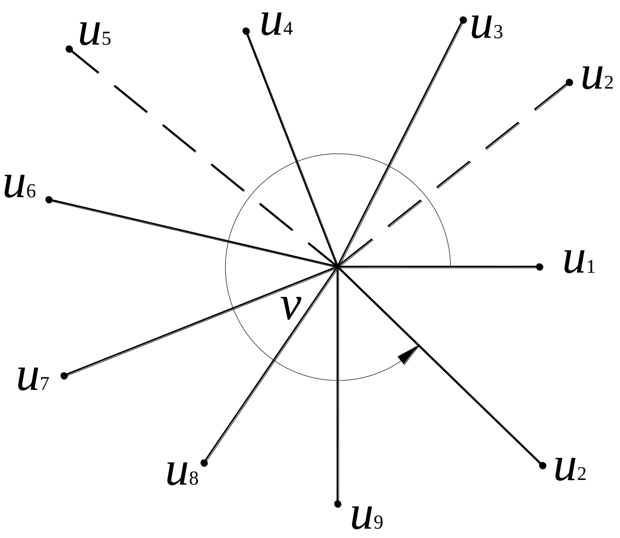

(b) delete unsatisfied edges shown by dash lines

Figure 4.4 computing Delaunay edges incident with vertex *v*

4.4 Delaunay Refinement Algorithm

In the Delaunay refinement algorithm, there are two kinds of vertices: (1) *required vertices*: those that are part of the boundary or those that are specifically chosen by the user; (2) *circumcenter vertices*: additional vertices that are introduced during the meshing algorithm. During the meshing process it is sometimes necessary to eliminate vertices. Note that only circumcenter vertices can be eliminated; the other vertices must be retained.

There are some undemanding preconditions that the initial problem must satisfy. The input to the algorithm is a set of data points and data edges which must satisfy the following two conditions (recall that *h* is a parameter chosen by the user; intuitively, it represents the desired side-length of triangles in the triangulation):

1. No two data points are closer than *h*.

2. All data edges have lengths between *h* and $\sqrt{3}h$.

In practice, it is trivial to subdivide long edges to comply with condition two, except for edges with lengths between $\sqrt{3}h$ and $2h$. Later in this section, it will be shown how these edges can, in effect, be hidden, although when this is done, care must be taken to ensure that condition 1 is not compromised. The following Delaunay refinement algorithm is introduced by Chew (1989).

Algorithm:

```
begin
    Compute the CDT of the data points and data edges;
    Let T be the portion of the CDT that is within the region to be triangulated;
while there is a Delaunay circle within T that has radius >$h$ do
    Add the center of the Delaunay circle as a new data point (see Figure 4.5);
    Computing Delaunay edges incident with the new data point;
end while
    Report T as the desired triangulation;
end
```

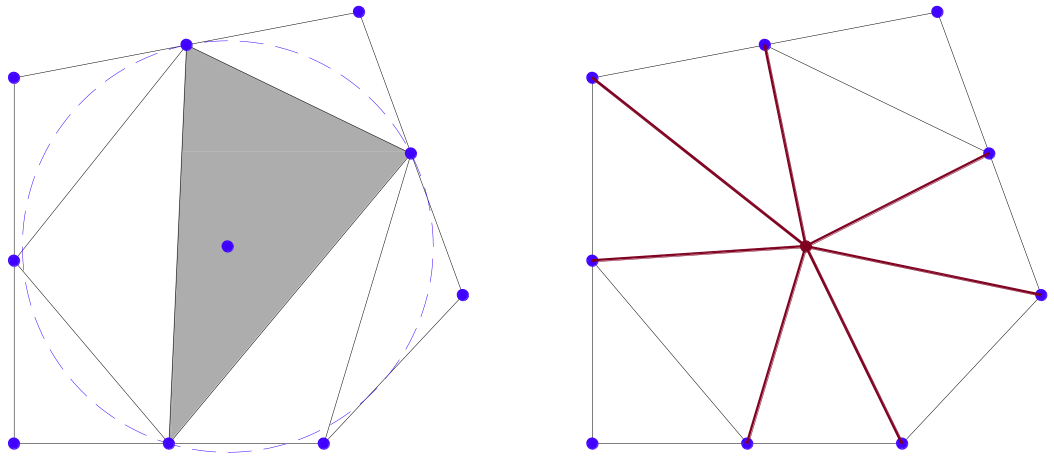

Figure 4.5 add the center point of a large-radius Delaunay circle and recomputed the CDT

Indeed, the second precondition (all data edges have length between h and $\sqrt{3}h$) can be relaxed. For an edge longer than 2*h*, new data points can be introduced to divide the edge into pieces with lengths in the required range. However, if an edge has length between $\sqrt{3}h$ and 2*h*, a problem occurs: such an edge cannot be divided into appropriately sized pieces. This difficulty can be avoided by, in effect, hiding such edges. To do this, place a new data point in the interior of the region to make a 45 ° isosceles triangle (with the problem edge as its hypotenuse); connect the endpoints of the problem edge to this new data point. These new edges have lengths in the required range. Now, when the algorithm is executed, no points can be placed within the triangle (such a new point would be too close to one of the vertices of the triangle) and the triangle itself satisfies the properties of the theorem (it fits within a circle of radius *h* and no two of its points are closer than *h*). Of course, care must be taken to ensure that any new data point introduced to hide an edge is no closer than *h* to any other data point.

The algorithm as outlined in this section can be implemented to run in worst-case time $O(n^2)$, where *n* is the number of triangles in the final triangulation. The efficiency of the above algorithm is very low when the number of elements is large. For a Pentium IV 3.0GHz computer, the triangulation time of one thousand elements can be up to 5 minutes. An important phenomenon is found that the insertion of a new data point only changes the mesh locally. The affected field is limited to the points which are connected to the vertexes of the current triangle. This fact can be used to improve the efficiency of refinement of the mesh. Since the number of points connected to the current triangle is very small and can be bounded by a small constant. In other words, it takes just constant time to update T for each new data point; thus, the total time is $O(n)$ where n is the number of data points. With this enhanced refinement algorithm, the triangulation time of one thousand elements is reduced to around 20 seconds.

4.5 Applications

The MESH code includes two main parts: (1) a modified DC code which forms block boundaries include holes and cracks according to input lines; (2) a refined Delaunay triangulation code which builds the required triangulation mesh inside each block. In the original DC code, pre-existing holes and cracks are not allowed inside blocks although the DDA supports such kind of blocks theoretically. Hence, it is necessary to modify corresponding part of the DC code so that the pre-existing holes and cracks can also be caught as boundaries of the triangulation. In the triangulation code, blocks are meshed one by one. In each block, different mesh density can be applied. After all blocks are meshed, the MESH code will collect the information of all triangular elements and nodes. The node number is mapped to its corresponding elements and each boundary node is marked out in the final output data file which will be used in the ANALYSIS code.

Two mesh examples are shown here. The first example is an irregular polygon area with holes and cracks inside it (see Figure 4.6a). The boundary of the polygon region is formed by intersected segments. This is the original input graph for the MESH program. Figure 4.6b shows the graph which is trimmed by the MESH program and is ready for further treatment such as triangulation. Figure 4.6c shows the triangulation result. The target number of elements from input is 500, and the region after meshing has 492 elements. Here, the target number of elements is a parameter in the MESH code for control mesh density. After meshing, the real number of elements obtained by the MESH code can only around the presetting value. The closer the obtained number of elements to the targeting number, the better the MESH code control the element size.

The second mesh example is a square block with four holes inside (Figure 4.7). The target number of elements for the region after meshing is 1000. And the program gives a result with 974 elements which are close enough to the requirement.

From these examples shown here, it can be said that the MESH program can control the element size and shape well.

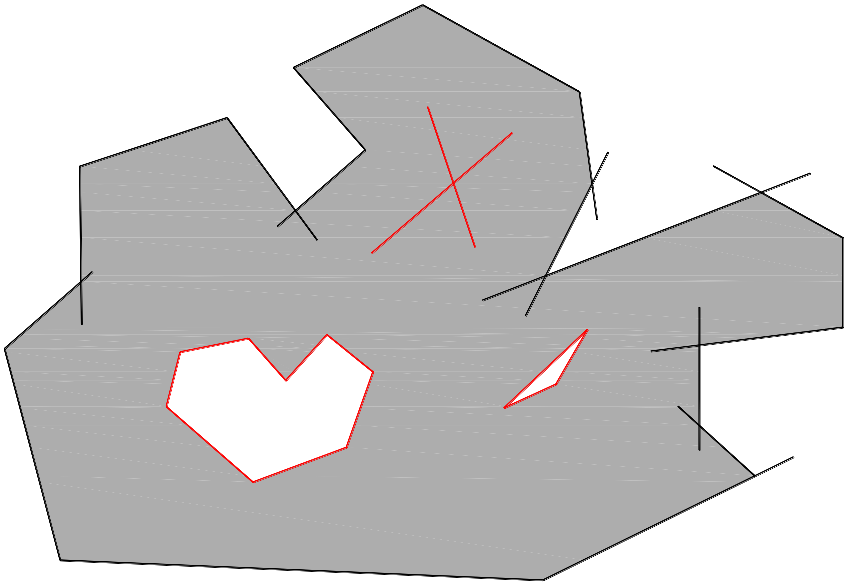

(a) separate lines (with the target region marked by gray)

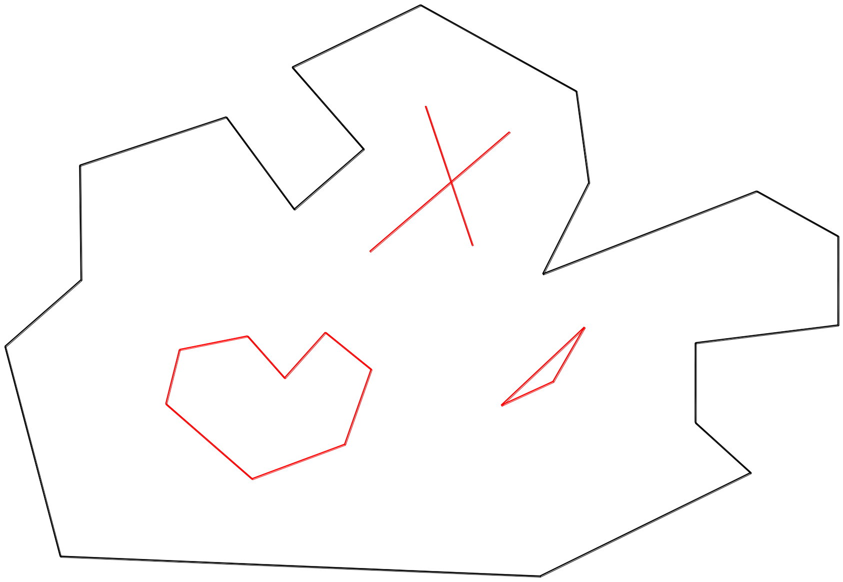

(b) block boundary

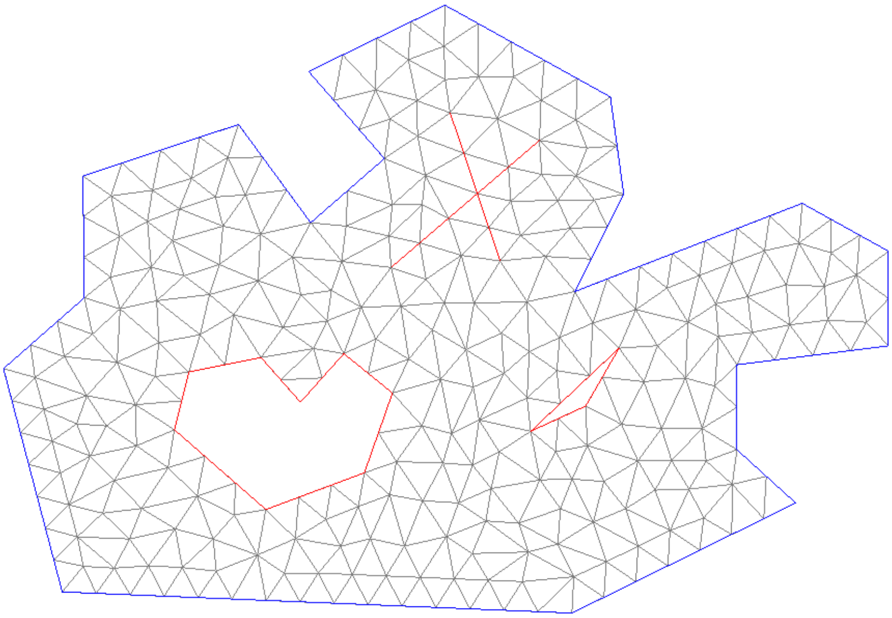

(c) triangular mesh (492 elements)

Figure 4.6 triangular mesh example 1

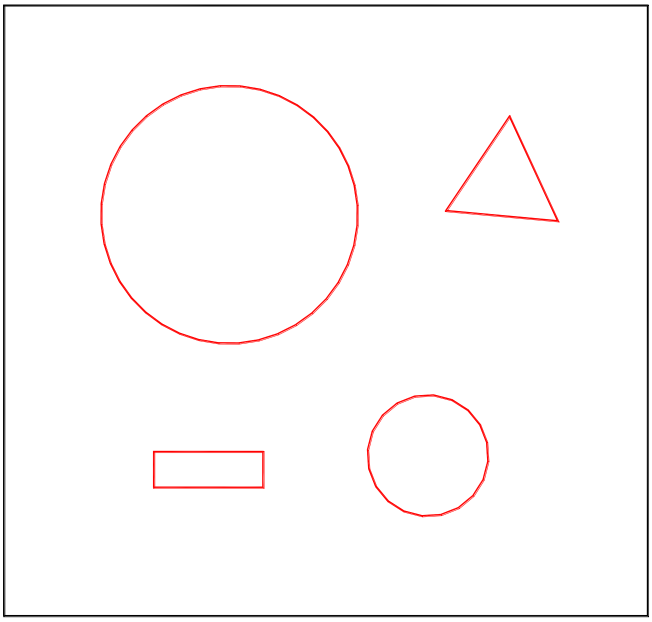

(a) a block with four holes

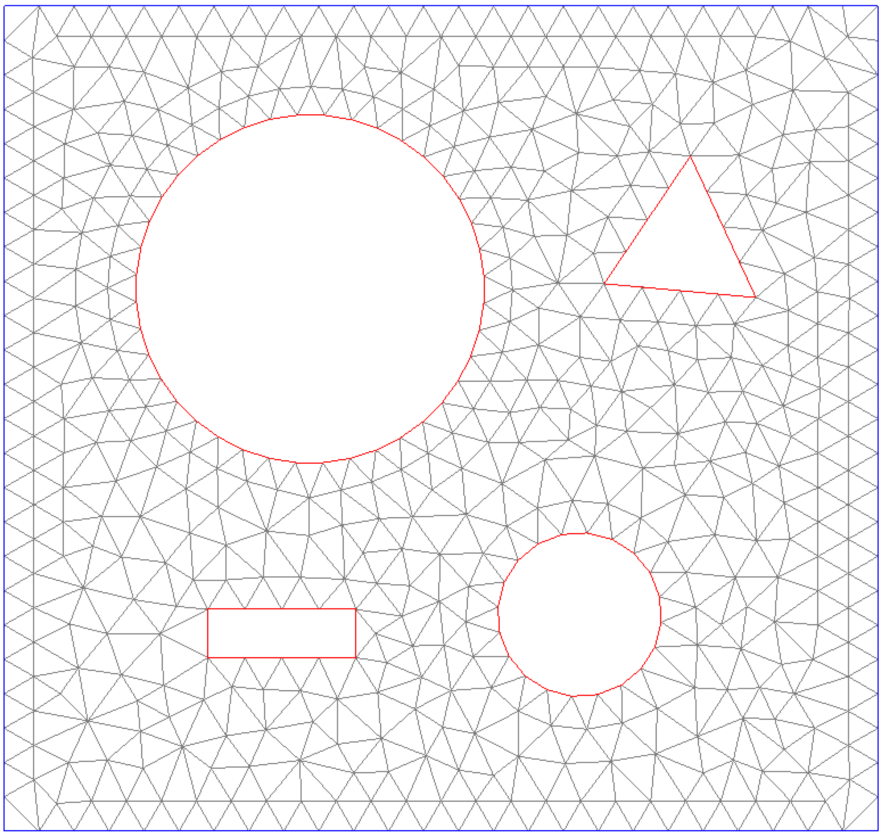

(b) triangulation result (974 elements)

Figure 4.7 triangular mesh example 2

4.6 Summary

This chapter collated most of the background knowledge that needed for programming the automatic mesh generator in the NDDA. The Delaunay refinement algorithm provided by Chew (1989) is presented in details. An enhancement to the original algorithm is provided based on the characteristic that the mesh updates only among the points that linked to the triangle, the center of which was added as a new data point. With this enhancement, the mesh generation time is largely reduced. The enhanced algorithm is employed in the preprocess code of the 2D-NDDA program.

CHAPTER 5 BLOCK FRACTURING

5.1 Introduction

In some problems, it may be the behaviour of the intact rock material that is of concern. This will be the case when considering the excavation of rock by drilling and blasting, or when considering the stability of excavations in good quality, brittle rock which is subject to rockburst conditions. In other instances, the behaviour of single discontinuities, or of a small number of discontinuities, will be of paramount importance. Examples of this class of problem include the equilibrium of blocks of rock formed by the intersections of three or more discontinuities and the roof or wall of an excavation, and cases in which slip on a major fault must be analyzed. A different class of problem is that in which the rock mass must be considered as an assembly of discrete blocks. The normal and shear force–displacement relations at block face-to-face and corner-to-face contacts are of central importance in this case. Finally, it is sometimes necessary to consider the global response of a jointed rock mass in which the discontinuity spacing is small on the scale of the problem domain. The behaviour of caving masses of rock is an obvious example of this class of problem.

No numerical method in the literature can solve all kinds of the above problems alone since each method is developed on specified assumptions to solve a given class of problem. When being applied to other kinds of problem, modification or extension must be carried out. Sometimes coupling with other method can fully inherit the advantages of both methods and overcome the limitation when being applied alone.

Many industrial and scientific problems are characterized by a transformation from continuum to discontinuum state. These phenomena can be found in many applications such as masonry or concrete structural failure, particle comminution and grinding in ball mills, rock blasting in open and underground mining, fracture of ceramic or glass-like materials under high velocity impact and high-speed machining operations, etc. In the standard DDA, a block is the smallest analysis object and the number of blocks is unchangeable throughout the analyzing process, which limited the application of DDA to this class of problems.

So far, the NDDA can solve the discontinuous problem with pre-existing discontinuities as well as the DDA. In addition, the NDDA can provide a better deformation ability of a block and a refined stress/strain distribution inside a block. However, in order to solve the problems involving a transformation from continuum to discontinuum state, the NDDA needs an important extension to provide the ability of fracture in the intact block. The fracture ability is an important feature of the newly developed NDDA because it provides the possibility of transition from the continuum-based analysis to a discontinuum-based analysis. This feature really connects the FEM and the DDA into a unified numerical method.

5.2 Fracture Criterion for Isotropic Rock Material

Fracture may be decomposed into two steps: the crack initiation and the crack propagation. The stage of crack initiation is crucial but quite problematic. General numerical models avoid this problem because their aim is to study the evolution of a pre-existing crack. Damage-based numerical models are more adapted to this problem because they study the evolution of damage continuously and a crack is initiated for a critical damage value. However these codes are often unable to model the crack propagation without a local collapse criterion.

In fact, it is very difficult to determine the location of a new crack. Micro-failure and inclusions always induce local stress concentrations which are at the origin of failure and cracks. As all these defects cannot be taken into account numerically (unless if we use statistical approaches), either the material is assumed to be perfect or homogenized, or the initiation location is imposed by positioning a pre-crack. Moreover, the initiation of a crack in a mesh induces a severe topological change which is rarely supported by numerical codes.

Rocks fail when the surrounding stress exceeds the tensile, the compressive, or the shear strengths of the rock formation, whichever is reached first. There are several types of failure depended on rock lithology, rock microstructures, and applied stresses. Correspondingly, there are various failure/strength criteria applied to compare rock stresses and strength to describe rock failures. Brittle materials such as rock experience fracture without appreciable plastic deformation. For such cases, the Griffith criterion and the Mohr-Coulomb criterion are popular. In the following contents, a brief derivation of the Mohr-Coulomb criterion, the Griffith criterion and the stress intensity factor criterion is listed and discussed for the purpose of integrity of the content.

5.2.1 Mohr-Coulomb criterion

Shear failure occurs when the shear strength of the formation is exceeded. According to the Mohr-Coulomb failure criterion, the shear strength on plane *ab* in Figure 5.1 is

$$|\tau| = c + \sigma_n \tan\phi \tag{5.1}$$

where τ and σ_n are shear and normal stresses at a point on the plane *ab* and compression is positive. c is the cohesion and ϕ is the angle of internal friction. In this regard, the algebraic sign of the shear stress is not physically significant, so the absolute value sign is used in Eq.(5.1).

The major and minor principal stresses are denoted by σ_1 and σ_3 (with $\sigma_1 \geq \sigma_3$), respectively.

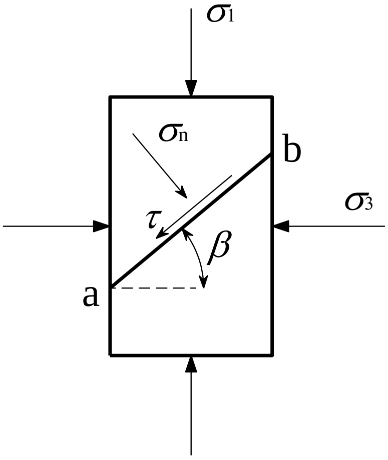

Figure 5.1 shear failure on plane *ab*

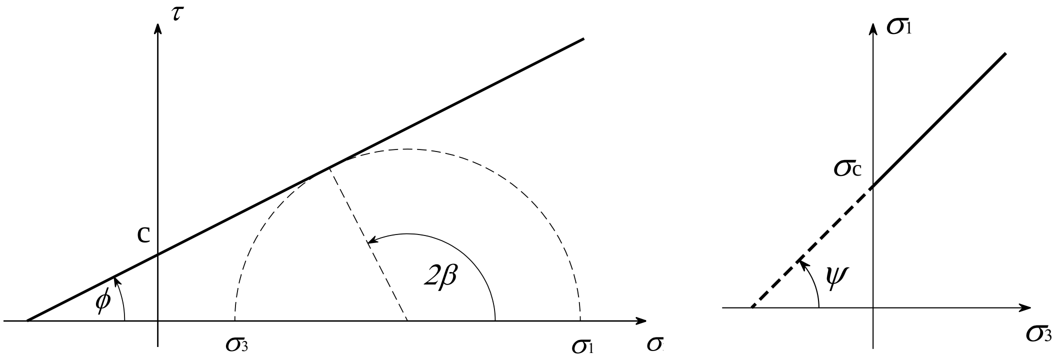

(a) shear and normal stresses (b) principal stresses

Figure 5.2 Coulomb strength envelopes

Applying the stress transformation equations to the case shown in Figure 5.1 gives

$$\sigma_n = \frac{1}{2}(\sigma_1 + \sigma_3) + \frac{1}{2}(\sigma_1 - \sigma_3)\cos 2\beta \tag{5.2}$$

and

$$|\tau| = \frac{1}{2}(\sigma_1 - \sigma_3)\sin 2\beta \tag{5.3}$$

Substitution for σ_n and $|\tau|$ in Eq.(5.1) and rearranging gives the limiting stress condition on any plane defined by β as

$$\sigma_1 = \frac{2c + \sigma_3\left[\sin 2\beta + \tan\phi(1-\cos 2\beta)\right]}{\sin 2\beta - \tan\phi(1+\cos 2\beta)} \tag{5.4}$$

There will be a critical plane on which the available shear strength will first be reached as σ_1 increasing. The Mohr circle construction of Figure 5.2a gives the orientation of this critical plane as

$$\beta = \frac{\pi}{4} + \frac{\phi}{2} \tag{5.5}$$

For the critical plan, $\sin 2\beta = \cos\phi$, $\cos 2\beta = -\sin\phi$, and Eq.(5.4) reduces to

$$\sigma_1 = \frac{2c\cos\phi + \sigma_3(1+\sin\phi)}{1-\sin\phi} \tag{5.6}$$

This linear relation between σ_3 and the peak value of σ_1 are shown in Figure 5.2b. It is noted that the slope of this envelope is related to ϕ by the equation

$$\tan\psi = \frac{1+\sin\phi}{1-\sin\phi} \tag{5.7}$$

here ψ is defined in Figure 5.2b and that the uniaxial compressive strength σ_c is related to *c* and ϕ by

$$\sigma_c = \frac{2c\cos\phi}{1-\sin\phi} \tag{5.8}$$

If the Coulomb envelope shown in Figure 5.2b is extrapolated to $\sigma_1 = 0$, it will intersect the σ_3 axis at an apparent value of uniaxial tensile strength of the material given by

$$\sigma_T = -\frac{2c\cos\phi}{1+\sin\phi} \tag{5.9}$$

The measurement of the uniaxial tensile strength of rock is normally too difficult to be carried out. However, when it is satisfactorily measured, it takes values that are generally lower than those predicted by Eq.(5.9) (Brady and Brown 2004). For this reason, a tensile cutoff is usually applied at a selected value of uniaxial tensile stress, T_0, as shown in Figure 5.3.

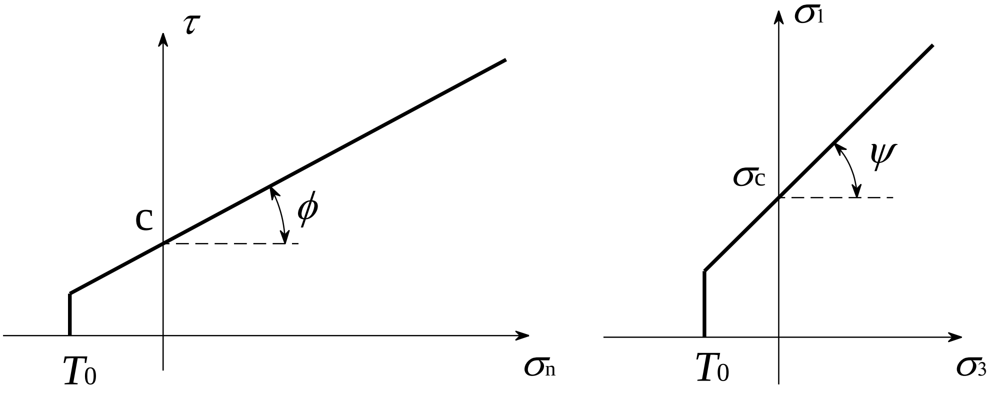

Figure 5.3 Coulomb strength envelopes with a tensile cut-off

Although it is widely used, Mohr-Coulomb's criterion is not a particularly satisfactory peak strength criterion for rock material and cannot fully show the mechanism of the failure. The limitations of Mohr-Coulomb's criterion are listed below:

(a) It implies that a major shear fracture exists at peak strength. Observations such as those made by Wawersik and Fairhurst (1970) show that this is not always the case.

(b) It implies a direction of shear failure which does not always agree with experimental observations.

(c) Experimental peak strength envelopes are generally non-linear. They can be considered linear only over limited ranges of σ_n or σ_3.

(d) The intermediate principal stress σ_2 does not affect failure and this may overestimate failure.

(e) It is not a good choice for tensile failure and for the case under a high confining pressure.

For these limitations, other peak strength criteria should be preferred for intact rock. However, the Coulomb criterion can provide a good representation of residual strength conditions, and more particularly, of the shear strengths of discontinuities in rock.

5.2.2 Griffith criterion

Griffith (1921) postulated that fracture of brittle materials, such as steel and glass, is initiated at tensile stress concentrations at the tips of minute, thin cracks (now referred to as Griffith cracks) distributed throughout an otherwise isotropic, elastic material. Griffith (1924) extended his theory to the case of applied compressive stresses. Neglecting the influence of friction on the cracks which will close under compression, and assuming that the elliptical crack will propagate from the points of maximum tensile stress concentration, Griffith obtained the following criterion for crack extension in plane compression for a dry material:

If $\sigma_1 + 3\sigma_3 > 0$,

$$(\sigma_1 - \sigma_3)^2 = 8T_0(\sigma_1 + \sigma_3) \tag{5.10}$$

If $\sigma_1 + 3\sigma_3 < 0$,

$$\sigma_3 = -T_0 \tag{5.11}$$

When $\sigma_3 = 0$, it is uniaxial compression, so that the uniaxial compressive strength (σ_c) predicted by Eq. (5.10) ($\sigma_c = \sigma_1$) is:

$$\sigma_c = 8T_0 \tag{5.12}$$

It should be noted that for some rocks, Eq. (5.12) underestimates the uniaxial compressive strength. For a number of reasons, the classical Griffith criterion did not provide a very good model for the peak strength of rock under multiaxial compression. Modified Griffith theory suggested that the uniaxial compressive strength and tensile strength have the following relationship:

$$\sigma_c = \frac{4(1+\sin\varphi)}{1-\sin\varphi}T_0 \tag{5.13}$$

where φ is the internal friction angle of the material.

McClintock and Walsh (1962) modified Griffith's original theory to account for the effects of crack closure in compression. It is assumed that the inherent cracks are initially closed, the relationship between the principal stresses required to initiate fracture is

$$\sigma_1 = \sigma_3 \frac{\sqrt{1+\mu^2}+\mu}{\sqrt{1+\mu^2}-\mu} + \sigma_c \tag{5.14}$$

where μ is the coefficient of friction between the crack faces and σ_c is the uniaxial compressive strength of the material.

The critical orientation of a closed crack is given by

$$\tan 2\psi_c = \frac{1}{\mu} \tag{5.15}$$

Eq.(5.14) and Eq.(5.15) are valid when the normal stress σ_n acting across the crack is compressive, i.e. when

$$\sigma_n = \frac{1}{2}[(\sigma_1 + \sigma_3) - (\sigma_1 - \sigma_3)\cos 2\psi] > 0 \tag{5.16}$$

When σ_n is tensile, the original Griffith theory is applicable.

The modified Griffith theory can be represented by a straight-line Mohr envelope having the following equation:

$$\tau = \mu\sigma - 2\sigma_t \tag{5.17}$$

The McClintock-Walsh modification does not consider the problem of stable crack propagation. The crack will still extend essentially as in the Griffith compression criterion, albeit at a still higher stress level (Fairhurst 2004).

Another extension of the Griffith criterion states that the uniaxial compressive strength is 12 times of the tensile strength (Murrell 1963):

$$\sigma_c = 12T_0 \tag{5.18}$$

It must be emphasized that both the original and modified Griffith theories cannot be applied to the fracture of a specimen because they considered the highly idealized situation in which a single, critically stressed crack begins to extend and propagate throughout the solid. It is implicitly assumed that there are no other cracks in the material or, equivalently, that any other cracks do not propagate. It has already been suggested by Brace and Bombolakis (1963) that a fracture propagation from a single crack follows a more complex path than is generally assumed and that it is the presence of favourable crack arrays which coalesce to form the macroscopic fracture surface, that make the Griffith theory applicable to predicting fracture of rock and rock specimens. A serious limitation of the Griffith theory lies in the fact that it can only be used to predict fracture initiation (Brace and Bombolakis 1963; Hoek and Bieniaws.Zt 1965). In its usual form, it yields no information on the rate or direction of fracture propagation.

5.2.3 Fracture mechanics and Stress Intensity Factors

Griffith's energy instability concept forms the basis of the engineering science of fracture mechanics which is being used increasingly to study a number of fracture propagation phenomena in rock mechanics. The outline of the essential concepts of fracture mechanics given here follows that of Paterson and Wong (2005).

Although non-elastic effects operate at the tips of cracks in rock, the practical analysis of the stresses in the vicinity of a crack tip is usually carried out using the classical theory of linear elasticity. In this case, the approach is referred to as linear elastic fracture mechanics. The purpose of this stress analysis is to estimate the "loading" applied to the crack tip and to determine whether or not the crack will propagate. In order to do this, the nature of the stress distribution in the vicinity of the crack tip must be determined.

The analysis of the stresses in the vicinity of the crack tip is approached by considering three basic modes of distortion, designated modes I, II and III, and defined with respect to a reference plane that is normal to the edge of a straight line crack. Modes I and II are the plane strain distortions in which the points on the crack surface are displaced in the reference plane normal and parallel, respectively, to the plane of the crack. Mode III is the anti-plane strain distortion in which the points on the crack surface are displaced normal to the reference plane. In simpler terms, modes I, II and III are the extension or opening, in-plane shear and out-of-plane shear modes, respectively. The stress and displacement fields around the crack tip in these three basic modes of distortion are obtained by considering the distributions resulting from the application of uniform loadings at infinity. In the absence of perturbations due to the crack, these loadings correspond, respectively, to a uniform tensile stress normal to the crack (mode I), a uniform shear stress parallel to the crack (mode II) and a uniform shear stress transverse to the crack (mode III).

It is found that, for each mode of distortion, each of the stress and displacement components can be expressed as the product of a spatial distribution function that is independent of the actual value of the applied stress and a scaling factor that depends only on the applied stress and the crack length. The same scaling factor applies for each of the stress and displacement components in a given mode. It is known as the stress intensity factor for that mode. The stress intensity factors for the three modes of distortion are designated K_I, K_{II} and K_{III}, respectively.

It is clear from the above that the values of K_I, K_{II} and K_{III} in any particular case depend on both the macroscopic stress field and the geometry of the specimen. The question then arises as to when a crack in a particular case will begin to extend. In linear elastic fracture mechanics, it is postulated that the crack will begin to extend when a critical intensity of loading as measured by the stress intensity factors is reached at its tip. That is, the failure criterion is expressed in terms of critical stress intensity factors designated K_{IC}, K_{IIC}, K_{IIIC} which are also known as fracture toughnesses are regarded as material properties.

$$\begin{aligned} K_I &= K_{IC} \quad \text{(mode I)} \\ K_{II} &= K_{IIC} \quad \text{(mode II)} \\ K_{III} &= K_{IIIC} \quad \text{(mode III)} \end{aligned} \tag{5.19}$$

It must be noted that in many practical problems, the applied stress field will be such that a mixed mode of fracture will apply.

$$f(K_I, K_{II}, K_{III}) = 0 \quad \text{(mixed mode)} \tag{5.20}$$

When a crack is initiated, one needs to check, at each time step, if the crack is going to propagate by a crack propagation criterion. Stress intensity factors are often used for crack propagation and cannot deal with the crack initiation.

The stress intensity factors are evaluated by the domain form of the interaction integral, which assumes a traction-free crack surface. In rock failure analysis, compressive loading condition is usually encountered. The joint surfaces usually involve frictional contact. Although some efforts have been done to account for the traction along the crack surface in the literature, it is still not an easy task.

In addition, the domain form of the interaction integral needs a domain around the crack tip to evaluate the stress intensity factors, the domain must not be intersected by other cracks, thus it is not applicable to the case where the crack tip is close to another crack surface or crack tip. In a rock failure analysis, crack coalesce is essential to form a complete failure surface to allow the final kinematic release.

5.3 Mesh Update

There are two situations favoring fracturing. One is fracturing along the well-defined boundaries between two types of rocks, i.e. rock joints. The other is fracturing within an intact block, where a fracture finds its way through the weakest point within the block. For the first situation, no mesh need to be updated, while for the second situation, new nodes or new boundary may be created, which makes it necessary to update the mesh topology so that new information can be considered in the next time step.

A crack is initiated inside a block in two steps. The first setp is separating the mesh grid line that satisfies the crack criterion and splitting node if necessary. When a grid line becomes a crack, two elements that share this line will be separated. During this process, new nodes might appear. According to the position of the grid line, three cases might happen: no new node, one new node, and two new nodes. Figure 5.4 shows the case that crack initiated without inserting any new node. In this case, the two nodes that linked by this grid line must lie inside the block, i.e., they are not boundary nodes which include nodes on the hole boundary, crack boundary, and block boundary. In this situation, the grid line is only marked by the program as a crack and the two nodes are updated as external nodes, which will be introduced later in this section. When one of the two nodes that linked by the cracked grid line is on the block boundary as shown in Figure 5.5a, the grid line 4-7, a new node will be created after cracking, as shown in Figure 5.5b. When two nodes of the grid line are boundary nodes, such as grid line 1-7 as shown in Figure 5.5b, two new nodes will be created after cracking as shown in Figure 5.5c.

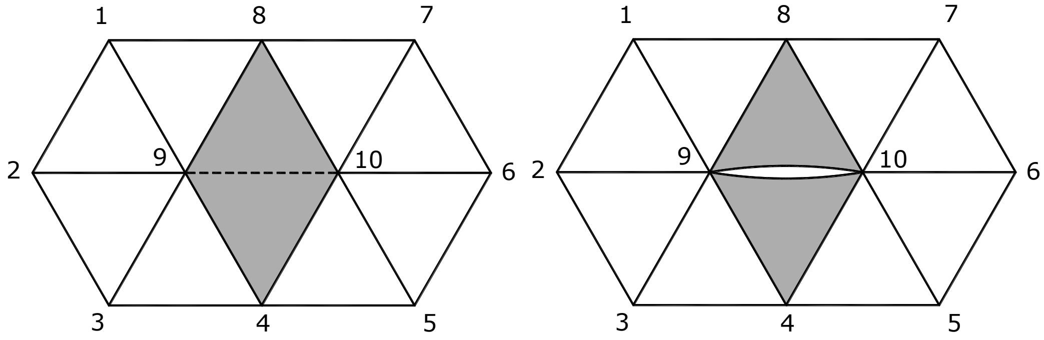

(a) (b)

Figure 5.4 schematic illustration of the process of a grid line becomes a crack: (a) two adjacent elements inside a block before splitting; (b) the separated grid line.

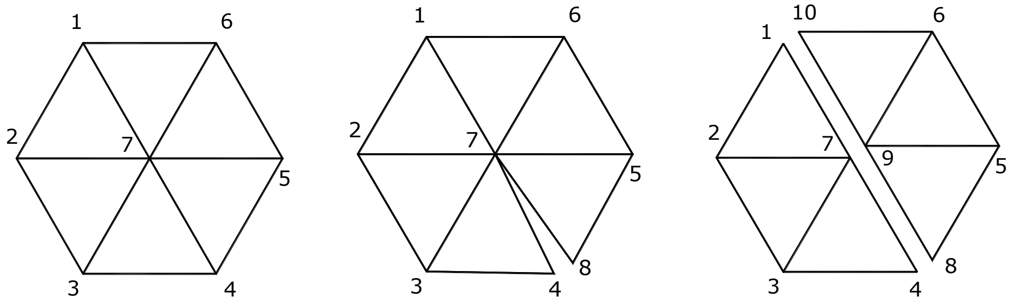

(a) (b) (c)

Figure 5.5 illustration of a block cracked into two blocks: (a) a block with 7 nodes; (b) one new node: node 8; (c) two new nodes: node 9 & 10.

The second step of crack initiation is updating the boundary of the new mesh. The updating of boundary is a process of loop searching. Since the searching work needs to be carried out in each time step, an efficient searching algorithm is necessary to assure the high performance of the NDDA program. In this section, a simple and fast searching scheme is provided. Before introducing the scheme, some concepts are listed and clarified below for a better understanding of it.

Internal node is the grid node that lies inside the region.

External node is the grid node that lies on the region boundary.

Loop is referred to here as the inside and outside boundary of a region. The outside boundary of a region builds the shape of a block and the inside boundary forms holes and cracks in a block. Cracks can be viewed as holes without volume.

Loop searching direction is the direction when walking along the loop in which, the domain restricted by the loop always lies on the left hand side of the loop, see Figure 5.6.

Upper node is the external node that lies on the loop next to the current node in the loop searching direction.

Lower node is the external node that lies on the loop next to the current node in the opposite searching direction.

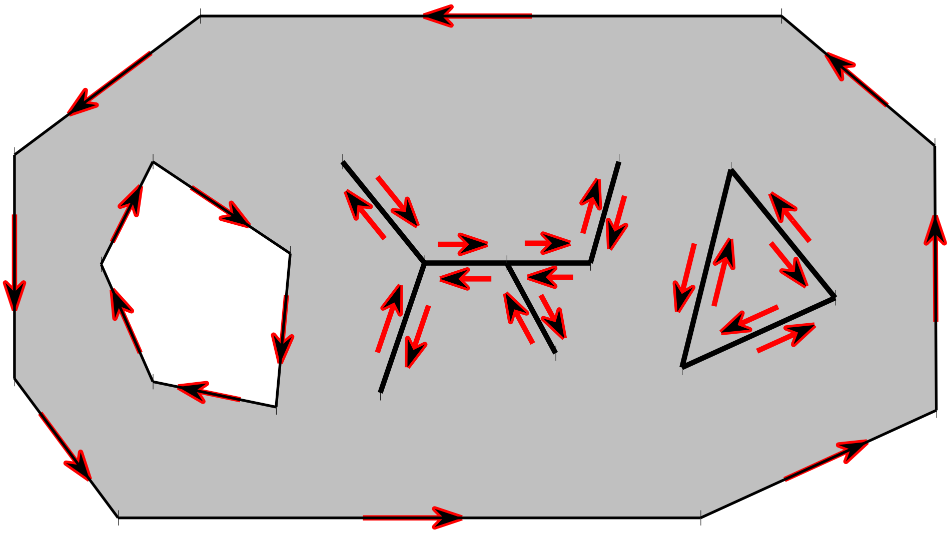

Figure 5.6 loop searching direction

Since a loop can only be constructed by external nodes, the priority thing is to find out all external nodes. In order to mark out all internal and external nodes, two lemmas are introduced as follows.

Lemma 1: For any grid node, define n_n as the number of nodes that are connected to it by a grid line and n_e as the number of elements that are connected by it. If $n_n = n_e$, the node is an internal node.

Lemma 2: For any grid node, define n_n as the number of nodes that are connected to it by a grid line and n_e as the number of elements that are connected by it. If $n_n = n_e + 1$, the node is an external node.

Proof to these two lemmas is obvious. Figure 5.7a shows an example of the internal node. Here, node N_1 is an internal node and surrounded by six elements and six nodes. Figure 5.7b shows an example of the external node. Here, node N_1 is an external node surrounded by six elements and seven nodes.

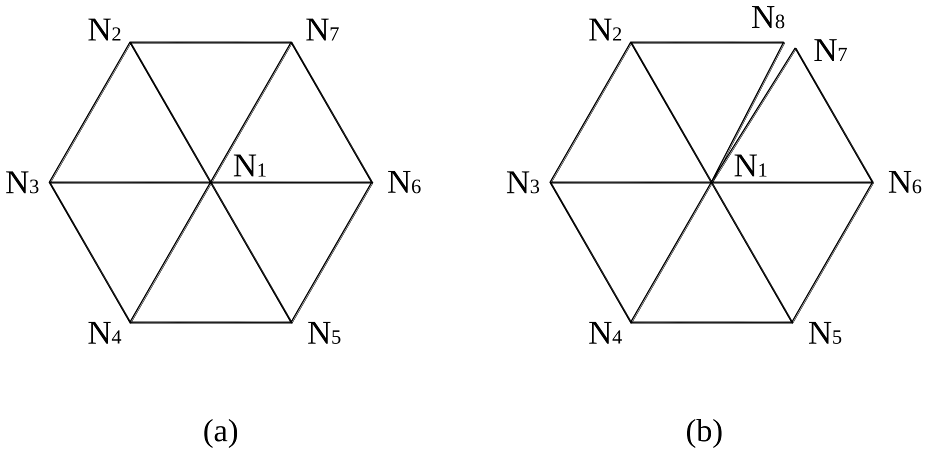

Figure 5.7 internal and external node judgment

It is assumed that an external node only can belong to one loop, i.e. no two loops can share an external node. For each external node, the following information must be provided before searching loops (see Figure 5.8):

- The upper node of it;
- The lower node of it;
- All elements surrounding it;
- The loop it belongs to.

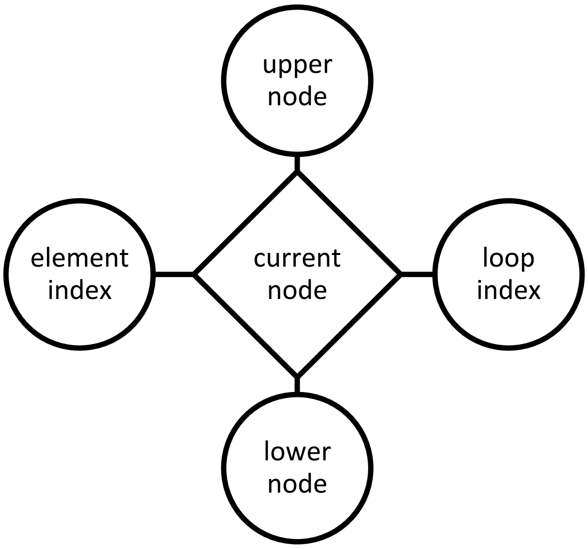

Figure 5.8 schematization of the information that must be provided on an external node for boundary searching

The searching process is started by departing from an external node that has not been used along the loop searching direction. For the current node, find its upper node and check whether the index of the upper node equals to the index of the starting node. If yes, searching is finished and the loop information of all external nodes on this loop is updated. If not, using the upper node instead of the current node and keep on searching for the next upper node until find the starting node again.

5.4 Fracture Scheme

From discussion in section 5.2 about different crack criteria for isotropic rock, it is obvious that the Mohr-Coulomb criterion is the simplest and easiest to apply in a multi-crack analysis. In this section, a fracture scheme is provided based on the Mohr-Coulomb criterion as a heuristic method although this criterion has a lot of limitations. In the fracture scheme, crack initiates at any mesh line that satisfies the crack criterion and a crack sequence is introduced to consider the stress redistribution after a crack nucleated. The fracture propagation is achieved by the coalescence of these initiated cracks. This scheme largely ignored the crack tip processes and fracture mechanics so that it can be applied in the complicated stress field and the case where the crack tips are too close to each other to apply the fracture mechanics.

In a continuum media, cracks are not independent of each other. Once a crack occurs somewhere, it will cause the stress redistribute in the area around it and release some energy. And it finally affects the behavior of the crack propagation in the nearby field. This fact should be taken into consideration in the numerical modelling.

In the NDDA, a fracture sequence is considered by a special crack inserting procedure inside each time step. The procedure includes four steps:

Step 1. Compute the average normal stress and shear stress on the grid lines among all elements.

Step 2. Look for the grid line which will crack first according to the time sequence.

Step 3. Separate the grid line which triggered the crack criterion and insert new nodes if necessary. Update the mesh and all related information of nodes and elements.

Step 4. Compute the updated system again and go back to *step 1* unless reach the last time step.

During the step 2, the most important thing is how to know the time sequence, which is based on the failure time of each mesh grid. The failure time of each mesh grid include two contents: tensile failure time and shear failure time. More details about them will be introduced in the following section.

For each grid line, compute the average normal stress and shear stress considering stresses of the elements sharing this grid line. Assume the current time step starts at time instant t_0 and the time interval of current step is T, then the time instant at the end of current time step is t_0+T. Denote the average normal and shear stresses on the grid line i at the beginning of current time step by $\sigma_i(t_0)$ and $\tau_i(t_0)$, respectively. Denote the average normal and shear stresses on grid line i at the end of this time step by $\sigma_i(t_0+T)$ and $\tau_i(t_0+T)$, respectively. The average stresses of grid line i can be obtained by the stresses of the two adjacent elements:

$$\sigma_x = \frac{\sigma_{1x}+\sigma_{2x}}{2}$$

$$\sigma_y = \frac{\sigma_{1y}+\sigma_{2y}}{2} \tag{5.21}$$

$$\tau_{xy} = \frac{\tau_{1xy}+\tau_{2xy}}{2}$$

where σ_{1x}, σ_{1y}, and τ_{1xy} are stresses of element 1 beside grid line i; σ_{2x}, σ_{2y}, and τ_{2xy} are stresses of element 2 beside grid line i. And the normal and shear stresses on grid line i are, respectively,

$$\sigma_i = \frac{1}{2}(\sigma_x+\sigma_y)+\frac{1}{2}(\sigma_x-\sigma_y)\cos 2\theta+\tau_{xy}\sin 2\theta \tag{5.22}$$

$$\tau_i = \frac{1}{2}(\sigma_x-\sigma_y)\sin 2\theta-\tau_{xy}\cos 2\theta \tag{5.23}$$

where θ is the direction angle of grid line *i*.

Since the time step interval *T* is small, the following assumption is tenable: the stress variation during this period can be considered as a linear variation. Hence the normal and shear stresses on mesh line *i* at any time instant $t_0 + \delta t$ within current step can be given in an interpolating form as

$$\sigma_i(t_0 + \delta t) = \sigma_i(t_0) + \frac{\sigma_i(t_0 + T) - \sigma_i(t_0)}{T} \delta t \tag{5.24}$$

$$\tau_i(t_0 + \delta t) = \tau_i(t_0) + \frac{\tau_i(t_0 + T) - \tau_i(t_0)}{T} \delta t \tag{5.25}$$

where $\delta t \in (0, T]$.

When the normal and shear stresses of all grid lines are obtained, the failure time of each grid line can be worked out. Each grid line needs to be calculated of both the tensile failure time and the shear failure time.

Let σ_u denotes the tensile strength of the block material. The normal stress acting on the grid line is defined here to be positive in compression. If $\max\{-\sigma_i(t_0), -\sigma_i(t_0 + T)\} < \sigma_u$, tensile crack of this grid line will not happen in current step.

If $-\sigma_i(t_0 + T) \geq \sigma_u$, substituting $\sigma_i(t_0 + \delta t) = -\sigma_u$ into Eq.(5.24), we have

$$-\sigma_u = \sigma_i(t_0) + \frac{\sigma_i(t_0 + T) - \sigma_i(t_0)}{T} \delta t \tag{5.26}$$

Solve the Eq.(5.26), then we obtain the tensile failure time

$$\delta t_n^i = \frac{-\sigma_u - \sigma_i(t_0)}{\sigma_i(t_0 + T) - \sigma_i(t_0)} T \tag{5.27}$$

If $0 < \delta t_n^i \leq T$ is not satisfied, tensile failure of the grid line cannot appear in the current step.

According to Mohr-Coulomb criterion, the shear strength for grid line *i* is

$$\tau_u = c + \sigma_i(t_0 + \delta t)\tan\phi \tag{5.28}$$

By substituting $\tau_i(t_0 + \delta t) = \tau_u$ into Eq.(5.25), we have

$$\tau_u = \tau_i(t_0) + \frac{\tau_i(t_0 + T) - \tau_i(t_0)}{T}\delta t \tag{5.29}$$

Combine Eq.(5.28) and Eq.(5.29), we have

$$c + \sigma_i(t_0 + \delta t)\tan\phi = \tau_i(t_0) + \frac{\tau_i(t_0 + T) - \tau_i(t_0)}{T}\delta t \tag{5.30}$$

Substituting Eq.(5.24), then

$$\tau_i(t_0) + \frac{\tau_i(t_0 + T) - \tau_i(t_0)}{T}\delta t - \left[\sigma_i(t_0) + \frac{\sigma_i(t_0 + T) - \sigma_i(t_0)}{T}\delta t\right]\tan\phi - c = 0 \tag{5.31}$$

Solve Eq.(5.31), we obtain the shear failure time

$$\begin{aligned}\delta t_s^i &= \frac{T\left(\tau_i(t_0) - \sigma_i(t_0)\tan\phi - c\right)}{\left[\sigma_i(t_0 + T) - \sigma_i(t_0)\right]\tan\phi - \tau_i(t_0 + T) + \tau_i(t_0)} \\ &= \frac{T\left(\tau_i(t_0) - \sigma_i(t_0)\tan\phi - c\right)}{\left[\tau_i(t_0) - \sigma_i(t_0)\tan\phi - c\right] - \left[\tau_i(t_0 + T) - \sigma_i(t_0 + T)\tan\phi - c\right]}\end{aligned} \tag{5.32}$$

Denote

$$f(t) = \tau_i(t) - \sigma_i(t)\tan\phi - c$$

and substitute it into Eq.(5.32), then the shear failure time can be expressed in a simple form as

$$\delta t_s^i = \frac{f(t_0)}{f(t_0) - f(t_0 + T)}T \tag{5.33}$$

If $0 < \delta t_s^i \le T$ is not satisfied, shear failure of this grid line cannot appear in the current step.

If both $0 < \delta t_n^i \le T$ and $0 < \delta t_s^i \le T$ are satisfied, it is necessary to compare the tensile failure time t_n^i and shear failure time t_s^i and the smaller one is the final failure time for grid line *i* in current time step, i.e.

$$\delta t^i = \min\{\delta t_n^i, \delta t_s^i\} \tag{5.34}$$

and the corresponding failure mode is the final failure mode of grid line *i*.

5.5 Stiffness Matrix Update

According to the number of new nodes generated in a step, the stiffness matrix needs to be updated correspondingly. In case one, when no new node is generated, the total degree of freedom of the system is unchanged. And the two nodes of the cracked grid line are marked as boundary nodes in the next step. In the other case, when one or two new nodes are generated, the total number of nodes in the system is increased by two or four because each new node will introduce two degrees of freedom.

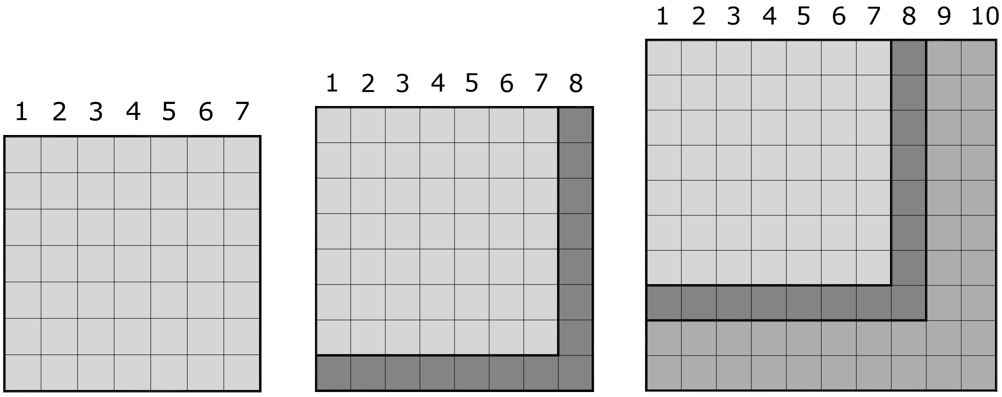

(a) (b) (c)

Figure 5.9 schematic illustration of the updating scheme of the stiffness matrix: (a) stiffness matrix of a block with 7 nodes; (b) insert a column and a row for the new born node 8; (c) insert two columns and two rows for the new born node 9 & 10

Figure 5.9a shows the structure of the stiffness matrix of the block system shown in Figure 5.5a. Each small square in the matrix is a 2×2 submatrix. Hence, the total dimension of the stiffness matrix is 14×14. When the grid line 4-7 is separated as shown in Figure 5.5b, node 8 was generated as a new node. The stiffness matrix needs to be updated as shown in Figure 5.9b. When the grid line 1-7 is separated as shown in Figure 5.5c, node 9 and node 10 are generated as new nodes. Two rows and two columns need to be appended to the stiffness matrix of Figure 5.9b, as shown in Figure 5.9c. Finally, one block is divided into two blocks and three new nodes are generated. The degrees of freedom are increased from 14 to 20.

5.6 Summary

The Mohr-Coulomb criterion is applied to the NDDA program as a crack criterion because of its widely used in the rock engineering and it is easy to apply in the code. However, the limitations of the Mohr-Coulomb criterion are obvious as discussed in section 5.2. Since it cannot serve as a kinking criterion, accurate propagating direction of the small cracks after initiated cannot be obtained under this fracture scheme. A rough fracture direction is achieved by a group of small cracks, which will be shown by examples in the Chapter 7. It is necessary to research the possibility of applying other crack initiation and propagation criteria in the future work.

During the process of fracture in a continuous region, update of the mesh is a big challenge to the numerical modelling. A mesh updating algorithm is provided in this chapter for the newly developed NDDA program. This algorithm is also applicable to other kinds of numerical method.

CHAPTER 6 VERTEX-VERTEX CONTACT IN THE DDA

6.1 Introduction

In the two-dimensional DDA, there are three kinds of contacts among blocks (see Figure 6.1): *vertex-vertex* (V-V), *vertex-edge* (V-E), and *edge-edge* (E-E). The vertex-vertex and edge-edge contacts can be finally translated into equivalent vertex-edge contacts during the analyzing procedure. And each vertex-edge contact deals with the relationship of three points: the contact vertex and two ends of the contact line, for instance, in Figure 6.1b, point A, B, and C are involved. The contact spring is added or removed between the vertex and the reference edge according to their status in each time step.

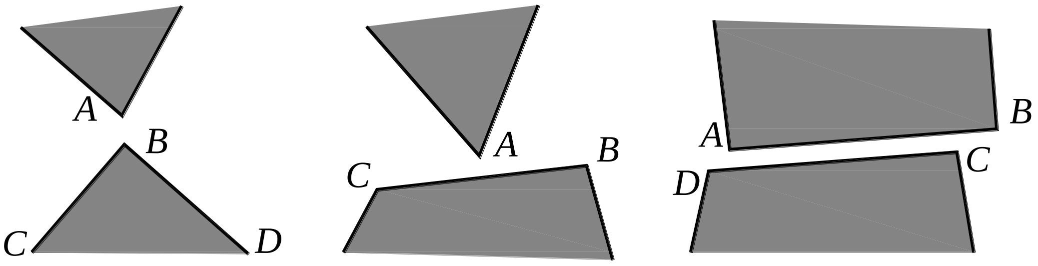

(a) vertex-vertex (b) vertex-edge (c) edge-edge

Figure 6.1 three types of contact in the DDA

The edge-edge contact can be decomposed as a combination of two vertex-edge contacts, such as in Figure 6.1c, the original edge-edge contact (denoted by *AB*-*CD*) can be replaced by a pair of vertex-edge contacts denoted by *A*-*DC* and *C*-*AB*.

Different from the edge-edge contact, the vertex-vertex contact is degenerate, hence the equivalent substitution is much more complex and indeterminate. Figure 6.1a shows a vertex-vertex contact: *A-B*, there have two potential vertex-edge contacts, *A-BC* and *A-BD*, for the vertex-vertex contact to degenerate into. The vertex *A* is facing two potential reference edges, *BC* and *BD*, because of the discontinuity of the normal direction at vertex *B*. The normal vector at the vertex *B* is arbitrary in the normal cone field (see Figure 6.2). If a contact spring is placed between vertex *A* and vertex *B* without considering the degeneration, "locking phenomenon" will arise, which means vertex *A* and vertex *B* will stuck together without further sliding. Such a phenomenon is purely a numerical problem associated with particular modelling techniques employed in the numerical method and does not exist in the physical world. In reality, crushing of the corner may happen as a result of the stress concentration or the corner in a microscopic view is rounded, which makes a further motion possible.

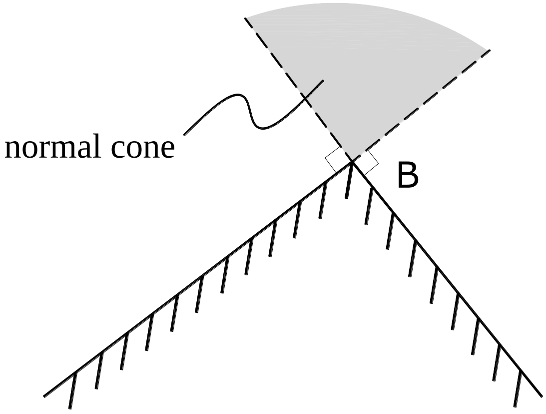

Figure 6.2 the normal cone of a vertex

Strictly speaking, the real vertex-vertex contact is referred to as a collision of two corners right at the vertex point, i.e. the distance between the two vertexes is zero at the instant of collision. In the DDA, if two vertexes are close enough to each other (the distance between them is smaller than the threshold value), they are detected to be a vertex-vertex contact candidate in this time interval. The so called 'candidate' means that they might be unqualified for a real vertex-vertex contact in the open-close iteration and will be removed from the contact list. To make a distinction from the real vertex-vertex contact, the detected vertex-vertex contact candidate is named as 'quasi vertex-vertex contact' in this work. After detecting all contact candidates, the DDA adds contact spring for each of them to reflect the contact interaction force. It is clear that the direction of the contact forces will be perpendicular to the edge in a vertex-edge contact, but it is unclear in which direction it will act in the vertex-vertex contact because of the discontinuity of the normal vector at the sharp corner. The ambiguity of contact force in the vertex-vertex contact leads to the indeterminacy when adding contact spring.

Two types of indeterminacy in the vertex-vertex contact model. The first type of indeterminacy is referred to as *genuine indeterminacy* (GI) in this thesis because it originated from the real vertex-vertex contact. When the trajectory of one vertex in the contact pair passes its target vertex, genuine indeterminacy will arise. A special case of genuine indeterminacy is when two vertexes are in contact without penetration before moving toward each other (see Figure 6.3a). When the upper block starts to move, two sliding cases are possible, depending on the choice of the reference edge at the beginning of the analysis. If the right edge of the bottom block is chosen as the reference edge, the case in Figure 6.3b might happen. While the case in Figure 6.3c might happen if the left edge of the bottom block is selected.

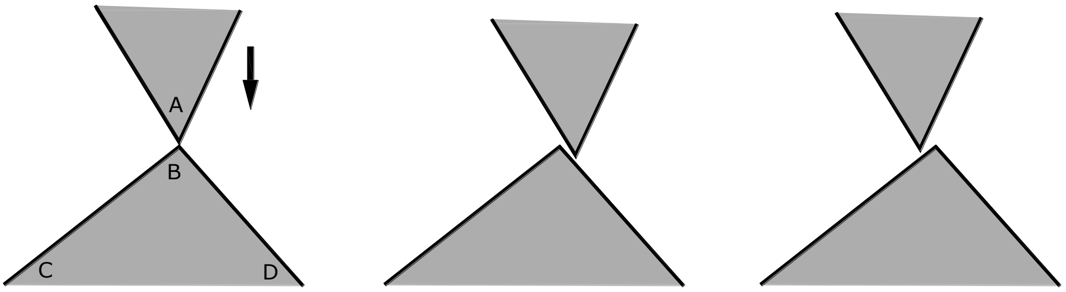

(a) a V-V contact (b) case I (c) case II

Figure 6.3 the indeterminacy of a V-V contact when degenerating into a V-E contact

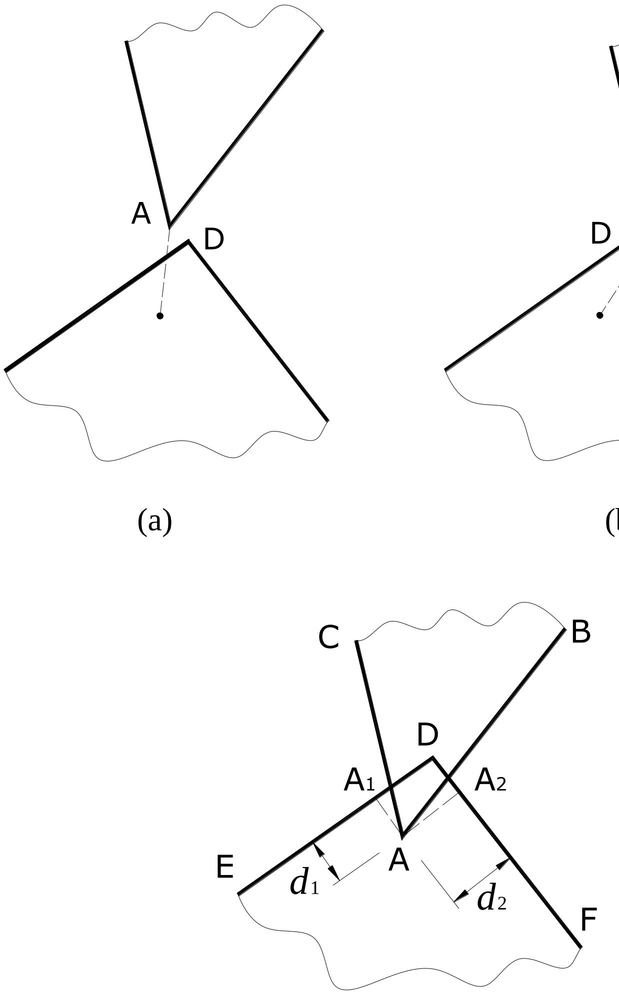

(a)

(b)

(c)

Figure 6.4 schematization of the shortest path method: (a) quasi V-V contact case 1; (b) quasi V-V contact case 2; (c) overlapped at the end of time interval

The second type of indeterminacy is referred to here as *pseudo indeterminacy* (PI) because it is a phenomenon that belongs to particular numerical modelling methods when dealing with the quasi vertex-vertex contact. Since the penalty method satisfies the contact displacement constraints only approximately, it therefore allows for small amount of overlap to occur so that the contact force is proportional to the penetration. The contact characterization scheme is based on the geometry of overlap at the instant of interest. However, the information provided by the geometry of overlap is insufficient for judging the direction of the contact force and in turn gives rise to the indeterminacy of choosing contact edge to add contact spring. For example, in Figure 6.4, vertex *A* invaded into vertex *D* at the end of time interval but the overlap information is insufficient to obtain the proper entrance edge, from which the vertex *A* enters the target block.

In the DDA, a quasi vertex-vertex contact is finally degenerated into a vertex-edge contact during the open-close iteration in the framework of the penalty method. If two possible reference edges are passed by the corresponding vertex simultaneously, a penetration takes place, as shown in Figure 6.4c, where the normal penetration distances are d_1 and d_2, respectively. The choice of contact edge is controlled by the shortest path method, which picks the one with smaller penetration among two potential reference edges. If $d_1 < d_2$, the entrance edge is *DE* and the final vertex-edge contact is *A*-*DE*, then a contact spring is attached between vertex *A* and the projecting point A_1 on the reference edge. Otherwise, the entrance edge is *DF* and the contact spring is attached between *A* and A_2.

The physical meaning of the shortest path method is pushing the invaded vertex out of the block along the shortest path (Shi 1988). However, the shortest path method has two obvious shortcomings: (1) it cannot work when the initial state of a quasi vertex-vertex contact does not have penetration; (2) it cannot resolve the case when the penetration distances from both reference edges are equal to each other. Furthermore, the precision of the shortest path is sensitive to the choice of the penalty value and the time step size. For example, in Figure 6.5a, the left block is moving horizontally toward the right block. From the trajectory shown by a dash line on the left picture, it is easy to find the contact edge is the upper edge of right block. However, the shortest path method will take the bottom edge of right block as the contact edge since $d_2<d_1$, as shown in the Figure 6.5b. This case is possible when the stiffness of the contact spring is not big enough and the time step size is not proper.

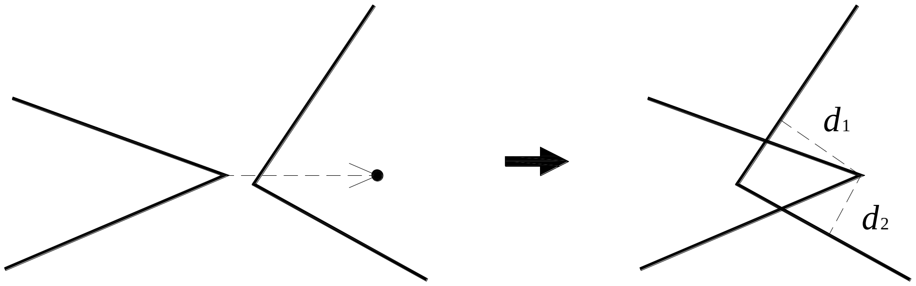

(a) at the beginning of interval (b) at the end of interval

Figure 6.5 a case where the shortest path method may select a wrong entrance edge

The vertex-vertex contact indeterminacy is a well-known problem and many other heuristic works have been proposed to solve it. Oden (Oden and Pires 1984) and Chaudhary (Chaudhary and Bathe 1986) used the minimum principle to select a unique trajectory for the vertex, but the method may fail when the possible scattered trajectories are indistinguishable by symmetry. Pandolfi (Pandolfi, Kane et al. 2002) and Kane (Kane, Repetto et al. 1999) provided the variational principle for selection of trajectories in problems where multiple trajectories of vertex are possible, but with the same limitation as the minimum principle. Feng and Owen (2004) used an energy-based normal contact model in which the normal and tangential directions, magnitude and reference contact position of the normal contact force are uniquely defined. Cundall (Cundall 2004) employed a corner rounding procedure so that blocks can smoothly slide past one another when two opposing corners interact. Krishnasamy and Jakiela (1995) provided a simple scheme to resolve the ambiguity of vertex-vertex contact in the penalty based model. Most of the above works have their own scheme dealing with the indeterminacy of vertex-vertex contact in the framework of specific contact interaction dealing method.

To overcome the limitations of the shortest path method, the original DDA code provides a simple scheme. For the quasi vertex-vertex contact without initial penetration at the beginning of time interval, the code specifies the initial entrance edge which is the steepest among the two potential reference edges. This scheme is proper in some cases but quite sensitive to the choice of stiffness of the contact spring and time interval size. Sometimes, the artificial choice of an entrance edge will affect the result of the analysis significantly. The original DDA code will not be able to deal with the case when two penetration distances from the potential reference edges are equal. To make the shortest path method employed in the DDA more precise and more applicable, an enhancement is provided in this chapter. More details about this enhancement are introduced in the following sections.

6.2 Solution to the Genuine Indeterminacy

When two blocks collide at the vertexes, the direction of the contact force is indeterminate because of the discontinuity of the normal vector at the vertex. Hence, a temporary contact spring between the two vertexes is necessary to reflect the contact interaction. The temporary contact spring will connect two vertexes and act as a hinge between them. The temporary contact spring will be removed right after the further motions are detected. If it is not removed after use, the temporary contact spring will arrest the degeneration of the vertex-vertex contact into the vertex-edge contact. Therefore, after obtaining the proper contact reference edge, it is necessary to remove the temporary springs according to the shortest path method and go on open-close iteration. This procedure will not affect the computational efficiency of the whole program because it is done in the normal open-close iteration.

Consider the motion of a vertex-vertex contact pair as shown in Figure 6.6, *vertex* P_1 on block A and *vertex* P_2 on block B, with a temporary contact spring attached between them. For clarity, the contact spring is not shown in the figure. At the end of the time interval, there will be relative displacements between points P_1 and P_2. The displacements of points P_1 and P_2, respectively, can be denoted in vector form as

$$\mathbf{d}_i = \begin{Bmatrix} u_i \\ v_i \end{Bmatrix} \qquad \mathbf{d}_j = \begin{Bmatrix} u_j \\ v_j \end{Bmatrix} \tag{6.1}$$

Then the relative displacements of P_1 with respect to P_2 is

$$\mathbf{u} = \mathbf{d}_i - \mathbf{d}_j \tag{6.2}$$

Assume that the direction vectors for the potential reference edge are $\mathbf{r}_1$ and $\mathbf{r}_2$, respectively, with origin at point P_2, the angle between $\mathbf{r}_1$ and $\mathbf{u}$ as θ_1 and the angle between $\mathbf{r}_2$ and $\mathbf{u}$ as θ_2, then

$$\sin\theta_1 = \frac{|\mathbf{r}_1 \times \mathbf{u}|}{|\mathbf{r}_1||\mathbf{u}|} \tag{6.3}$$

$$\sin\theta_2 = \frac{|\mathbf{r}_2 \times \mathbf{u}|}{|\mathbf{r}_2||\mathbf{u}|} \tag{6.4}$$

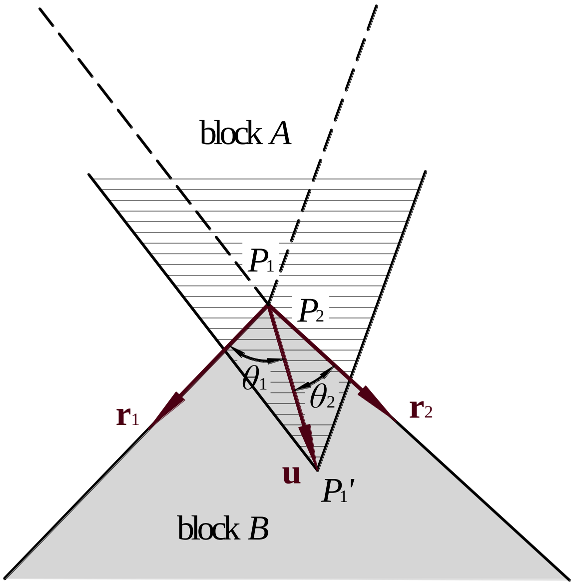

(a) two potential reference edge on the same block

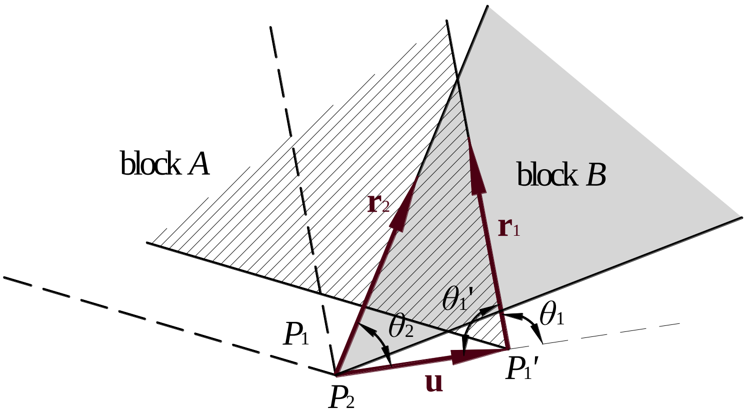

(b) two potential reference edge on different block

Figure 6.6 relationship between relative displacement vector and potential reference edge vectors

By comparing the value of $\sin\theta_1$ and $\sin\theta_2$, it is easy to find the proper reference edge onto which the vertex will slide when removing the vertex-vertex contact spring. If $\sin\theta_1 < \sin\theta_2$, the proper reference edge is **r**$_1$, otherwise it is **r**$_2$. If $\sin\theta_1 = \sin\theta_2$, the vertex-vertex contact will not degenerate into corresponding vertex-edge contact and the temporary vertex-vertex contact spring is kept in this step until the symmetry is destroyed in the following steps. Indeed, the above selection procedure is another form of the shortest path method because $|u|\sin\theta$ is the penetration distance.

The formulas for the contact are derived as follows. Assume the coordinates of the two vertexes in contact are $P_1(x_i, y_i)$ and $P_2(x_j, y_j)$, respectively. Assume the deformation of the contact spring along *x* direction and *y* direction are u_x and u_y, respectively. We have

$$\mathbf{u} = \begin{Bmatrix} u_x \\ u_y \end{Bmatrix} = \begin{Bmatrix} u_i - u_j \\ v_i - v_j \end{Bmatrix} = \mathbf{d}_i - \mathbf{d}_j \tag{6.5}$$

And assume the stiffness of the contact spring is *p*. Then the spring forces are

$$\mathbf{f} = p\mathbf{u} \tag{6.6}$$

The strain energy of the spring forces is

$$\Pi_s = \frac{1}{2}\mathbf{f}^{\mathrm{T}}\mathbf{u} = \frac{p}{2}\mathbf{u}^{\mathrm{T}}\mathbf{u} \tag{6.7}$$

substituting Eq.(6.5), we have

$$\begin{aligned} \Pi_s &= \frac{p}{2}\left(\mathbf{d}_i^{\mathrm{T}} - \mathbf{d}_j^{\mathrm{T}}\right)\left(\mathbf{d}_i - \mathbf{d}_j\right) \\ &= \frac{p}{2}\left(\mathbf{d}_i^{\mathrm{T}}\mathbf{d}_i - 2\mathbf{d}_i^{\mathrm{T}}\mathbf{d}_j + \mathbf{d}_j^{\mathrm{T}}\mathbf{d}_j\right) \end{aligned} \tag{6.8}$$

To minimize the strain energy Π_s the derivatives are computed, thus

$$\mathbf{k}_{ii} = \frac{\partial^2 \Pi_s}{\partial \mathbf{d}_i^2} = \begin{bmatrix} p & 0 \\ 0 & p \end{bmatrix} \tag{6.9}$$

$$\mathbf{k}_{ij} = \frac{\partial^2 \Pi_s}{\partial \mathbf{d}_i \partial \mathbf{d}_j} = \begin{bmatrix} -p & 0 \\ 0 & -p \end{bmatrix} \tag{6.10}$$

$$\mathbf{k}_{ji} = \frac{\partial^2 \Pi_s}{\partial \mathbf{d}_j \partial \mathbf{d}_i} = \begin{bmatrix} -p & 0 \\ 0 & -p \end{bmatrix} \tag{6.11}$$

$$\mathbf{k}_{jj} = \frac{\partial^2 \Pi_s}{\partial \mathbf{d}_j^2} = \begin{bmatrix} p & 0 \\ 0 & p \end{bmatrix} \tag{6.12}$$

here four 2×2 submatrices are obtained: $\mathbf{k}_{ii}, \mathbf{k}_{ij}, \mathbf{k}_{ji},$ and $\mathbf{k}_{jj}$, which are added to the corresponding position inside global stiffness matrix $\mathbf{K}$ according to the node index i and j.

6.3 Solution to the Pseudo Indeterminacy

For the pseudo indeterminacy, since the shortest path method is sensitive to the penalty parameter and the time step size, an alternative scheme is proposed here by considering the trajectories of vertexes during the time interval. For any vertex-vertex contact which does not have any penetration at the start of the current time interval, the new scheme can work out the proper entrance edge for it unless it falls into the genuine indeterminacy.

The new scheme is based on the fact that no block can jump to the final position from the start position. Hence, each vertex must have its own trajectory which must intersect with the boundary of the target block if the vertex invades into the target block. It is easy to find the proper entrance edge of this vertex from the intersection point. If the intersection point is also a vertex on the opposite block, this vertex-vertex indeterminacy falls into the genuine indeterminacy which can be resolved by the enhanced shortest path method provided in the previous section.

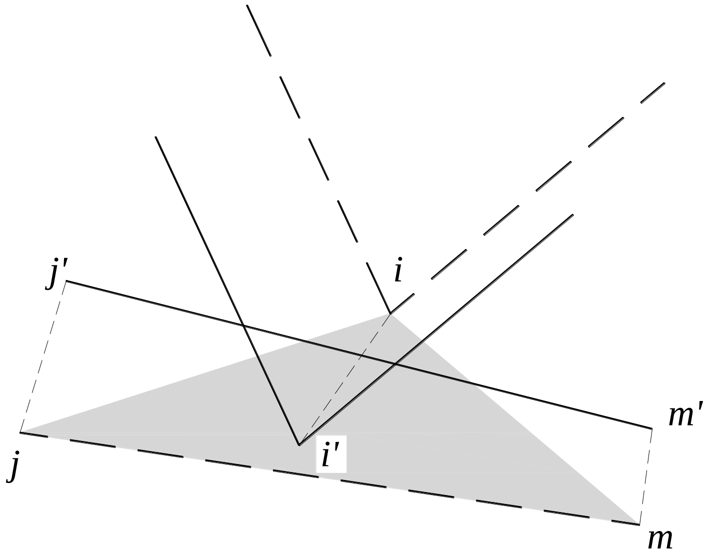

Figure 6.7 relationship of three points in a vertex-edge contact

Suppose we have a vertex-edge case shown in Figure 6.7. The positions of points *i*, *j*, and *m* are corresponding to the beginning of current time step, and the positions of points i', j' and m' are corresponding to the end of current time step. The coordinates of point *i*, *j*, and *m* are $P_i(x_i, y_i)$, $P_j(x_j, y_j)$, and $P_m(x_m, y_m)$, respectively. The displacement vectors of points *i*, *j*, and *m* of current time step are, respectively,

$$\mathbf{d}_i = \begin{Bmatrix} u_i \\ v_i \end{Bmatrix}$$

$$\mathbf{d}_j = \begin{Bmatrix} u_j \\ v_j \end{Bmatrix} \tag{6.13}$$

$$\mathbf{d}_m = \begin{Bmatrix} u_m \\ v_m \end{Bmatrix}$$

then the coordinates of points *i*, *j*, and *m*, at any time instant within current time step, can be written by a linear interpolation as follows:

$$\begin{aligned} x_i(t) &= \frac{u_i}{T} t + x_i \\ y_i(t) &= \frac{v_i}{T} t + y_i \end{aligned} \tag{6.14}$$

with the other coefficients obtained by a cyclic permutation of subscripts in the order *i*, *j*, *m*, And denote $\Delta(t)$ as the area of $\triangle ijm$ at time instant *t*, obtained by

$$\Delta(t) = \begin{vmatrix} 1 & x_i(t) & y_i(t) \\ 1 & x_j(t) & y_j(t) \\ 1 & x_m(t) & y_m(t) \end{vmatrix} = \begin{vmatrix} x_j(t) - x_i(t) & y_j(t) - y_i(t) \\ x_m(t) - x_i(t) & y_m(t) - y_i(t) \end{vmatrix} \tag{6.15}$$

substituting Eq.(6.14), we have

$$\Delta(t) = \begin{vmatrix} \frac{u_j}{T} t + x_j - \frac{u_i}{T} t - x_i & \frac{v_j}{T} t + y_j - \frac{v_i}{T} t - y_i \\ \frac{u_m}{T} t + x_m - \frac{u_i}{T} t - x_i & \frac{v_m}{T} t + y_m - \frac{v_i}{T} t - y_i \end{vmatrix}$$

$$= \begin{vmatrix} u_j - u_i & v_j - v_i \\ u_m - u_i & v_m - v_i \end{vmatrix} \frac{t^2}{T^2} + \begin{vmatrix} u_j - u_i & y_j - y_i \\ u_m - u_i & y_m - y_i \end{vmatrix} \frac{t}{T}$$

$$+ \begin{vmatrix} x_j - x_i & v_j - v_i \\ x_m - x_i & v_m - v_i \end{vmatrix} \frac{t}{T} + \begin{vmatrix} x_j - x_i & y_j - y_i \\ x_m - x_i & y_m - y_i \end{vmatrix}$$

$$\approx \begin{vmatrix} u_j - u_i & y_j - y_i \\ u_m - u_i & y_m - y_i \end{vmatrix} \frac{t}{T} + \begin{vmatrix} x_j - x_i & v_j - v_i \\ x_m - x_i & v_m - v_i \end{vmatrix} \frac{t}{T} + \begin{vmatrix} x_j - x_i & y_j - y_i \\ x_m - x_i & y_m - y_i \end{vmatrix}$$

which can be rewritten in a more concise form as

$$\Delta(t) = b\frac{t}{T} + c \tag{6.16}$$

in which

$$b = \begin{vmatrix} u_j - u_i & y_j - y_i \\ u_m - u_i & y_m - y_i \end{vmatrix} + \begin{vmatrix} x_j - x_i & v_j - v_i \\ x_m - x_i & v_m - v_i \end{vmatrix}$$

$$c = \begin{vmatrix} x_j - x_i & y_j - y_i \\ x_m - x_i & y_m - y_i \end{vmatrix}$$

At the time instant that *vertex i* contacts *edge jm*, we have

$$\Delta(t) = 0 \tag{6.17}$$

Solve Eq.(6.17) with respect to t, we will obtain the time instant when contact happens. Eq.(6.17) is solved for both potential reference edges. If the root of Eq.(6.17) is negative, it means that *vertex i* will not collide with *edge jm* in the current time step. Even if a nonnegative root is found for Eq.(6.17), it is not necessarily the right one because *vertex i* may drop on the extension line of segment *jm*. Further judgment is needed before we can obtain the proper one.

Assume the *vertex i* is colliding with *edge jm* at time instant t_1, and the coordinates of point *i*, *j*, and *m* at that instant are denoted as $P_i(x_i^1, y_i^1)$, $P_j(x_j^1, y_j^1)$, and $P_m(x_m^1, y_m^1)$, respectively. If the following inequality holds, the *vertex i* is colliding with *edge jm* and it is the proper reference edge for vertex-vertex contact. Otherwise, the reference edge must be the other potential reference edge.

$$\begin{cases} \left(x_i^1 - x_j^1\right)\left(x_i^1 - x_m^1\right) \le 0 \\ \left(y_i^1 - y_j^1\right)\left(y_i^1 - y_m^1\right) \le 0 \end{cases} \tag{6.18}$$

After obtaining the proper entrance edge, the vertex-vertex contact is transformed into a vertex-edge contact and the open-close iteration will continue.

6.4 Applications

6.4.1 Example 1

The block system consists of two blocks, as shown in Figure 6.8. The upper block is asymmetric while the lower block is symmetric. The lower block has two points fixed at both x and y directions. Under the action of gravity, the upper block will finally fall down along one side of the lower block. It is assumed that there is no friction between the interfaces of the two blocks.

The material properties for both blocks are as follows: mass density = 0.28 kg/m^3; Young's Modulus = 50000 Pa, Poisson's ratio = 0.25, gravity acceleration = 10 m/s^2. The maximum allowed displacement ratio is 0.01, and the maximum time increment for each time step is 0.03s. In addition, the stiffness of the normal contact spring is 5×10^5 N/m, which is 10 times of the Young's Modulus of the blocks.

Both blocks are at rest at the beginning. Since there is no friction between the interface and the gravity force on the upper block is vertical and downward, the interacting force at the corner-corner contact point should be vertical and upward. These two forces are not aligned vertically, which forms a moment for the upper block to rotate in the clockwise direction.

The results obtained by the revised DDA code are shown in Figure 6.9. It shows that the upper block will rotate in the clockwise direction because its gravity center is at the right side of the contact point. And the rotation tendency makes the vertex of the upper block moves to the left side of the corner of the lower block first.

For comparison purpose, the results from the original DDA code are also shown in Figure 6.10, where the upper block moves to the right side first and then rotates along the anticlockwise direction because the original DDA code chooses the right edge of the lower block as its initial contact reference edge which finally affected the motion of the upper block.

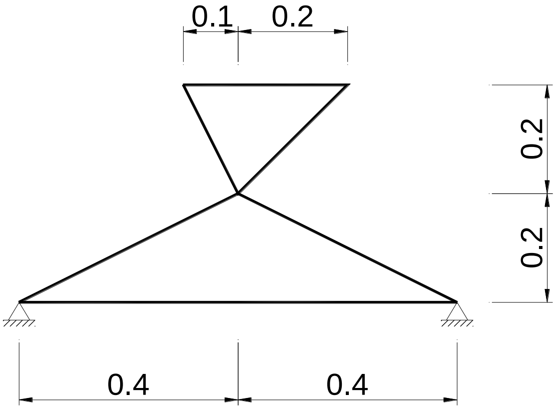

Figure 6.8 configuration of example 1 for calibration of the vertex-vertex contact (unit: m)

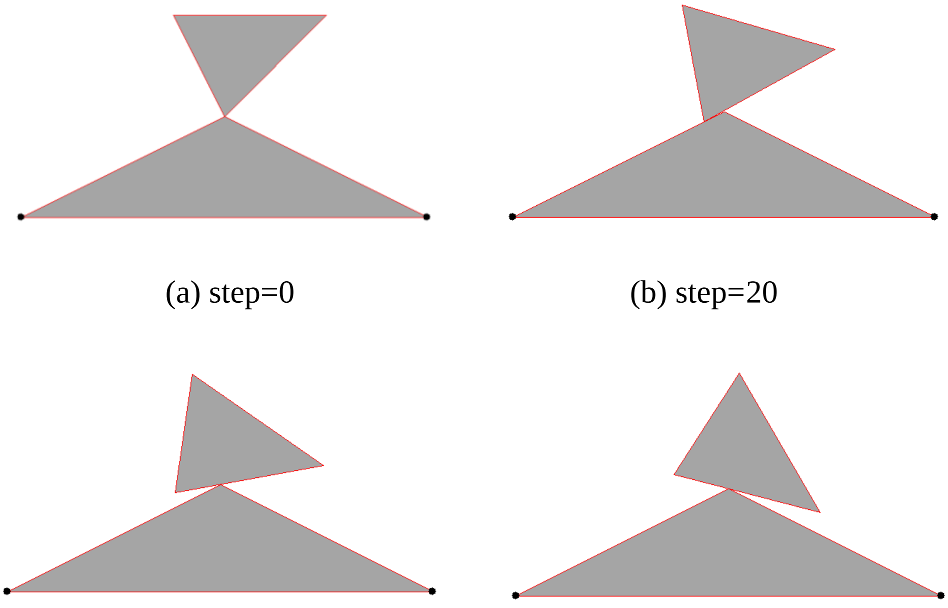
(a) step=0

(b) step=20

(c) step=40

(d) step=60

Figure 6.9 simulation results from revised DDA code

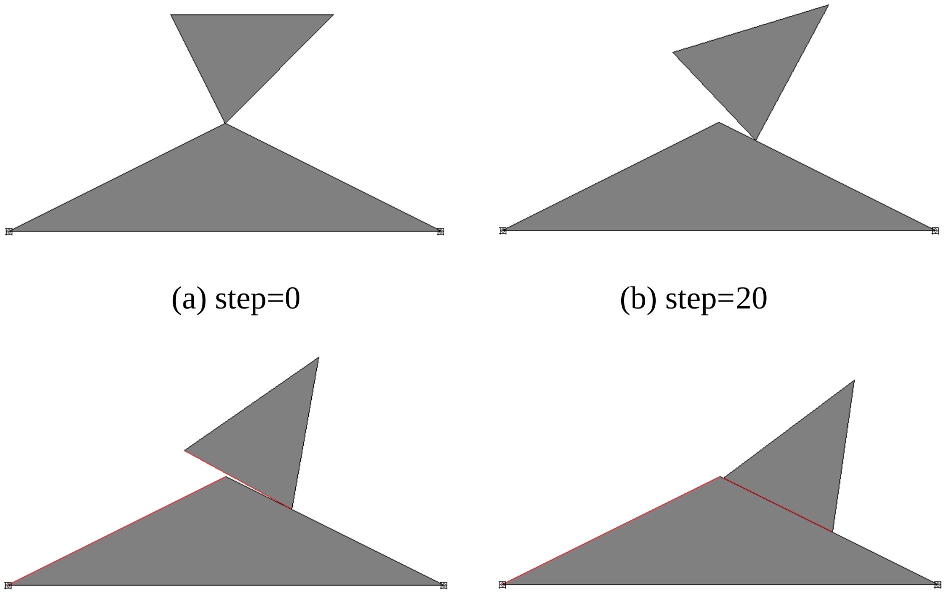

(a) step=0 (b) step=20

(c) step=40 (d) step=60

Figure 6.10 simulation results from original DDA code

6.4.2 Example 2

A two-block system under gravity is at rest at the beginning of analysis (see Figure 6.11). The bottom block is fixed by two points as shown in the figure. There will be a vertex-vertex contact between the bottom vertex of the upper block and the top vertex of the bottom block after the upper block starts to move. At the initial position, there is a small gap between them and the vertex of the upper block will land on the right edge of the bottom block after move.

The material properties for both blocks are as follows: mass density = 2.8×10^3 kg/m^3; Young's Modulus = 50MPa, Poisson's ratio = 0.25, body force is f_x = 0N and f_y = -2.8×10^4N. Friction angle and cohesion of joint material is zero. The allowed displacement ratio is 0.1, and the maximum time increment for each time step is 0.05s. It is assumed that there is no friction between the interfaces.

In the first test, the time step is set to 0.05s and the penalty value is 40 times the value of Young's Modulus. The results from the original DDA code are shown in Figure 6.12 and the results from the revised DDA code is shown in Figure 6.13. In the second test, the time step size is the same as it is in the first test but the penalty value is increased to 80*E*, both the original DDA code and the revised DDA code obtained the supposed results as shown in Figure 6.13. In the third test, the penalty value is fixed and the time step size is reduced to 0.025s, both codes obtained the supposed phenomenon as shown in Figure 6.14.

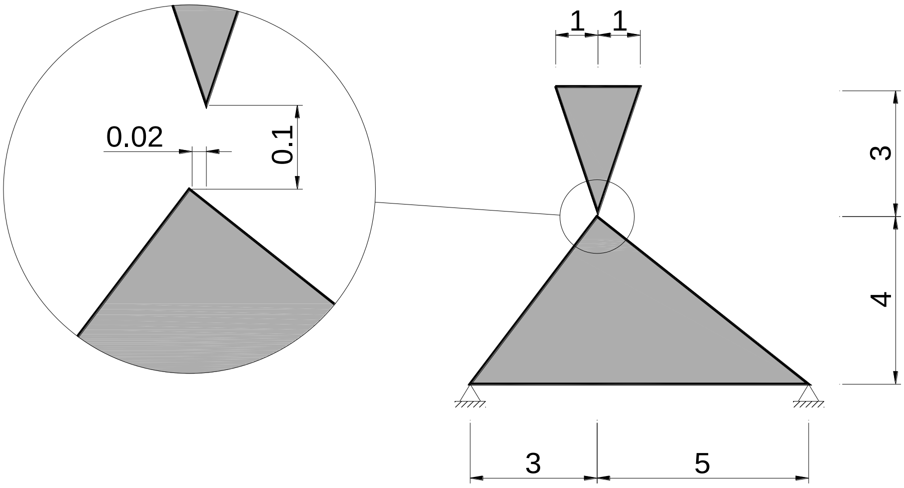

Figure 6.11 configuration of example 2 for calibration of the vertex-vertex contact (unit: m)

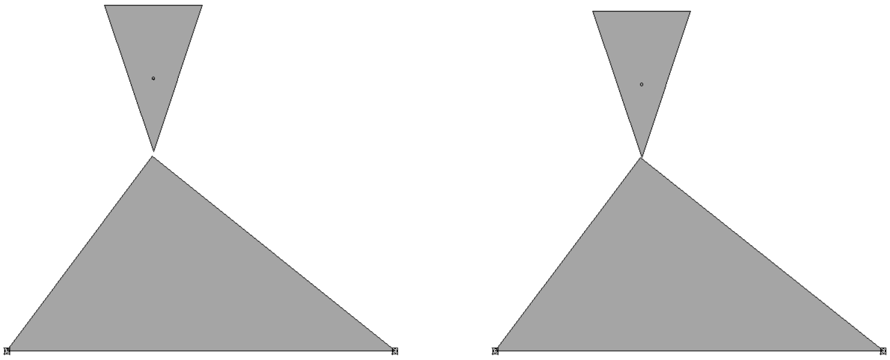
(a) step=0

(b) step=1

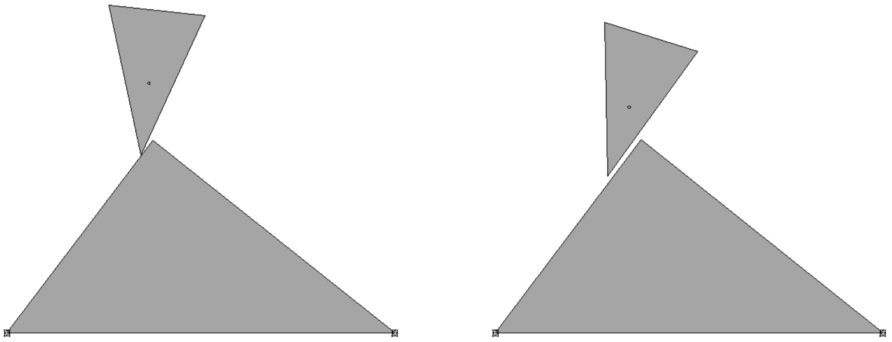

(c) step=2

(d) step=3

Figure 6.12 simulation results from original DDA code (p=40E, T=0.05s)

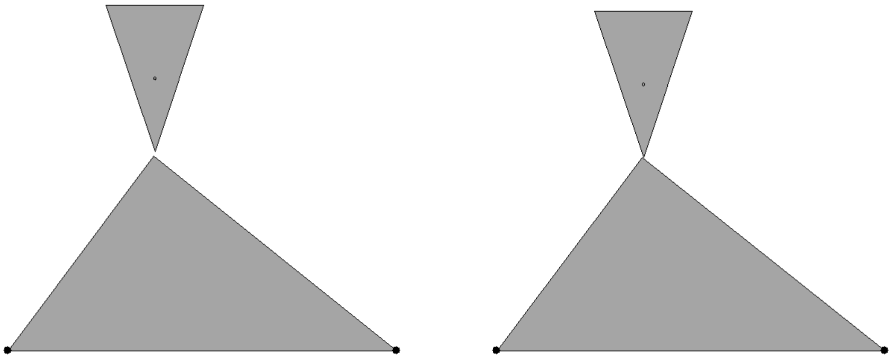

(a) step=0

(b) step=1

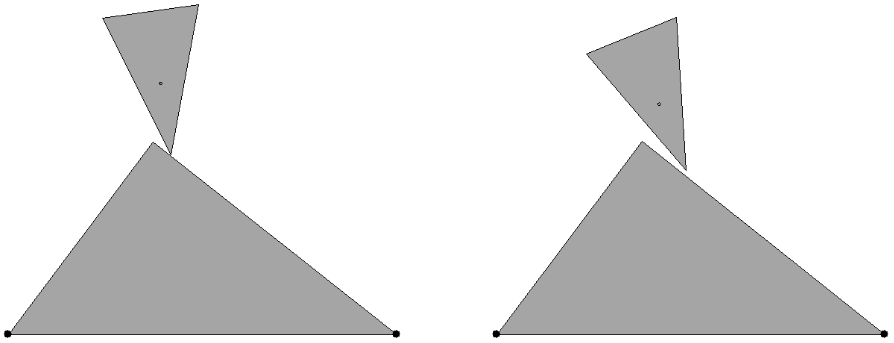

(c) step=2

(d) step=3

Figure 6.13 simulation results from revised DDA code (p=40E, T=0.05s)

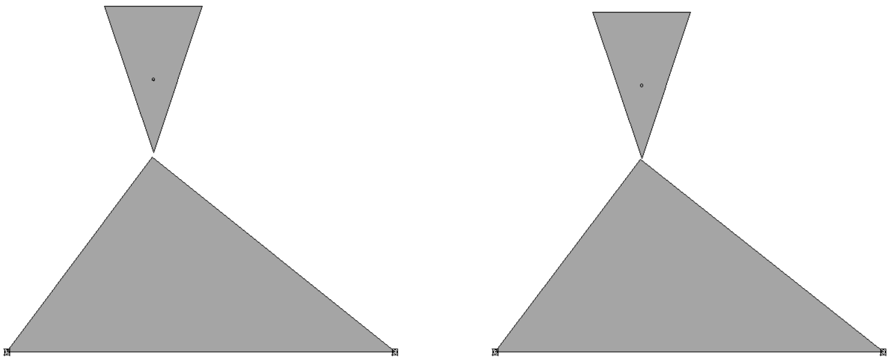

(a) step=0 (b) step=2

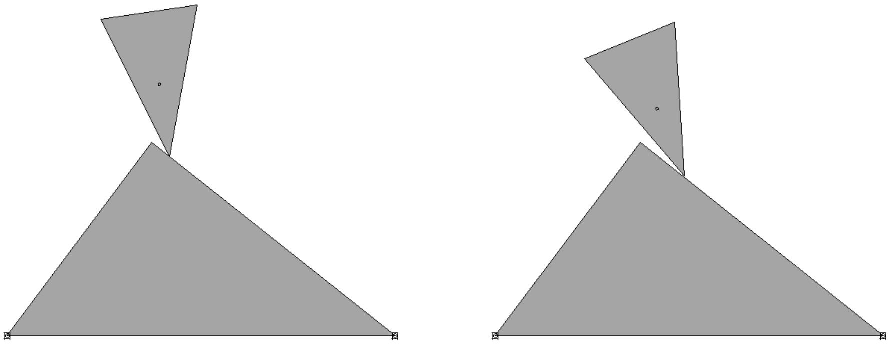

(c) step=4 (d) step=6

Figure 6.14 simulation results from original DDA code (*p*=40*E*, *T*=0.025s)

6.5 Summary

In this chapter, detailed discussion about the vertex-vertex indeterminacy is provided. Two types of indeterminacy are involved. For the first type of indeterminacy, also referred to as genuine indeterminacy in this work, an enhanced shortest path method is introduced. For the second type indeterminacy, also referred to as pseudo indeterminacy in this work, a simple scheme based on trajectory of vertexes is provided. Two examples showed that the improved algorithm can solve the vertex-vertex contact more precisely. The algorithm is applied in both the original DDA code and the newly developed 2D-NDDA code.

CHAPTER 7 APPLICATIONS OF THE NDDA

7.1 Introduction

The NDDA not only extends the deformation ability, but also the fracture ability of blocks, without losing any merit of the standard DDA. A new computer program called “2D-NDDA” is developed based on the formulations and method provided in the previous chapters. The program includes two main parts: MESH and ANALYSIS.

The first part, MESH, is a model generating code which enhances the corresponding part ‘DC’ of the original DDA code with a triangulation code. The triangulation algorithm is based on the Delaunay refinement algorithm provided in Chapter 4. In the mesh procedure, raw lines are cut into blocks first and then a triangulation mesh is generated in each block according to user’s specifications. The second part, ANALYSIS, is the analysis code which detects contacts, computes displacements and fractures blocks. The contact detection algorithm and kinematics of blocks are built into the original DDA code but with an enhancement of the vertex-vertex contact, based on the scheme proposed in Chapter 6. The crack criterion for block fracturing is based on the discussion in Chapter 5. The 2D-NDDA program is validated by several numerical examples in the following sections.

7.2 Modeling Wave Propagation in Continuous and Elastic Media

7.2.1 Theory of One-dimensional Compressional Waves in an Elastic Material

A brief introduction of the equations for one-dimensional compressional waves in an elastic material is provided in this section follows that of Bedford and Drumheller (1994). Figure 7.1a shows a half-space of material which is assumed to be unbounded to the right of the infinite plane boundary. A Cartesian coordinate system is oriented with the positive x_1 direction pointing into the material and the $x_2 x_3$ plane coincident with the boundary of the half-space.

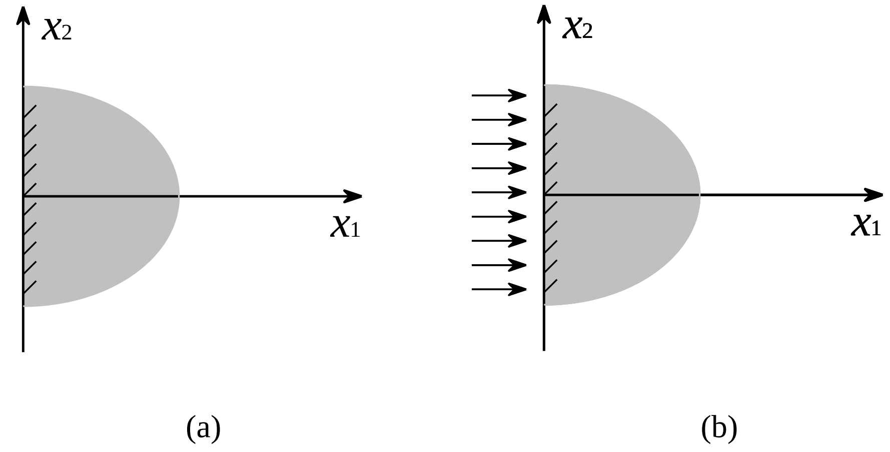

(a) (b)

Figure 7.1 (a) a half-space of material; (b) displacement boundary condition

The motion of the material is specified by its displacement field $\mathbf{u} = \mathbf{u}(\mathbf{x}, t)$. Suppose that the half-space of material is initially undisturbed, that is, $\mathbf{u}(\mathbf{x}, 0) = 0$, and the boundary is given a uniform displacement in the x_1 direction described by the equation

$$\mathbf{u}(0,t) = p(t) \tag{7.1}$$

where $p(t)$ is the displacement boundary condition which defined on $t \geq 0$ Figure 7.1b. The resulting motion of the material is described by the displacement field

$$\begin{aligned} u_1 &= u_1(x_1,t) \\ u_2 &= 0 \\ u_3 &= 0 \end{aligned} \tag{7.2}$$

Since the motion of the boundary in the x_1 direction is uniform – that is, it is the same at each point of the boundary – the resulting motion of the material cannot depend on x_2 or x_3, and the material has no motion in the x_2 or x_3 directions. Each point of the material moves only in the x_1 direction. This is a one-dimensional motion which depends on only one spatial dimension and the time.

For the one-dimensional motion described by Eq.(7.2), the displacement equation of motion is

$$\frac{\partial^2 u_1}{\partial t^2} = \alpha^2 \frac{\partial^2 u_1}{\partial x_1^2} \tag{7.3}$$

where the constant α is called the compressional, or P wave speed and defined by the following equation

$$\alpha = \sqrt{\frac{\lambda + 2\mu}{\rho_0}} \tag{7.4}$$

Where ρ_0 is density, λ and μ are called Lamé constant, and for an isotropic material, they can be given in terms of the Young’s modulus and Poisson’s ratio of the material by

$$\lambda = \frac{\nu E}{(1+\nu)(1-2\nu)}, \qquad \mu = \frac{E}{2(1+\nu)} \tag{7.5}$$

Consider the initial boundary condition described by Eq.(7.1). The solution of the one-dimensional motion described by Eq.(7.3) is

$$u_1(x_1,t)=\begin{cases} p(t-\dfrac{x_1}{\alpha}) & (t>\dfrac{x_1}{\alpha}) \\ 0 & (t\le\dfrac{x_1}{\alpha}) \end{cases} \tag{7.6}$$

If the boundary of the half-space is subjected to a normal-stress boundary condition

$$T_{11}(0,t)=\overline{p}(t) \tag{7.7}$$

where $\overline{p}(t)$ is a prescribed function of time that vanishes for $t\le 0$. The stress component T_{11} is related to the displacement field by

$$T_{11}=(\lambda+2\mu)\frac{\partial u_1}{\partial x_1} \tag{7.8}$$

so the boundary condition of Eq.(7.7) can be rewritten as

$$\frac{\partial u_1}{\partial x_1}(0,t)=\frac{\overline{p}(t)}{\lambda+2\mu} \tag{7.9}$$

And the solution of the one-dimensional wave described by Eq.(7.3) is

$$u_1(x_1,t)=\frac{\alpha}{\lambda+2\mu}\int_0^{t-x_1/\alpha}\overline{p}(\xi)d\xi \tag{7.10}$$

where ξ is an integration variable.

7.2.2 P-Wave Propagation in an Elastic Bar

An elastic rock bar is one meter long and 0.03 meter high as shown in Figure 7.2, with three measure points: node 343, node 679 and node 363. Node 343 is located at the start point of the bar, node 679 is located at the midpoint of the bar, and node 363 is located at a distance of 0.03m away from the end of the bar. The elastic bar is discretized by 1670 triangular elements and the enlarged mesh detail is shown in Figure 7.3. The material properties and analysis parameters are shown in Table 1.

Table 1 analysis parameters for the elastic bar

Rock sample	Density (kg/m^3)	2600
	Young's modulus (GPa)	50
	Poisson ratio	0.25
	Friction angle	30°
	Cohesion strength (MPa)	24
	Tensile strength (MPa)	18
Joint/crack	Friction angle	25°
	Cohesion strength (MPa)	0
	Tensile strength (MPa)	0
Control parameter	Penalty stiffness (GN/m)	500
	Time step size (s)	1×10^{-6}
	Max displacement ratio	0.1
	SOR factor	1.0
	Total analysis time (s)	0.0015

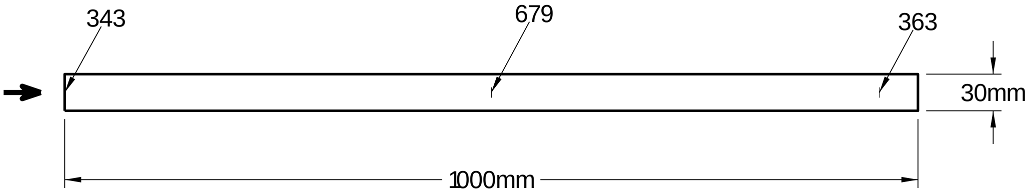

Figure 7.2 configuration of the elastic bar (unit: mm)

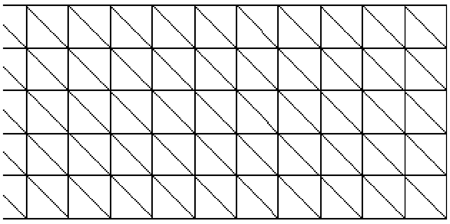

Figure 7.3 mesh details for the right end part of the elastic bar

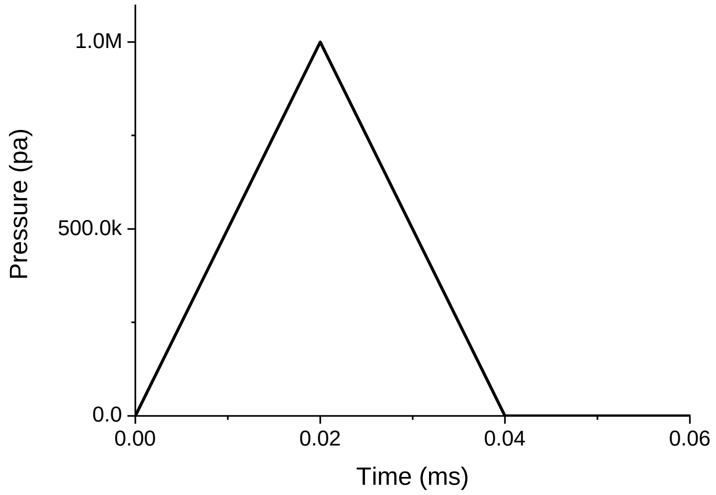

Figure 7.4 the incident P-wave pulse with peak value at 1Mpa

In this example, the P-wave pulse is generated by a pressure applied to the left boundary of the bar, and the right-hand boundary is considered as a free end. The time history of the P-wave pulse is shown in Figure 7.4 with a peak value at 1Mpa. The results obtained by the 2D-NDDA program are shown in Figure 7.5 where the dark moving area is the main part of the stress wave. At around 0.000133s, the stress wave peak reached the midpoint of the bar, see Figure 7.6b. The calculated P-wave velocity according to the wave peak is 4425m/s while the analytical value according to Eq.(7.4) is 4803m/s. The relative error is 7.9%. There is a problem when calculating the wave speed due to the precision of float variable in computer. It is found that there is no zero value in the data file and the displacement and stress at the measure points change smoothly at where they should have an obvious turning point according to the analytical solution, which can be seen from Figure 7.6. Therefore, it is difficult to obtain an exact time instant when the wave front arrives the midpoint of the bar. An alternative scheme employed here to calculate the wave speed is using the time that wave peak travels from the start point to the midpoint of the bar because the maximum displacement of the midpoint is determinable in the data file. However, the wave speed obtained by this approach will be smaller than the theoretical one.

Figure 7.5b shows an instant after the compressive stress wave reflected at the free end as a tensile stress wave and superposed with the original wave at that instant. The status of the stress wave is marked out by color in the 2D-NDDA: blue for compressive stress, red for tensile stress, and white for zero stress. The two-color scheme is employed only for a rough expression of the compressive and tensile state of the region, hence no color scale bar provided. Figure 7.5c shows that the peak of the reflected tensile stress wave peak reaches the midpoint at 0.000363s.

The time history of the horizontal particle velocity and *x*-direction normal stress at the midpoint is shown in Figure 7.6 comparing with the theoretical cure. The first peak value of the horizontal particle velocity at the midpoint appears at around 0.000133s while the theoretical value is 0.0001241s. The peak value is smaller than the theoretical value because of the numerical damping due to the time integration scheme employed by the NDDA as well as the DDA. The numerical damping phenomenon in the DDA is discussed in details by Ohnishi, Nishiyama et al. (2005). This attenuation can be viewed as a system error which should be avoided in the future work.

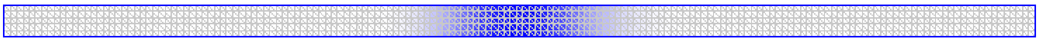

(a) step 133 (0.000133s)

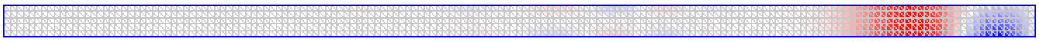

(b) step 248 (0.000248s)

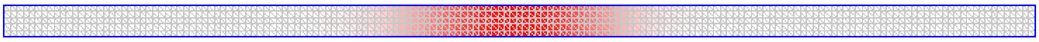

(c) step 363 (0.000363s)

Figure 7.5 simulation results from NDDA in the case of low impulse

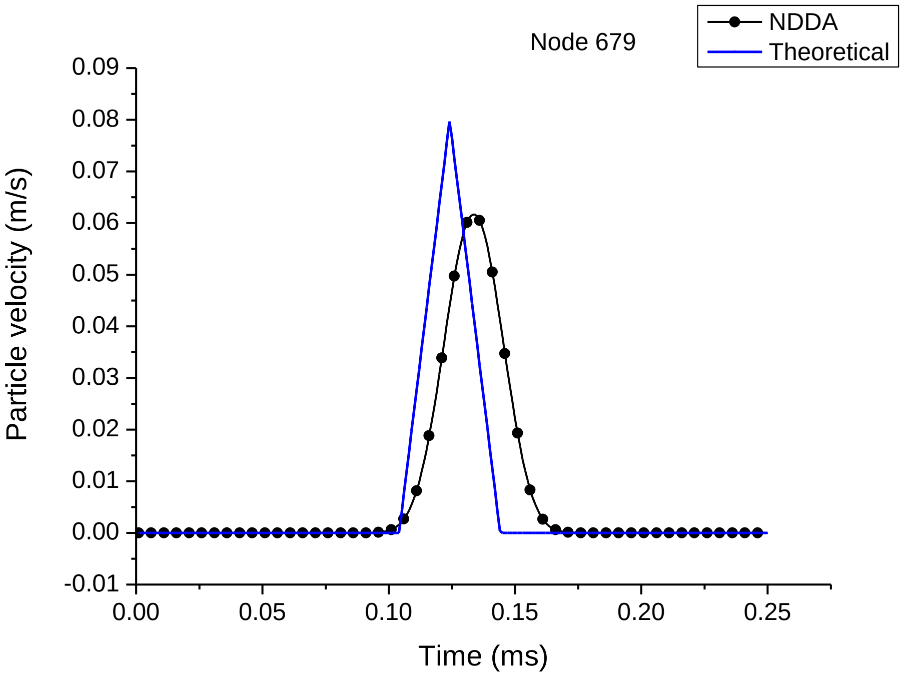

(a) particle velocity at midpoint

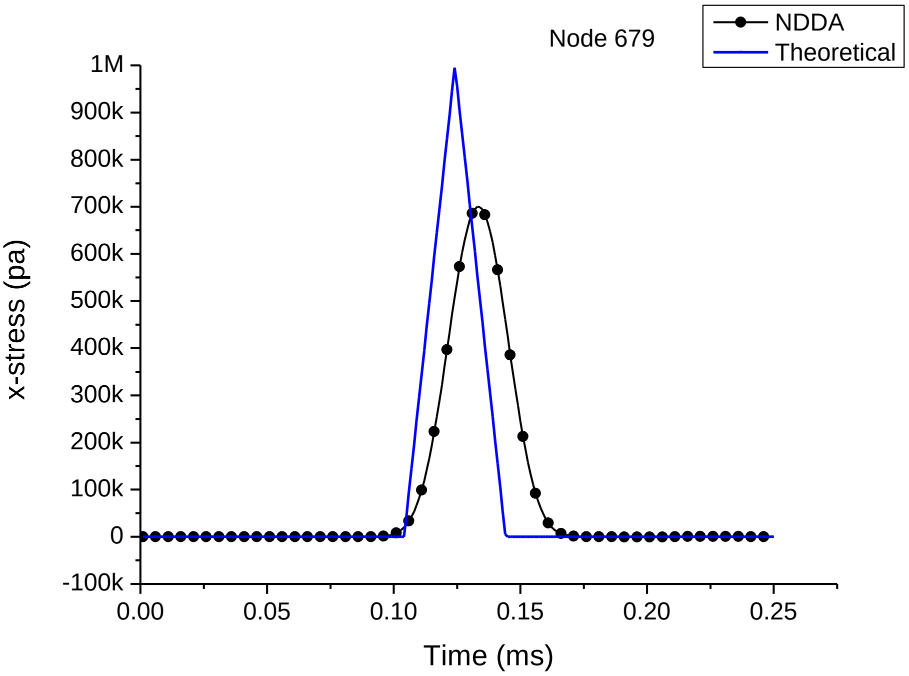

(b) *x*-direction normal stress at midpoint

Figure 7.6 NDDA results vs. theoretical results for one-dimensional wave propagation in an elastic bar

7.2.3 Modeling Spalling Phenomenon Due to P-wave Propagation

In this test, a higher impulse with the maximum value at 35MPa was applied (Figure 7.7). The analysis parameters are the same as in the previous example as shown in Table 1. Since the *x*-direction normal stress reflected at the free end of bar is a tensile stress and the peak value is higher than the tensile strength of the material, cracks will occur near the end. The spalling phenomenon is shown in the results obtained by the 2D-NDDA code (Figure 7.8). The first crack appeared at step 262 (time instant 256μs), and ran through the whole section of the bar rapidly which takes only 0.44μs. After that, the residual stress in the detached part will reduce to zero (Figure 7.9b) and the horizontal particle velocity will attenuate to a constant value (Figure 7.9a). The horizontal particle velocity and *x*-direction normal stress time histories at the midpoint of the bar are presented in Figure 7.10. Both the particle velocity and the *x*-direction normal stress curve exhibit attenuation due to the numerical damping effect (Ohnishi, Nishiyama et al. 2005).

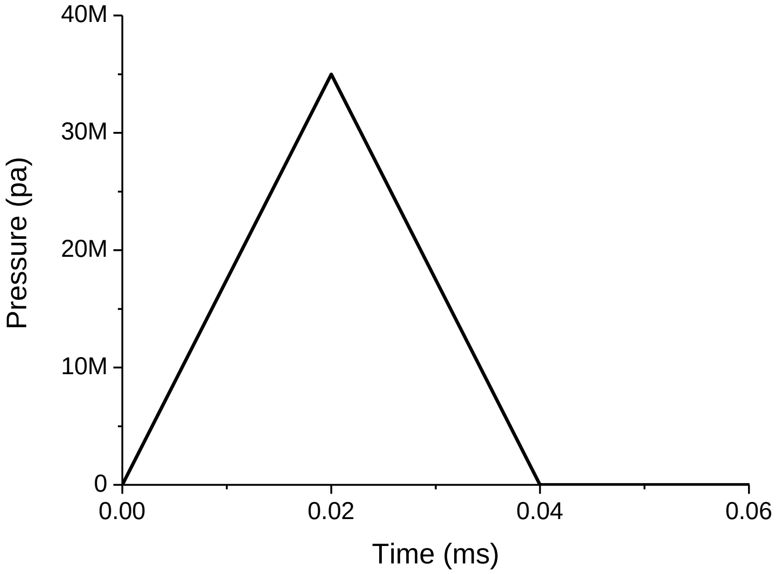

Figure 7.7 the incident P-wave pulse with peak value at 35Mpa

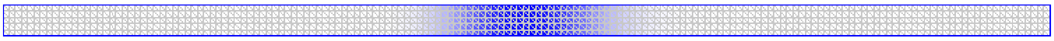

(a) step 134 (0.000134s)

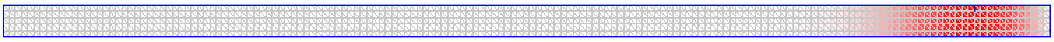

(b) step 262 (0.000262s)

(c) step 267 (0.00026244s)

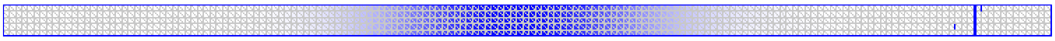

(d) step 1005 (0.001s)

Figure 7.8 simulation results from NDDA in the case of high impulse

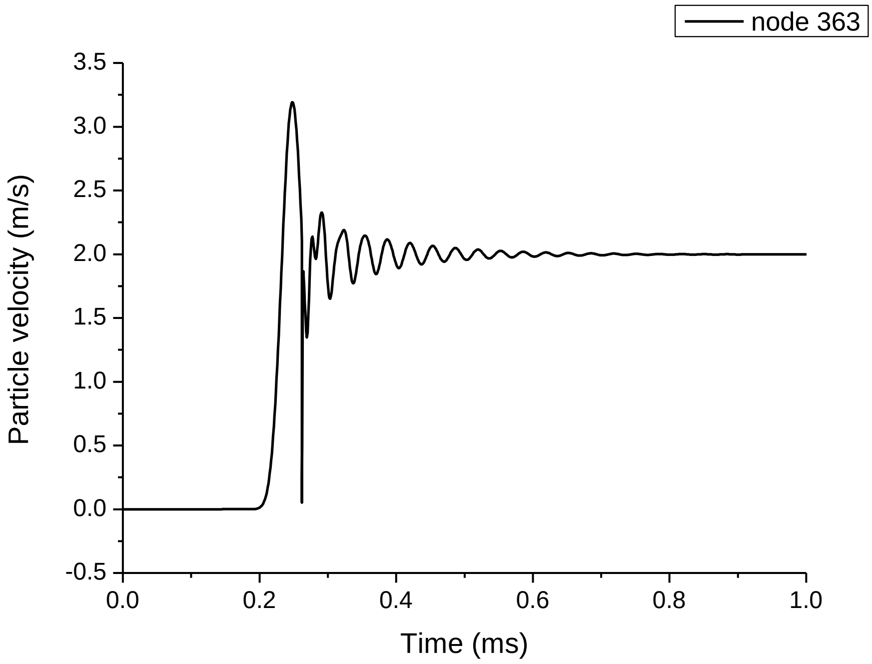

(a) particle velocity

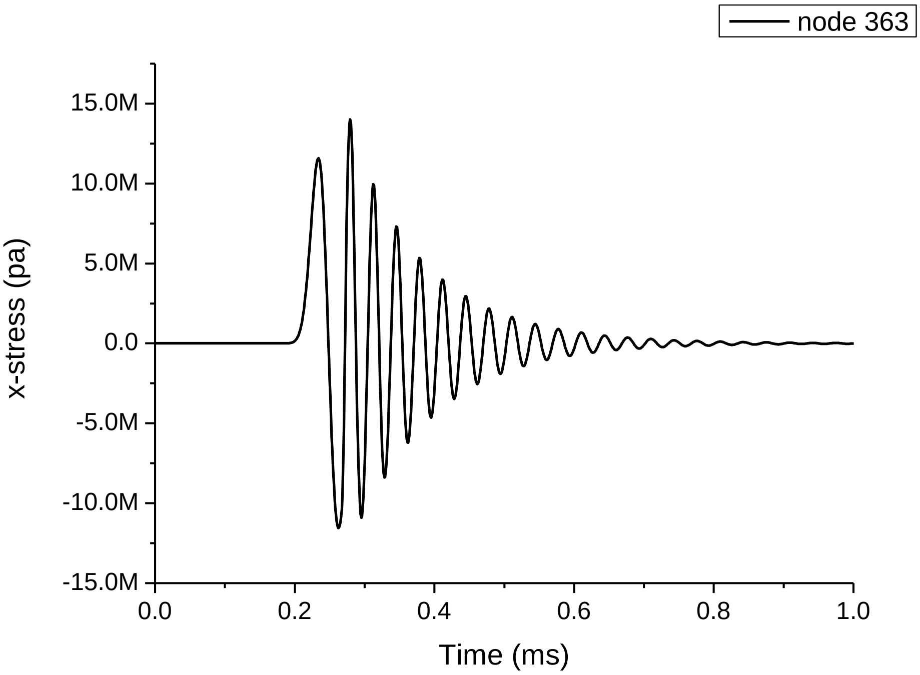

(b) *x*-direction normal stress

Figure 7.9 measured results from NDDA for node 363

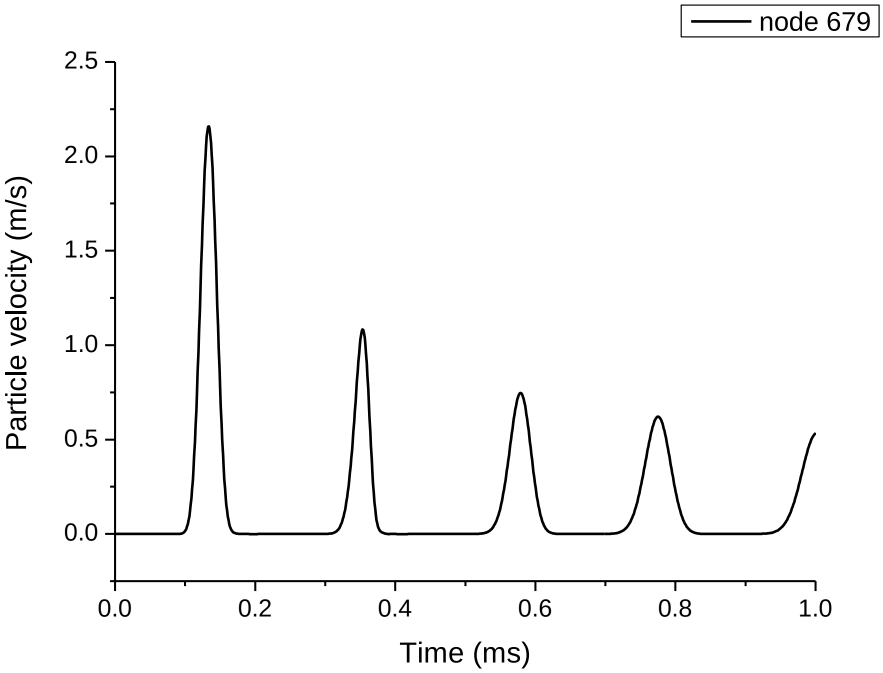

(a) particle velocity

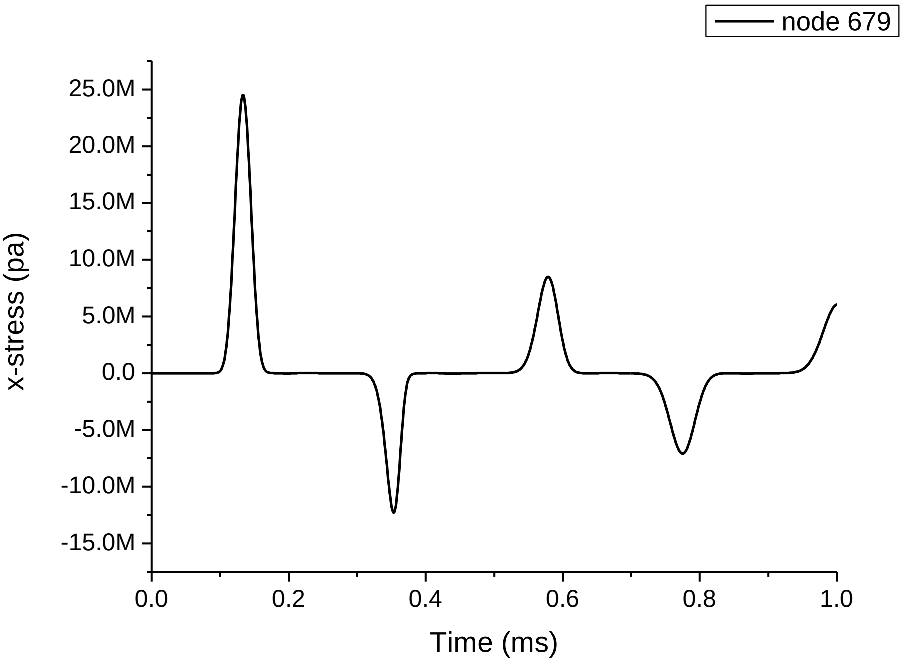

(b) *x*-direction normal stress

Figure 7.10 measured results from NDDA for the midpoint: node 679

7.3 Propagation of a Pre-existing Inclined Crack under Uniaxial Tension

7.3.1 Background theory

Consider a crack in a mixed-mode stress field governed by the values of the opening-mode K_I and sliding-mode K_{II} stress intensity factors (Figure 7.11). According to the maximum circumferential stress criterion (Gdoutos 2005), the crack extension angle θ_c is calculated by

$$K_I \sin\theta + K_{II}(3\cos\theta - 1) = 0 \tag{7.11}$$

Since the stress intensity factors K_I and K_{II} are given by

$$K_I = \sigma\sqrt{\pi a}\sin^2\beta \qquad K_{II} = \sigma\sqrt{\pi a}\sin\beta\cos\beta \tag{7.12}$$

Substituting into Eq.(7.11), then

$$\sin\theta + (3\cos\theta - 1)\,\mathrm{ctan}\,\beta = 0 \tag{7.13}$$

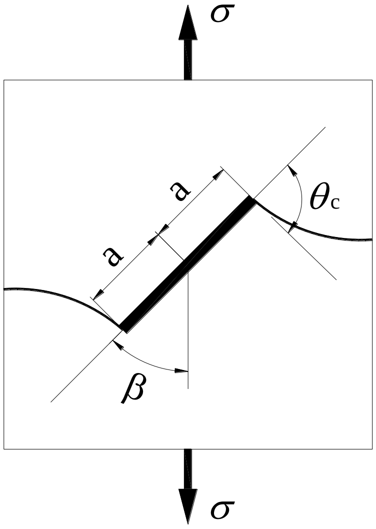

Figure 7.11 mixed-mode extension

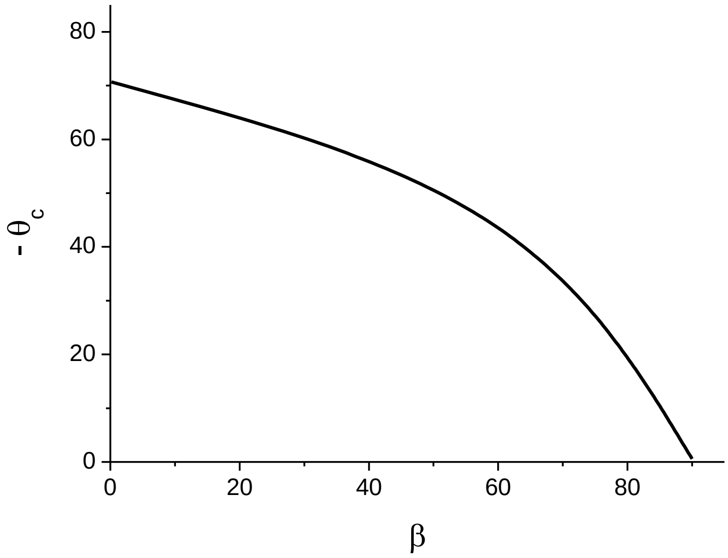

Figure 7.12 variation of the crack extension angle $-\theta_c$ versus the crack inclination angle β under plane stress condition for tensile applied loads (unit: degree)

7.3.2 Example

The specimen used in this numerical modelling is a square block with an edge length of 100 mm (see Figure 7.13). The test block has a 45° angle 42mm length initial crack through the center of it. The specimen is discretized by 1890 triangular elements. The block is loaded by boundary displacement with a speed at 0.4m/s as shown in Figure 7.14. The bottom boundary is fixed and the upper boundary is fixed in *y* direction only. The black thick arrow marks the support displacement direction. The material studied here is a typical rock material with the properties shown in Table 2.

Table 2 analysis parameters for the uniaxial tension

Rock sample	Density (kg/m^3)	2600
	Young's modulus (GPa)	10
	Poisson ratio	0.25
	Friction angle	25°
	Cohesion strength (MPa)	20
	Tensile strength (MPa)	10
Joint/crack	Friction angle	20°
	Cohesion strength (MPa)	0
	Tensile strength (MPa)	0
Control parameter	Penalty stiffness (GN/m)	200
	Time step size (s)	1×10^{-5}
	Max displacement ratio	0.01
	SOR factor	1.0
	Total analysis time (s)	0.01

The results from the numerical simulation are shown in Figure 7.15. In the first time step, the elements near the upper and bottom boundary of the specimen ran quickly into tensile stress than the middle elements which are far from the boundary. The tensile stress is marked by red color in Figure 7.15a, the darker the higher stress for that element. After a while of loading, two wing cracks start to appear at the ends of the initial crack and the highest tensile stress occurs around the crack tip area. In the crack tip area, opposite to the tensile region is a compressive region on the other side of the crack. The compressive stress is marked by blue color and the darker the higher stress value. The wing cracks are formed by many small cracks instead of a single crack. The explanation to this phenomenon lies mainly in the shape of the elements: triangular, which cannot guarantee smooth stress distribution. With loading increase, the wing cracks propagate rapidly toward the free surface of the specimen until the specimen is separated into two parts, and the stresses inside both parts reduce rapidly to zero level, see Figure 7.15d. The crack extension angle measured from the results is 60 ° which is the angle of the mesh in that region, while the calculated angle from Eq.(7.13) is 53.2 °. The final crack path is near normal to the load direction which is agree with the analytical prediction.

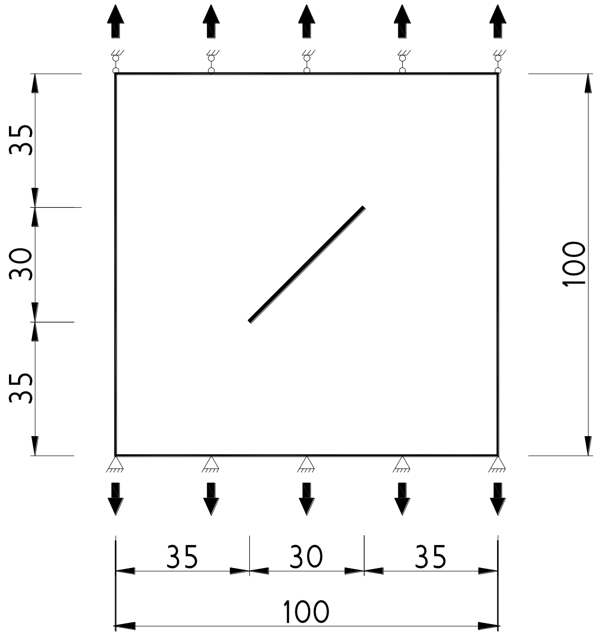

Figure 7.13 configuration of the specimen for single crack under uniaxial tension (unit: mm)

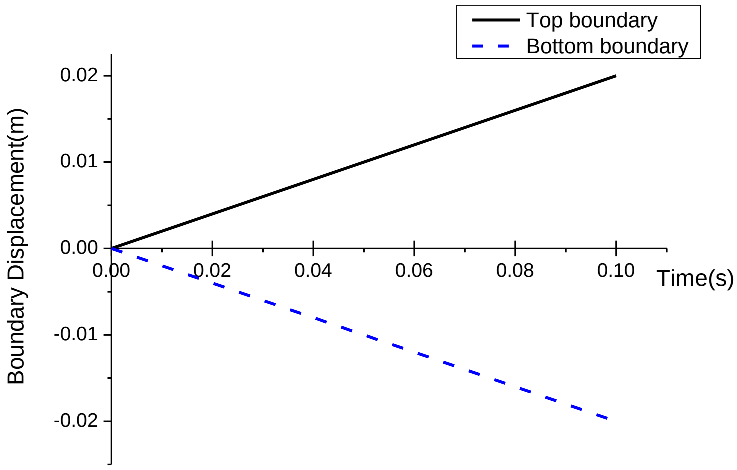

Figure 7.14 boundary displacement time history

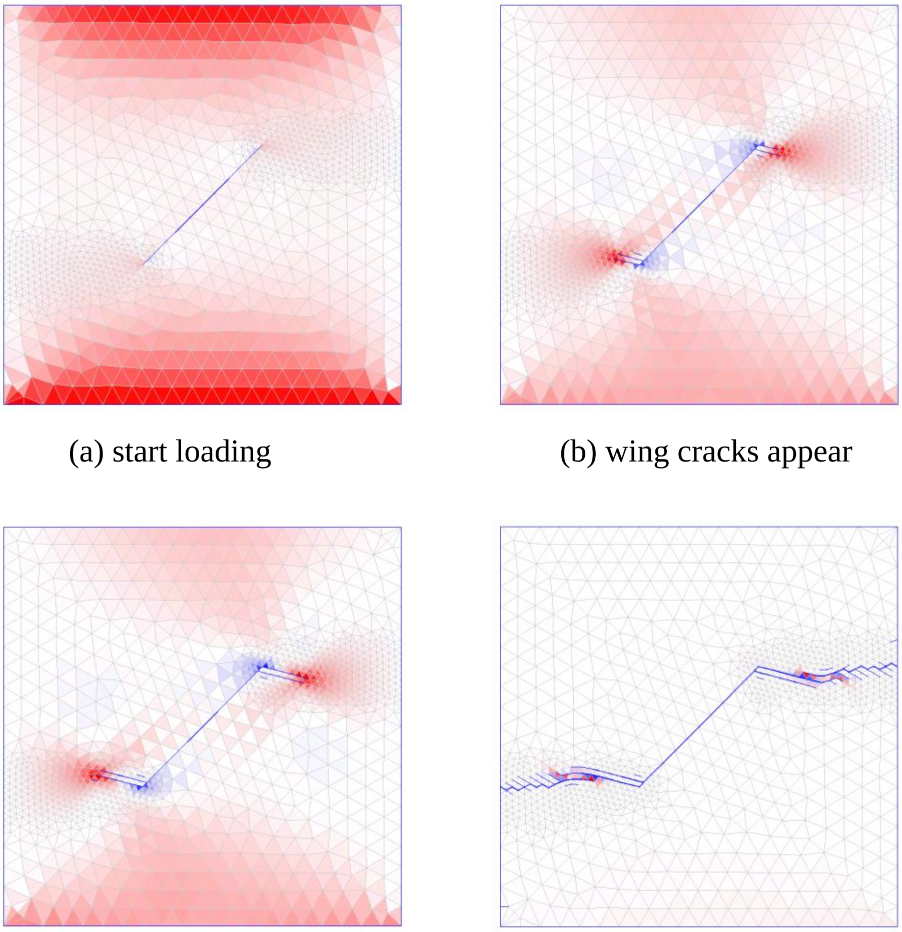

(a) start loading

(b) wing cracks appear

(c) crack propagation

(d) final failure

Figure 7.15 simulation results from the NDDA for single crack under uniaxial tension

7.4 Propagation of Pre-existing Cracks under Uniaxial Compression

7.4.1 Background

The two-dimensional sliding wing crack model is a typical model for brittle fracture in compression. It was initially proposed by Brace and Bombolakis (1963), and later quantified analytically, as well as confirmed experimentally, by other researchers (Hoek and Bieniaws.Zt 1965; Bieniawski 1967; Ingraffea and Heuze 1980; Nemat-Nasser and Horii 1982; Horii and Nemat-Nasser 1985). For a pre-existing crack subject to shear and normal stresses derived from the overall far-field compression, once the relative sliding of the two crack faces occurs, local tensile stresses at the crack tips produce two tensile “wing cracks” (Figure 7.16). The orientation of incremental crack extension is the one which maximizes the Mode I stress intensity factor K_I at the extended crack tips (Nemat-Nasser and Horii 1982). The equilibrium length of incremental extension is then obtained by assigning a critical value to K_I. The model shows that the tensile wing cracks grow with increasing axial load, curving toward the direction of the dominant axial compression, which was observed in early experimental works (Brace and Bombolakis 1963; Hoek and Bieniaws.Zt 1965; Fairhurs and Cook 1966).

There is a quite obvious difference between cracks subjected to pure tensile stresses and those subjected to uniaxial compression. In tension, the crack extension force (or tensile stress concentration) increases with crack length, accelerating the crack forward. In compression, the crack extension force decreases after initial propagation, so the crack reaches a stable position. If the axial compression is accompanied by any amount of lateral tension, the crack growth becomes unstable after a certain crack length is attained, resulting in axial splitting. However, if some lateral compression accompanies the axial load, the tensile cracks grow to a certain length and then stop. Thus, some researchers draw the conclusion that, under compression, a macroscopic fault cannot develop from a single, pre-existing crack, but must be a result of the coalescence of crack branches, grain boundaries and pores (Brace and Bombolakis 1963; Hoek and Bieniaws.Zt 1965).

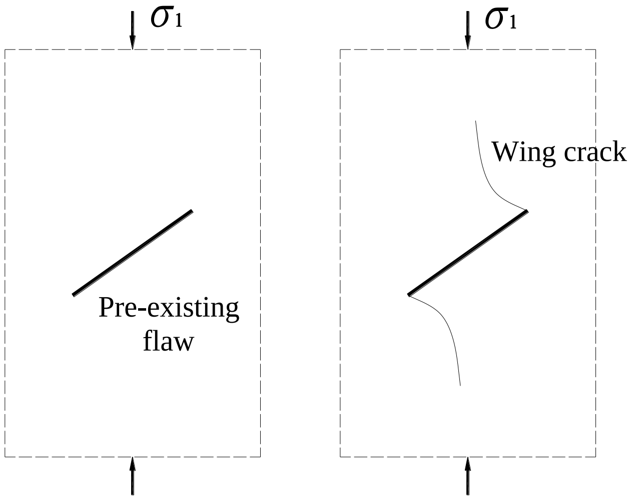

Figure 7.16 schematic illustration of the development of tensile wing cracks under uniaxial compression

The formation of both microcracks and macrocracks in rocks has received considerable attention since the fracture for rocks subjected to compressive stresses is not the result of a single "Griffith crack" (Kranz 1979). The crack-crack interaction in brittle fracture has attracted the attention of many investigators during the past decades (Brace and Bombolakis 1963; Hoek and Bieniaws.Zt 1965; Lange 1968; Lajtai 1971; Nesetova and Lajtai 1973; Swain and Hagan 1978; Kranz 1979; Ashby and Hallam 1986; Baud and Reuschle 1997). However, contrary to expectations, some of the experimental observations do not show an obvious coalescence of primary cracks (Brace and Bombolakis 1963; Ingraffea and Heuze 1980), see Figure 7.17 and Figure 7.19. Objective to the coalescence hypothesize, Ingraffea and Heuze (1980) state that "*vertical splitting typical in the failure of uniaxially loaded rock specimens is the result of unstable, secondary crack* *propagation, rather than of coalescence of stable primary cracks.*”

Two qualitative examples are provided in this section to show the capability of the NDDA for modeling brittle fracture under uniaxial compression condition. Although the material parameters employed in the examples are from rock, the results can hardly say agree well with the experimental observation from real rock material but agree well with the PMMA experiments as shown in Figure 7.18 and Figure 7.19. The reason may lie in that in the numerical model no flaw existing as well as the real rock.

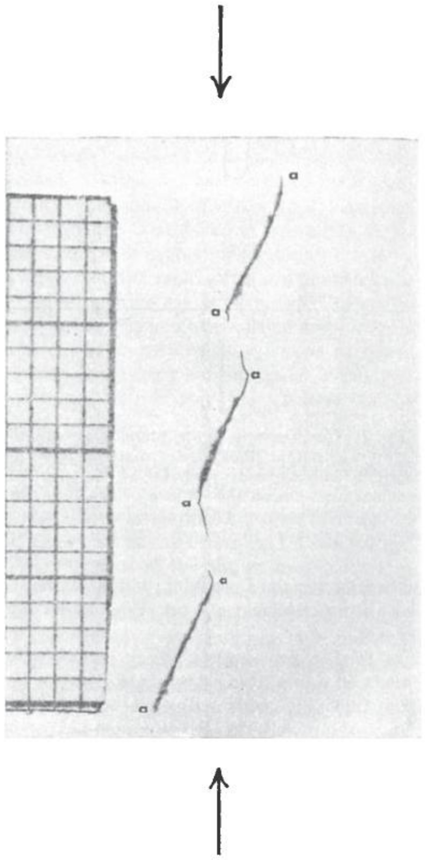

Figure 7.17 fracture response of an array of cracks in glass: there was no tendency for the cracks to run together or for neighboring branch fracture to ‘attract’ one another. (Brace and Bombolakis 1963)

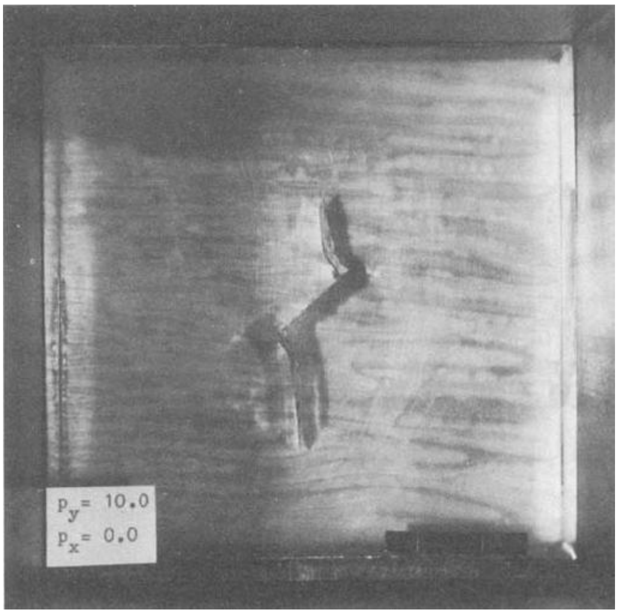

Figure 7.18 fracture response of an inclined notch in a PMMA plate: stable primary crack propagation without plate rupture. (Ingraffea and Heuze 1980)

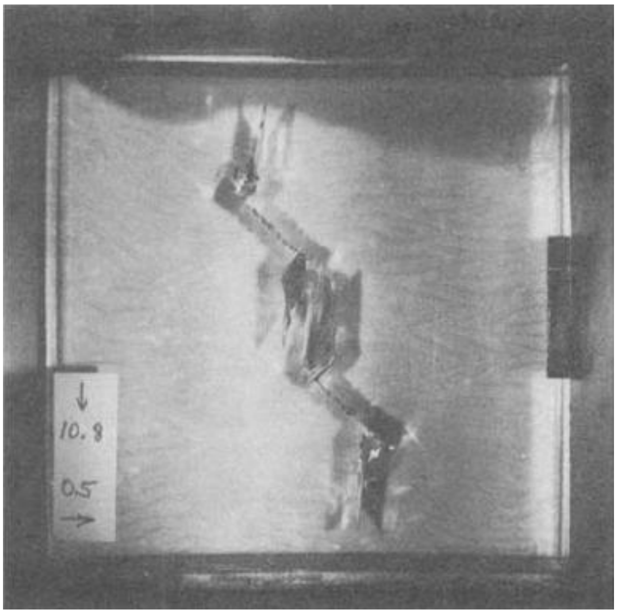

Figure 7.19 fracture response on an en echelon array of notches in a PMMA plate: stable primary crack propagation. Although interaction effect is evident, cracks do not coalesce, and plate does not rupture. (Ingraffea and Heuze 1980)

7.4.2 Single inclined crack

The specimen used in this numerical modelling is a rectangular block with dimensions 200 mm high and 100mm wide (see Figure 7.21) and was discretized by 2568 triangular elements. The test block had a 45° angle flaw through the center of it. The block material properties are shown in Table 3. The uniaxial compression was applied by boundary displacement at an imposed velocity of 0.4m/s as shown in Figure 7.20. The results from the numerical test are shown in Figure 7.22.

Table 3 analysis parameters for the uniaxial compression

Rock sample	Density (kg/m^3)	2600
	Young's modulus (GPa)	10
	Poisson ratio	0.25
	Friction angle	25°
	Cohesion strength (MPa)	20
	Tensile strength (MPa)	10
Joint/crack	Friction angle	20°
	Cohesion strength (MPa)	0
	Tensile strength (MPa)	0
Control parameter	Penalty stiffness (GN/m)	200
	Time step size (s)	1×10^{-5}
	Max displacement ratio	0.01
	SOR factor	1.0
	Total analysis time (s)	0.01

At the beginning of loading, the elements near the upper and bottom support area enter a compressive stress state faster and higher than the elements far from the boundary. A two-color scheme is employed to show the compressive and tensile region in the specimen: blue for compressive stress, red for tensile stress. The wing cracks appear first in the vertical direction at the tip of the initial crack. There exist two different regions, compressive and tensile regions, beside the initial crack near the tip area, as well as that in the tensile simulation. The crack propagates with the increment of the loading and curve toward the direction of the compression, which is agree with the experimental observation (Figure 7.18). The stress-strain relationship of the specimen is plotted in Figure 7.23.

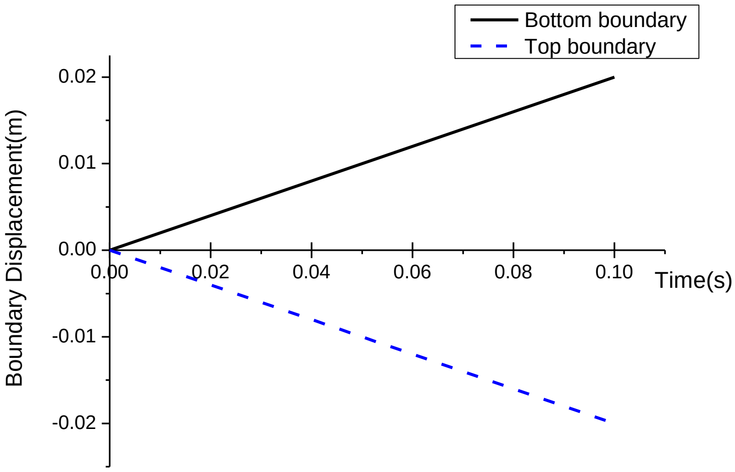

Figure 7.20 boundary displacement time history

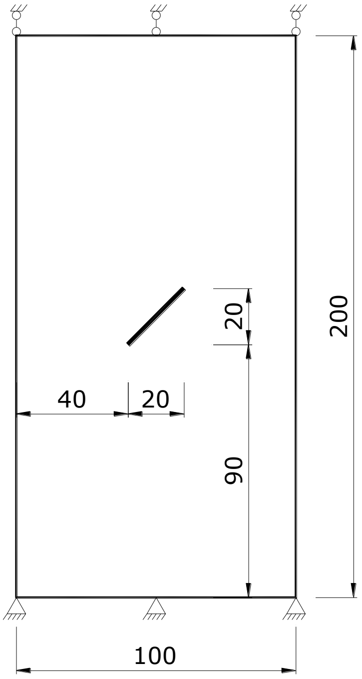

Figure 7.21 configuration of the specimen for single crack under uniaxial compression (unit: mm)

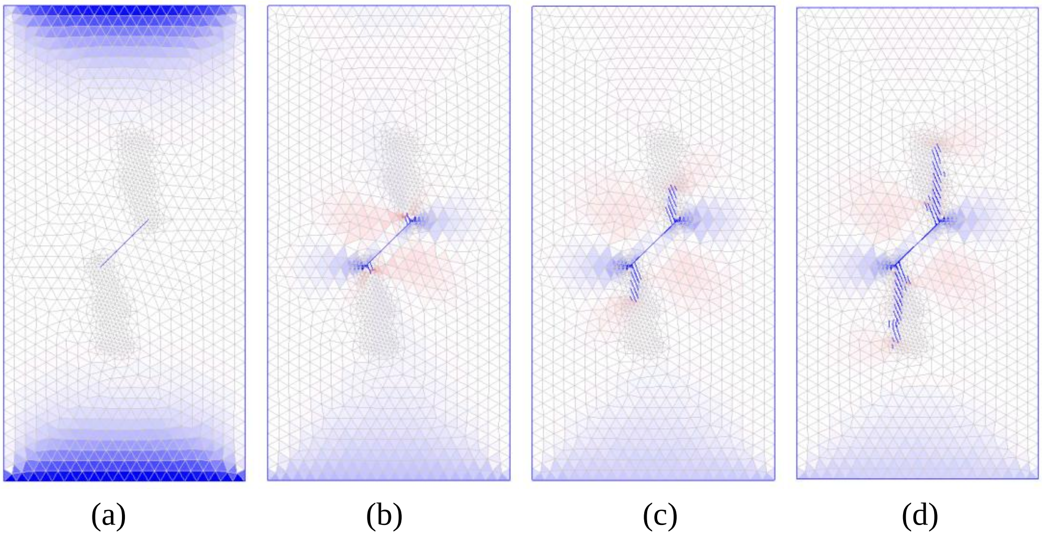

Figure 7.22 simulation results from the NDDA for single crack under uniaxial compression: (a) at the beginning of test; (b) wing cracks appear; (c) crack propagation; (d) at the end of test

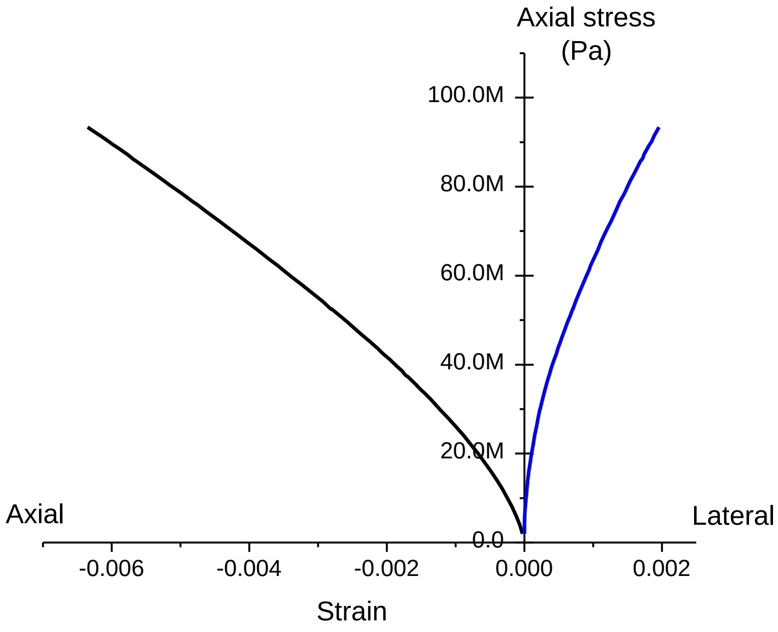

Figure 7.23 Stress-strain diagram of the single pre-existing crack specimen

7.4.3 Double inclined cracks

A model with the same geometry as the previous example but with two initial flaws is employed in the simulation (see Figure 7.24). The block material properties are shown in Table 4, and loaded by boundary displacement at a constant velocity of 0.4m/s. The simulation results are shown in Figure 7.25.

There are total 2388 triangular elements inside the block. The mesh is refined near the initial crack area so that the crack propagation can occur with a higher accuracy. Two initial cracks are designed in a position so that they can interact with each other when extension. Each crack is around 28mm length and in 45° angle to the direction of the compression.

At the beginning of the loading, the phenomenon is similar to the case with one initial crack test, and then wing cracks appear near the tips of the two existing cracks. After a while, the crack tips of the nearing side (near the other initial crack) gain a higher propagation speed and two wing cracks finally linked together (Figure 7.25c). After that, two wing cracks keep on extension as if no interact between them and finally form a crack region between two pre-existing cracks. The simulation result is similar to the experimental observation shown in Figure 7.19. This numerical simulation is only a qualitative test to show the capability of applying the NDDA to the numerical simulation of the brittle fracture of rock kind materials. Although the proper crack model was caught in the simulation, more research work is necessary to be done to reveal the interaction between multi cracks in numerical modelling.

Table 4 analysis parameters for the double-crack uniaxial compression

Rock sample	Density (kg/m^3)	2600
	Young’s modulus (GPa)	10
	Poisson ratio	0.25
	Friction angle	25°
	Cohesion strength (MPa)	20
	Tensile strength (MPa)	10
Joint/crack	Friction angle	20°
	Cohesion strength (MPa)	0
	Tensile strength (MPa)	0
Control parameter	Penalty stiffness (GN/m)	200
	Time step size (s)	1×10^{-5}
	Max displacement ratio	0.01
	SOR factor	1.0
	Total analysis time (s)	0.01

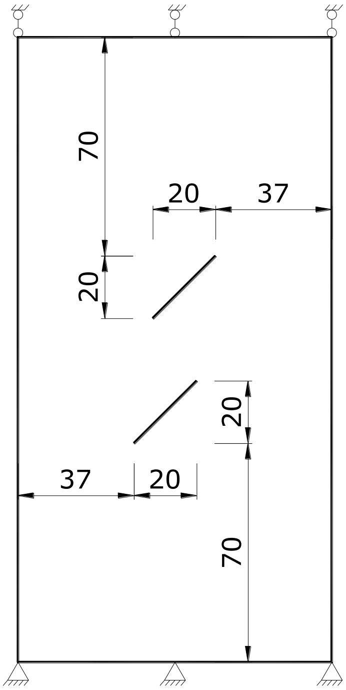

Figure 7.24 configuration of the specimen for multi crack under uniaxial compression (unit: mm)

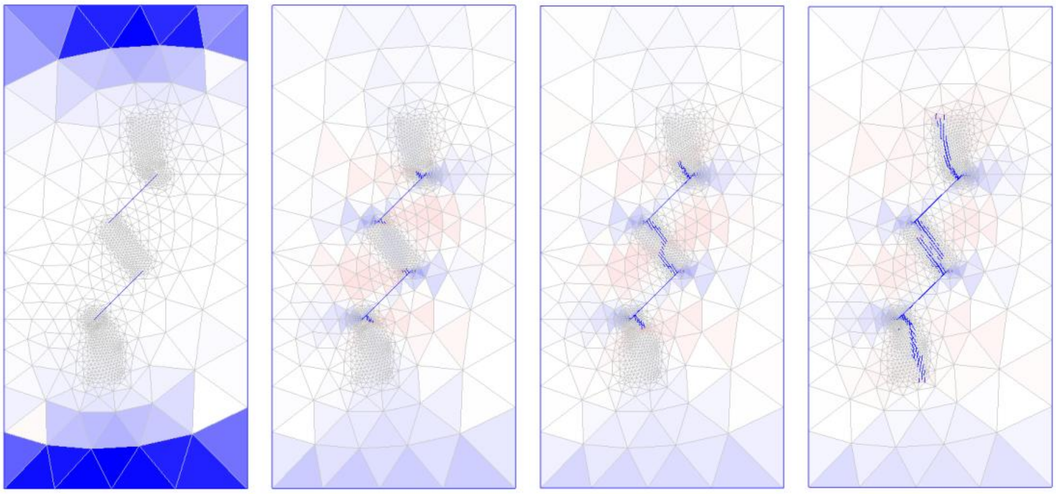
(a) (b) (c) (d)

Figure 7.25 simulation results from NDDA for the two-crack specimen under uniaxial compression: (a) at the beginning of test; (b) wing cracks appear; (c) crack propagation; (d) at the end of test

7.5 Modeling Brazilian Test

7.5.1 Background

The Brazilian test is used as a standardized test method to determine the tensile strength of brittle materials such as rock and concrete. A cylindrical specimen is compressed along two diametrically opposed generators so that a nearly uniform tensile stress normal to the diameter is induced in the loading plane. To prevent local failure in compression at the loading generators, two thin strips, usually made of plywood are placed between the loading platens and the specimen to distribute the load (Figure 7.26). The induced tensile stress state causes the specimen to fail by splitting. The maximum value of the tensile stress, compute at failure from the theory of elasticity, is the splitting tensile strength.

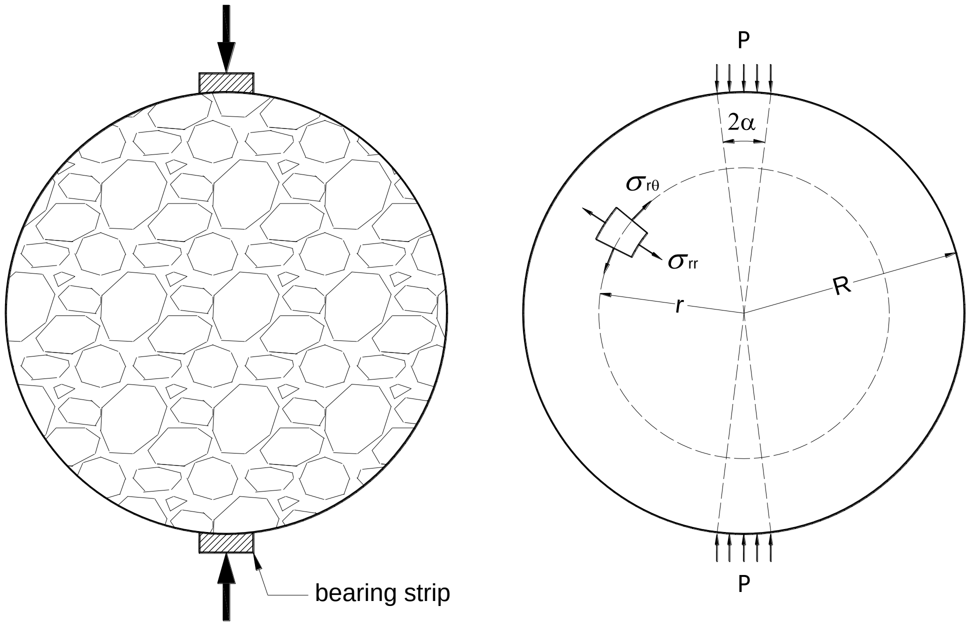

Figure 7.26 schematization of the Brazilian Test

In the case of concentrated loads, the maximum tensile stress is at the center and can be calculated by (Fairhurst 1964):

$$\sigma_{\max,P} = \frac{2P}{\pi D t} \tag{7.14}$$

Eq.(7.14) is the same as that given by point loads P applied at the ends of the diameter according the theory of elasticity (Timoshenko and Goodier 1969).

7.5.2 Intact Brazilian disk under diametrical load

A series of tests on the Brazilian disc of rock materials are executed to validate the capability of the NDDA to model crack initiation and propagation in brittle materials. Assume the test material is a continuous, isotropic and homogeneous elastic body. The diameter of the disc is 50 mm. The dimension for the rectangular loading plate is 50×10 mm. The thickness of disc and rigid plate are 25 mm, namely the thickness-to-diameter (t/D) ratio is 0.5. The configuration of the numerical experiment is shown in Figure 7.27. The material properties are shown in Table 5. The tests are divided into two groups: one with normal mesh and the other with a local refined mesh. A normal mesh is employed by test I while a local refined mesh is used in test II.

In test I, Two measure points are placed: P1 is at the center of the disc and P2 is at the midpoint of the upper vertical radius (see Figure 7.28a). The compression is applied by a boundary displacement at a constant velocity of 0.2 m/s. The simulation results provided by the NDDA are shown in Figure 7.28. The first crack initiates at around 0.0022s then propagates toward the contact point with rigid plate very quickly. The simulation results are seen to agree with the experimental observation in laboratory (Figure 7.29). The horizontal stress time histories of both measure points are shown in Figure 7.30, in which, the stresses of both points rise linearly until first crack occurs at around 0.0023s. After that, both stress-time curves drop quickly to a zero level. At point P1, the maximum horizontal stress is around 12 MPa, which agrees well with the tensile strength of the block material. However, stress-time curve of P2 has a sudden rise during crack propagation, then dropping down to zero level. From the curve, it is found that the maximum stress obtained at point P2 is a bit higher than the tensile strength of material. The reason for this phenomenon may due to the stress redistribution after first crack occurred in the disc and point P2 is at a crack tip which has stress intensity.

In test II, the compression is applied by a loading boundary instead of the displacement boundary employed in test I. The load is applied on the top of the upper plate at 10GPa/s while the lower plate fixed. The mesh zone around the vertical diameter of the disc is local refined (Figure 7.31a). A measure point is placed at the center of the disc. The simulation results are shown in Figure 7.31 and the horizontal stress-time curve of the center is drawn in Figure 7.32 accompanied by the theoretical curve based on Eq.(7.14). It is obvious that test II provides a more precise failure zone than that in test I because of a refined mesh.

Table 5 analysis parameters for the intact Brazilian disc test

Rock sample	Density (kg/m^3)	2600
	Young’s modulus (GPa)	10
	Poisson ratio	0.25
	Friction angle	25°
	Cohesion strength (MPa)	25
	Tensile strength (MPa)	12
Rigid plate	Density (kg/m^3)	7800
	Young’s modulus (GPa)	2000
	Poisson ratio	0.25
	Friction angle	25°
	Cohesion strength (MPa)	2500
	Tensile strength (MPa)	2500
Joint/crack	Friction angle	20°
	Cohesion strength (MPa)	0
	Tensile strength (MPa)	0
Control parameter	Penalty stiffness (GN/m)	4000
	Time step size (s)	1×10^{-5}
	Max displacement ratio	0.01
	SOR factor	1.0
	Total analysis time (s)	0.003

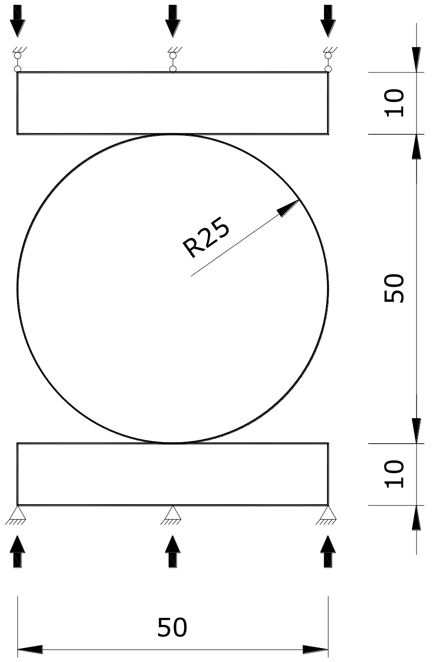

Figure 7.27 configuration of the disc for Brazilian test (unit: mm)

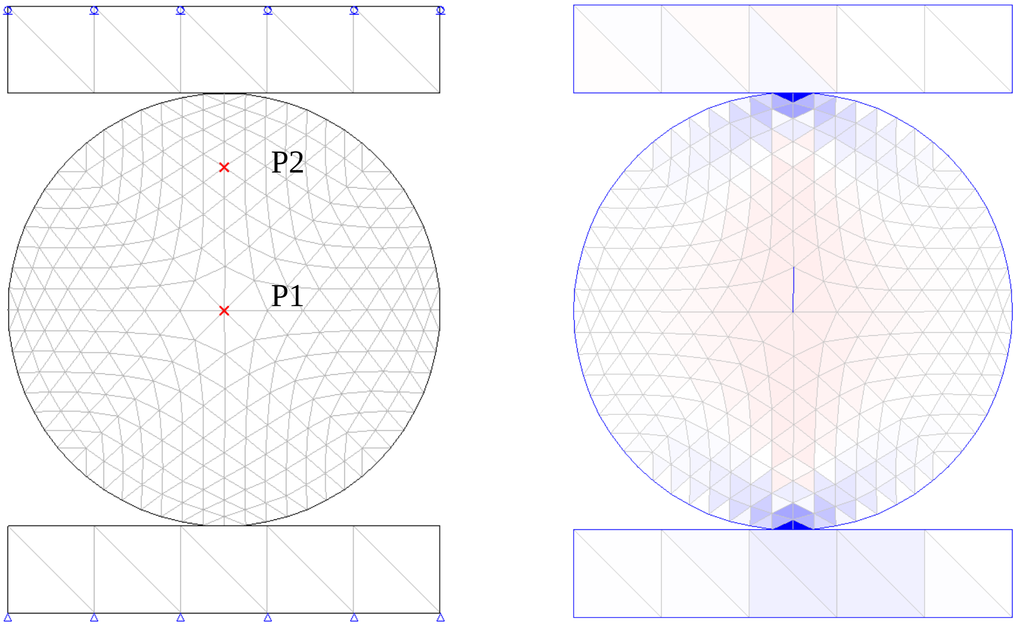

(a) NDDA model

(b) first crack appear at2.3ms

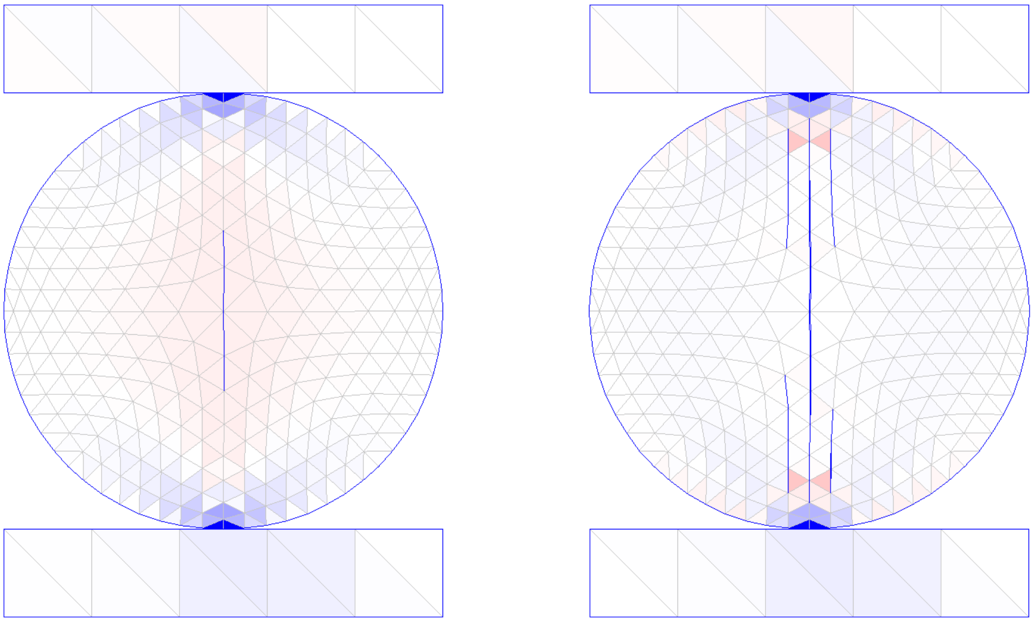

(c) crack propagation at 2.306ms

(d) after failure

Figure 7.28 simulation results from NDDA for the model with normal mesh (3 blocks, 532 elements)

Figure 7.29 the specimen used in experimental Brazilian test after failure (Yu, Zhang et al. 2009)

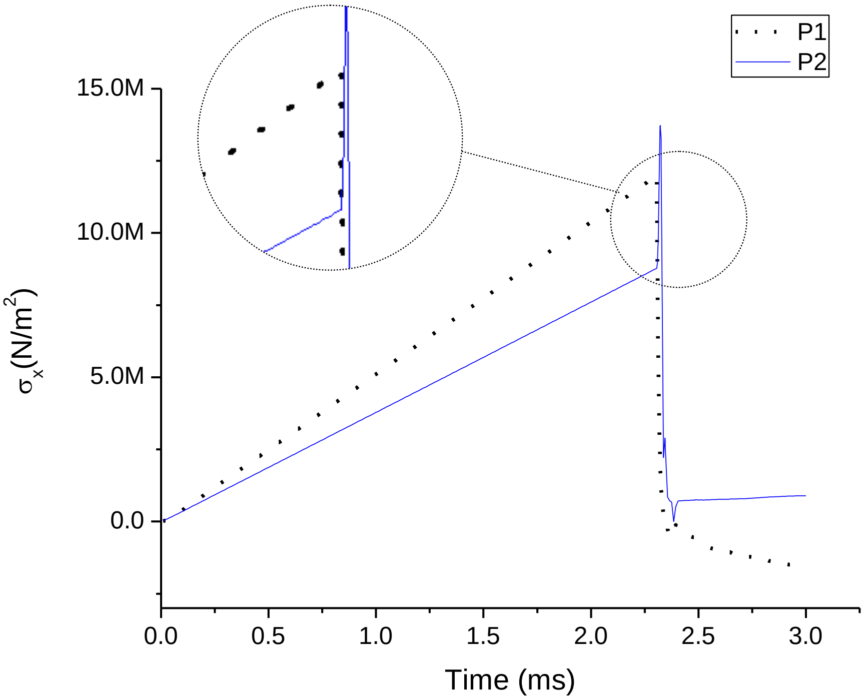

Figure 7.30 *x* direction stress time histories of measure point P1 and P2 in test I

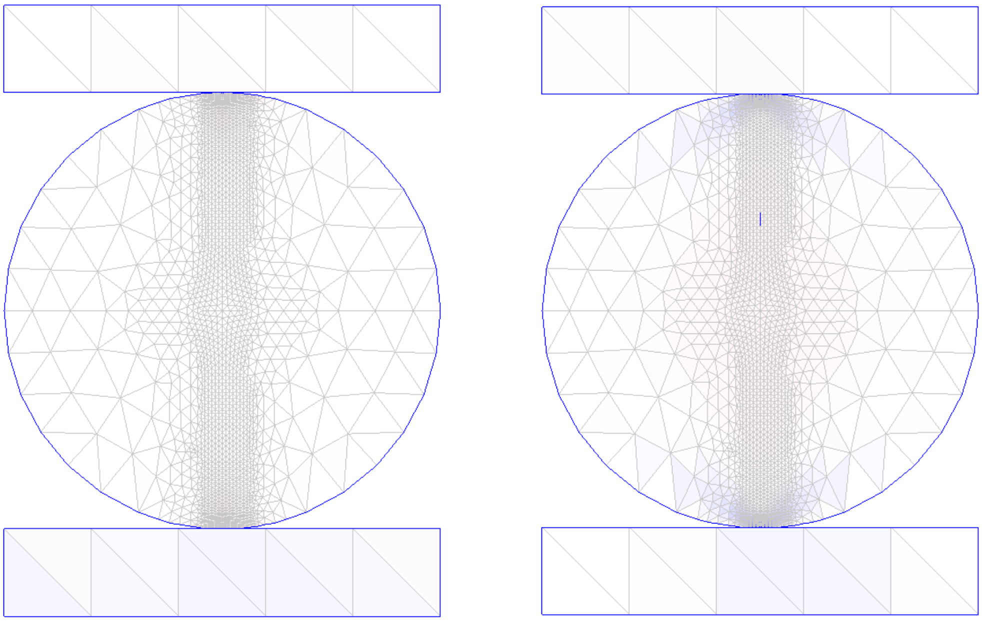

(a) at the beginning of test

(b) cracks appear (t=0.002141s)

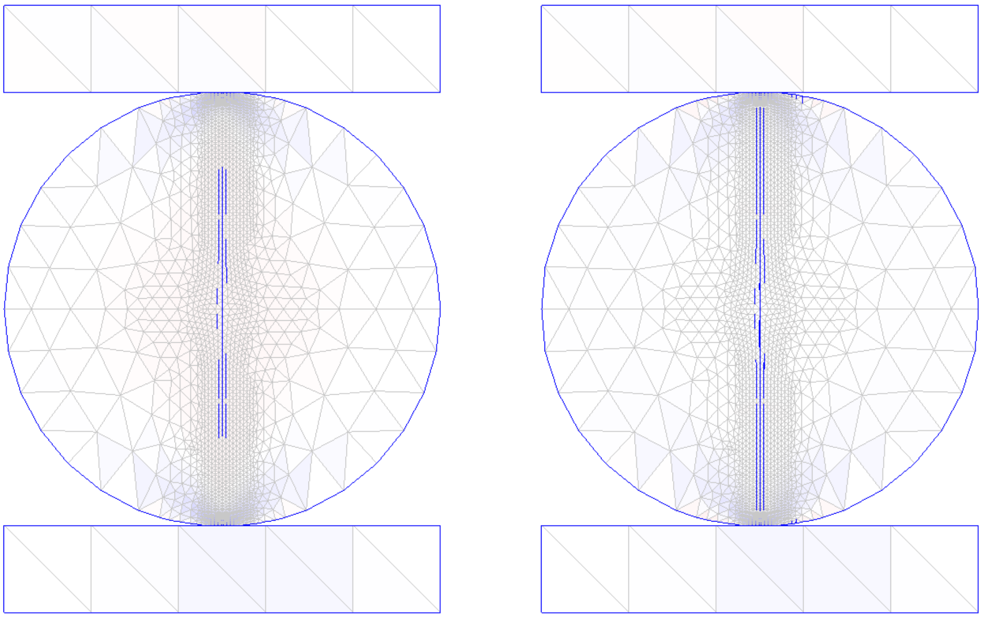

(c) cracks propagation (t=0.002143s)

(d) after failure

Figure 7.31 simulation results from NDDA for the model with local refined mesh (3 blocks, 3650 elements)

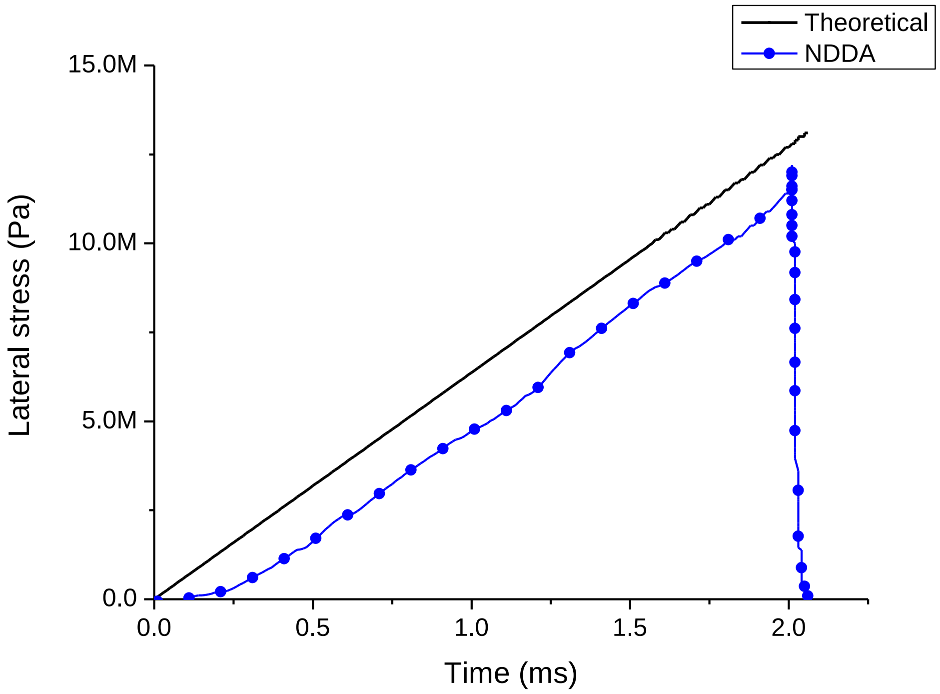

Figure 7.32 lateral stress-time curve at the center of the disc in test II, accompanied by the theoretical curve

7.5.3 Brazilian disc with an initial crack

This example is designed to show the modelling of crack initiation and propagation under mixed mode I-II loading condition. The disc is 50 mm in diameter and 25 mm in thickness with the material properties and analysis parameters shown in Table 6. A straight initial crack with the length of 14 mm (i.e., a/R=0.28) and inclination angle 45˚ is made at the center of the disc. A boundary displacement is applied to the rigid plates at a speed of 0.1m/s. The simulation results for the fracture and failure procedure of the disc are shown in Figure 7.35. Comparing with the experimental result of a limestone rock specimen (see Figure 7.34), it is found that the numerical results approximately simulated the experimental results. Theoretically, the crack initiates at the tip of the original crack and propagates very rapidly along a curvilinear path towards the point on the boundary of the disc where the compression load is applied. When the propagating crack reaches the upper and lower boundaries of a sample, the sample failed and broke into two pieces. In the numerical results from the NDDA, the propagation path is combined by a group of small cracks, which is different from the experimental results. The reason is mainly because the crack propagation in the NDDA model can only proceed along the boundary of the element and the stress jump between triangular elements.

Table 6 analysis parameters for the Brazilian disc with an initial crack

Rock sample	Density (kg/m^3)	2600
	Young's modulus (GPa)	10
	Poisson ratio	0.25
	Friction angle	25°
	Cohesion strength (MPa)	25
	Tensile strength (MPa)	12
Rigid plate	Density (kg/m^3)	7800
	Young's modulus (GPa)	2000
	Poisson ratio	0.25
	Friction angle	25°
	Cohesion strength (MPa)	2500
	Tensile strength (MPa)	2500
Joint/crack	Friction angle	20°
	Cohesion strength (MPa)	0
	Tensile strength (MPa)	0
Control parameter	Penalty stiffness (GN/m)	4000
	Time step size (s)	1×10^{-5}
	Max displacement ratio	0.01
	SOR factor	1.0
	Total analysis time (s)	0.003

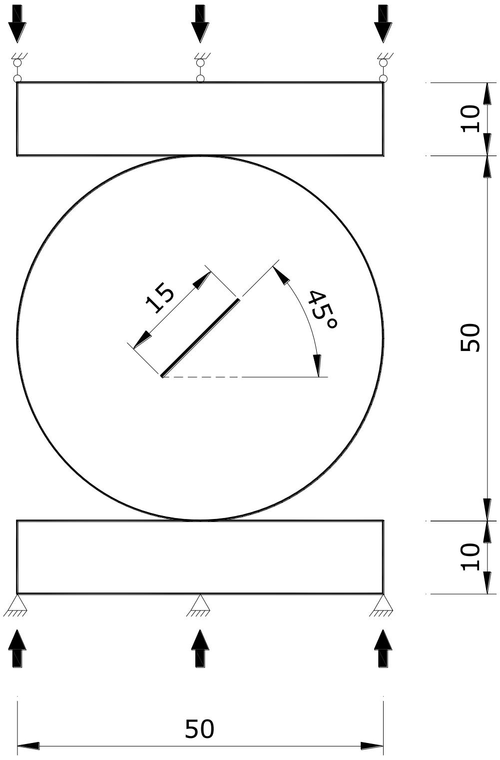

Figure 7.33 configuration of the NDDA model with pre-existing inclined crack (unit: mm)

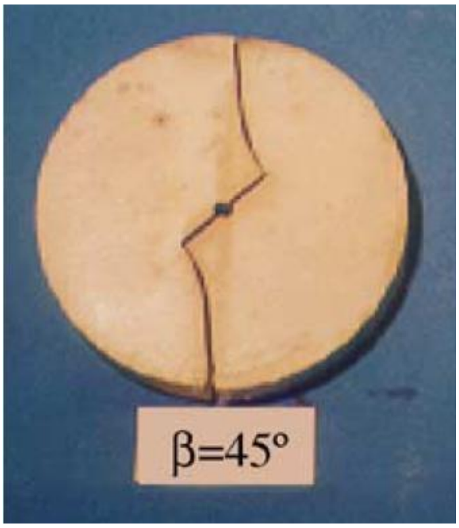

Figure 7.34 The specimen with pre-existing flaw after failure (Al-Shayea 2005)

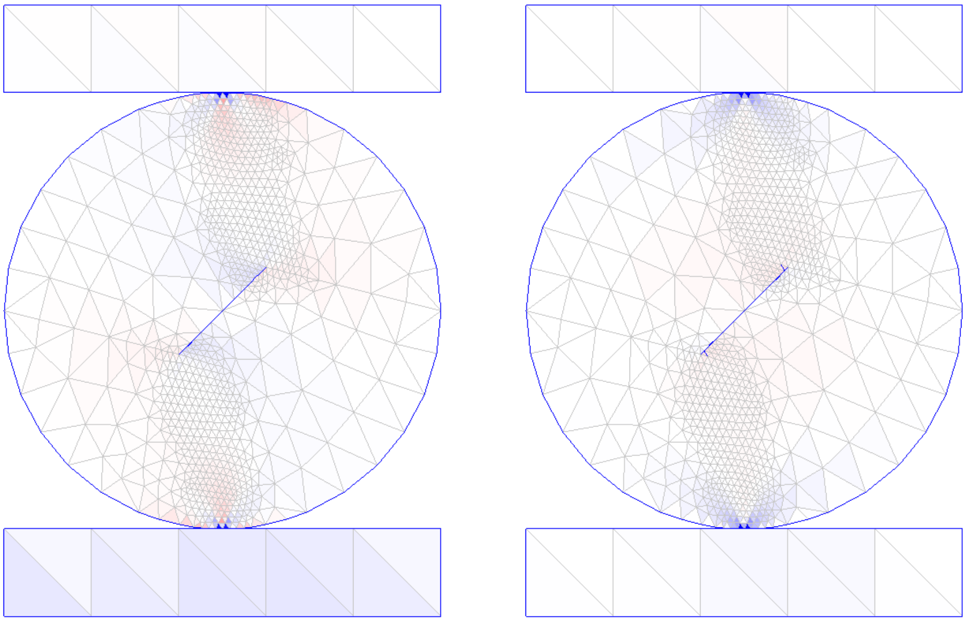

(a) at the beginning of test

(b) wing cracks appear

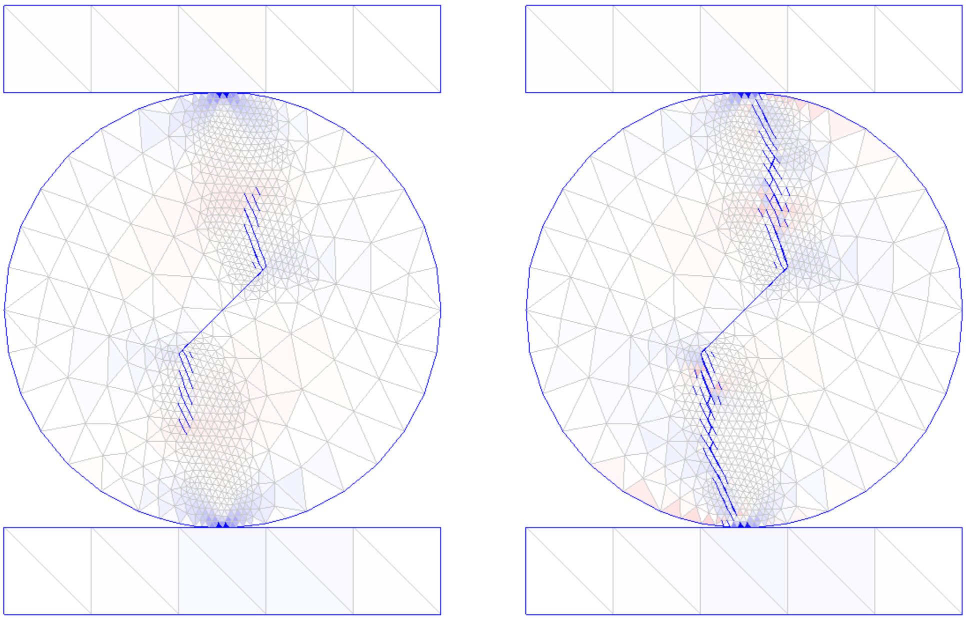

(c) cracks propagation

(d) failure

Figure 7.35 simulation results from NDDA for Brazilian disc with pre-existing inclined crack (3 blocks, 1588 elements)

7.5.4 Brazilian disc with an initial hole

In the Brazilian test configuration, a disc is loaded diametrically, inducing an almost uniform tensile stress in the direction perpendicular to the loading along most of the loaded diameter. When a hole is drilled parallel to the sample axis, and centered on the diameter perpendicular to the loaded diameter (see Figure 7.36), the material above and below the hole is subjected to a rapid decreasing tensile stress (Van de Steen, Vervoort et al. 2005). The disc material properties and the analysis parameters are shown in Table 7. In the results from the NDDA simulation (see Figure 7.37), the cracks first appear above and below the hole and propagate toward the platen contacts quickly, which agrees with the experiment (see Figure 7.38).

Table 7 analysis parameters for the Brazilian disc with an initial hole

Rock sample	Density (kg/m^3)	2600
	Young's modulus (GPa)	10
	Poisson ratio	0.25
	Friction angle	25°
	Cohesion strength (MPa)	25
	Tensile strength (MPa)	12
Rigid plate	Density (kg/m^3)	7800
	Young's modulus (GPa)	2000
	Poisson ratio	0.25
	Friction angle	25°
	Cohesion strength (MPa)	2500
	Tensile strength (MPa)	2500
Joint/crack	Friction angle	20°
	Cohesion strength (MPa)	0
	Tensile strength (MPa)	0
Control parameter	Penalty stiffness (GN/m)	4000
	Time step size (s)	1×10^{-5}
	Max displacement ratio	0.01
	SOR factor	1.0
	Total analysis time (s)	0.003

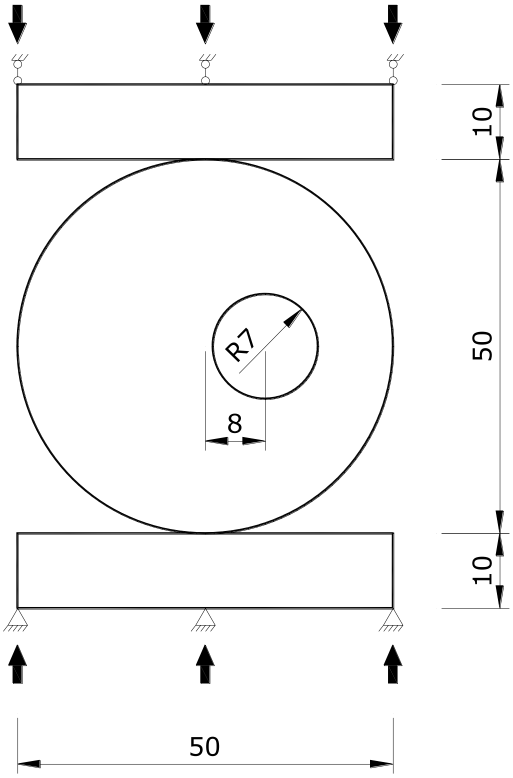

Figure 7.36 configuration of the Brazilian disc with pre-existing hole (unit: mm)

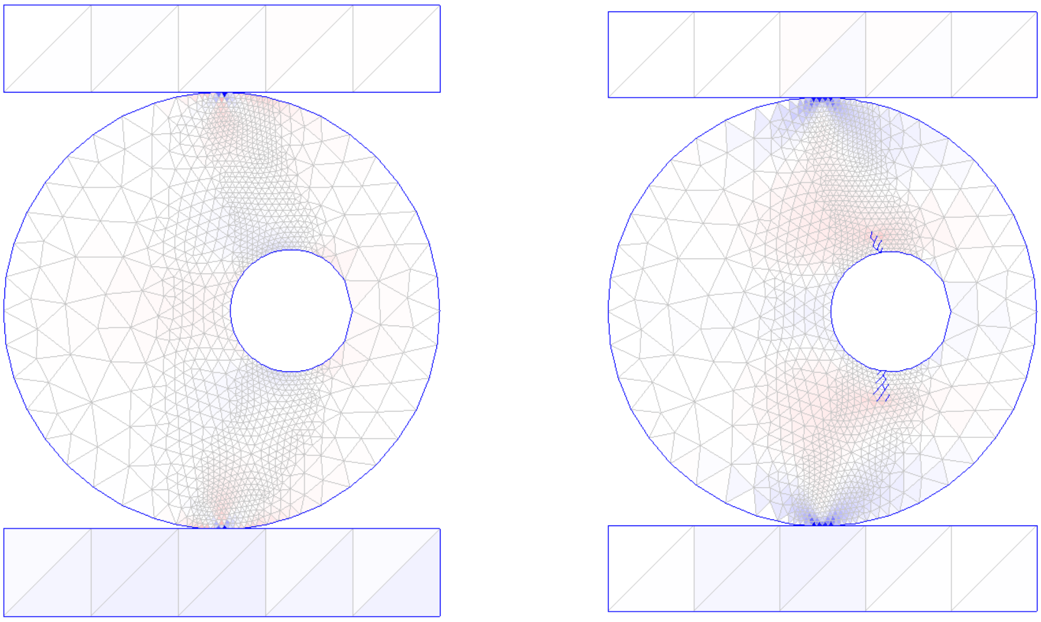

(a) configuration

(b) cracks initiation

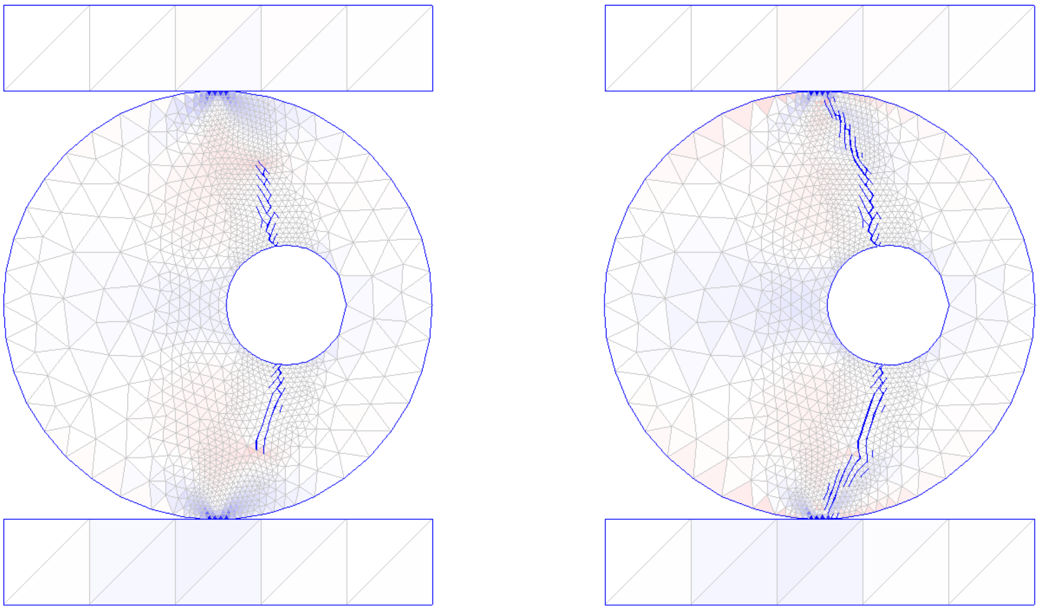

(b) cracks propagation (c) after failure

Figure 7.37 simulation results from NDDA for Brazilian disc with initial hole (3 blocks, 2288 elements)

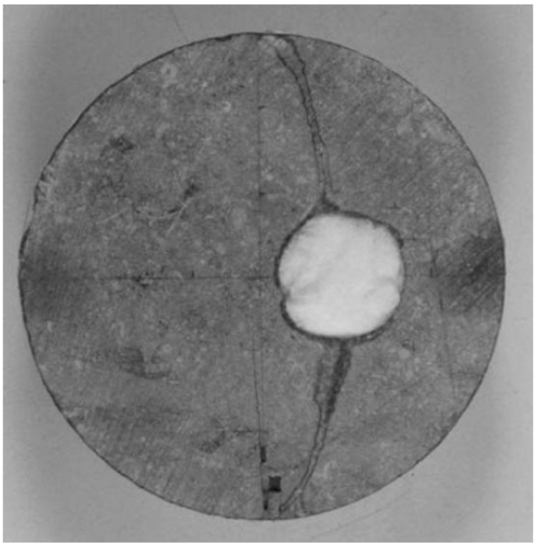

Figure 7.38 diametrically loaded disc with hole with the primary fractures intersecting the hole (Van de Steen, Vervoort et al. 2005)

7.6 Summary

This chapter shows the possible applications of the newly developed NDDA by several qualitative examples. The applications can be sorted into two main parts: (1) modeling wave propagation in continuous elastic media; (2) modeling brittle fracture. The simulation results shows that the NDDA can handle these problems though further development is necessary to the current program.

In the simulation of wave propagation in elastic materials, the existence of numerical damping is a shortcoming of the current algorithm, which need to be solved in the future work.

In the modeling of brittle fracture, the crack propagation path is formed by many tiny cracks instead of a smooth curve, which is not real although it predicted the correct fracture model and extension direction of the fracture. The main reason for this phenomenon is because the current mesh splitting scheme is based on the stresses of grid line which is determined by the neighboring elements. And it is well known that the stress distribution in triangular mesh is discontinuous in neighboring elements, an element in tensile stress may neighbored by a compressive element.

Furthermore, most of the examples in this chapter are qualitative only to show what the newly developed NDDA program can do. To show quantitative calibrations of the NDDA, further development of the NDDA program is necessary.

CHAPTER 8 CONCLUSIONS AND RECOMMENDATIONS

8.1 Summary and Conclusions

Generally, numerical modelling methods are sorted into two groups: continuum-based method and discontinuum-based method. Two famous members, the FEM and the DDA, which belong to the continuum-based method and discontinuum-based method, respectively, are involved in the current work.

The FEM can transform the partial differential equations into integral differential equations in order to solve the problems of continuous structures by using a piecewise smooth approach. The stress distribution in the body was used to successfully predict and detect weak zones. The FEM is now a well-developed and powerful method for solving continuous deformation problems, but lacks efficiency in dealing with discontinuous deformation problems.

The DDA is more like a complementary method of the FEM because it analyses the stability and stress of a totally discontinuous system containing pre-existing cracks or joints. It was primarily applied in rock mechanics with great success in the stability analysis of tunnels and slopes. It adopts the step by step linear kinematics approach to evaluate the failure modes and global stability of a discontinuous blocky system. In the DDA, movement of a block is controlled by the Coulomb’s friction law, the contact modes with other blocks, and the kinematic restrictions of no-tension and no-penetration at the block boundary. With the employment of inertial force in the governing equation, the stability of open-close iteration during the analysis of the system is guaranteed, and provides DDA the capability of solving large displacement and deformation for problems with numerous discontinuous blocks.

The standard DDA approach uses a complete first order polynomial approximation of deformation in each block, therefore, the stress or strain distribution in each block is constant. Since the DDA uses the same implicit algorithm as in the FEM, it is natural and convenient to add a finite element mesh into DDA block to improve the deformation field in the block. In order to applying the finite element mesh, the unknowns of the original DDA are replaced by the displacements of node in the finite element mesh. The modified DDA is called nodal-based DDA (NDDA) because all unknowns in the NDDA are nodal displacements, same as in the FEM. When analyzing a continuous system, the NDDA works in a way the same as the FEM. When the system contains discontinuous deformation, the block kinematics of DDA will come into work and make the NDDA behaving like the DDA but with deformation enhanced blocks. Hence, the NDDA provides a connection between the FEM and DDA, and provides a platform to unify them.

One of the advantages of the NDDA is providing a more precise deformation description of the blocks, which is due to the mesh refinement inside blocks. Mesh refinements for a block are necessary when dealing with the following situations: (1) a system encompassed a few blocks which have complex features, and a precise solution is desired; (2) a system contains few giant blocks and many tiny blocks (comparing with the giant block), and deformation of the giant blocks are of special interest; and (3) a system involves fracturing inside blocks. Two schemes for mesh refinement in a block have been developed by previous researchers in this field: one is applying finite element mesh and the other is employing a sub-block system.

In a sub-block system, a big block is divided into many small sub-blocks glued together by strong joint (Lin 1995; Jiao, Zhang et al. 2008). This scheme provides the DDA the capability of modelling crack propagation in continuous material. However, this scheme will introduce large amount of artificial contacts and reduce the computational efficiency. This drawback does not exist in the scheme of applying finite element mesh inside blocks. The NDDA is developed under the scheme of applying finite element mesh inside blocks, which makes the NDDA have the same efficiency as the FEM when analyzing continuous materials.

With the fine element discretization in each block, the NDDA can provide more realistic deformation ability in each block and consequently more precise stress distribution filed. The NDDA had inherited the block kinematics algorithm from the original DDA, which makes it more suitable for modelling brittle fracture of intact rock than continuum-based methods. From the simulation results of examples in Chapter 7, it is seen that the NDDA can model the wave propagation in continuous elastic media because it is indeed a continuum-based method when no crack occurs. When cracks appear inside a block, it becomes a discontinuum-based method and the kinematics of blocks comes into work. In the simulation of crack propagation under uniaxial force, the NDDA catches the correct fracture model and the results qualitatively agreed with the laboratory observation. Different from the experimental observation, the crack propagating path obtained by the NDDA program is formed by a group of small cracks instead of a main crack. This is a drawback of the current NDDA algorithm and is caused by the crack criterion and node splitting scheme employed in the program.

In determining the applicability of the NDDA to real world applications, the assumptions and limitations inherent in it should not be overlooked. The NDDA is currently restricted to two-dimensional representations, and the employment of only triangular mesh limits the stress distribution in each element to constant. In addition, the crack can only propagate along the boundary of elements, so a relative dense mesh is necessary to reduce the mesh influence on the crack propagation path.

In summary, the present study has made the following contributions to the DDA:

1) Developed a user friendly software environment for generation of triangular mesh inside DDA blocks and other operations such as inputting boundary condition and loading condition.
2) Enhanced the deformation ability of DDA blocks by coupling a triangular finite element mesh into DDA blocks.
3) Provided a node splitting algorithm for the fragmentation of an intact block along the boundary of the finite element in it according to proper crack criterion.
4) Improved the computational efficiency of DDA when dealing with continuous media under the scheme of applying finite element mesh in blocks.
5) Developed a scheme for effectively dealing with the vertex-vertex contact problems not only in the DDA but also in the NDDA.

8.2 Recommendations for Future Work

Although the idea of coupling the DDA with the finite element mesh was introduced since 1990s, little advance in this area had been made during the past decades. This thesis may become a milestone in attempting to unify the continuum-based FEM and the discontinuum-based DDA. However, due to the limitation of time, there are many limitations lie in this work but which will not affect it serving as a building block for advanced research. Further research on this topic is definitely necessary to improve the performance of the NDDA program as well as enhance the method of NDDA.

The fracture scheme including crack criterion and node splitting algorithm in the NDDA program is still in the developing and testing stage. Although Coulomb’s criterion has been widely used for materials with confinements below the brittle-ductile transition, it is not a particularly satisfactory peak strength criterion for rock material. It implies a direction of shear failure which does not always agree with experimental observations. And the linear approximation of the Mohr-Coulomb model is poor at a low confinement, where the experimental strength-confinement curves exhibit greatest non-linearity (convexity). The Mohr-Coulomb failure criterion is independent of the intermediate principal stress σ_2, resulting in the failure plane manifesting itself necessarily parallel to this direction. The poor approximation of the tensile region of the conventional Mohr-Coulomb yield surface to the mutually orthogonal tensile planes is a major shortcoming in terms of application to quasi-brittle fracture. For these reasons, other peak strength criteria, such as Griffith criterion or maximum principal stress criterion, may perform better than the Mohr-Coulomb law for a specified material.

The node splitting scheme employed in the program is also too simple to provide a continuous crack propagation path and to model complex crack propagation problem. The current splitting scheme is based on the average stresses of the grid line which is the main reason that the program cannot obtain a continuous crack extension path. In the future development, a weighted-average nodal stress based splitting scheme may be preferred (Klerck, Sellers et al. 2004).

Since the triangular element is not suitable for bending problem, the employment of the quadrilateral element is necessary in the future work.

Inclusion of nonlinear rock joint properties, tensile strains, cohesion and different friction angles between the contact interfaces of the cracks are necessary to model more realistic rock mass behavior.

For real world applications, it is necessary to develop three-dimensional nodal-based discontinuous deformation analysis and to propose a suitable fracture scheme to model the complex engineering problems.

REFERENCES

Al-Shayea, N. A. (2005). "Crack propagation trajectories for rocks under mixed mode I-II fracture." Engineering Geology **81**(1): 84-97.

Amadei, B. (1999). Proceedings of the Third International Conferences on Analysis of Discontinuous Deformation, Vail, Colorado.

Amadei, B., C. T. Lin and J. Dwyer (1996). Recent extensions to the DDA method. Proceedings of the First International Forum on DDA and Simulations of Discontinuous Media. M. R. Salami and D. Banks. Berkeley, California, TSI Press, Albuquerque, New Mexico**:** 1-30.

Asano, T., L. Guibas, J. Hershberger and H. Imai (1986). "Visibility of disjoint polygons." Algoritnmica **1**: 49-63.

Ashby, M. F. and S. D. Hallam (1986). "The failure of brittle solids containing small cracks under compressive stress states." Acta Metallurgica **34**(3): 497-510.

Babuska, I. and J. E. Osborn (1983). "Generalized Finite Element Methods: Their Performance and Their Relation to Mixed Methods." SIAM Journal on Numerical Analysis **20**(3): 510-536.

Bailey, C. and M. Cross (1995). "A finite volume procedure to solve elastic solid mechanics problems in three dimensions on an unstructured mesh." International Journal for Numerical Methods in Engineering **38**(10): 1757-1776.

Bathe, K.-J. r. (1982). Finite element procedures in engineering analysis. Englewood Cliffs, N.J., Prentice-Hall.

Baud, P. and T. Reuschle (1997). "A theoretical approach to the propagation of interacting cracks." Geophysical Journal International **130**(2): 460-468.

Bedford, A. and D. S. Drumheller (1994). Introduction to elastic wave propagation. Chichester [England] ; New York, Wiley.

Belytschko, T. and T. Black (1999). "Elastic crack growth in finite elements with minimal remeshing." International Journal for Numerical Methods in Engineering **45**(5): 601-620.

Bicanic, N. (2001). Proceedings of the Fourth International Conferences on Analysis of Discontinuous Deformation, University of Glasgow Scotland, UK.

Bieniawski, Z. T. (1967). "Mechanism of brittle fracture of rock: Part II--experimental studies." International Journal of Rock Mechanics and Mining Sciences & Geomechanics Abstracts **4**(4): 407-408, IN413-IN414, 409-418, IN415-IN418, 419-423.

Brace, W. F. and E. G. Bombolakis (1963). "A note on brittle crack growth in compression." Journal of Geophysical Research **68**(12): 3709-3713.

Brady, B. H. G. and J. W. Bray (1978). "The boundary element method for determining stresses and displacements around long openings in a triaxial stress field." International Journal of Rock Mechanics and Mining Science & Geomechanics Abstracts **15**(1): 21-28.

Brady, B. H. G. and E. T. Brown (2004). Rock Mechanics for Underground Mining, Springer.

Camacho, G. T. and M. Ortiz (1996). "Computational modelling of impact damage in brittle materials." International Journal of Solids and Structures **33**(20-22): 2899-2938.

Chang, C. T. (1994). Nonlinear dynamic discontinuous deformation analysis with finite element meshed block system. United States -- California, University of California, Berkeley. **Ph.D.**

Chang, C. T., P. Monteiro, K. Nemati and K. Shyu (1996). "Behavior of marble under compression." Journal of Materials in Civil Engineering **8**(3):

157-170.

Chaudhary, A. B. and K.-J. Bathe (1986). "A solution method for static and dynamic analysis of three-dimensional contact problems with friction." Computers & Structures **24**(6): 855-873.

Chen, S. (1993). Slope stability assessment based upon discontinuous deformation analysis. Civil and Environmental Engineering. United States -- Pennsylvania, University of Pittsburgh. **Ph.D**.

Cheng, Y. M. and Y. H. Zhang (2000). "Rigid body rotation and block internal discretization in DDA analysis." International Journal for Numerical and Analytical Methods in Geomechanics **24**: 567-578.

Chew, L. P. (1989). "Constrained Delaunay triangulation." Algorithmica **4**: 97-108.

Chew, L. P. (1989). Guaranteed-quality triangular meshes. Ithaca, NY, Cornell University.

Christophe, D., M. Nicolas, D. John, S. Natarajan and B. Ted (2000). "Arbitrary branched and intersecting cracks with the extended finite element method." International Journal for Numerical Methods in Engineering **48**(12): 1741-1760.

Chuhan, Z., O. A. Pekau, J. Feng and W. Guanglun (1997). "Application of distinct element method in dynamic analysis of high rock slopes and blocky structures." Soil Dynamics and Earthquake Engineering **16**(6): 385-394.

Clatworthy, D. and F. Scheele (1999). A method of sub-meshing in discontinuous deformation analysis (DDA). Proceedings of the Third International Conference on Analysis of Discontinuous Deformation. B. Amadei. Vail, Colorado, American Rock Mechanics Association, Balkema: Rotterdam, Washington DC**:** 85-96.

Clough, R. W. (1960). The finite element in plane stress analysis. Proceedings of ASCE 2nd Conference on Electronic Computation. Pittsburgh, Pa.

Combescure, A., A. Gravouil, D. Gr 間 oire and J. R 閩 hor (2008). "X-FEM a good candidate for energy conservation in simulation of brittle dynamic crack propagation." Computer Methods in Applied Mechanics and Engineering **197**(5): 309-318.

Crouch, S. L. and A. M. Starfield (1983). Boundary element methods in solid mechanics : with applications in rock mechanics and geological engineering. London ; Boston, Allen & Unwin.

Cundall, P. A. (1971). A computer model for simulating progressive, large scale movements in blocky rock systems. Proceedings of the International Symposium on Rock Mechanics. Nancy, France**:** 11-18.

Cundall, P. A. (2004). UDEC 4.0 Manual - Theory and Background, ITASCA Consulting Group, Inc.

Desai, C. S., M. M. Zaman, J. G. Lightner and H. J. Siriwardane (1984). "Thin-layer element for interfaces and joints." International Journal for Numerical and Analytical Methods in Geomechanics **8**(1): 19-43.

Doolin, D. M. and N. Sitar (2002). "Displacement accuracy of discontinuous deformation analysis method applied to sliding block." Journal of Engineering Mechanics **128**(11): 1158-1168.

Duarte, C. A., I. Babuska and J. T. Oden (2000). "Generalized finite element methods for three-dimensional structural mechanics problems." Computers & Structures **77**(2): 215-232.

Duarte, C. A., O. N. Hamzeh, T. J. Liszka and W. W. Tworzydlo (2001). "A generalized finite element method for the simulation of three-dimensional dynamic crack propagation." Computer Methods in Applied Mechanics and Engineering **190**(15-17): 2227-2262.

Edelsbrunner, H. (1987). Algorithms in Combinatorial Geometry, Springer-Verlag.

Esaki, T., Y. Jiang, T. N. Bhattarai, A. Nozaki and T. Mizokami (1998). "Stability Analysis and Reinforcement System Design in a Progressively Failed Steep Rock Slope by the Distinct Element Method." International Journal of Rock

Mechanics and Mining Sciences **35**(4-5): 664-666.

Fairhurs, C. and N. G. W. Cook (1966). The phenomenon of rock splitting parallel to the direction of maximum compression in the neighbourhood of a surface. Proceedings of the First Congress of the International Society of Rock Mechanics. Lisbon, Laboratório Nacional de Engenharia Civil**:** p. 687.

Fairhurst, C. (1964). "On the validity of the 'Brazilian' test for brittle materials." International Journal of Rock Mechanics and Mining Sciences & Geomechanics Abstracts **1**(4): 535-546.

Fairhurst, C. (2004). Fundamental considerations relating to the strength of rock. Report on the Workshop on Extreme Ground Motions at Yucca Mountain. Menlo Park, California.

Fairhurst, C. and J. Pei (1990). "A comparison between the distinct element method and the finite element method for analysis of the stability of an excavation in jointed rock." Tunnelling and Underground Space Technology **5**(1-2): 111-117.

Fallah, N. A., C. Bailey, M. Cross and G. A. Taylor (2000). "Comparison of finite element and finite volume methods application in geometrically nonlinear stress analysis." Applied Mathematical Modelling **24**(7): 439-455.

Feng, Y. T. and D. R. J. Owen (2004). "A 2D polygon/polygon contact model: algorithmic aspects." Engineering Computations **21**(2/3/4): 265-277.

Fryer, Y. D., C. Bailey, M. Cross and C. H. Lai (1991). "A control volume procedure for solving the elastic stress-strain equations on an unstructured mesh." Applied mathematical modelling **15**(11): 639-645.

Gdoutos, E. E. (2005). Fracture Mechanics An Introduction. Solid Mechanics and Its Applications,. Dordrecht, Springer.

Ghaboussi, J., E. L. Wilson and J. Isenberg (1973). "Finite element for rock joints and interfaces." Journal of the Soil Mechanics and Foundations Division, ASCE **99**(10): 849-862.

Goodman, R. E., R. L. Taylor and T. L. Brekke (1968). "A model for the mechanics of jointed rock." Journal of the Soil Mechanics and Foundations Division, ASCE **94**: 637-660.

Grayeli, R. and A. Mortazavi (2006). "Discontinuous deformation analysis with second-order finite element meshed block." International Journal for Numerical and Analytical Methods in Geomechanics **30**(15): 1545-1561.

Greenspan, D. (1965). Introductory numerical analysis of elliptic boundary value problems. London, Harper and Row.

Griffith, A. A. (1921). "The Phenomena of Rupture and Flow in Solids." Philosophical Transactions of the Royal Society of London. Series A, Containing Papers of a Mathematical or Physical Character **221**: 163-198.

Griffith, A. A. (1924). The theory of rupture. 1st International Congress of Applied Mechanics. Delft**:** 55-63.

Guidault, P. A., O. Allix, L. Champaney and C. Cornuault (2008). "A multiscale extended finite element method for crack propagation." Computer Methods in Applied Mechanics and Engineering **197**(5): 381-399.

Hatzor, Y. H. (2002). Proceedings of the Fifth International Conferences on Analysis of Discontinuous Deformation, Ben-Gurion University of the Negev, Beer Sheva, Israel.

Hatzor, Y. H., A. A. Arzi, Y. Zaslavsky and A. Shapira (2004). "Dynamic stability analysis of jointed rock slopes using the DDA method: King Herod's Palace, Masada, Israel." International Journal of Rock Mechanics and Mining Sciences **41**(5): 813-832.

Hatzor, Y. H., M. Talesnick and M. Tsesarsky (2002). "Continuous and discontinuous stability analysis of the bell-shaped caverns at Bet Guvrin, Israel." International Journal of Rock Mechanics and Mining Sciences **39**(7): 867-886.

Hoek, E. and Bieniaws.Zt (1965). "Brittle rock fracture propagation in rock under compression." International Journal of Fracture Mechanics **1**(3): 137-155.

Hoek, E. and E. T. Brown (1981). Underground excavations in Rock. London, Institution of Mining and Metallurgy.

Horii, H. and S. Nemat-Nasser (1985). "Compression-Induced Microcrack Growth in Brittle Solids: Axial Splitting and Shear Failure." J. Geophys. Res. **90**(B4): 3105-3125.

Hsiung, S. M. (2001). Discontinuous deformation analysis (DDA) with nth order polynomial displacement functions. Rock Mechanics in the National Interest, Proceedings of the 38th U.S. Rock Mechanics Symposium. D. Elsworth, J. P. Tinucci and K. A. Heasley, American Rock Mechanics Association, Balkema: Rotterdam, Washington DC**:** 1437-14444.

Huang, T. (1997). "Mechanical behavior of interconnected concrete-block retaining wall." Journal of Geotechnical and Geoenvironmental Engineering **123**(3): 197-203.

Ingraffea, A. R. and F. E. Heuze (1980). "Finite element models for rock fracture mechanics." International Journal for Numerical and Analytical Methods in Geomechanics **4**(1): 25-43.

Ishikawa, T., E. Sekine and Y. Ohnishi (2002). Shaking table tests of coarse granular materials with discontinuous deformation analysis. Stability of Rock Structures - Proceedings of the Fifth International Conference on Analysis of Discontinuous Deformation. Y. H. Hatzor. Beer-Sheva, Israel, Taylor & Francis**:** 181-188.

Jiang, Y., B. Li and Y. Yamashita (2009). "Simulation of cracking near a large underground cavern in a discontinuous rock mass using the expanded distinct element method." International Journal of Rock Mechanics and Mining Sciences **46**(1): 97-106.

Jiao, Y. Y., X. L. Zhang, Q. S. Liu and W. Z. Chen (2007). "Simulation of rock crack propagation using discontinuous deformation analysis method."

Chinese Journal of Rock Mechanics and Engineering **26**(4): 682-691.

Jiao, Y. Y., X. L. Zhang, S. L. Wang and J. Zhao (2008). Some potentials of discontinuous deformation analysis method. Boundaries of Rock Mechanics: Recent Advances and Challenges for the 21st Century. M. Cai and J. Wang**:** 889-893.

Jing, L. (1998). "Formulation of discontinuous deformation analysis (DDA) -- an implicit discrete element model for block systems " Engineering Geology **49**(3): 371-381.

Jing, L. (2003). "A review of techniques, advances and outstanding issues in numerical modelling for rock mechanics and rock engineering." International Journal of Rock Mechanics and Mining Sciences **40**(3): 283-353.

Jing, L., Y. Ma and Z. Fang (2001). "Modeling of fluid flow and solid deformation for fractured rocks with discontinuous deformation analysis (DDA) method." International Journal of Rock Mechanics and Mining Sciences **38**(3): 343-355.

Ju, Y., X. Fang and H. Bian (2008). Proceedings of the Eighth International Conferences on Analysis of Discontinuous Deformation, Beijing, China.

Kane, C., E. A. Repetto, M. Ortiz and J. E. Marsden (1999). "Finite element analysis of nonsmooth contact." Computer Methods in Applied Mechanics and Engineering **180**(1-2): 1-26.

Ke, T. C. (1993). Simulated testing of two-dimensional heterogeneous and discontinuous rock masses using discontinuous deformation analysis. Civil Engineering. Berkeley, University of California. **Ph.D.**

Ke, T. C. (1995). Modification of DDA with respect to rigid body rotation. Proceedings of the First International Conference on Analysis of Discontinuous Deformation. J. C. Li, C. Y. Wang and J. Sheng. Chungli, Taiwan, National Central University, Chungli, Taiwan, ROC**:** 260-273.

Ke, T. C. (1996). Artificial joint-based DDA. Proceedings of the First International Forum on DDA and Simulations of Discontinuous Media. M. R. Salami and D. Banks. Berkeley, California, TSI Press, Albuquerque, New Mexico**:** 326-333.

Ke, T. C. (1996). The issue of rigid body rotation in DDA. Proceedings of the First International Forum on DDA and Simulations of Discontinuous Media. M. R. Salami and D. Banks. Berkeley, California, TSI Press, Albuquerque, New Mexico**:** 318-325.

Ke, T. C. (1997). Application of DDA to simulate fracture propagation in solid. Proceedings of the Second International Conference on Analysis of Discontinuous Deformation. Y. Ohnishi. Kyoto, Japan, Japan Institute of Systems Research**:** 155-185.

Ke, T. C. and J. D. Bray (1995). "Modeling of particulate media using discontinuous deformation analysis." Journal of Engineering Mechanics **121**(11): 1234-1243.

Kim, M. K., S. E. Kim, K. H. Oh and W. J. Kim (1997). "A study on the behavior of rock mass subjected to blasting using modified distinct element method." International Journal of Rock Mechanics and Mining Sciences **34**(3-4): 156.e151-156.e114.

Kim, Y.-I. (1998). Modeling the effect of water, excavation sequence and reinforcement on the response of blocky rock masses. United States -- Colorado, University of Colorado at Boulder.

Kim, Y.-I., B. Amadei and E. Pan (1999). "Modeling the effect of water, excavation sequence and rock reinforcement with discontinuous deformation analysis." International Journal of Rock Mechanics and Mining Sciences **36**: 949-970.

Klerck, P. A., E. J. Sellers and D. R. J. Owen (2004). "Discrete fracture in quasi-brittle materials under compressive and tensile stress states." Computer Methods in Applied Mechanics and Engineering **193**(27-29):

3035-3056.

Koo, C. Y. and J. C. Chern (1996). The development of DDA with third-order displacement function. Proceedings of the First International Forum on DDA and Simulations of Discontinuous Media. M. R. Salami and D. Banks. Berkeley, California, TSI Press, Albuquerque, New Mexico**:** 342-349.

Koo, C. Y. and J. C. Chern (1997). Modeling of progressive fracture in jointed rock by DDA method. Proceedings of the Second International Conference on Analysis of Discontinuous Deformation. Y. Ohnishi. Kyoto, Japan, Japan Institute of Systems Research**:** 186-201.

Koo, C. Y. and J. C. Chern (1998). "Modification of the DDA mehtod for rigid block problems." International Journal of Rock Mechanics and Mining Sciences **35**(6): 683-693.

Koo, C. Y., J. C. Chern and S. Chen (1995). Development of second order displacement function for DDA. Proceedings of the First International Conference on Analysis of Discontinuous Deformation. J. C. Li, C. Y. Wang and J. Sheng. Chungli, Taiwan ROC, National Central University**:** 91-108.

Kranz, R. L. (1979). "Crack-crack and crack-pore interactions in stressed granite." International Journal of Rock Mechanics and Mining Sciences & Geomechanics Abstracts **16**(1): 37-47.

Krishnasamy, J. and M. J. Jakiela (1995). "A method to resolve ambiguities in corner-corner interactions between polygons in the context of motion simulations." Engineering Computations **12**: 135-144.

Kusano, N., T. Aoyagi, J. Aizawa, H. Ueno, H. Morikawa and N. Kobayashi (1992). "Impulsive local damage analyses of concrete structure by the distinct element method." Nuclear Engineering and Design **138**(1): 105-110.

Lajtai, E. Z. (1971). "A theoretical and experimental evaluation of the Griffith theory of brittle fracture." Tectonophysics **11**(2): 129-156.

Lange, F. F. (1968). "Interaction between overlapping parallel cracks - a photoelastic study." International Journal of Fracture Mechanics **4**(3): 287-294.

Lee, D. T. (1978). Proximity and reachability in the plane. Computer Science, University of Illinois at Urbana-Champaign. **Ph.D.**

Lee, D. T. and A. K. Lin (1986). "Generalized Delaunay triangulation for planar graphs." Discrete and Computational Geometry **1**: 201-217.

Li, J. C., C. Y. Wang and J. Sheng (1995). Proceedings of the First International Conference on Analysis of Discontinuous Deformation, Chungli, Taiwan, National Central University, Chungli, Taiwan, ROC.

Lin, C. T. (1995). Extensions to the discontinuous deformation analysis for jointed rock masses and other blocky systems. Civil Engineering. Berkeley, University of California. **Ph. D.** .

Lin, C. T., B. Amadei, J. Jung and J. Dwyer (1996). "Extensions of discontinuous deformation analysis for jointed rock masses." International Journal of Rock Mechanics and Mining Science & Geomechanics Abstracts **33**(7): 671-694.

Lin, J.-S. and M.-E. Hynes (1998). Augmented lagrangian for dynamic seismic discontinuous deformation analysis. Proceedings for Geotechnical Earthquake Engineering and Soil Dynamics III. P. Dakoulas, M. Yegian and D. R. Holtz. **1**.

Lin, J. S. and S. Chen (1997). Soil-slope stability analysis using DDA. Proceedings of the Second International Conference on Analysis of Discontinuous Deformation. Y. Ohnishi. Kyoto, Japan, Japan Institute of Systems Research.

Lin, J. S. and D. H. Lee (1996). Manifold method using polynomial basis functions of any order. Proceedings of the First International Forum on DDA and Simulations of Discontinuous Media. M. R. Salami and D. Banks. Berkeley, California, TSI Press, Albuquerque, New Mexico**:** 365-372.

Lu, M. (2003). Proceedings of the Sixth International Conference on the Analysis of Discontinuous Deformation, Trondheim, Norway, Taylor & Francis Group.

Ma, G. and Y. Zhou (2009). Proceedings of the Ninth International Conferences on Analysis of Discontinuous Deformation, NTU, Singapore.

Ma, M. Y. (1999). Development of discontinuous analysis, the first ten years (1986-1996). Proceedings of the Third International Conference on Analysis of Discontinuous Deformation. B. Amadei. Vail, Colorado, American Rock Mechanics Association, Balkema: Rotterdam, Washington DC**:** 17-32.

MacLaughlin, M. and N. Sitar (2005). Proceedings of the Seventh International Conferences on Analysis of Discontinuous Deformation, Honolulu, Hawaii.

MacLaughlin, M. M. (1997). Discontinuous deformation analysis of the kinematics of landslides. Department of Civil Engineering. Berkeley, University of California **Ph.D.**

MacLaughlin, M. M. and D. M. Doolin (2006). "Review of validation of the discontinuous deformation analysis (DDA) method." International Journal for Numerical and Analytical Methods in Geomechanics **30**: 271-305.

MacLaughlin, M. M. and M. A. Hayes (2005). Validation of DDA block motions and failure modes using laboratory models. Proceedings of the Seventh International Conference on the Analysis of Discontinuous Deformation. M. MacLaughlin and N. Sitar. Honolulu, Hawaii**:** 71-78.

MacLaughlin, M. M. and N. Sitar (1996). Rigid body rotations in DDA. Proceedings of the First International Forum on DDA and Simulations of Discontinuous Media. M. R. Salami and D. Banks. Berkeley, California, TSI Press, Albuquerque, New Mexico**:** 620-636.

MacLaughlin, M. M., N. Sitar, D. Doolin and T. Abbot (2001). "Investigation of slope-stability kinematics using discontinuous deformation analysis." International Journal of Rock Mechanics and Mining Sciences **38**(5): 753-762.

Maini, T., P. A. Cundall, J. Marti, N. L. Beresford and M. Asgian (1978). Computer modeling of jointed rock masses. Technical Report N-78-8. Vicksburg, MS, US Army Waterways Experiment Station.

McClintock, F. A. and J. B. Walsh (1962). Friction of Griffith cracks in rock under pressure. Proceedings of the fourth U.S. National Congress of Applied Mechanics. Berkeley, American Society of Mechanical Engineers**:** 1015-1021.

Michael, G. K. (1983). "A simple contact-friction interface element with applications to buried culverts." International Journal for Numerical and Analytical Methods in Geomechanics **7**(3): 371-384.

Moon, T., M. Nakagawa and J. Berger (2007). "Measurement of fracture toughness using the distinct element method." International Journal of Rock Mechanics and Mining Sciences **44**(3): 449-456.

Mortazavi, A. (1999). Modelling of rock blasting in jointed media using discontinuous deformation analysis. Canada, Queen's University at Kingston (Canada). **Ph.D.**

Murrell, S. A. F. (1963). A criterion for brittle fracture of rocks and concrete under triaxial stress and the effect of pore pressure on the criterion. Proceedings of 5th Symposium on Rock Mechanics C. Fairhurst. University of Minnesota, Pergamon**:** 563-577.

Needleman, A. (1987). "A continuum model for void nucleation by inclusion debonding." Journal of Applied Mechanics-Transactions of the Asme **54**(3): 525-531.

Needleman, A. (1990). "An analysis of tensile decohesion along an interface." Journal of the Mechanics and Physics of Solids **38**(3): 289-324.

Nemat-Nasser, S. and H. Horii (1982). "Compression-induced nonplanar crack extension with application to splitting, exfoliation, and rockburst." Journal of Geophysical Research **87**(B8): 6805-6821.

Nesetova, V. and E. Z. Lajtai (1973). "Fracture from compressive stress concentrations around elastic flaws." International Journal of Rock Mechanics and Mining Sciences & Geomechanics Abstracts **10**(4): 265-284.

Nicolas, M., D. John and B. Ted (1999). "A finite element method for crack growth without remeshing." International Journal for Numerical Methods in Engineering **46**(1): 131-150.

O'Sullivan, C. and J. D. Bray (2003). "Modified shear spring formulation for discontinuous deformation analysis of particulate media." Journal of Engineering Mechanics **129**(7): 830-834.

Oden, J. T. and E. B. Pires (1984). "Algorithms and numerical results for finite element approximations of contact problems with non-classical friction laws." Computers & Structures **19**(1-2): 137-147.

Ohnishi, Y. (1997). Proceedings of the Second International Conference on Analysis of Discontinuous Deformation, Kyoto, Japan.

Ohnishi, Y., G. O. Chen and S. Miki (1995). Recent development DDA in rock mechanics. Proceedings of the First International Conference on Analysis of Discontinuous Deformation. J. C. Li, C. Y. Wang and J. Sheng. Chungli, Taiwan ROC, National Central University**:** 26-47.

Ohnishi, Y. and S. Nishiyama (2007). Recent insights of analyses using discontinuous methods in rock engineering in Japan. Proceedings of the Eighth International Conference on the Analysis of Discontinuous Deformation. Y. Ju, X. Fang and H. Bian. Beijing, China**:** 15-26.

Ohnishi, Y., S. Nishiyama, T. Sasaki and T. Nakai (2005). The application of DDA to partical rock engineering problems: issue and recent insights. Proceedings of the Seventh International Conference on the Analysis of Discontinuous Deformation. M. MacLaughlin and N. Sitar. Honolulu, Hawaii**:** 277-287.

Pande, G. N., G. Beer and J. R. Williams (1990). Numerical methods in rock mechanics. Chichester ; New York, Wiley.

Pandolfi, A., C. Kane, J. E. Marsden and M. Ortiz (2002). "Time-discretized variational formulation of non-smooth frictional contact." International Journal for Numerical Methods in Engineering **53**: 1801-1829.

Paterson, M. S. and T.-f. Wong (2005). Experimental Rock Deformation - The Brittle Field. Berlin, Springer.

Pearce, C. J., A. Thavalingam, Z. Liao and N. Bicanic (2000). "Computational aspects of the discontinuous deformation analysis framework for modelling concrete fracture." Engineering Fracture Mechanics **65**(2-3): 283-298.

Perrone, N. and R. Kao (1975). "A general finite difference method for arbitrary meshes." Computers & Structures **5**(1): 45-57.

Richtmyer, R. D. and K. W. Morton (1967). Difference methods for initial value problems. New York, Interscience.

Salami, M. R. and D. Banks (1996). Proceedings of the First International Forum on Discontinuous Deformation Analysis (DDA) and Simulations of Discontinuous Media, University of California, Berkeley, California.

Sasaki, T., I. Hagiwara, K. Sasaki, S. Horikawa, Y. Ohnishi, S. Nishiyama and R. Yoshinaka (2005). Earthquake response analysis of a rock-fall by discontinuous deformation analysis. Proceedings of the Seventh International Conference on the Analysis of Discontinuous Deformation. M. MacLaughlin and N. Sitar. Honolulu, Hawaii**:** 137-146.

Schroeder, W. J. and M. S. Shephard (1988). "Geometry-based fully automatic mesh generation and the Delaunay triangulation." International Journal for Numerical Methods in Engineering **26**: 2503-2515.

Selmin, V. (1993). "The node-centred finite volume approach: Bridge between finite differences and finite elements." Computer Methods in Applied Mechanics and Engineering **102**(1): 107-138.

Shi, G. (1988). Discontinuous deformation analysis - a new numerical model for the statics and dynamics of block systems. Civil Engineering. Berkeley, University of California. **Ph.D.**

Shi, G. and R. E. Goodman (1985). "Two dimensional discontinuous deformation analysis." International Journal for Numerical and Analytical Methods in Geomechanics **9**(6): 541-556.

Shi, G. H. (1991). Manifold method of material analysis. Transactions of the Conference on Applied Mathematics and Computing (9th). Minneapolis, Minnesota**:** 57-76.

Shi, G. H. (1992). Modeling rock joints and blocks by manifold method. The 33th U.S. Symposium on Rock Mechanics (USRMS). Santa Fe, New Mexico**:** 639-648.

Shi, G. H. (2007). Application of discontinuous deformation analysis (DDA) to rock stability analysis. Proceedings of the Eighth International Conference on the Analysis of Discontinuous Deformation. Y. Ju, X. Fang and H. Bian. Beijing, China**:** 1-13.

Shyu, K. (1993). Nodal-based discontinuous deformation analysis. Civil Engineering. Berkeley, University of California **Ph.D.**

Sitar, N. and M. M. MacLaughlin (1997). Kinematics and discontinuous deformation analysis of landslide movement (Invited keynote lecture in Session on Mass Movement). Proceedings of 2nd Panamerican Symposium on Landslides. Rio de Janeiro, Brazil. **3:** 65-73.

Sitar, N., M. M. MacLaughlin and D. Doolin (2005). "Influence of kinematics on landslide mobility and failure mode." Journal of Geotechnical and Geoenvironmental Engineering **131**(6): 716-728.

Strouboulis, T., I. Babuska and K. Copps (2000). "The design and analysis of the Generalized Finite Element Method." Computer Methods in Applied Mechanics and Engineering **181**(1-3): 43-69.

Strouboulis, T., K. Copps and I. Babuska (2001). "The generalized finite element method." Computer Methods in Applied Mechanics and Engineering

190(32-33): 4081-4193.

Su, S. and O. Stephansson (1999). "Effect of a fault on in situ stresses studied by the distinct element method." International Journal of Rock Mechanics and Mining Sciences **36**(8): 1051-1056.

Sukumar, N., N. Moes, B. Moran and T. Belytschko (2000). "Extended finite element method for three-dimensional crack modelling." International Journal for Numerical Methods in Engineering **48**(11): 1549-1570.

Sukumar, N. and J. H. Prevost (2003). "Modeling quasi-static crack growth with the extended finite element method Part I: Computer implementation." International Journal of Solids and Structures **40**(26): 7513-7537.

Swain, M. V. and J. T. Hagan (1978). "Some observations of overlapping interacting cracks." Engineering Fracture Mechanics **10**(2): 299-304.

Tabarraei, A. and N. Sukumar (2008). "Extended finite element method on polygonal and quadtree meshes." Computer Methods in Applied Mechanics and Engineering **197**(5): 425-438.

Thomas, P. A. (1997). Discontinuous deformation analysis of particulate media. Department of Civil Engineering. Berkeley, University of California. **Ph.D.**

Thomas, P. A. and J. D. Bray (1999). "Capturing nonspherical shape of granular media with disk clusters." Journal of Geotechnical and Geoenvironmental Engineering **125**(3): 169-178.

Timoshenko, S. and J. N. Goodier (1969). Theory of elasticity. New York, McGraw-Hill.

Tsesarsky, M., Y. H. Hatzor and N. Sitar (2002). Dynamic block displacement prediction - validation of dda using analytical solutions and shaking table experiments. Stability of Rock Structures - Proceedings of the Fifth International Conference on Analysis of Discontinuous Deformation. Y. H. Hatzor. Beer-Sheva, Israel, Taylor & Francis**:** 195-206.

Van de Steen, B., A. Vervoort and J. A. L. Napier (2005). "Observed and simulated fracture pattern in diametrically loaded discs of rock material." International Journal of Fracture **131**(1): 35-52.

Wawersik, W. R. and Fairhurs.C (1970). "A study of brittle rock fracture in laboratory compression experiments." International Journal of Rock Mechanics and Mining Sciences **7**(5): 561-&.

Wright, A. C., M. M. MacLaughlin and P. R. Donovan (2005). Comparison of the deformation of externally loaded DDA and UDEC blocks with an analytical solution. Proceedings of the Seventh International Conference on the Analysis of Discontinuous Deformation. M. MacLaughlin and N. Sitar. Honolulu, Hawaii**:** 79-90.

Xu, X. P. and A. Needleman (1994). "Numerical simulations of fast crack growth in brittle solids." Journal of the Mechanics and Physics of Solids **42**(9): 1397-1434.

Xu, X. P. and A. Needleman (1996). "Numerical simulations of dynamic crack growth along an interface." International Journal of Fracture **74**(4): 289-324.

Yeung, M. R. (1991). Application of Shi's discontinuous deformation analysis to the study of rock behaviour. Civil Engineering. Berkeley, University of California. **Ph.D.**

Yeung, M. R. (1993). "Analysis of a mine roof using the DDA method." International Journal of Rock Mechanics and Mining Sciences & Geomechanics Abstracts **30**(7): 1411-1417.

Yeung, M. R. and L. L. Leong (1997). "Effects of joint attributes on tunnel stability." International Journal of Rock Mechanics and Mining Sciences **34**(3-4): 348.e341-348.e318.

Yu, Y., J. Zhang and J. Zhang (2009). "A modified Brazilian disk tension test." International Journal of Rock Mechanics and Mining Sciences **46**(2): 421-425.

Zhao, Z. and J. Gu (2009). "Stress recovery procedure for discontinuous deformation analysis." Advances in Engineering Software **40**: 52-57.

Zhao, Z., J. Gu and H. Bao (2007). Understanding fracture patterns of rock mass due to blast load – a DDA approach. Proceedings of the Eighth International Conference on the Analysis of Discontinuous Deformation. Y. Ju, X. Fang and H. Bian. Beijing, China**:** 147-150.

Zienkiewicz, O. C. (1977). The finite element method. London ; New York, McGraw-Hill.

Zienkiewicz, O. C., B. Best, C. Dullage and K. Stagg (1970). Analysis of nonlinear problems in rock mechanics with particular reference to jointed rock systems. Proceedings of the Second International Congress on Rock Mechanics. Belgrade.

Zienkiewicz, O. C. and R. L. Taylor (2000). The finite element method. Oxford ; Boston, Butterworth-Heinemann.

LIST OF PUBLICATIONS

- Zhao, Z.Y., Gu, J. and Bao, H.R., 2007. Stress recovery procedure for discontinuous deformation analysis. 11th International Congress on Rock Mechanics (ISRM), pp. 435-438, 9-13 July, 2007, Portugal.
- Zhao, Z.Y., Gu, J and Bao, H.R. (2007). Understanding fracture patterns of rock mass due to blast load - A DDA approach, 8th International Conference on Analysis of Discontinuous Deformations (ICADD-8): 151-156.
- Bao, H.R. and Zhao, Z.Y. (2009). Indeterminacy of the vertex-vertex contact in the 2D discontinuous deformation analysis, 9th International Conference on Analysis of Discontinuous Deformation (ICADD9): 99-107.
- Bao, H.R. and Zhao, Z.Y. (2009). Modelling crack propagation with nodal-based discontinuous deformation analysis, 9th International Conference on Analysis of Discontinuous Deformation (ICADD9): 161-167.
- Bao, H.R. and Zhao, Z.Y. (2010). An alternative scheme for the corner-corner contact in the two-dimensional discontinuous deformation analysis, Advances in Engineering Software, 41(2): 206-212.
- Bao, H.R. and Zhao, Z.Y., Contact indeterminacy in the two-dimensional discontinuous deformation analysis, this paper is under review.
- Bao, H.R. and Zhao, Z.Y., Nodal-based Discontinuous Deformation Analysis – A Hybrid FEM/DDA Method, the paper is under preparation.